Lehrstuhl für Allgemeine und Analytische Chemie
Chair of General and Analytical Chemistry

Dissertation

Hydrogen Trapping in Iron and Iron-Based Alloys

Wolfgang Siegl

November 2020

MONTANUNIVERSITÄT LEOBEN
www.unileoben.ac.at

EIDESSTATTLICHE ERKLÄRUNG

I declare on oath that I wrote this thesis independently, did not use other than the specified sources and aids, and did not otherwise use any unauthorized aids.

I declare that I have read, understood, and complied with the guidelines of the senate of the Montanuniversität Leoben for "Good Scientific Practice".

Furthermore, I declare that the electronic and printed version of the submitted thesis are identical, both, formally and with regard to content.

Date 20.11.2020

Signature Author
Wolfgang Siegl
00635287

Submitted by

Dipl.-Ing. Wolfgang Siegl

00635287

Supervisor

Ao.Univ.-Prof. Dipl.-Ing. Dr.mont. Gregor Mori

Mentor

Univ.-Prof. Dipl.-Ing. Dr.mont. Ronald Schnitzer

Acknowledgement

The present thesis is the result of my work at the Chair of General and Analytical Chemistry of the Montanuniversitaet Leoben in cooperation with Materials Center Leoben Forschungs GmbH, voestalpine Tubulars GmbH & Co KG, voestalpine Stahl Donawitz GmbH, and Robert Bosch GmbH.

I am deeply grateful to my supervisor Ao.Univ.-Prof. Dipl.-Ing. Dr. Gregor Mori for his unconditional trust, support, and dedication. Not only am I profoundly impressed by his professional knowledge, analytical approach, and zeal for work, also his appreciation, respect, and honesty towards others will serve as inspiration and example for my future life.

During my time at the Chair, I had the honor to experience the direction of two heads of institute. I thank Univ.Prof. Dipl.-Ing. Dr. Thomas Prohaska and em.O.Univ.-Prof. Dipl.-Ing. Dr. Wolfhard Wegscheider for their excellent leadership and guidance.

I would like to thank my project partners Dr. Werner Ecker for productive debates and project coordination and Dr. Jürgen Klarner, Dr. Gerald Klösch, Dr. Holger Schnideritsch, and Dr. Gerald Winter for the excellent cooperation and for providing the valorous link between fundamental research and practical application.

I am grateful to my mentor Univ.-Prof. Dipl.-Ing. Dr. Ronald Schnitzer for his support and for passing on his extensive knowledge of materials, and I thank Univ.Doz. Univ.-Prof. Dipl.-Ing. Dr. Reinhard Pippan for his invaluable advice and expertise on material treatment and interpretation of results.

It was a pleasure to work with my colleague Dipl.-Ing. Anton Trautmann, I am very thankful for his help in technical and organizational matters and for the time we spent together at conferences. I want to thank my co-workers Dipl.-Ing. Mathias Truschner, Dipl.-Ing. Bernd Loder, and Dr. Jojo Vidic for the constructive exchange as well as Melissa Eberhard, Hubert Falk, and Christine Opper for assisting me with their practical know-how. I am grateful to all colleagues and staff for the pleasant working atmosphere at the Chair of General and Analytical Chemistry.

I am thankful to Dr. Andreas Drexler, Prof. Dr. Tom Depover, and Prof. Dr. Kim Verbeken for their valuable contribution and discussions. Thanks is due to Dipl.-Ing. Peter Kutleša, Silke Modritsch, Franz Hubner, Robin Neubauer, Mag. Velislava Terziyska, Dr. Michael Tkadletz, Dr. Vsevolod Razumovskiy, Wolfgang Rostig, and Antoine Trutmann for their help and collaboration as well as Alexander Wheeldon for linguistic assistance. I thank Morgane Bonvin for the beautiful illustrations.

Finally, I want to thank my parents Irmtraut and Elmar Siegl for their lifelong support, encouragement, and motivation. They made it possible for me to write this thesis, I dedicate this work to them.

The author gratefully acknowledges the financial support under the scope of the COMET program within the K2 Center “Integrated Computational Material, Process and Product Engineering (IC-MPPE)” (Project No 859480). This program is supported by the Austrian Federal Ministries for Climate Action, Environment, Energy, Mobility, Innovation and Technology (BMK) and for Digital and Economic Affairs (BMDW), represented by the Austrian research funding association (FFG), and the federal states of Styria, Upper Austria and Tyrol.

Kurzfassung

Wasserstofffallen in Eisen und eisenbasierten Legierungen

Ziel dieser Arbeit war die Untersuchung des Verhaltens von Wasserstoff in Reineisen und eisenbasierten Werkstoffen sowie der Beeinflussung dieses Verhaltens durch die Mikrostruktur. Versetzungen, Korngrenzen und Ausscheidungen können als Wasserstofffallen im Material wirken, speichern Wasserstoff und verlangsamen die Wasserstoffdiffusion.

Eine Reihe von unterschiedlich behandelten Eisenmaterialien und Eisenlegierungen mit verschiedenen Arten und Dichten von Wasserstofffallen wurden analysiert. Elektrochemische Permeationsversuche wurden durchgeführt, um die Diffusivität von Wasserstoff zu ermitteln, und thermische Desorptionsspektrometrie wurde zur exakten Bestimmung der vorhandenen Fallen im Material sowie deren Bindungsenergien für Wasserstoff eingesetzt.

Die Ergebnisse zeigen, dass Fallen durch mechanische Verformung des Materials erzeugt werden können, dabei bewirken stärkere Verformungsgrade größere Fallendichten. Die Erholung des Metallgitters durch entsprechende Wärmebehandlung führt zum Ausheilen von Gitterfehlern und verringert die Fallenkonzentration. Aktivierungsenergien von Versetzungen, Korngrenzen und Martensitphasengrenzen liegen im Bereich von 27 bis 37 $kJ\,mol^{-1}$, stärkere Fallen sind Leerstellen in Eisen mit einer Aktivierungsenergie von rund 51 $kJ\,mol^{-1}$. Ein nennenswerter Einfluss von Korngrenzen auf die Aufnahme von Wasserstoff wurde nur in Materialien mit Korngrößen im Nanometerbereich beobachtet, nicht jedoch bei Korngrößen im Mikrometerbereich und darüber. Carbidausscheidungen sind wirksame Wasserstofffallen, Aktivierungsenergien von knapp 61 $kJ\,mol^{-1}$ wurden für Titancarbide ermittelt. Ein positiver Beitrag von tiefen Fallen auf die Widerstandsfähigkeit eines Materials gegenüber Wasserstoffversprödung wird vermutet, während sich flache Fallen im Material nachteilig auswirken könnten. Zusätzlich wird eine hohe Diffusivität für Wasserstoff als vorteilhaft eingeschätzt.

Abstract

Hydrogen Trapping in Iron and Iron-Based Alloys

The aim of this research was to analyze the behavior of hydrogen in iron and iron-based materials and how it is influenced by different microstructural components. Dislocations, grain boundaries, and precipitates can act as hydrogen traps, accumulating hydrogen and hindering hydrogen diffusion in the material.

A series of pure iron and iron-based alloys was analyzed, each containing different types and densities of hydrogen traps. Electrochemical permeation experiments were done to determine hydrogen diffusivity, thermal desorption spectroscopy was used to gain detailed information on the number and types of traps present in the material as well as their trapping energy for hydrogen.

The results show that hydrogen traps can be created by mechanical material deformation. More severe deformation increases the number of generated traps. Appropriate heat treatment allows lattice recovery and reduces the trap density. Trap activation energies of dislocations, grain boundaries, and martensite lath boundaries range from 27 to 37 $kJ\,mol^{-1}$, vacancies in iron are stronger traps with an activation energy of around 51 $kJ\,mol^{-1}$. A significant trapping effect of grain boundaries was only observed in materials with grain sizes in the nanometer region but not in materials of larger grain sizes. Carbide precipitates are effective hydrogen traps with activation energies of up to 61 $kJ\,mol^{-1}$ for Ti-carbide. It is assumed that strong traps have a positive effect on a material's resistance against hydrogen embrittlement while weak traps have the opposite effect. In addition, increased diffusivity for hydrogen may reduce the susceptibility to hydrogen embrittlement.

Contents

Page

1 Introduction

Hydrogen uptake by metals poses a serious problem in numerous industrial fields, as it can result in severe impairment of physical and mechanical properties. Especially high-strength ferritic steels are prone to hydrogen-induced failure at stresses below their normal load-bearing level. Hydrogen encourages brittle material fraction by segregating at lattice imperfections and accumulating in strained lattice regions, a phenomenon widely known as hydrogen embrittlement. [1–3]

The behavior of hydrogen in iron and iron-based materials and the mechanisms of the embrittling effect have been studied since the 19th century [4]. In 1949, Darken and Smith [5] were the first to suggest that hydrogen diffusion is hindered by imperfections in the lattice, introduced by cold working and denominated as hydrogen traps. In addition to affecting the diffusivity, significant amounts of hydrogen can be accumulated at lattice defects. In the 1960s, Devanathan and Stachurski [6] developed a method for studying hydrogen permeation through metal membranes. It is to this day one of the most common techniques to investigate hydrogen diffusion and trapping in iron and steel. In the 1980s, thermal desorption studies became popular for characterizing hydrogen traps in metal. The analysis of effusing hydrogen in dependence of the temperature gives insights on the trapping ability of lattice defects and allows the determination of their binding energies for hydrogen.

Despite the great effort invested in clarifying the interactions of hydrogen and material microstructure, uncertainties remain in the understanding of large parts of the processes and mechanisms. The aim of this work is to contribute to the comprehension of the principles of hydrogen diffusion and trapping, and how they promote or reduce the susceptibility of iron and steel to hydrogen embrittlement.

2 Hydrogen in Iron and Steel: Theoretical Overview

2.1 Hydrogen Uptake

During the life cycle of iron and steel materials, various possibilities arise for hydrogen uptake. Metallurgical operations during material production can act as sources for hydrogen as well as processing and finishing operations on workpieces and components, such as pickling, welding, and galvanizing. During operation, hydrogen atmospheres and pressure, corrosion in aqueous electrolytes, and cathodic corrosion protection can cause undesirable hydrogen ingress. [2]

In a hydrogen gas atmosphere, hydrogen molecules are physisorbed on the metal surface. They may directly dissociate to hydrogen atoms in the presence of an active site or diffuse on the surface before dissociating. The process of adsorption and dissociation can be described as [7]

$$H_2(g) \rightleftharpoons H_{ads} + H_{ads} \quad . \qquad (1)$$

The adsorbed hydrogen atoms are subsequently absorbed into the metal lattice:

$$H_{ads} \rightleftharpoons H_{abs} \quad . \qquad (2)$$

Recombination to gaseous hydrogen can take place at the surface if two adsorbed hydrogen atoms get the chance to interact before being absorbed:

$$H_{ads} + H_{ads} \rightleftharpoons H_2(g) \quad . \qquad (3)$$

The overall uptake reaction can be written as the sum of adsorption and absorption reactions as

$$H_2(g) \rightleftharpoons 2\,H_{abs} \quad . \qquad (4)$$

In case of thermodynamic equilibrium between gaseous hydrogen and hydrogen dissolved in the first atomic layers under the metal surface, the hydrogen concentration in the metal is described by Sieverts' law as

$$c_H = K_S \cdot \sqrt{p_{H_2}} \quad , \qquad (5)$$

where c_H is the hydrogen concentration within the metal, K_S the Sieverts' constant, and p_{H2} the partial pressure of hydrogen [8,9]. Above hydrogen pressures of 30 MPa, the fugacity f_{H2} should be used instead of the pressure p_{H2}, as the gas no longer exhibits ideal behavior [10]. For iron, Sieverts' law is valid and produces reliable results up to around 10 MPa. At higher pressures, this law gives larger values for hydrogen dissolved in the material than detected in practical experiments. [11] The hydrogen concentration c_H at a given pressure and temperature is referred to as solubility S [8].

A common source of hydrogen is anodic corrosion of iron in the presence of electrolytes. In laboratory testing, electrochemical hydrogen charging is used to load samples with hydrogen

in a controlled manner. The processes can be described by different equations, depending on the pH of the electrolytes. In acidic and neutral solutions by [7]

$$H^+ + e^- \rightleftharpoons H_{ads} \quad , \qquad (6)$$

and in alkaline solutions by [12]

$$H_2O + e^- \rightleftharpoons H_{ads} + OH^- \quad . \qquad (7)$$

The next step consists of the absorption of adsorbed hydrogen atoms into the lattice:

$$H_{ads} \rightleftharpoons H_{abs} \quad . \qquad (8)$$

In electrolytical environments, hydrogen recombination can take place. If the hydrogen in solution exceeds the solubility limit, gas bubbles will form at the surface according to [7]:

$$H_{ads} + H_{ads} \rightleftharpoons H_2 \quad . \qquad (9)$$

Hydrogen absorption and desorption reactions are described in further detail in Section 2.4.1.

In transition metals, the absorbed hydrogen atom is considered to exist as a proton with a delocalized electron, which is lost to the electronic band of the metal. The Fermi electrons shield the proton's positive charge and make it effectively charge neutral. Diffusing hydrogen is often referred to as hydrogen atom and even though not formally correct, this simplified designation will also be adopted in this work. [7,13]. The macroscopical charge neutrality of the metal lattice is preserved by a higher electron concentration in the vicinity of the proton. In areas of radial distances below approximately 10^{-10} m around the proton, its positive charge is not fully shielded, resulting in repulsive forces between interstitial protons and positively charged iron atoms, causing local expansion and distortion of the lattice [14,15]. [2] Hydrogen occupies interstitial lattice sites in iron, both tetrahedral and octahedral sites are available. In body-centered cubic (bcc) α-iron, tetrahedral sites with an inner radius of $0.36 \cdot 10^{-10}$ m offer more space than octahedral sites with an inner radius of $0.19 \cdot 10^{-10}$ m (see Figure 1), whereas in face-centered cubic (fcc) γ-iron, the octahedral sites are larger than tetrahedral, with inner radii of $0.52 \cdot 10^{-10}$ m and $0.28 \cdot 10^{-10}$ m, respectively [2,16]. A given site is only occupied once [17]. For α-iron, the occupancy of (larger) tetrahedral sites is preferred at lower temperatures, octahedral sites tend to get occupied only with increasing temperatures. At temperatures above 100 °C, entropic factors are the cause for a beginning occupation of octahedral sites [7,18]. Da Silva et al. calculated the fractions of filled octahedral sites to be 2 % at 300 °C, 23 % at 1023 °C, and around 50 % at 1450 °C [19]. Hydrogen occupying interstitial lattice sites is designated as *ideally dissolved*. In addition to ideal lattice solution, hydrogen readily accumulates at lattice imperfections in iron and steel, such as grain boundaries, dislocations and vacancies, a process commonly known as *hydrogen trapping*. Trapped hydrogen does per definition not count as dissolved [2].

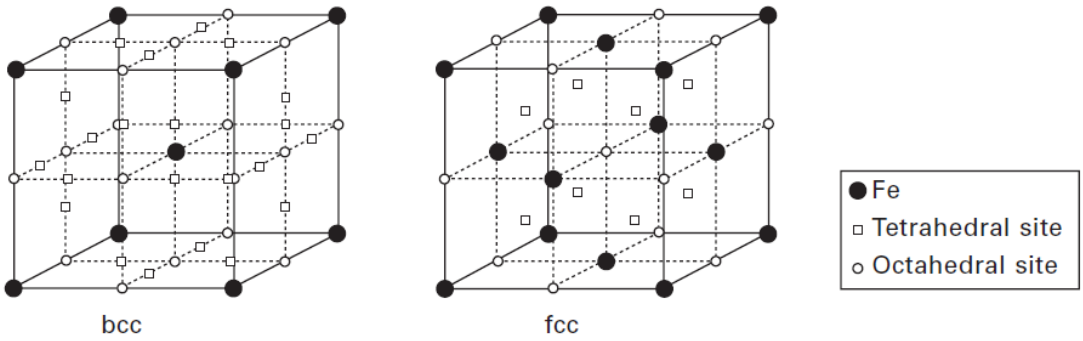

Figure 1: Tetrahedral and octahedral lattice sites in bcc and fcc iron [1]

The solid solubility S of hydrogen in iron is temperature-dependent and its value is usually determined under specific conditions of exposure of the metal to gaseous hydrogen. Figure 2 shows solubility data collected by Kiuchi and McLellan [18] for pure α-iron under a hydrogen atmosphere of 0.1 MPa, the solubility S given as the atomic ratio of hydrogen atoms per iron atom. While the solubility values match well for higher temperatures, a pronounced scatter is evident for temperatures below approximately 300 °C, which is caused by the contribution of hydrogen trapping in different types of traps. Another observation is a lack of conformity of the data with an Arrhenius plot of ln S vs. $1/T$, which is independent of the scattering. [7,18] Da Silva et al. showed this deviation to be consistent with the varying relation of occupied tetrahedral and octahedral lattice sites along the temperature range [19].

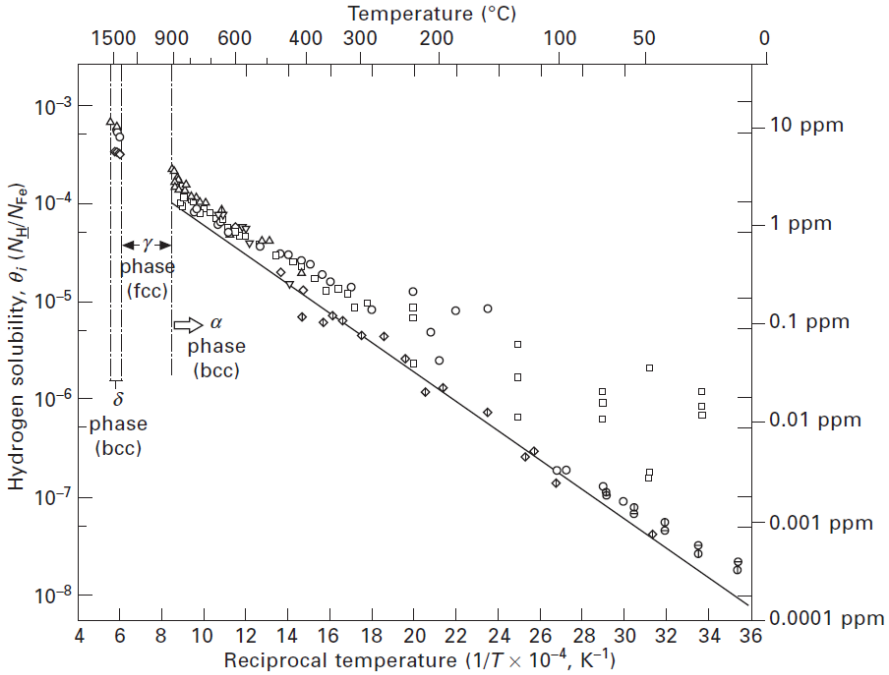

Figure 2: Various data sets of hydrogen solubility vs. temperature under a hydrogen atmosphere of 0.1 MPa. Taken from [1], originally from [18].

An expression for the solubility S was derived by Hirth [20] from the analysis of a set of data as

$$S = 0.00185\sqrt{p} \cdot \exp\left(\frac{-3440}{T}\right) \quad , \qquad (10)$$

with S in atomic ratio, the pressure p in multiples of 10^5 Pa, and the temperature T in K. In equilibrium at room temperature and a hydrogen atmosphere of 0.1 MPa, solubility of hydrogen in α-iron has an atomic ratio of around $2 \cdot 10^{-8}$, correspondent to approximately $3 \cdot 10^{-4}$ ppmw [20–22].

Hydrogen solubility is higher for face-centered cubic γ-iron than for body-centered cubic α-iron, as apparent in Figure 3.

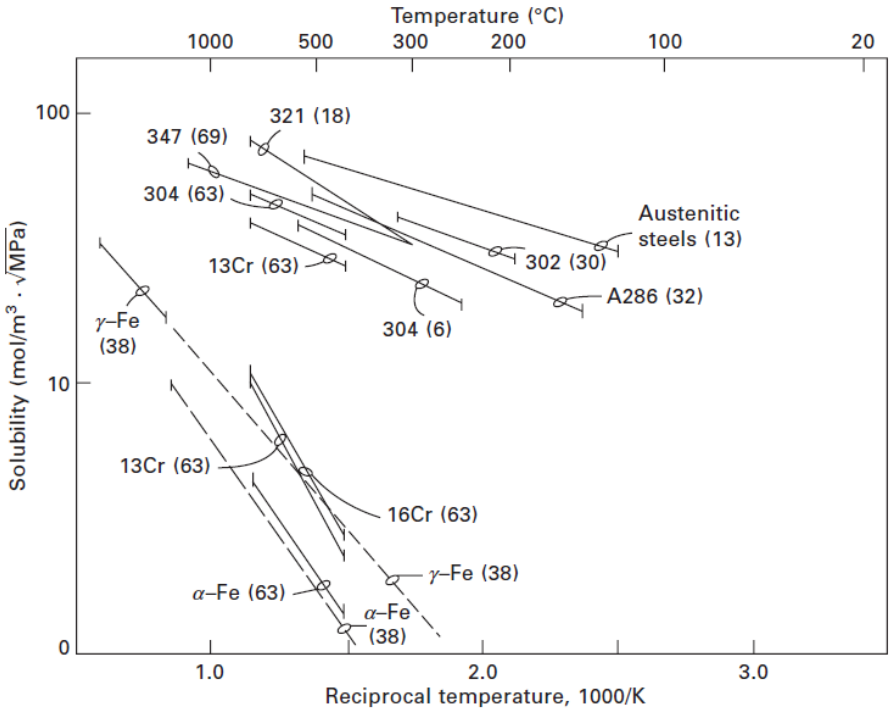

Figure 3: Hydrogen solubilities of iron and stainless steels. The two sets of data for 13Cr steel represent its ferritic and austenitic forms. Taken from [7], originally from [23].

Figure 4 illustrates the temperature dependence of the solid solubility S of various metals in a hydrogen atmosphere of 0.1 MPa. A negative slope in this Arrhenius plot of $1/T$ vs. S indicates an endothermic hydrogen absorption, meaning that the energy of hydrogen is higher in solid solution in the metal than in the gaseous molecule. [21]

The heat release per absorbed hydrogen atom is denoted as the enthalpy of solution ΔH^0_{sol} [17]. A positive ΔH^0_{sol} indicates an endothermic hydrogen absorption into the metal, while for an exothermic absorption, ΔH^0_{sol} is negative. Metals with more negative enthalpies of solution have higher affinities for hydrogen uptake, whereas the solubility for materials with highly positive

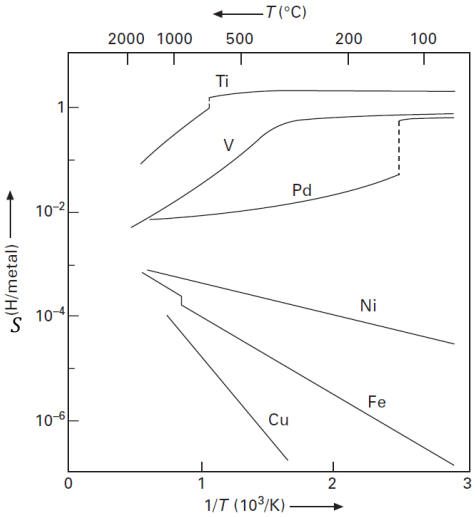

Figure 4: Hydrogen solubility for pure metals in hydrogen gas of 0.1 MPa. Adapted from [7], originally from [17].

values is often negligible [24]. Table 1 lists the enthalpies of solution of hydrogen for different metals. It is important to note that ΔH^0_{sol} is valid only for hydrogen absorption into the ideal lattice and cannot be used to describe hydrogen accumulating at trap sites [25]. Hydrogen traps can potentially cause considerably higher hydrogen concentrations than would be expected from the enthalpy of solution. From an atomistic point of view, elastic and electronic contributions play an important role for determining the value of ΔH^0_{sol}. Elastic energy input is necessary for expanding the metal lattice during the dissolution of hydrogen. If no change of the electronic structure is assumed during dissolution, the hydrogen atom's electron experiencing delocalization has to take on states above the Fermi level, resulting in a positive contribution to the enthalpy of solution. [8]

Table 1: Enthalpy of solution ΔH^0_{sol} of hydrogen in various metals

Element	ΔH^0_{sol} [kJ mol^{-1}]	Ref.
α-Ti	-45.2	[26]
Pd	-9.6	[27]
Ni	16.7	[28]
α-Fe	28.6	[21]
Cr	47.7	[29]
Mo	51.4	[29]
Cu	54.8	[30]

2.2 Hydrogen Trapping

2.2.1 Principles of Trapping

Hydrogen concentrations in iron and steel can reach significantly higher values than the theoretical lattice solubility or Sieverts' law would predict, especially at temperatures below 300 °C. This is explained by hydrogen not only undergoing solid solution in the lattice, but also being accumulated at microstructural features and crystal defects, which provide an energetically favored environment for occupancy by hydrogen [31]. These sites of elevated hydrogen concentration are referred to as *hydrogen traps*, the process as *trapping*.

The primary effects of hydrogen trapping are the increase of hydrogen concentration or apparent hydrogen solubility and the decrease of the effective hydrogen diffusivity [32,33]. The total hydrogen concentration c_{total} in the material is the sum of lattice hydrogen concentration c_L and trapped hydrogen concentration c_T [34]:

$$c_{total} = c_L + c_T \quad . \qquad (11)$$

When defining the hydrogen concentration c as the number of hydrogen atoms per unit volume, it can be written as the product of the number of lattice or trap sites per unit volume N and the fractional occupancy of these sites θ:

$$c_L = N_L \, \theta_L \quad , \qquad (12)$$

and

$$c_T = N_T \, \theta_T \quad , \qquad (13)$$

where the subscripts L and T stand for lattice and traps, respectively [21].

Basically, all kinds of defects and lattice imperfections can act as trapping sites. Among these are vacancies, microvoids, dislocations, and grain boundaries. Additionally, segregations and inclusions as e.g. carbides of the elements Ti, V, Mo, and Cr as well as the internal interfaces can work as hydrogen traps. Figure 5 illustrates various hydrogen trap sites in an iron matrix. The strength of a trap is characterized by the trap activation energy E_a or the trap binding energy E_b and the number of traps in the material by the trap density N_T [35,36].

An accumulation of hydrogen atoms in ideal lattice areas other than neighboring interstitial sites is unlikely, recombination of atoms to hydrogen gas is not to be expected in the ideal lattice [2]. Recombination of atoms to molecular hydrogen can however occur in zones of large free internal volumes, such as voids or fissures. The resulting internal pressure rise can lead to cracking and progressive failure of the material. [37]

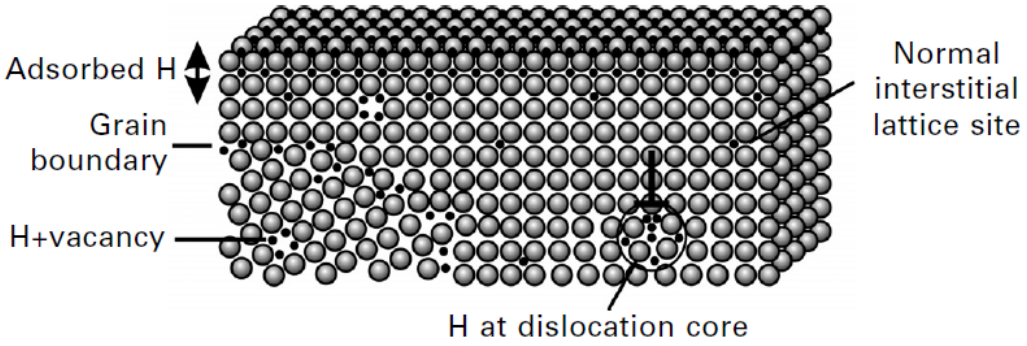

Figure 5: Schematic illustrations of different trap sites in iron and steel on the atomic scale. Taken from [38], originally from [39].

The formation of metal hydrides can have detrimental embrittling effects in materials as e.g. Titanium-based alloys. In iron, this effect is not expected due to iron hydrides being reported to exist in stable form only at hydrogen pressures in the gigapascal range [40,41].

2.2.2 Energy Analysis

Traps can be classified according to their activation energy or binding energy for hydrogen. So called weak or shallow traps have low activation or binding energies, strong or deep traps exhibit large energies. Choo and Lee described the trapping process based on the adsorption/desorption kinetics of hydrogen, from a chemical viewpoint it can be interpreted as a reversible reaction of an interstitial hydrogen atom with a vacant trap site [42–44]:

$$\boxed{\mathrm{H}}_{\mathrm{trap}} \rightleftarrows \square_{\mathrm{trap}} + \mathrm{H}_{(\mathrm{in\ lattice})} \quad . \qquad (14)$$

Figure 6 depicts the energy levels in the metal lattice in the vicinity of a hydrogen trap. The horizontal lines represent levels of constant energy, these are different for trapping sites (A) and normal interstitial lattice sites (B). The difference between the trap and the lattice energy level is the interaction energy between the trap site and hydrogen and is defined as the trap's binding energy for hydrogen *(E_b)*. To escape a trap, a hydrogen atom must overcome the trap activation or detrapping energy *(E_a)*, which is the sum of the binding energy and the saddle point energy around the trap *(E_s)*. The trap activation energy E_a is usually higher than the energy of normal lattice diffusion *(E_D)*, also called migration energy. [44,45] Trapping energies are commonly given in kJ per mole of hydrogen, kJ mol(H)$^{-1}$, customarily abbreviated as kJ mol^{-1}.

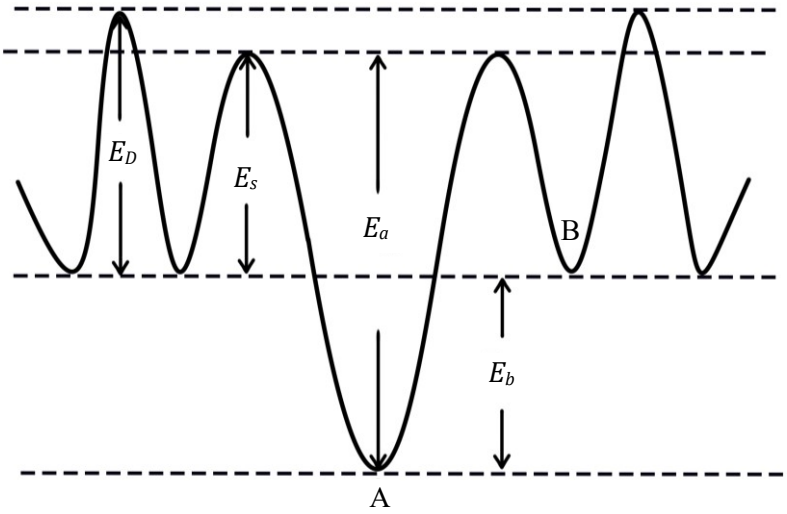

Figure 6: Energy levels at trap sites (A) and lattice sites (B) in a metal lattice. Adapted from [46].

It is common practice to designate weak traps as reversible and strong traps as irreversible. A trap is considered reversible if fluctuations of thermal energy at a certain temperature (generally room temperature or slightly above) are sufficient to cause hydrogen atoms to jump out of the trap and an equilibrium is achieved between lattice site and trap site. Hence, at a given temper-

ature, reversible traps release hydrogen and can act as hydrogen sources for the lattice or for stronger traps. Irreversible traps, on the other hand, are characterized by a potential energy well which is deep enough to keep hydrogen trapped at a specific temperature. The hydrogen's thermal energy is not enough to overcome the energy barrier for detrapping, temperatures significantly higher than room temperature are necessary. Irreversible traps therefore act as sinks with minimal probability of hydrogen escaping. It is to be noted that, apart from temperature, also mechanical stress can cause hydrogen release from traps. [7,13,47,48] Figure 7 schematically illustrates the energy levels of normal interstitial lattice sites and reversible and irreversible traps in a metal matrix.

There is no strictly defined energy demarcation for distinguishing weak, reversible and strong, irreversible traps, several conventions are common. Grabke and Riecke [9] use the trap binding energy for the definition and determine weak traps with $E_b < 30$ kJ mol^{-1} and strong traps with $E_b > 50$ kJ mol^{-1}. Troiano [49] classified traps according to the value of their binding energy in relation to hydrogen's heat of solution in iron ($\Delta H^0_{sol} = 29$ kJ mol^{-1}): traps are defined as weak if $E_b < \Delta H^0_{sol}$, traps are moderate if $E_b \approx \Delta H^0_{sol}$, and traps are strong if $E_b > \Delta H^0_{sol}$. Pressouyre and Bernstein's [50] classification is based on the trap activation energy and describes weak traps with $E_a < 60$ kJ mol^{-1} and strong traps with $E_a > 60$ kJ mol^{-1}.

The occupancy of trap sites is determined by the trap's binding energy and the hydrogen concentration in the neighboring lattice sites [51]. Strong traps are already saturated at low concentrations of hydrogen, they exhibit high occupancy due to a high capture rate and low release rate [51]. As hydrogen is available in the lattice, the strongest traps are the first to become filled, regardless of their density. Subsequently, the occupancy of weaker traps is increased before hydrogen diffuses to nearby locations. [9,52]

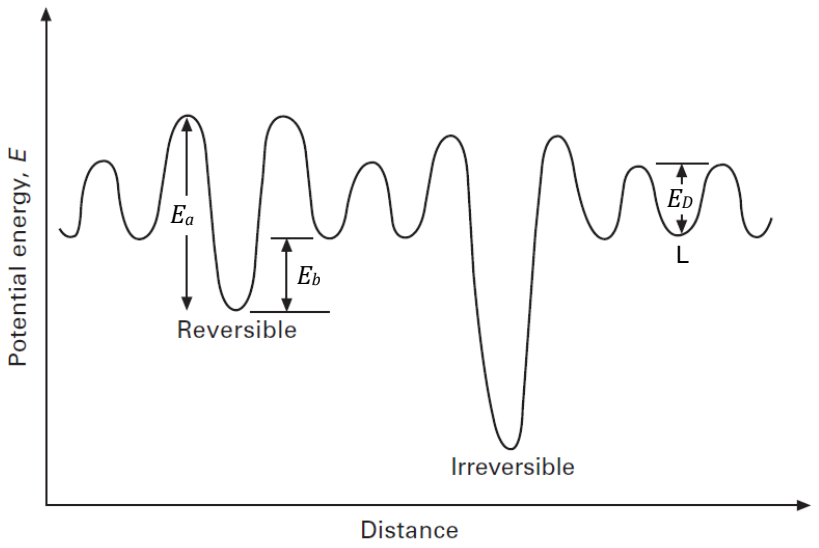

Figure 7: Schematic illustration of potential energy levels of lattice sites (L) and reversible and irreversible trap sites [7]

2.2.3 Trapping Mechanisms

Two types of trapping mechanisms can be distinguished: attractive and physical. Most traps are of mixed attractive and physical nature. Attractive traps are characterized by exerting attractive force on diffusing hydrogen atoms. The force can be a result of electrical fields, stress fields, or temperature gradients. Typically, the disorder of the electron allocation and lattice expansion in the surrounding of dissolved hydrogen in iron cause interactions between hydrogen atoms and trap sites. As a hydrogen atom gives up its electron to the metal's electron gas, defects introducing electron vacancies will attract hydrogen in an attempt to achieve local neutrality. This occurrence is an example of electrical force, it causes hydrogen to be attracted to impurities of elements located on the left in the periodic table of the element composing the surrounding matrix [15]. Stress fields induced by defects such as dislocations, coherent and semi-coherent grain boundaries, inclusions, as well as crack tips cause a distortion of the metal lattice. Changes in the chemical potential of hydrogen as a result of increasing hydrostatic compressive or tensile stresses cause the diffusion of hydrogen out of compressed lattice zones into elastically dilated areas, an event commonly known as Gorsky effect. Hydrogen tends to migrate towards centers of dilation and is consequently trapped there. For example, stress fields around cracks produce high triaxial stresses that lead to a dilation of the metal lattice and hence draw hydrogen towards the crack. Thermal gradients cause attractive forces, as the solubility of hydrogen in iron increases with temperature, hydrogen will therefore be attracted to hotter areas of the metal.

Physical traps do not actively attract hydrogen. A diffusing hydrogen atom will rather fall into these traps randomly and subsequently have difficulty escaping. Physical traps are related to discontinuities in the lattice, at which it is energetically more favorable for hydrogen to remain, such as voids, high angle grain boundaries, and incoherent internal interfaces.

Only in extreme cases can traps accurately be characterized as purely of one type, attractive or physical, as most traps exhibit combined attractive and physical character. For example, all defects provoke an electronic perturbation, inducing electrical forces, and traps associated with stress fields tend to have additional physical nature. It is, however, customary to define a certain trap as attractive or physical, if this character is clearly dominant over the other. [2,13,53,54]

Attractive trapping is generally more reversible than physical trapping. This becomes apparent when comparing a purely attractive and a purely physical trap of the same activation energy E_a, as shown in Figure 8. A hydrogen atom can escape the attractive trap by a series of small, very probable jump increments. To escape the physical trap, one large and less probable jump is necessary. [54]

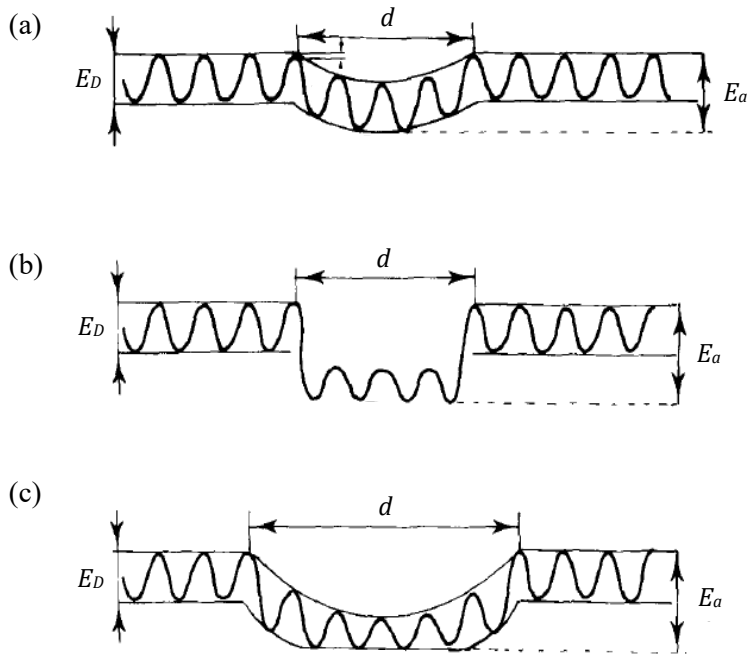

Figure 8: Schematic illustration of the energy steps necessary for the diffusion of a hydrogen atom through a metal lattice when encountering (a) an attractive trap, (b) a physical trap, (c) a mixed trap. The hydrogen atom experiences an attractive force in the lattice region of dimension *d*. [54]

In practical operation, hydrogen traps can be either beneficial or detrimental, depending on the hydrogen exposition of the workpiece and the type of trap. Reversible or weak traps can act as internal reservoirs and sources of hydrogen, which can be released by thermal or mechanical energy input, diffuse to highly stressed lattice sites and induce hydrogen embrittlement [35,55,56]. Irreversible traps may increase the resistance to cracking by accumulating hydrogen atoms or by acting as a sink for hydrogen migrating towards zones of high stresses and high risk of embrittling. Especially when a limited amount of hydrogen is present, well distributed irreversible traps can have a positive effect and delay hydrogen cracking. [49,55,57–59]

2.2.4 Trapping at Lattice Defects

As discussed before in this section, lattice defects are the main cause of hydrogen trapping in iron and steel. The most commonly found defects and their hydrogen trapping abilities are discussed hereinafter.

2.2.4.1 Grain Boundaries

Grain boundaries are the earliest discovered lattice defects and have been profoundly studied. Nevertheless, the interface of grains of different orientations is highly intricate and many uncertainties remain for a complete understanding. Types, structures, and misorientations of grain boundaries can be very diverse and therefore exhibit a broad range of binding energies between hydrogen atoms and the boundary structure. The binding energy depends on the structural complexity of the interface, with the possibility of a variety of trap sites with different energy values at and around one boundary line. Generally, the number of trap sites available at grain boundaries is rather small. The overall number can obviously be increased by grain refinement. [21,60]

The trapping energies of grain boundaries are relatively low, making them rather weak traps. The values are substantially lower than for vacancy trapping in the same material, suggesting that grain boundaries do not exhibit an open-volume character as vacancy defects do. As mentioned above, a complex atomic structure at the interface can result in a series of different trapping positions with varying binding energies. While the number of differing energies is low for coinciding grain boundaries, the energetical situation of less regular boundaries is more complicated. [60] Du et al. [61] studied different types of grain boundaries in bcc and fcc iron by DFT. For bcc iron, close-packed low energy grain boundaries show little deviations in the local atomic coordination and the distance between the atoms along the boundary. In the grain boundary's vicinity, the interstitial sites resemble those of the undisturbed lattice. Modified sites, which attract hydrogen, are only available directly at the interface. Higher-energy grain boundaries with more open interface structures lead to a considerably stronger disturbed lattice accompanied with different local coordinations and atomic distances. This results in various altered sites at and around the grain boundary that can act as trap sites, including relatively large interstitial voids, which may possibly accommodate more than one hydrogen atom. Consequently, higher-energy, more unfitting grain boundaries can trap more hydrogen. Matsumoto et al. [62] drew similar conclusions from DFT calculations on bcc iron, finding a correlation between grain boundary energy, free volume, and hydrogen concentration. The larger gaps at higher-energy grain boundaries allow more hydrogen atoms to be trapped.

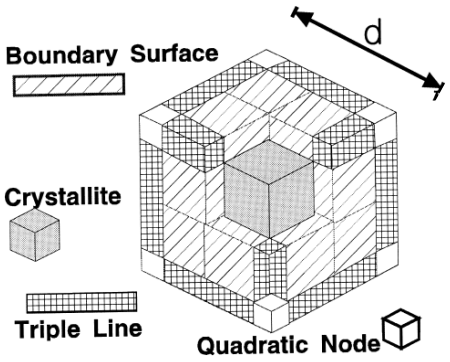

Figure 9: Schematic illustration of the phase mixture in a grain of polycrystalline material of grain size d. Adapted from [63].

Constituent elements determining structure and characteristics of a conjunction of singular grains are the crystallites themselves and intercrystalline phases such as grain boundaries, triple line junctions, and quadratic nodes, as well as pores, as illustrated in Figure 9. With decreasing grain size, especially in the nanometer region, the volume fraction of crystallites decreases exponentially, while the volume fractions of grain boundaries, triple line junctions, and quadratic nodes increase, as illustrated in Figure 10. [63] In 2D simulations of X70 steel, Yazdipour et al. [64] observed an exponential increase of grain boundary surface area per unit volume with decreasing grain size. With grain boundaries acting as hydrogen traps, a strong increase in trap density can be expected with diminishing grain size, particularly for nanosized grains.

Data published in literature for energy values for hydrogen trapped at grain boundaries in iron and iron-based materials as well as the method of determination is shown in Table 2 on the following page.

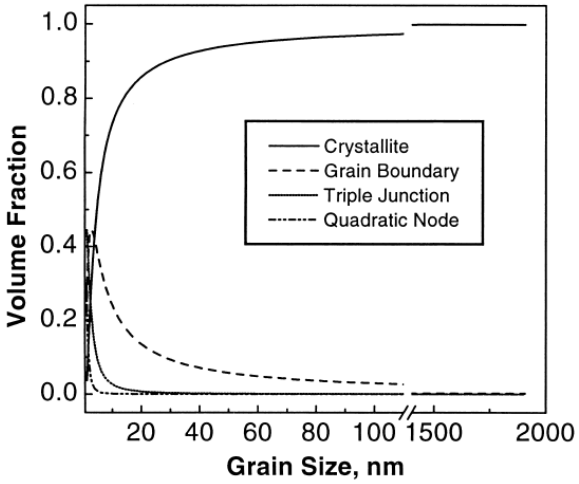

Figure 10: Volume fractions of crystallites and intercrystalline phases as function of grain size [63]

Table 2: Energy values published for hydrogen trapped at grain boundaries

Material	Details	E_b [kJ mol^{-1}]	E_a [kJ mol^{-1}]	Method	Ref.
Pure iron		9.6	17.2	TDA	[44]
Pure iron			19.7	TDA	[3]
Pure iron		49		TDS	[65]
Fe-0.15Ti		26.1		Hall-Petch-slope	[66]
0.05C-0.22Ti-2.0Ni steel	Combined grain boundaries and dislocations		~ 22	TDS	[67]
0.42C-0.30Ti steel	Combined grain boundaries and dislocations		~ 32	TDS	[67]
Experimental low alloyed steel			24–33	TDS	[68]
Steel		17.2		EP and TDS modeling	[69]
Duplex stainless steel			22.5–28.5	TDS	[70]
13 % Cr steel	Grain boundaries or dislocation	38.7		EP	[71]
AISI 4340 steel		55		TDS	[72]

2.2.4.2 Dislocations

Dislocations are linear defects in the metal lattice. An edge dislocation can be imagined as a plane of atoms ending inside the crystal, as if two faces of the ideal crystal in Figure 11(a) were separated and an extra half-plane of atoms inserted. In Figure 11(b), the additional plane of atoms is illustrated as plane ABCD, the line DC constitutes an edge dislocation. The atoms along either side of plane ABCD are displaced by one atom spacing compared to the undisturbed state, yet the only large disturbances of atom positioning relative to their neighbors are close to the dislocation line DC. A screw dislocation is created by displacing the ideal crystal in Figure 11(a) on one side of ABCD relative to the opposing side in direction AB by the length of one atom distance. This geometry corresponds to a single surface helicoid and is visualized in Figure 11(c), the line DC represents the screw dislocation. Dislocations can also be of mixed character, combining both edge and screw components. [73,74]

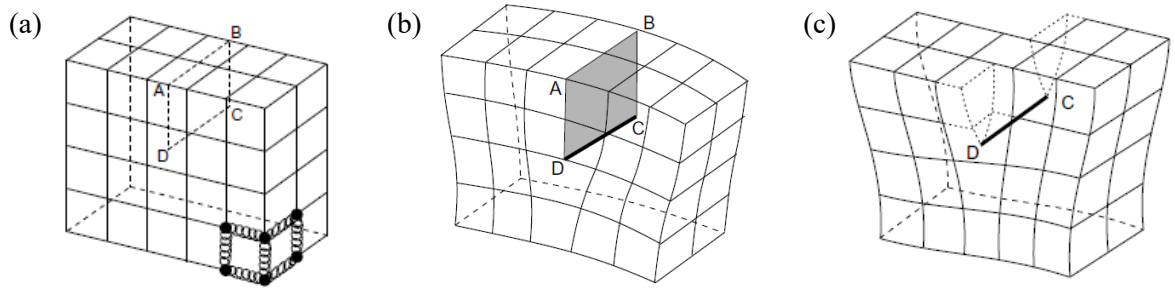

Figure 11: Schematic visualization of dislocations:
(a) ideal crystal, (b) edge dislocation, (c) screw dislocation [73]

Theoretical models describe hydrogen trapping by dislocations as an elastic interaction between the stress fields of dislocations and the strain field around interstitially dissolved hydrogen atoms. The effect is stronger for edge dislocations because hydrogen atoms cause an expansion of the lattice by cubic distortion and the created hydrostatic strain field results in a forceful interaction with the dilatational stress field below the edge dislocation line. In contrast, shear components, which are dominant in screw dislocations, do not interact with the hydrogen atom's hydrostatic strain component, causing an overall weaker and shorter-ranging elastic interaction. [8,21,39,60,75]

Tensile and compressive stresses around edge, screw, and mixed dislocations increase continuously with proximity to the core. Thus, binding energy for hydrogen can vary along the stress field of the dislocation, with augmenting energy towards the dislocation core. Atomistic calculations by Taketomi et al. [76] on iron suggest the strongest trap sites to be along the slip plane near the dislocation core. The overall binding energy of a dislocation is composed of the elastic and hydrogen-hydrogen interactions. Especially at large hydrogen concentrations near dislocations, interactions of hydrogen atoms between each other have an influence on the

overall energetical outcome. Although dislocations dispose over a spectrum of trapping energies, common trapping models usually assume one constant trapping energy for dislocations, as the distinction of trapping in the dislocation core and in the surrounding stress field is challenging. [60] At large hydrogen concentrations, hydrogen atoms are densely packed within the dislocation stress fields and trap sites can become saturated along a distance of several nanometers [75,77]. The density of trap sites in the dislocation core ranges from around 1 to 2 sites per metal atom [60,77,78]. Hydrogen concentrations in the material can be augmented by dislocations by a factor of 10^2 to 10^3. Around 20 % of the total hydrogen is in energetical interaction with the dislocation core. [2]

The dislocation-hydrogen-system has been studied in a large number of metals. The most extensive work was done on palladium, with many findings being generally valid. In palladium, it is currently believed that hydrogen accumulates at the core of edge dislocations in form of a cylinder-shaped hydrogen enriched zone below the dislocation line. The cylinder diameter is dependent on the hydrogen concentration and ranges between 0.8 and 2.8 nm. It is assumed that this cylindrical region of hydrogen enrichment is fragmented in order to avoid large coherency stresses. [79,80]

A high energy barrier for diffusion along as well as across dislocations makes it improbable that they work as accelerated diffusion paths in α-iron [81]. The maximum achievable dislocation density in iron is in the range of 10^{16} m^{-2} [82].

Energy values published in literature for hydrogen trapping at dislocations in iron and iron-based materials are given in Table 3 on the following page.

Table 3: Energy values published for hydrogen trapped at dislocations

Material	Details	E_b [kJ mol^{-1}]	E_a [kJ mol^{-1}]	Method	Ref.
Single-crystalline iron			45	TDS	[65]
Pure iron			19.3	Internal friction	[83]
Pure iron		19.2	26.8	TDA	[44]
Pure iron		24.1		Internal friction	[84]
Pure iron		25.6		Gas phase charged permeation	[85]
Pure iron		27.0		EP	[86]
Pure iron	Edge dislocation	40.5		Fermi-Dirac statistics	[87]
Pure iron	Dislocation core	42		Atomistic calculation	[76]
Pure iron		~ 45		TDS	[65]
Pure iron	Dislocation or dislocation debris	59.9		Gas phase charged permeation	[78]
Fe-0.2C martensite			33.9	TDS	[88]
0.05C-0.22Ti-2.0Ni steel	Combined dislocations and grain boundaries		~ 22	TDS	[67]
0.42C-0.30Ti steel	Combined dislocations and grain boundaries		~ 32	TDS	[67]
Fe-Ti-C alloy			26.1	EP	[59]
Low carbon steel		22–31		TDA	[89]
Steel		26.4		EP	[90]
Steel		26.8		EP and TDS modeling	[69]
13 % Cr steel	Dislocations or grain boundaries	38.7		EP	[71]
AISI 4340 steel		25		TDS	[72]
Duplex stainless steel	Strain region around dislocations		20	TDS	[70]
Duplex stainless steel	Dislocation core		34.8–40.3	TDS	[70]

2.2.4.3 Vacancies

Vacancies are point defects and consist of an atom missing in the lattice, creating an empty lattice site with slight surrounding relaxation. Vacancy defects are equilibrium defects, which are entropically stabilized [91]. They are inevitably present in materials: in negligible numbers at room temperature, induced to some degree by plastic deformation, and generated to a larger extent at elevated temperatures or in radiation environments. [39,60,92]

Vacancies can be considered as considerably large open volume defects, which may appear to hydrogen atoms as a free internal surface. From the energetical point of view, hydrogen prefers a state of surface chemisorption over interstitial solution and is therefore prompted to enter the vacancy and becomes trapped with a relatively large binding energy, comparable to the value in chemisorbed state [93]. Monovacancies can be occupied by more than one hydrogen atom, denoted as VH_N complexes, with N being the number of hydrogen atoms. Up to six hydrogen atoms are reported to be present in one vacancy, although DFT calculations show VH_6 complexes to be unstable and most vacancies probably exist as VH_2 [94–96]. Generally, it can be observed that the binding energy for additional hydrogen atoms decreases with increasing occupation of the vacancy, the values for VH and VH_2 being around 60 kJ mol^{-1} [97,98]. [21,60]

The hydrogen atom does not take the position in the exact center of a vacancy but seeks optimum electron density for energy minimization by taking a place slightly shifted away from the center. In channeling experiments and calculations, the location of the H atom was found to be located between 0.04 and 0.06 nm away from the octahedral position along the <100> direction towards the vacancy center, as shown in Figure 12. [21,60,99–101]

Energy values found in literature for hydrogen trapping in vacancies and microvoids in iron and iron-based materials are shown in Table 4.

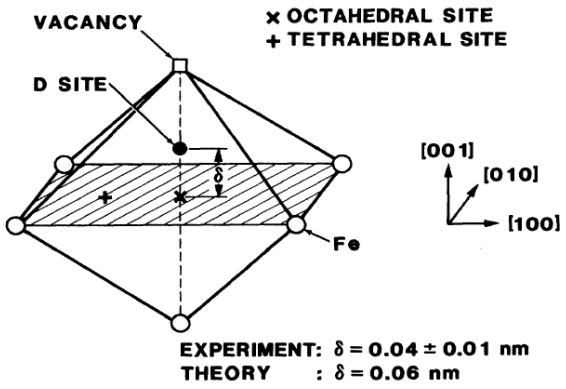

Figure 12: Position of the hydrogen atom in a monovacancy in iron [60]

Table 4: Energy values published for hydrogen trapped in vacancies

Material	Detail	E_b [kJ mol^{-1}]	E_a [kJ mol^{-1}]	Method	Ref.
Pure iron	Vacancy (occupied by 4–6 D atoms)	43		Ion implantation of Deuterium	[97]
Pure iron	Monovacancy	46		Ion implantation of Deuterium	[99]
Pure iron	Monovacancy	51		Ion implantation of Deuterium	[102]
Pure iron	Vacancy (occupied by 1–2 D atoms)	61		Ion implantation of Deuterium	[97]
Duplex stainless steel	Vacancy		50.2–57.4	TDS	[70]
Pure iron	Vacancy cluster	69		Ion implantation of Deuterium	[102]
Pure iron	Microvoid	27.6	35.2	TDA	[44]
Pure iron	Microvoid	29.1		Gas-charged permeation	[85]
Pure iron	Microvoid		40.3	TDA	[3]
AISI 4340 steel	Microvoid		48.3	TDA	[103]

2.2.4.4 Precipitates and Inclusions

Dispersions of fine precipitates as carbides and nitrides are added to steels for grain refinement and particle hardening, while nonmetallic inclusions (e.g. MnS, SiO_2, Al_2O_3) usually cause unwanted deterioration of material properties. Both precipitates and nonmetallic inclusions can work as hydrogen traps with potentially high trapping energies in bcc iron [104]. In high strength steels, finely dispersed titanium carbides, vanadium carbides, or niobium carbides, among others, increase the tensile strength and simultaneously provide strong trapping sites and can enhance the resistance against hydrogen embrittlement, as described in Section 2.2.3 [59,105–107].

Precipitation can create several possible trap sites with different or multiple binding energies, such as the precipitate/matrix interface, the coherency strain region around the precipitate, and crystal defects in the precipitate itself [60,108]. The binding energies for hydrogen depend on chemical composition, shape and size of the particles, as well as the orientation relationship and the coherency between the particle and the matrix [104,109]. As in grain boundaries, energetics of less regular interfaces tend to be more complicated [60]. Titanium carbide is one of the most thoroughly investigated precipitates. Several studies [59,67,104,110] show coarse, incoherent TiC to trap more strongly than finer, more coherent ones. The increase of particle size comes along with a loss of coherency, resulting in higher trap activation energies. Semi-coherent TiC trap hydrogen at the interface of particle and matrix, cores of misfit dislocations presumably act as traps. The amount of trapped hydrogen depends on the size of the interface area. [48,110] The active trap sites of incoherent TiC particles are assumedly carbon vacancies inside the precipitates, the precipitate volume is therefore decisive for the quantity of hydrogen trapped [48,110,111]. From comparing fine coherent TiC particles to coarse incoherent ones of the same volume fraction, Wei et al. [48] deduced that the former trap hydrogen more effectively. Asaoka et al. [109] found trapping to be stronger for spherical TiC than for needle- and plate-shaped precipitates as Fe_4N and TiN, and suggest that the reason for the difference is not only the chemical composition but also due to the precipitate shape and size having an influence on the interaction of hydrogen with their interfaces. A similar finding concerning a lower trapping ability for needle-shaped Mo_2C in comparison with disk-shaped TiC was published by Wei and Tsuzaki [1]. Different findings exist on the trapping effect of cementite. While Wei and Tsuzaki [1,88] claim that cementite precipitates do not show a significant trapping ability due to the low binding energy with hydrogen, trap activation energies for cementite and its interface of up to roughly 50 kJ mol^{-1} have been published, as shown in Table 5.

As mentioned above, the precipitate size is a parameter for its trapping ability. However, there are observations of critical maximum particle sizes above which certain particles lose their trapping capability. In a series of investigations, Depover et al. [108,112–114] found the maximum precipitate size for trapping for V_4C_3 to be 20 nm, for TiC 70 nm, for Mo_2C 75 nm, and for $Cr_{23}C_6$ 100 nm. Wei et al. [111] electrolytically charged materials at room temperature

and reported that coherent and semi-coherent TiC, VC, and NbC were able to trap hydrogen, while only for TiC the incoherent particles also worked as traps. In another work, the trapping capacity of different carbides was investigated, they resulted to be, in descending order: NbC > TiC > VC > Mo_2C, in proportion to the interface area [1]. Wei et al. [110] published that the semi-coherent interface of TiC precipitates formed in an iron-carbon matrix during tempering in the region of 550 to 800 °C trapped 1.3 atoms of hydrogen per square nanometer of interface area. The total amount of trapped hydrogen depends on the total internal interface area.

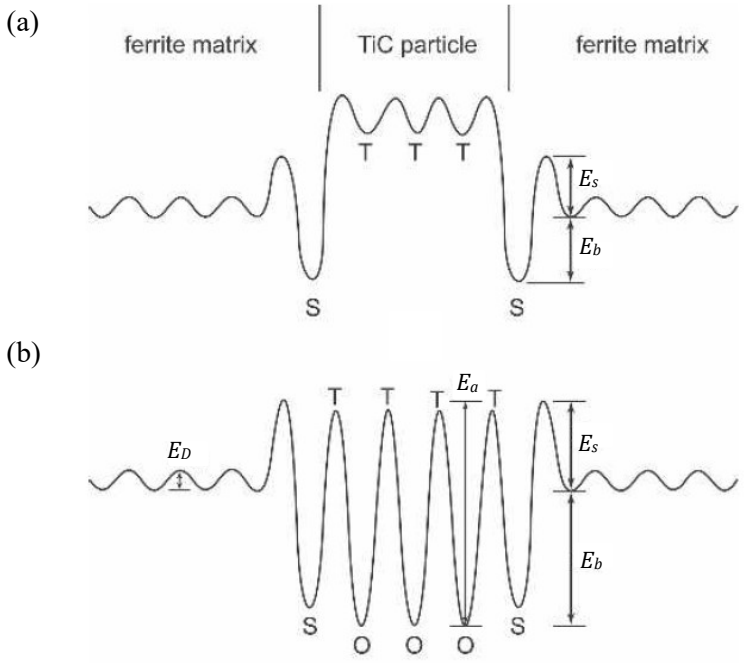

Figure 13: Schematic visualization of the energy levels of hydrogen trapped by (a) (semi-)coherent and (b) incoherent TiC particles at tetrahedral interstitial sites (T), octahedral carbon vacancies (O), and TiC/ferrite interface (S). Adapted from [110].

The presence of a nonmetallic phase or segregated species capable of covalently binding with hydrogen can lead to very high binding energies. For example, Huang et al. [115,116] located very strong traps in Pd at Pd/Al_2O_3 and Pd/MgO interfaces.

Energy values for hydrogen trapped at different precipitates and inclusions in iron and iron-based materials published in literature are shown in Table 5.

Table 5: Energy values published for hydrogen trapped at precipitates and inclusions

Precipitate/inclusion	Matrix	E_b [kJ mol^{-1}]	E_a [kJ mol^{-1}]	Method	Ref.
Ferrite-Fe_3C interface	Carbon steel	9.7	18.4	TDA	[46]
Ferrite-Fe_3C interface	Carbon steel	10.9	18.4	Gas-charged permeation	[117]
Fe_3C interface	Low carbon steel	13		TDA	[89]
Fe_3C interface	Carbon steel	19–23		EP	[118]
Fe_3C	Steel	30		EP and TDS modeling	[69]
Fe_3C interstitial	Bcc iron		41	Ab-initio calculations	[119]
Ferrite-Fe_3C interface	Bcc iron		47	Ab-initio calculations	[119]
Pearlitic Fe_3C	Steel	43		EP and TDS modeling	[69]
Fe-oxide interface	AISI 5160 steel		50–70	TDA	[120]
Al_2O_3	Pure iron		79.0	TDA	[3]
MnS	AISI 4340 steel		72.3	TDA	[103]
MnS	Steel	83		TDA	[121]
Small NbN	Experimental low alloyed steel		23–24	TDS	[68]
Incoherent NbN	Experimental low alloyed steel		100–143	TDS	[68]
M_2C	Steel	30		EP and TDS modeling	[69]
M_4C_3	Steel	35		EP and TDS modeling	[69]
CrC	Austenitic stainless steel		73–96	TDS	[122]
VC	Steel		33–35	TDA	[123]
Coherent VC interface	Fe-V-C alloy	32		FEM/TDS	[43]
V_4C_3 (vacancy in interface)	Fe-C-V alloy	58–73		TDS	[43]
Small NbC	Experimental low alloyed steel		39–48	TDS	[68]
Incoherent NbC	Experimental low alloyed steel		63–68	TDS	[68]
Coherent TiC interface	Fe-Ti-C alloy	24		FEM/TDS	[124]
Coherent TiC	Iron		22	Thermokinetic simulations	[125]
Nanosized coherent TiC	0.42C-0.30Ti steel		46–59	TDS	[67]
Semi-coherent TiC	0.05C-0.20Ti-2.0Ni steel		49.9	TDS	[126]
Semi-coherent TiC	0.05C-0.20Ti-2.0Ni steel		55.8	TDS	[110]
TiC (vacancy in interface)	Fe-C-Ti alloy	58–76		TDS	[43]

Incoherent TiC	0.05C-0.20Ti-2.0Ni steel	53	74–88	TDS (gas phase charging)	[127]
Incoherent TiC	0.42C-0.30Ti steel		68–116	TDS	[67]
Incoherent TiC,	0.05C-0.20Ti-2.0Ni steel		68–137	TDS	[110]
Incoherent TiC	0.05C-0.22Ti-2.0Ni steel		85.7	TDS	[67]
TiC interface	Iron	28.1	86.9	TDA	[128]
TiC	Fe-Ti-alloy	> 60.7		High resolution autoradiography	[109]
TiC	Fe-Ti-C alloy		94.5	EP	[59]
TiC	0.025C-0.09Ti steel		145	TDS	[129]
TiC	Experimental low alloyed steel		145	TDS	[129]
Martensitic lath boundaries	Fe-Cr-C alloy		23–30	TDS	[114]
Martensitic lath boundaries	Fe-Mo-C alloy		25–30	TDS	[113]
Martensitic lath boundaries	Fe-V-C alloy		26–33	TDS	[112]
Martensitic lath boundaries	Fe-V-C alloy	13–21		Model-based evaluation of TDS data	[43]
Martensitic lath boundaries	Fe-Ti-C alloy		26–48	TDS	[108]
Martensitic lath boundaries	Fe-Ti-C alloy	14–20		Model-based evaluation of TDS data	[43]

2.3 Hydrogen Diffusion

2.3.1 Ideal Diffusion

Hydrogen diffusion in metal is a process driven by concentration gradients and occurs by hydrogen atoms jumping between interstitial lattice sites. Atoms jump from the interstitial site they occupy to an adjacent vacant one, long distances in the matrix can be covered this way. There is a high probability of finding a free neighboring interstitial site for a diffusive jump, leading to a high diffusibility of hydrogen in many metals, especially in those with a bcc lattice structure like α-iron and ferritic steels. As described in Section 2.1, hydrogen atoms prefer tetrahedral sites in bcc iron at ambient temperatures and only start occupying octahedral sites above 100 °C. [7,13,17,18] The activation energy for diffusion E_D of hydrogen in α-iron is in the range of 4 to 7 kJ mol^{-1}, depending on the temperature, compared to around 80 kJ mol^{-1} for carbon and nitrogen [9,18,65,130]. This low value suggests that hydrogen diffuses through the lattice as a shielded proton with the possibility of tunneling through interstitial sites. [2,9,18] Hydrogen diffusion through the metal is controlled by the rate at which the atoms jump or quantum tunnel between interstitial lattice sites [57,131].

In 1855, Fick postulated that a concentration gradient results in a particle flow seeking to compensate this imbalance [132]. He observed the particle flux j_D – in the present case hydrogen flux – to be proportional to the concentration gradient, a relation known as Fick's first law. In absence of hydrogen interaction with lattice defects, it can be described in one-dimensional form as

$$j_D = -D \frac{dc}{dx} \quad , \qquad (15)$$

where D is the (constant) diffusion coefficient, c the concentration, and x the location. The negative sign results from diffusion occurring down the concentration gradient with particles flowing in direction of decreasing concentration. The multidimensional form of Fick's first law is:

$$j_D = -D \operatorname{grad} c \equiv -D \nabla c \quad , \qquad (16)$$

where ∇ is the nabla operator and the vector ∇c is defined as

$$\nabla c = \left(\frac{\partial c}{\partial x}, \frac{\partial c}{\partial y}, \frac{\partial c}{\partial z}\right) \quad . \qquad (17)$$

The proportionality factor D is the diffusion coefficient or diffusivity, usually given in cm^2 s^{-1} for the diffusing species in a specific matrix. It represents the jumping frequency of atoms in the lattice but is generally averaged over diffusion paths to give a macroscopically valid coefficient [21]. The diffusivity is usually considered to be independent of the concentration, but this is a simplification. Concentration can influence the diffusivity by hydrogen-induced changes in the lattice constant or the electronic density, hydrogen trapping, formation of im-

mobile clusters, or the blocking of interstitial sites by high hydrogen concentrations, among others. [13,74,133]

Fick's second law describes the change of concentration in a volume element with time for non-steady diffusion. For the diffusivity being constant and independent of location and concentration, it is given for unidirectional diffusion as

$$\frac{\partial c}{\partial t} = D\,\frac{\partial^2 c}{\partial x^2} \quad , \qquad (18)$$

and in multidimensional form it results in

$$\frac{\partial c}{\partial t} = D\nabla\cdot(\nabla c) = D\,\Delta c \equiv D\left(\frac{\partial^2 c}{\partial x^2}+\frac{\partial^2 c}{\partial y^2}+\frac{\partial^2 c}{\partial z^2}\right) \quad , \qquad (19)$$

where t is the time and Δ the Laplace operator. [21,74,134] The Laplace operator is defined as

$$\Delta \equiv D\left(\frac{\partial^2}{\partial x^2}+\frac{\partial^2}{\partial y^2}+\frac{\partial^2}{\partial z^2}\right) \quad . \qquad (20)$$

In summary, Fick's laws refer to the balancing of concentration variations in a system with the physical background of this phenomenon being the thermal movement of atoms [74].

The diffusion coefficient D is a function of temperature and is strongly influenced by trapping. For hydrogen diffusing in pure and undeformed α-iron at room temperature, D is in the order of $1 \cdot 10^{-4}$ cm^2 s^{-1} to $8 \cdot 10^{-4}$ cm^2 s^{-1}, compared to around $1 \cdot 10^{-16}$ cm^2 s^{-1} for carbon and nitrogen [9,18,65,130,135–138]. The more pure the material and the less hydrogen traps present, the higher the obtained value of D, as discussed in Section 2.3.2. When describing diffusion in the ideal homogeneous lattice, the diffusion coefficient is also referred to as lattice diffusion coefficient D_L. Strictly speaking, D is not a number but a direction-dependent second-order tensor, however, this can be neglected in highly symmetrical cubic metal lattices. The general notation for the temperature-dependent diffusion coefficient can be written as

$$D = D_0 \cdot \exp\left(\frac{-E_D}{RT}\right) \quad , \qquad (21)$$

where D_0 is the pre-exponential or frequency factor, E_D the activation energy for diffusion, and R the universal gas constant. Hagi [130] presented a relation for the diffusivity in cm^2 s^{-1} of hydrogen in 99.99 % pure iron free of dislocations as

$$D_L = (5.8 \pm 0.1) \cdot 10^{-4} \cdot \exp\left(\frac{-(4.5 \pm 0.2)}{RT}\right) \quad . \qquad (22)$$

Kiuchi and McLellan [18] analyzed over 60 data sets existing in 1982 to give a formulation for the hydrogen diffusion coefficient in iron in the temperature range of -40 to 80 °C in $cm^2\ s^{-1}$ as

$$D_L = 7.23 \cdot 10^{-4} \cdot \exp\left(\frac{-5.69}{RT}\right) \quad . \qquad (23)$$

The expression given by Grabke and Riecke [9] for hydrogen diffusivity in pure and undeformed α-iron at room temperature in $cm^2\ s^{-1}$ is

$$D_L = (5.12 \pm 0.6) \cdot 10^{-4} \cdot \exp\left(\frac{-(4.15 \pm 0.3)}{RT}\right) \quad . \qquad (24)$$

Applying above equations, the values for the hydrogen diffusion coefficient in pure and undeformed α-iron at a temperature of 298 K result in approximately $5.1 \cdot 10^{-4}\ cm^2\ s^{-1}$ according to Grabke and Riecke [9], $5.8 \cdot 10^{-4}\ cm^2\ s^{-1}$ according to Hagi [130], and $7.2 \cdot 10^{-4}\ cm^2\ s^{-1}$ according to Kiuchi and McLellan [18].

Hydrogen diffusivity is lower in close-packed γ-iron than in α-iron because of the higher activation energy for diffusion in fcc structures [21].

2.3.2 Diffusion Influenced by Hydrogen Trapping

At low temperatures, measured values of hydrogen diffusivities in α-iron exhibit a wide scattering over four orders of magnitude in an Arrhenius plot, as shown in Figure 14. Diffusion coefficients at low temperatures are considerably smaller than those determined at high temperatures and deviate notably from extrapolations of high temperature data. By analogy with solubility, where the same phenomenon can be observed (see Sect. 2.1), the reason is trapping of hydrogen at various lattice imperfections. Higher thermal energy leads to higher diffusivity and an increasing chance of hydrogen atoms escaping trap sites, the influence of trapping on diffusivity consequently decreases with increasing temperature. The scatter of diffusivity data is up to four orders of magnitude at room temperature, approximately one order of magnitude above 250 °C, and diminishes further at higher temperatures. [7,13,21,128,139] As illustrated in Figure 15, the scatter in diffusivity is even more pronounced for different steel grades, resulting from the usually higher trap density and presence of higher-energy traps.

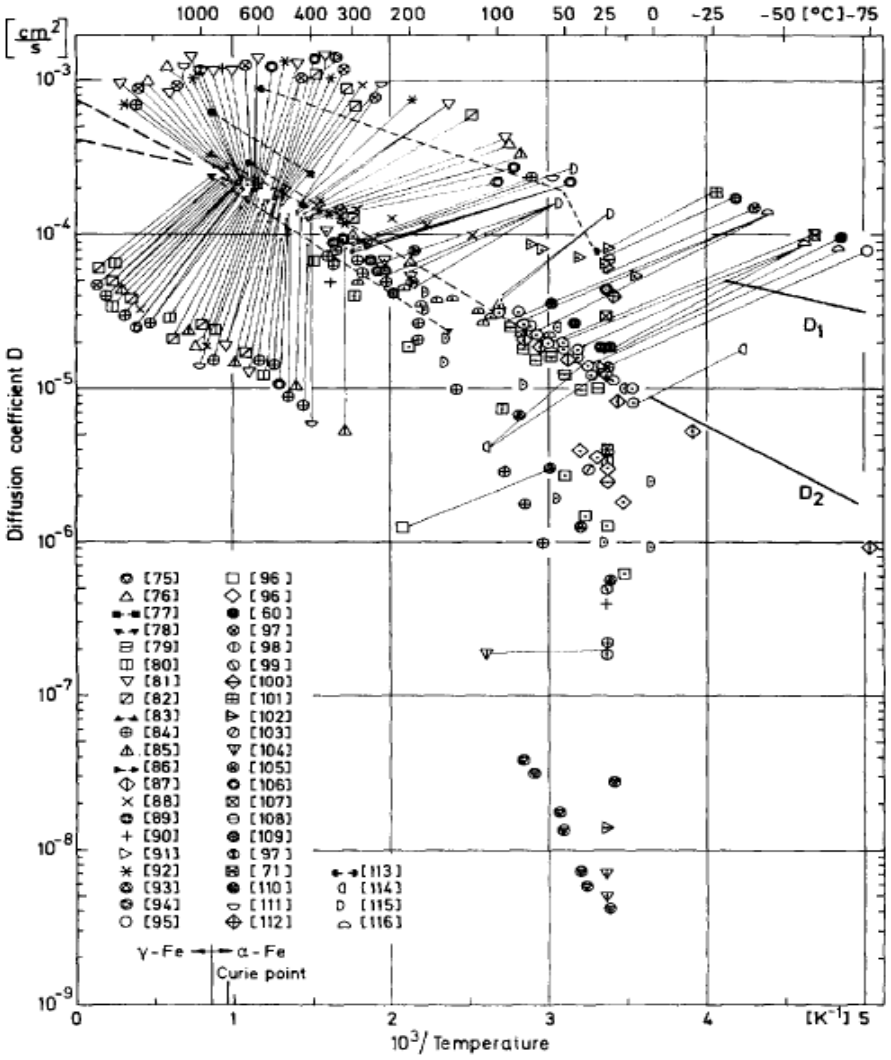

Figure 14: Data for diffusion coefficients of hydrogen in α-iron.
Numbers in brackets refer to the original references. [139]

The energy levels a diffusing hydrogen atom has to overcome are visualized in Figure 16. In a trap-free ideal lattice, only the activation energy for diffusion is necessary for the atom to migrate, as seen in Figure 16(a). In Figure 16(b), one type of trap is present with no visible saddle point energy around the trap, i.e. $E_a = E_b + E_D$, and in Figure 16(c), one type of trap with a pronounced saddle point is available, i.e. $E_a = E_b + E_s$. In Figure 16(d), two traps with different activation energies can be seen. [51]

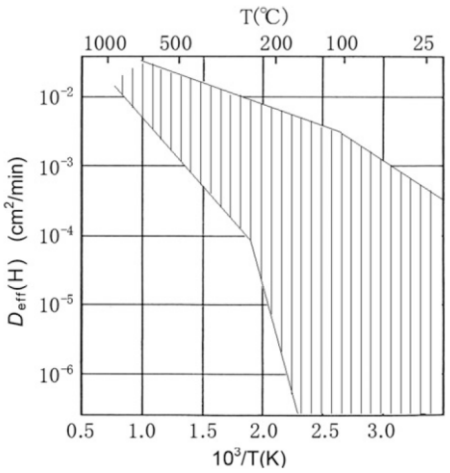

Figure 15: Literature data range of effective hydrogen diffusivities in iron and steels [21]

Different findings and opinions exist on the possibility of accelerated hydrogen diffusion along grain boundaries or dislocation lines and cores, a phenomenon commonly referred to as *pipe diffusion*. Kirchheim [77,140] attributed dislocations a contribution to pipe diffusion in palladium and Kiuchi and McLellan [18] described increased diffusion along dislocation lines in α-iron. Castaño-Rivera et al. [141] assume that weak traps along dislocation lines in X60 steel could serve as short circuit paths for diffusion, which is, however, not plausible as diffusion in α-iron is fast enough as for short circuit paths to emerge. [142] In ab-initio simulations, Kimizuka and Ogata [81] observed that hydrogen diffusion along dislocations is significantly lower than lattice diffusion in α-iron and hence doubt the occurrence of pipe diffusion. Du et al. [61] and Teus and Gavriljuk [143] state that grain boundaries in γ- and α-iron do not provide fast diffusion paths, based on the results of diffusion modeling.

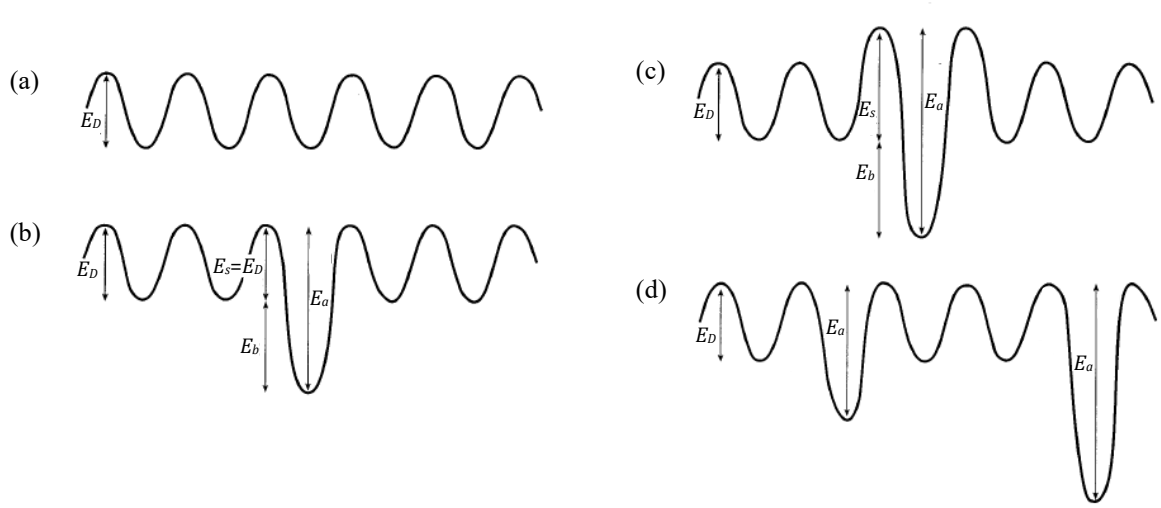

Figure 16: Schematic illustration of potential energy profiles for (a) lattice diffusion, (b) diffusion with a single type of trap, (c) diffusion with a single type of trap with pronounced saddle point energy, (d) diffusion with two types of traps. Adapted from [51].

When diffusion is delayed by hydrogen trapping, the delayed diffusion coefficient is often referred to as apparent D_{app} or effective diffusion coefficient D_{eff}. The influence of the traps on the diffusivity is determined by the trap's activation or binding energy and the density of trap sites. Because traps act as hydrogen sinks or sources, Fick's second law is no longer valid. This observation was first made by Darken and Smith [5] in 1949. Consequently, several diffusion models were developed to take into account the impact of trapping, either basing on the assumption of equilibrium between lattice and traps or on trapping/detrapping rates. [46,128,144]

2.3.3 Diffusion Models Considering Hydrogen Trapping

2.3.3.1 McNabb-Foster Model

The first adaptation of Fick's law to consider trapping was published by McNabb and Foster [145] in 1963. By adding a term for the exchange of hydrogen atoms between lattice and trap sites to Fick's second law, they developed a general modelistic formulation for one-dimensional diffusion integrating kinetics of trapping and detrapping for one type of uniformly distributed traps. The model was originally intended to describe reversible trapping but was subsequently also applied to evaluate trapping by irreversible trap sites. [21,69,144,146]

Assuming a sparse distribution of traps and no direct interchange of hydrogen atoms between traps, McNabb and Foster's model comprises two coupled partial differential diffusion equations for the concentrations for lattice hydrogen and trapped hydrogen in space and time:

$$\frac{\partial c_L}{\partial t} + N_T \frac{\partial \theta_T}{\partial t} = D \frac{\partial^2 c_L}{\partial x^2} \quad , \qquad (25)$$

and

$$\frac{\partial \theta_T}{\partial t} = k c_L (1 - \theta_T) - p \theta_T \quad , \qquad (26)$$

where c_L is the hydrogen concentration in the normal lattice, N_T the trap density, θ_T the fraction of occupied trap sites, D the lattice hydrogen diffusion coefficient in the system, k the trapping rate parameter (probability of hydrogen jumping from a normal interstitial lattice site to a trap site), p the detrapping rate parameter (probability of releasing hydrogen from a trap site to a normal interstitial lattice site), x the direction of diffusion, and t time. [1,21,35,69]

Trapping and detrapping are described by the terms $N_T k c_L (1 - \theta_T)$ and $N_T p \theta_T$, respectively, which specify the number of hydrogen atoms captured and released by a trap. As trapping and detrapping are thermally activated processes, the trapping and detrapping parameters k and p are related to potential energies of the trap-lattice system, schematically illustrated in Figure 17. The parameters are interdependent and defined as:

$$k = k_0 \exp\left(-\frac{E_t}{RT}\right) \quad , \qquad (27)$$

and

$$p = p_0 \exp\left(-\frac{E_b + E_t}{RT}\right) \quad , \qquad (28)$$

where k_0 and p_0 are pre-exponential constants for the capture and release rate, respectively, E_t is the trapping energy or saddle point energy in the vicinity of a trap, and E_b the trap binding energy.

For a low trap occupancy, it can be shown that

$$\frac{k_0}{p_0} = \frac{1}{N_L(1-\theta_T)} \approx \frac{1}{N_L} = \text{const.} \quad . \qquad (29)$$

The ratio k_0/p_0 is inversely proportional to the number of lattice sites and is constant for a specific material. [21,51]

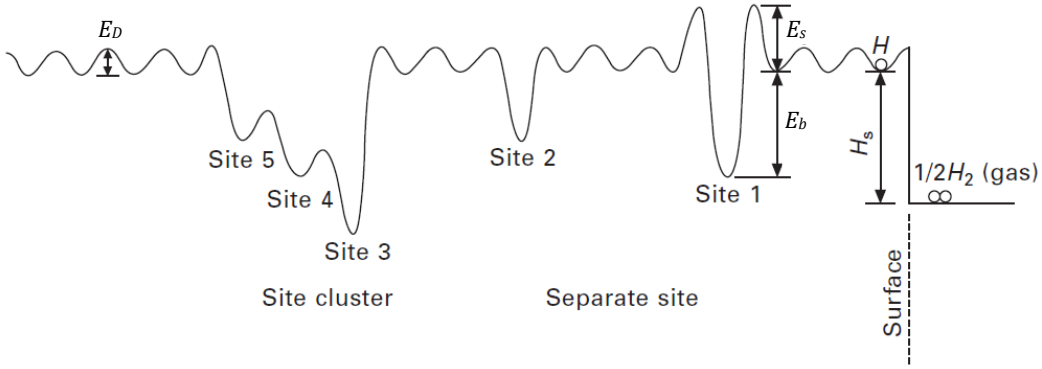

Figure 17: Schematic representation of the energy levels in a metal lattice.
The single circle represents a hydrogen atom on a normal interstitial lattice site,
the double circle represents a hydrogen molecule outside the material. Adapted from [1].

The McNabb-Foster model is a general theory which does not rely on the assumption of dynamical equilibrium between trapped hydrogen and lattice hydrogen. Despite this, no analytical solutions exist to Equations (25) and (26), since Equation (26) is not linear with respect to the hydrogen concentration. However, it becomes linear and therefore analytically solvable for two cases: first, for small specimens with negligible trapping term and the desorption being described solely by the detrapping rate parameter p, and second, for the terminal phase of hydrogen desorption from a specimen, where the hydrogen concentration c_L and the trap occupancy θ_T become negligibly small. [1] The McNabb-Foster diffusion equations have been solved numerically, e.g. by Caskey and Pillinger [147] and Pressouyre and Bernstein [59].

2.3.3.2 Oriani Model

In 1970, Oriani [31] suggested a simplification of the McNabb-Foster model by assuming a local thermodynamic equilibrium between hydrogen atoms in traps and interstitial lattice positions. This interpretation is confined to reversible trapping and the assumption of equilibrium is based on very fast trapping and detrapping processes. By implementing the local equilibrium condition, the differential equation for trapping kinetics can be replaced by an algebraic relation between the concentrations of trapped and lattice hydrogen, allowing to find analytical solutions to the McNabb-Foster model. [34,35,148]

Oriani analyzed the time required to establish the local equilibrium condition and showed that dynamic equilibrium can be achieved. He assumed that a variation in the lattice hydrogen concentration is immediately compensated by trapped hydrogen atoms to maintain the balance. In equilibrium and for very low lattice hydrogen concentrations, i.e. very low occupancy of lattice sites, the trap occupancy can be expressed as

$$K = \left(\frac{\theta_T}{1-\theta_T}\right)\left(\frac{1-\theta_L}{\theta_L}\right) = \exp\left(-\frac{E_b}{RT}\right) \quad , \qquad (30)$$

where K is the equilibrium constant, defined as the ratio of hydrogen activity in trap sites to hydrogen activity in lattice sites, θ_L and θ_T are the fractions of lattice and trap sites occupied, respectively, and E_b is the trap binding energy. [7,31,149]

For both very low lattice site and very low trap site occupancies ($\theta_L << 1$ and $\theta_T << 1$), Equation (33) simplifies to

$$c_T \approx c_L \frac{N_T}{N_L} \exp\left(\frac{E_b}{RT}\right) \quad , \qquad (31)$$

where c_T and c_L are the hydrogen concentrations in trap sites and lattice, respectively, and N_T and N_L are the number of trap sites and lattice sites per unit volume, respectively [149]. The connections between concentrations, absolute number of sites, and fractions of sites occupied are given by Equations (12) and (13) above.

Consequently, Oriani derived an expression for the effective diffusion coefficient D_{eff} as

$$D_{eff} = D_L \frac{c_L}{c_L + c_T(1-\theta_T)} \quad . \qquad (32)$$

When considering a low trap occupancy, the effective diffusion coefficient can furthermore be described by explicit trapping parameters as

$$D_{eff} = \frac{D_L}{1 + \frac{N_T}{N_L}\exp\left(\frac{E_b}{RT}\right)} \quad . \qquad (33)$$

The facilitations in trapping calculations due to the equilibrium approach become apparent when considering Equation (33). The effective diffusivity is easily accessible through experiments, e.g. by electrochemical permeation, and allows the determination of trapping parameters such as binding energy and trap density.

The validity of the Oriani model was verified by Kirchheim [75] by means of Monte Carlo simulations. There are, however, limitations, as pointed out e.g. by Koiwa [150]: the activation energy for hydrogen diffusion E_D must be equal to the saddle point energy around the trap E_s, otherwise the effective diffusivity is not only a function of the trap's binding energy E_b, but also of the saddle point energy. [1,21]

2.4 Hydrogen Analysis

2.4.1 Electrochemical Permeation (EP)

2.4.1.1 Method and Processes

The electrochemical permeation method was developed by Devanathan and Stachurski [6] in 1962 to study the diffusion behavior of hydrogen in palladium. It was thereafter applied to many different materials, including iron [33,142,151], steel [152–154], aluminum [155,156], and nickel [157,158]. [159,160] Today, electrochemical permeation is the most popular technique to determine hydrogen permeation kinetics and diffusivity in metals, and is further used to deduce numerous parameters such as hydrogen concentrations, trap activation energies, and trapping capacities [159,161,162]. Reasons for the method's popularity are its relative simplicity and flexibility with respect to variations in experimental conditions [163].

The sample to be analyzed is usually a flat membrane. One side of the membrane is subjected to hydrogen charging (entry or charging side), while a constant anodic potential is applied to the other side (exit or oxidation side). Hydrogen atoms are generated and absorbed at the entry side, diffuse through the sample and are oxidized by the applied potential when reaching the membrane surface at the exit side. The anodic current resulting from the hydrogen oxidation is measured. It depicts diffusion-controlled transport through the material, which is influenced by the microstructure of the material and trapping effects. [7,135,164] A typical permeation transient is shown in Figure 18, the oxidation current density is recorded over time. After logging the background current, the first charging cycle is started. When the oxidation current reaches a maximum at a steady state, hydrogen charging at the entry side is stopped and hydrogen is discharged from the membrane, resulting in a decay of the oxidation current. After reaching a constant value at a low level, a second charging cycle can begin. Multiple charging-discharging cycles are useful to evaluate the presence of reversible and irreversible traps. In the

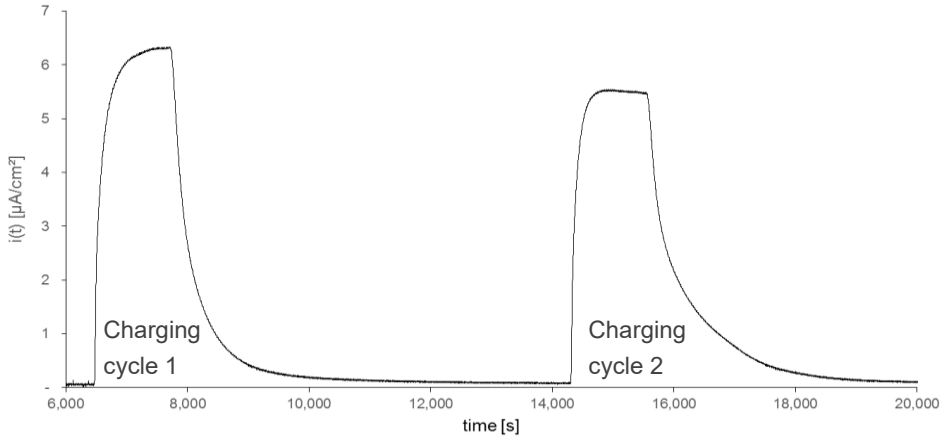

Figure 18: Permeation transient for two hydrogen charging cycles with intermediate discharge of pure iron cold rolled to 30 % reduction. Adapted from [165].

first charging process, both reversible and irreversible traps are occupied by hydrogen. During the discharge, hydrogen remains bound in irreversible traps, while lattice hydrogen and reversibly trapped hydrogen effuse from the sample. Consequently, only reversible traps are effective in successive charging cycles and later transients progressing faster than the first one indicate the existence of irreversible trapping. [7,59,166] After subtraction of the background current, the steady-state oxidation current is a direct measure of the permeation flux of hydrogen at the membrane exit side. When a steady state is reached, a local equilibrium exists between interstitially diffusing and trapped hydrogen. [167] Surface effects can have severe influence on the permeation process, therefore well-defined conditions of hydrogen entry are necessary in order to ensure that the measured permeation rate is entirely controlled by diffusion [168,169].

Hydrogen charging is generally done by gas phase charging with pressurized hydrogen or hydrogen containing gas or by electrolytic charging from aqueous solutions. The second option is more common, especially at experimental temperatures below 100 °C [7,164,167].

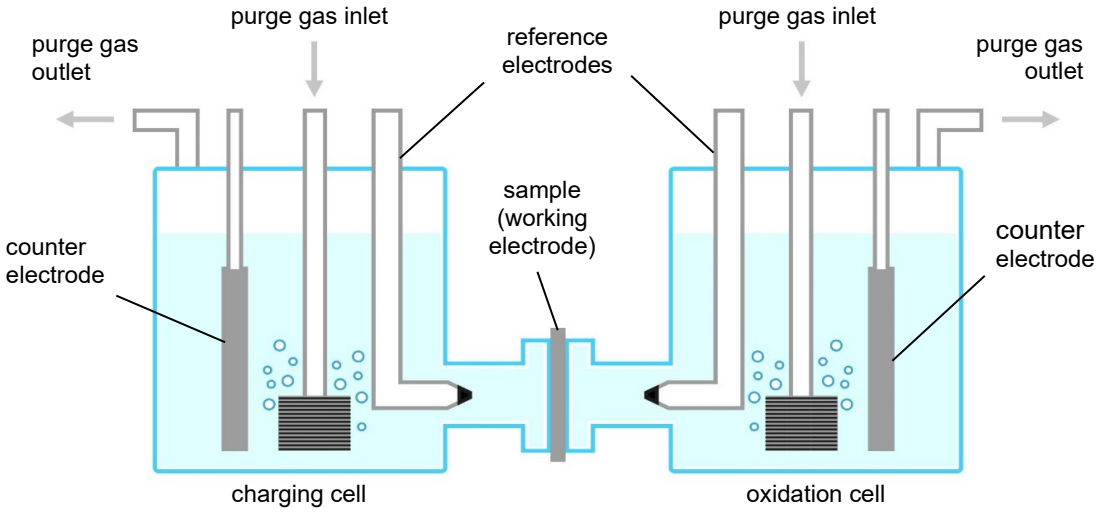

Figure 19: Permeation double cell according to Devanathan and Stachurski [165]

An electrochemical permeation setup with electrolytic charging according to Devanathan and Stachurski is shown in Figure 19. It consists of two single cells, a charging cell and an oxidation cell, filled with electrolytes, and with the sample membrane clamped in between. Commonly used electrolytes can be alkaline (e.g. NaOH solution), acidic (e.g. H_2SO_4 solution), or neutral (e.g. NaCl solution). In each cell, the metal specimen surface facing the cell acts as the working electrode. Each cell is additionally equipped with a counter electrode and a reference electrode to measure the electric potential or current. Inert gas purging of the liquid electrolytes is generally implemented to remove dissolved oxygen and by keeping the cells at a constant temperature with a thermostat, uniform experimental conditions are ensured.

In the cathodic charging cell, hydrogen is generated by applying a cathodic potential or imposing a cathodic current and is adsorbed on the metal membrane surface [162]. The hydrogen evolution reaction (HER) is composed of two steps. The first step is hydrogen adsorption (Volmer reaction), the process varies depending on the pH of the electrolyte solution. In acidic media, hydrogen ions are discharged at the metal surface according to

$$H_3O^+ + M + e^- \rightarrow MH_{ads} + H_2O \quad . \qquad (34)$$

In neutral or alkaline media, water is reduced to produce adsorbing hydrogen atoms by

$$H_2O + M + e^- \rightarrow MH_{ads} + OH^- \quad , \qquad (35)$$

where M is an empty adsorption site on the metallic surface and MH_{ads} represents hydrogen adsorbed at the surface. [161,170]

The second step consists of the formation of gaseous hydrogen by electrochemical desorption or chemical recombination. Electrochemical desorption (Heyrovsky reaction) happens as a result of the combination of adsorbed hydrogen atoms with hydrated protons or water molecules, depending on the pH [170]. The metal serves as a catalyst for the discharge and removal of hydrogen atoms [171]. In acidic media, the reaction involves the simultaneous reduction of a proton according to

$$MH_{ads} + H^+ + e^- \rightarrow M + H_2 \quad , \qquad (36)$$

while in neutral or alkaline media, the hydrogen atom reacts with water as [170]

$$MH_{ads} + H_2O + e^- \rightarrow H_2 + OH^- + M \quad . \qquad (37)$$

Chemical recombination (Tafel reaction) produces hydrogen molecules via the recombination of adsorbed hydrogen atoms and simultaneous desorption from the metal surface [172]:

$$2\,MH_{ads} \rightarrow H_2 + 2\,M \quad . \qquad (38)$$

Adsorbed hydrogen, which is not discharged as gaseous hydrogen by electrochemical desorption (Heyrovsky reaction) or chemical recombination (Tafel reaction), may be absorbed into the metal. This happens by hydrogen atoms penetrating into a sublayer beneath the surface before subsequently diffusing into the bulk metal. The hydrogen absorption reaction can be described as [161,162,170]

$$(M)H_{ads} + [M] \rightarrow [M]H_{abs} + (M) \quad , \qquad (39)$$

where $(M)H_{ads}$ represents a hydrogen atom adsorbed at a surface site, [M] an empty interstitial lattice site beneath the surface, $[M]H_{abs}$ an absorbed hydrogen atom at an interstitial site beneath the surface, and (M) an empty site at the metal surface.

The adsorption-absorption mechanism of hydrogen consists of two stages: first, equilibrium between hydrogen adsorbed at the surface and absorbed hydrogen just beneath the surface, and second, equilibrium between the sub-surface and the metal bulk [57,162,173]. Heyrovsky, Tafel, and absorption reactions are in direct competition, influenced by factors such as pH, overpotential, and imposed current. Additionally, process kinetics dependent on the surface state have an influence. A major part of the adsorbed hydrogen reacts to form molecular hydrogen, only a fraction enters the metal bulk via absorption. Even though absorption of hydrogen is normally the least favorable reaction, it has most practical relevance. It is desired when conducting electrochemical permeation experiments or intentionally charging samples with hydrogen and highly undesired when presenting a source of hydrogen which can potentially cause hydrogen embrittlement in practical applications. [161,162,174]

Hydrogen entry into metals can be promoted by several species, such as compounds containing elements from group 15 (P, As, and Sb) and group 16 (S, Se, and Te) of the periodic table, compounds containing carbon, such as CS_2, CO, and CSN_2H_4 (thiourea), as well as certain anions, as e.g. CN^-, CNS^-, and I^- [172]. For iron and steel, especially elements forming hydrides of the type AsH_3, H_2Se, H_2S, PH_3, and SbH_3 increase hydrogen absorption [7]. The promoting effect of hydrogen uptake can result from blocking or reducing the rate of the hydrogen recombination reaction or from increasing the hydrogen coverage of the metal surface [175–177]. In electrochemical permeation experiments, CSN_2H_4 (thiourea) and As_2O_3 are commonly added to the charging side electrolyte to increase hydrogen uptake into the sample.

During the permeation experiment, hydrogen atoms diffuse through the sample membrane after being absorbed and reach the surface at the exit side of the membrane, which faces the oxidation cell. Its function is to anodically oxidize hydrogen, usually by applying a constant potential. [13] The anodic oxidation current or hydrogen permeation current is recorded and provides a direct measure of the hydrogen permeation flux through the membrane. In most cases, an alkaline electrolyte such as e.g. NaOH is used in the oxidation cell. Oxidation of hydrogen on the exit surface of the membrane takes place in conformity with the inverse Volmer reaction according to

$$\mathrm{MH_{ads}} + \mathrm{OH^-} \rightarrow \mathrm{H_2O} + \mathrm{M} + \mathrm{e^-} \quad , \qquad (40)$$

with the generated electrons allowing for the determination of the oxidation current. A rivaling process to the oxidation is the recombination of hydrogen adsorbed at the exit surface according to the Tafel reaction:

$$2\,\mathrm{MH_{ads}} \rightarrow \mathrm{H_2} + 2\,\mathrm{M} \quad . \qquad (41)$$

Hydrogen recombination at the exit side of the membrane is highly undesired as it makes atoms exiting the sample inaccessible for detection by oxidation. The competition between hydrogen oxidation and hydrogen recombination is determined by the kinetics and the anodic overpoten-

tial applied in the oxidation cell. The potential applied must be high enough to ensure that the oxidation current density is limited by the diffusion of hydrogen atoms and that the oxidation flux is substantially larger than the recombination flux. Only this allows the assumption that the concentration of hydrogen atoms at the membrane exit surface as well as the recombination flux are close to zero, thereby providing appropriate boundary conditions for the analysis. [7,162,178] The permeation process is schematically illustrated in Figure 20.

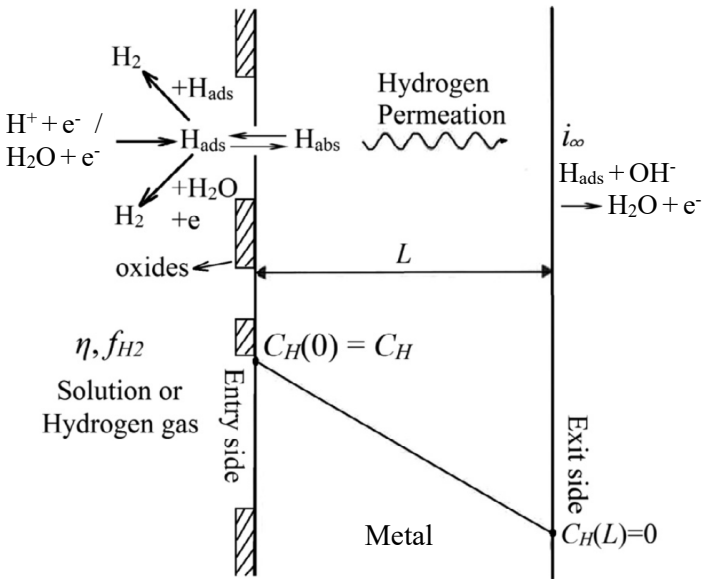

Figure 20: Schematic illustration of a permeation experiment and hydrogen concentrations in steady state. Adapted from [12], originally from [170].

The conditions in the oxidation cell can cause the formation of oxide layers on unprotected iron and iron-based materials, even with low oxygen contents in the cell due to inert gas purging. These passive layers hinder hydrogen permeation by forming a barrier and impede stabilization of the hydrogen concentration on the exit side, preventing a steady state to be reached [146,179]. Furthermore, a potential higher than the hydrogen equilibrium potential does not always guarantee the complete oxidation of the hydrogen flux, and recombination to its molecular form can cause significant amounts of hydrogen to escape without being detected [180]. The solution consists in coating the exit side of the membrane with a thin palladium layer, usually between 50 nm and several µm in thickness, applied by electroplating or sputtering. The coating impedes the formation of an oxide film and ensures complete and fast oxidation, as hydrogen is consistently oxidized on palladium surfaces [180,181]. It is common opinion that a palladium layer is essential for obtaining reliable and reproducible electropermeation results, as it ensures the validity of the boundary condition of zero hydrogen concentration on the membrane exit side and does not interfere with the permeation process [180–183]. The requirements for the coating are high purity and uniformity, strong adherence to the sample surface, as well as the absence of pores and cracks [184].

Applying a palladium layer to the hydrogen entry side is rarely done when using electrolytic charging. It is, however, useful when employing gas phase charging, as it prevents the formation of oxide films, which can hinder hydrogen absorption [164,167,181]. When permeation is investigated under the influence of tensile stresses, nickel can be used instead of palladium. Due to higher elongation levels, nickel coatings are less prone to suffer fractures or defects resulting from deformation. [183,185]

Fick's first law of diffusion is applicable to describe hydrogen transport from the entry side to the exit side of the membrane when assuming one-directional flow and hydrogen diffusion as the rate-determining step. For potentiostatic charging and the corresponding conditions (i.e. hydrogen kinetics fast enough to maintain an equilibrium at the input surface, resulting in constant hydrogen concentration, as well as immediate oxidation at the exit surface, resulting in a hydrogen concentration close to zero), the hydrogen flux at the exit side can be formulated as

$$j = -D \cdot \left(\frac{\partial c}{\partial x}\right)_{x=L} \quad , \qquad (42)$$

where j is the hydrogen flux per membrane area, D the diffusion coefficient for hydrogen in the sample material, c the hydrogen concentration, x the distance from the entry surface, and L the membrane thickness. [171]

The concentration gradient of hydrogen and therefore the hydrogen flux through the membrane are functions of time and distance from the entry side. The measured anodic oxidation current at the exit side is proportional to the hydrogen output flux. Its continuous logging provides information on the momentary rate of hydrogen permeation changing with time. [13,21] For both potentiostatic and galvanostatic charging regimes, a certain amount of time after polarizing the entry side of the membrane and generating hydrogen atoms, a steady state of hydrogen permeation is reached, as the concentration gradient in the membrane becomes linear and the oxidation current takes on a constant value. The steady-state hydrogen permeation flux per area j_∞ at the exit side of the membrane (at distance $x = L$) can be calculated as

$$j_\infty = \frac{D(c_\infty - c_{x=L})}{L} = \frac{Dc_\infty}{L} \quad , \qquad (43)$$

where c_∞ is the steady-state hydrogen concentration at the entry side of the membrane and $c_{x=L}$ the hydrogen concentration at the exit side, which is assumed to be zero. Applying Faraday's law to Equation (43) allows determination of the steady-state hydrogen permeation flux at the membrane exit from the measured steady-state hydrogen oxidation current or oxidation current density. Furthermore, the lattice hydrogen concentration directly below the surface at the charging side of the membrane can be calculated from the steady-state oxidation current:

$$j_\infty = \frac{Dc_\infty}{L} = \frac{I_\infty}{AF} = \frac{i_\infty}{F} \quad , \qquad (44)$$

where I_∞ is the steady-state oxidation current, i_∞ the steady-state oxidation current density, A the membrane area exposed to electrolyte in the oxidation cell, and F the Faraday constant. [13,186,187]

The permeation coefficient or permeability Φ is defined as the product of the hydrogen concentration at the membrane entry side at steady state and the diffusivity [9,188]:

$$\Phi = c_\infty \cdot D \quad . \qquad (45)$$

Mathematical models have been proposed to estimate the hydrogen trap density in the material from electrochemical permeation data. A commonly used approach is based on the ratio of lattice diffusivity to effective diffusivity and is formulated as

$$N_T = \frac{c_\infty}{3}\left(\frac{D_L}{D_{eff}} - 1\right) N_A \quad , \qquad (46)$$

where N_T is the trap density, D_L the lattice diffusion coefficient, D_{eff} the effective diffusion coefficient, and N_A the Avogadro constant. [144]

Shape and progression of experimental permeation transients can provide useful information for estimating the material's trapping characteristics. The time delay between the start of the charging cycle and the first hydrogen atoms arriving at the membrane exit surface, resulting in the oxidation current signal beginning to rise, is generally referred to as breakthrough time (see Figure 21). It is not to be mistaken with the time characteristic of the same name, which is discussed in Section 2.4.1.3. This time delay is associated with the overall trap density of a material, a longer breakthrough time indicates a higher trap density, as hydrogen is more likely to get trapped before reaching the membrane exit side. A steep transient slope suggests a low number of trap sites, the steady-state permeation current is reached in a short amount of time due to a small number of traps to be saturated. The time to reach the steady state increases with a flatter slope, a higher trap density causes more hydrogen to become trapped before a uniform flux is attained. [189–192] A less common interpretation is the attribution of the breakthrough time specifically to irreversible traps and the slope to reversible traps [193].

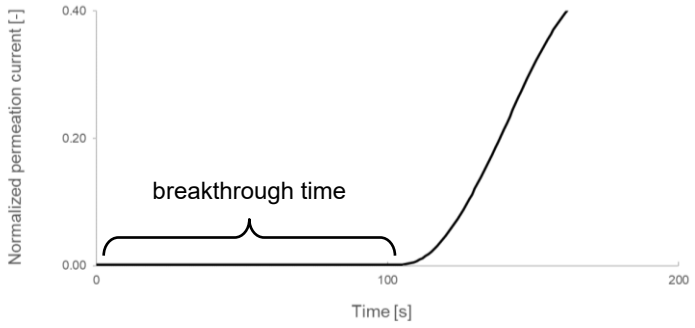

Figure 21: Hydrogen is first detected on the membrane exit side after the time span needed for the first hydrogen atoms to migrate through the membrane (breakthrough time)

2.4.1.2 Constant Concentration and Constant Flux Models

Two physical-chemical models of hydrogen entry can be distinguished at the membrane surface on the hydrogen charging side, each with characteristic boundary conditions: the equilibrium theory of constant concentration, which is applied when the hydrogen charging is potentiostatic, and the kinetic theory of constant flux, generally used to describe galvanostatic charging conditions.

The constant concentration model or equilibrium model does not define a limitation of the rate of hydrogen entry into the material but assumes a constant subsurface hydrogen concentration at the entry side. This concentration remains unchanged from the beginning of the polarization throughout the duration of the measurement, the concentration taking the form of a step function (see Figure 22). The constant concentration results from the assumption of the kinetics of hydrogen entry being fast enough to maintain an equilibrium between the external hydrogen-providing phase and the first metallic layers of the entry surface. No condition is imposed on the hydrogen entry flux, hydrogen ingress is entirely dependent on the diffusion process in the bulk beneath the surface. As to maintain an equilibrium as hydrogen diffuses through metal, the external system must be able to quickly react to the hydrogen demand from the inside of the material. The hydrogen concentration at the entry side only depending on the thermodynamic state of the external phase results in the stationary hydrogen flux being inversely proportional to the membrane thickness. Furthermore, under diffusion-controlled conditions, time characteristics should be proportional to the square of the membrane thickness. A further assumption in this model is the hydrogen concentration at the exit side being zero due to the immediate oxidation of arriving hydrogen atoms. [13,162,194]

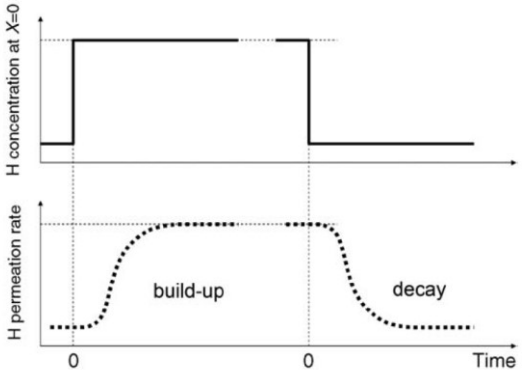

Figure 22: Schematic representation of hydrogen concentration at the entry side and hydrogen permeation rate for an ideal EP experiment under potentiostatic charging conditions [168]

The constant concentration model is suitable in the case of potentiostatic charging conditions [13,195–199].

The boundary conditions for the constant concentration model are:

$$c = 0 \qquad \text{for } t = 0 \text{ and } 0 \le x \le L$$

$$\left.\begin{aligned} c_{x=0} &= c_0 \\ c_{x=L} &= 0 \end{aligned}\right\} \quad \text{for } t > 0$$

where c is the hydrogen concentration, t the time, x the distance from the membrane entry side, L the membrane thickness, $c_{x=0}$ the hydrogen concentration at the entry side, c_0 the equilibrium hydrogen concentration determined by the applied electric potential at the entry side, and $c_{x=L}$ the hydrogen concentration at the exit side of the membrane [162,163,195,199–201]. With these boundary conditions, the time-dependent permeation flux can be formulated according to Zhang et al. [195] as

$$j = \frac{Dc_0}{L}\left[1 + 2\sum_{n=1}^{\infty}(-1)^n \exp\left(-\frac{Dn^2\pi^2}{L^2}t\right)\right] \quad , \qquad (47)$$

where j is the hydrogen permeation flux and D the diffusion coefficient.

The constant flux model assumes a uniform hydrogen entry flux into the membrane and a hydrogen concentration at the input side that increases from zero at the beginning of the polarization to a maximum value throughout the progress of the experiment. The system is not in equilibrium with the external phase, the quantity of hydrogen entering the metal depends on kinetic parameters of hydrogen transfer processes between the external phase and the metal membrane. The constant steady-state hydrogen flux is independent of the sample thickness. As in the constant concentration model, also in the case of constant flux, the time characteristics should be proportional to the square of the membrane thickness if the process is diffusion-controlled. [13,162,194]

Constant flux conditions are generally considered to be valid in galvanostatic charging. Models considering fluxes at the membrane entry side are more realistic than models assuming constant concentrations, as they are better suited to describe the adsorption-absorption mechanism. [57,162,195,198,202] Nonetheless, in some cases, these models may encounter difficulties precisely reproducing parts of the adsorption-absorption steps [162,195].

The boundary conditions for the constant flux model are:

$$c = 0 \qquad \text{for } t = 0 \text{ and } 0 \le x \le L$$

$$\left.\begin{aligned} j_\infty &= -D\frac{\partial c}{\partial x} \\ c_{x=L} &= 0 \end{aligned}\right\} \quad \text{for } t > 0$$

where c is the hydrogen concentration, t the time, x the distance from the membrane entry side, L the membrane thickness, j_∞ the constant flux, which is also the permeation flux at steady state, D the diffusion coefficient, and $c_{x=L}$ the hydrogen concentration at the exit side of the membrane [162,163,195,199–201]. Considering these boundary conditions, the time-dependent permeation flux can be described according to Zhang et al. [195] as

$$j = j_\infty \left[1 - \frac{4}{\pi} \sum_{n=1}^{\infty} \frac{(-1)^n}{(2n+1)} \exp\left\{-\frac{D(2n+1)^2\pi^2}{4L^2} t\right\}\right] \quad . \qquad (48)$$

For both the constant concentration and constant flux models, variations in surface conditions resulting in changes of equilibrium or kinetic properties or in the concentration of adsorbed or absorbed hydrogen will have an effect on the magnitudes of the entry side hydrogen concentration and hydrogen entry flux. Distortions of the permeation transient are usually caused by changes of the hydrogen concentration on the entry side of the membrane. [194] Figure 23 illustrates the hydrogen concentration over the distance from the entry side of the membrane for the constant concentration and the constant flux models.

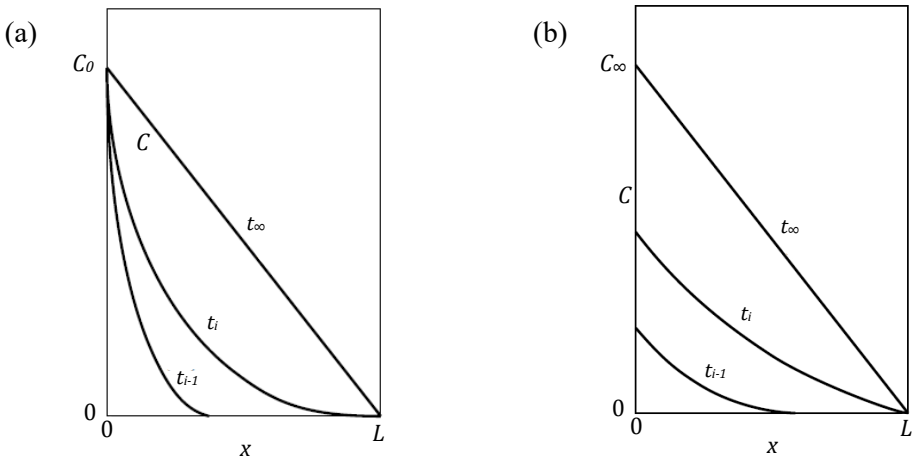

Figure 23: Variation in hydrogen concentration gradient with time along a membrane of thickness L for (a) constant concentration at the input side and (b) constant flux at the input side, given at times t_{i-1}, t_i, and steady state (t_∞), where $t_{i-1} < t_i < t_\infty$. Adapted from [13], originally from [163].

2.4.1.3 Time Characteristics

Permeation transients can typically be characterized by time-related parameters. These time characteristics allow the determination of the apparent or effective diffusion coefficient and are obtained by solving Fick's second law with the appropriate boundary conditions. The adopted entry and exit boundary conditions are hydrogen concentrations, not considered are absorption and desorption processes. The time characteristics are the time lag *(t_{lag})*, inflection-point time *(t_i)*, breakthrough time *(t_b)*, and half-rise time *($t_{1/2}$)*, they are shown for an exemplary permeation transient in Figure 24. Time characteristics can have different formulations depending on the boundary conditions, i.e. for potentiostatic and galvanostatic regimes. Under diffusion control, they are proportional to the square of the membrane thickness. [13,163,171,203]

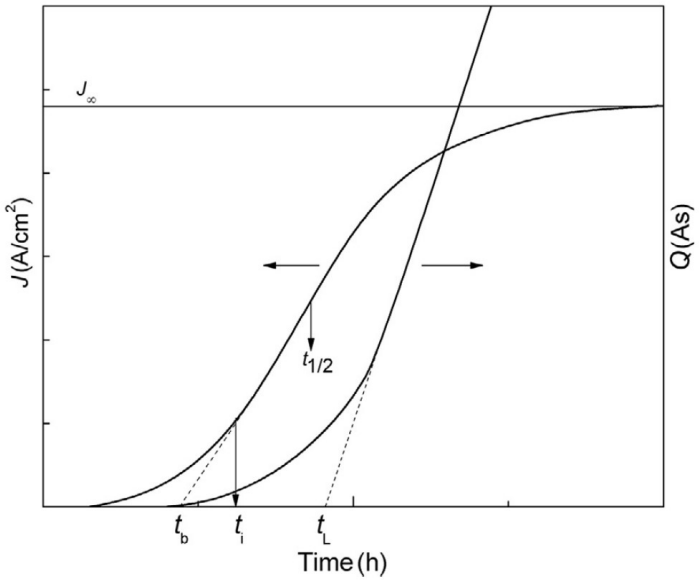

Figure 24: Time characteristics and their determination from the permeation transient. Taken from [171], originally from [163].

Time Lag

The time lag approach was originally formulated in 1920 by Daynes [204] to describe the gas transport through a rubber membrane. The time lag is the most commonly used time characteristic to determine the diffusivity, as it is generally seen as reliable for most experimental conditions [59,203]. Daynes defined the time lag as the intersection of the integrated flux with the time axis, which corresponds to a value of L^2/MD_{eff}, with M being a factor dependent on the boundary conditions [203]. Devanathan [6] showed that the time lag is equivalent to the time necessary for the oxidation current density to reach 0.63 times its steady-state value i_∞. For potentiostatic control, the time lag is

$$t_{lag}{}^{p} = \frac{L^2}{6D_{eff}} = t(0.63i_\infty) \quad , \qquad (49)$$

where $t_{lag}{}^{p}$ is the time lag for potentiostatic charging, L the membrane thickness, D_{eff} the efficient diffusion coefficient of the sample material for hydrogen, i_∞ the steady-state current density, and $t(0.63i_\infty)$ the time for the oxidation current density to reach 0.63 times its steady-state value. The correspondent formulation for galvanostatic charging conditions is

$$t_{lag}{}^{g} = \frac{L^2}{2D_{eff}} = t(0.63i_\infty) \quad . \qquad (50)$$

Inflection Point

The time for the permeation transient to reach the inflection point is defined for potentiostatic control by [13]

$$t_i{}^{p} = \frac{0.924L^2}{\pi^2 D_{eff}} \quad , \qquad (51)$$

and for galvanostatic charging the relation is

$$t_i{}^{g} = \frac{1.65L^2}{\pi^2 D_{eff}} \quad . \qquad (52)$$

Breakthrough Time

The breakthrough time is defined as the intersection of the tangent at the inflection point of the transient with the initial current level or background current level before charging. For potentiostatic charging it corresponds to [13]

$$t_b{}^p = \frac{0.5L^2}{\pi^2 D_{eff}} \quad , \qquad (53)$$

and for galvanostatic conditions

$$t_b{}^g = \frac{0.76L^2}{\pi^2 D_{eff}} \quad . \qquad (54)$$

Half-rise Time

The half rise time is the time for the transient to reach 0.5 times its steady-state value. It is only applied for potentiostatic charging conditions and corresponds to [13]

$$t_{1/2} = \frac{0.14L^2}{D_{eff}} = t(0.5i_\infty) \quad . \qquad (55)$$

Time characteristics allow a simple and quick determination of the effective or apparent diffusion coefficient from electrochemical permeation experiments. The testing procedure was standardized as ISO 17081 [187] and ASTM G147-97 [205] to ensure the experiments satisfy the necessary boundary conditions. The downside of describing the diffusion process based on time characteristics is the assumption of a constant diffusion coefficient, which may not always reflect the real situation, as diffusivity can change with factors such as hydrogen concentration and trap parameters. A more precise description of the diffusion process can be obtained by fitting mathematical models to the permeation transient, as done e.g. by Fischer et al. [36,146,206], Castaño Rivera et al. [154], Vecchi et al. [162], among others.

2.4.2 Thermal Desorption Analysis (TDA/TDS)

2.4.2.1 Method and Process

Thermal desorption analysis (TDA) or thermal desorption spectroscopy (TDS) is a method to study the temperature-dependent release of gases from solid materials. It is a destructive thermal technique which generates desorption spectra by heating a sample at a constant heating rate and measuring the desorption rate of species released. The spectra can provide information on the number and population of desorbing phases, the activation energy of desorption, as well as the order of the desorption reaction [207]. The general designation for the method is *thermal desorption analysis*, when a mass spectrometer is used for gas detection the term *spectroscopy* is often applied.

TDA was first used in the 1950s and 1960s to determine the binding energies of species adsorbed at surfaces [207–210] and has been applied to analyze species absorbed in the bulk and trapped at microstructural defects since the 1980s [44,210–213]. In the 1990s, the use of quadrupole mass spectrometers for the detection of effusing phases led to an improvement of accuracy and detection limits [45].

The common procedure to generate comparable and reproducible thermal desorption analyses of hydrogen usually includes the following steps: charging the sample with hydrogen electrochemically or from a gas phase, heating the sample with a specific temperature profile at a constant heating rate, and simultaneously detecting the hydrogen release from the sample while continuously recording it as a function of the sample temperature or time [34,214]. Most systems quantify the amount of hydrogen by measuring the thermal conductivity of the effusing gas or by mass spectrometry, the latter being a more selective and sensitive method [215]. A crucial requirement is a heating rate slow enough to avoid temperature gradients in the sample. In metals and metallic alloys, this is usually simple to achieve, as the thermal diffusivity is typically significantly larger than the hydrogen diffusion coefficient. [34]

Hydrogen is released from different trap sites in the metal sample, visible as peaks in the desorption rate spectrum. The spectrum of a certain material is composed of the individual peaks of the different traps, as shown in Figure 25. The analysis of the spectrum reveals trap sites and allows their quantitative and qualitative classification by providing information on trap densities and binding energies. The positions and heights of the single peaks are defined by the interaction energy between hydrogen and the trap site and the amount of hydrogen trapped at that site, respectively [44]. Different peak temperatures in the spectrum correspond to desorption from different types of traps, with weaker traps releasing hydrogen at lower temperatures and stronger traps being activated at higher temperatures. The temperature profile and the desorption behavior can therefore be used to gain insights on defects in the material and the associated activation energies, desorption kinetics, and hydrogen distribution within the metal lattice. [214,216,217] Assuming the presence of multiple kinds of traps and a moderate trap

density, overall hydrogen kinetics can be described by adding the individual contributions of each trap [69].

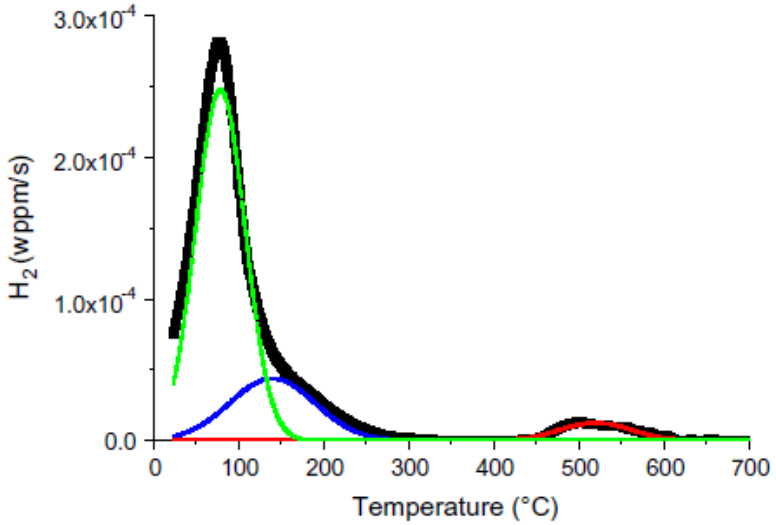

Figure 25: TDS spectrum of a TRIP steel at a heating rate of 400 K/h. The deconvolution of the overall spectrum (black curve) shows individual peaks of different trap sites (green, blue, and red curves). [218]

The area under a peak is proportional to the amount of hydrogen trapped at the corresponding site. With various species of non-interacting traps present in the material, it has been shown experimentally [110,129,219–221] and by modeling approach [222] that the total hydrogen concentration can be estimated from the sum of the individual concentrations corresponding to the single peaks. [69] Randerson et al. [223] visualized this relation as

$$c_{total} = c_L + c_{T,1} + c_{T,2} + c_{T,3} + \ \ldots \quad , \qquad (56)$$

where c_{total} is the total hydrogen concentration in the material, c_L is hydrogen dissolved in the lattice, and $c_{T,1}$, $c_{T,2}$, $c_{T,3}$ etc. are hydrogen concentrations in different types of trap sites.

The idea of TDA is to evaluate a specific trap without influence from other traps present in the material. This is not always straightforward, as hydrogen desorption from different defects can take place in overlapping temperature regions and make the identification of individual traps difficult. The challenge in this case is fitting a model to the desorption data in order to extract desired trapping characteristics. The number and shape of peaks a desorption spectrum is best fitted with can occasionally be considered an arbitrary decision. In all cases, it is to be considered which approach gives the best correlation or is thought to be most appropriate as well as incorporating potentially available information on material and microstructure. [51,216,217,224]

The rate-determining step of hydrogen desorption depends on the trapping energy. For strong trapping, the thermally activated release of hydrogen from traps (detrapping) with increasing temperature is rate-limiting, and several mathematical models can be applied to calculate the trapping energies (see Sect. 2.4.2.3). Detrapping-controlled desorption is independent of the sample geometry and size, a simple experimental way to identify detrapping as the rate-determining step is therefore the variation of the sample size. When trapping is weak, on the other hand, and local equilibrium exists between dissolved lattice hydrogen and trapped hydrogen, the rate-determining step is thermally activated diffusion, with the diffusivity depending on the trap density and trapping energies. In the case of diffusion-controlled desorption, TDA can provide useful information on lattice defects, but a precise assessment of traps present and binding energies has proven to be challenging. [21] When the activation energy for lattice diffusion is large relative to trapping energies, i.e. when trap activation energies are small, TDA measurements will show diffusion-controlled hydrogen evolution and the spectrum will show a peak corresponding to bulk diffusion. In summary, the character of the desorption peaks is deter-mined by the rate-determining step of the process. [225]

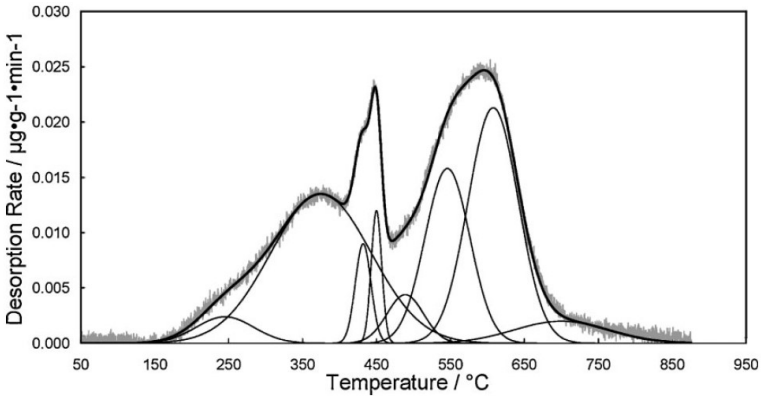

Figure 26: TDS spectrum of a coated steel sample containing eight Gaussian peaks [45]

The hydrogen distribution among trap sites and neighboring normal interstitial lattice sites can be described by a Fermi-Dirac function, assuming a low fractional occupancy and neglecting mutual interaction between trapped hydrogen atoms [21,226]. By heating the metal sample and thereby providing it with thermal energy, hydrogen atoms are enabled to escape the trap sites at a rate determined by the derivative of the occupation of trapped hydrogen with respect to temperature, referred to as hydrogen evolution and apparent as Gaussian-shaped peaks in the spectrum [216]. Kirchheim [75,227] reported that the distribution of hydrogen energy in the metal matrix follows a Gaussian probability distribution, which is centered on a maximum energy value, the trap's activation energy. Therefore, thermal desorption spectra and the hydrogen evolution can be described and deconvoluted by a series of Gaussian functions, and for each Gaussian peak a corresponding temperature can be identified. Figure 26 shows a spectrum containing several Gaussian peaks. A variation of peak temperatures indicates a

difference in binding forces between hydrogen and trap site. [228] When the heating rate is increased, a displacement of peaks towards higher temperatures is observed (see Figure 27), suggesting a dependence of desorption kinetics on the heating rate. This so called peak shift is the base for calculating the trap activation energy (see Sect. 2.4.2.3). [44,228]

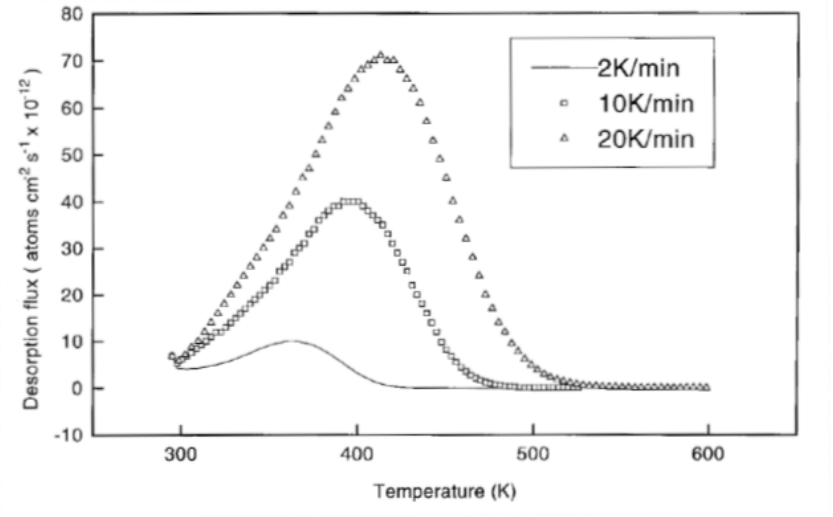

Figure 27: Effect of the heating rate on a TDS spectrum with a single trap type [51]

The shape of the desorption curve can give information on the reaction order *n* of the hydrogen desorption reaction. The influence of the value of *n* on the curve shape is shown in Figure 28. With increasing reaction order, the height of the desorption peak decreases and a more pronounced tailing can be observed. The reaction order *n* can be determined experimentally [207,229,230]. Empirically, the relation $n = 1$ is generally satisfied for hydrogen released from metals and alloys, resulting in close to Gaussian-shaped peaks. [110]

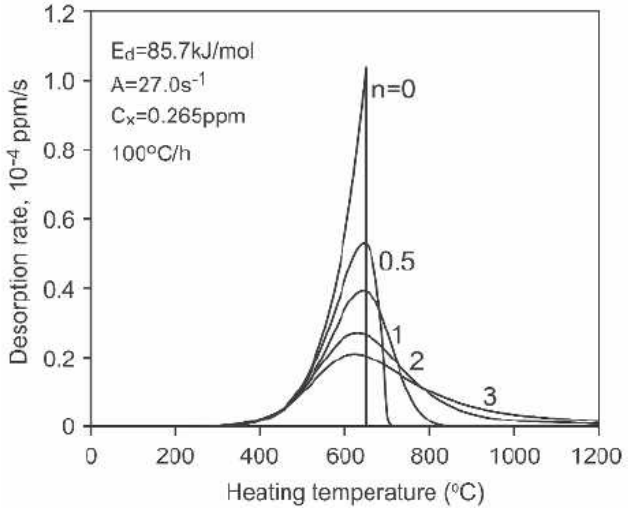

Figure 28: Effect of the hydrogen desorption reaction order *n* on the desorption spectrum shape [110]

The shape and form of the thermal desorption spectrum of a hydrogen charged material is influenced by several factors, such as the aforementioned heating rate, the reaction order, as well as the hydrogen content and its distribution among traps. The latter two are in turn affected by the hydrogen charging conditions. Wei and Tsuzaki [110] observed the trap activation energy to change with hydrogen content. They reported an increasing hydrogen concentration resulting in a peak shift towards lower temperatures, as hydrogen first occupies higher-energy traps and starts filling up lower-energy traps only when the deeper traps are saturated (see Figure 29). This can be the case for a material with either a variety of traps or with one trap comprising positions or sites for hydrogen of different binding energies. Short-time charging of samples can therefore be a suitable method for studying deep traps in a material. Desorption spectra can also be influenced by the sample's surface preparation and roughness and by the sample geometry, especially the sample thickness. [51,110,214]

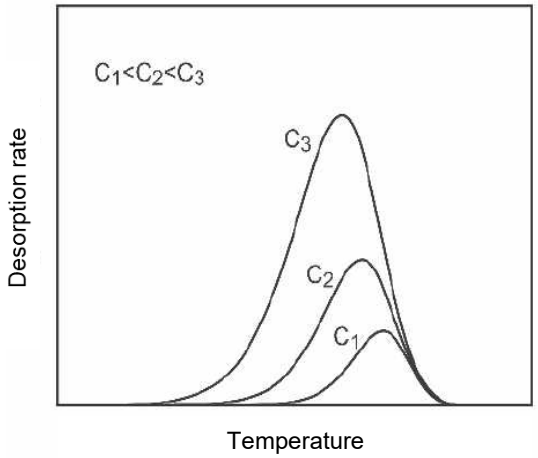

Figure 29: Schematic illustration of a TDS spectrum for one kind of trap with varying site energies at increasing hydrogen concentrations c_1, c_2, c_3 [110]

2.4.2.2 Modes of Operation

There are two main technical process designs to be distinguished in thermal desorption analysis, characterized by the pressure level of the system: the vacuum method and the carrier gas method.

Vacuum Method

Vacuum or ultrahigh vacuum systems consist of a sealed gas-tight enclosure, which contains both the specimen chamber and a mass spectrometer. The enclosure is evacuated during the analysis, as the mass spectrometer requires high vacuum for operation. Hydrogen and other species effusing form the sample are directly ionized and accelerated by the mass analyzer into the detector.

Advantages of vacuum systems are a high detection sensitivity due to the lack of additional gas atoms from a carrier gas. A fast response to changes of the desorption rate and a negligible chance of hydrogen retrapping allows highly accurate determination of trap activation energies. The obligatory vacuum, however, demands elaborate construction and tightness of the aggregate and goes along with a high vulnerability of the system to pressure changes. The biggest downside of the vacuum method is the considerable time required to evacuate the system, it can take up to one or two hours to reach a vacuum level low enough for the measurement to start. As the sample chamber is located inside the vacuum enclosure, the hydrogen effusing from the sample in this time span is lost for detection. This especially poses a problem when analyzing materials exhibiting a high lattice diffusivity, as significant parts of the stored hydrogen can desorb at room temperature inside the system before the measurement has started. [45,214]

Carrier Gas Method

In carrier gas systems, the sample compartment is at ambient pressure level, usually open to the environment, and easily accessible. The species desorbed from the sample during heating are taken up by an inert carrier gas, such as nitrogen or helium, and transported to the detector. In case of detection by a thermal conductivity sensor, no evacuation is necessary, as it functions at ambient pressure. In this case it is, however, crucial to eliminate species from the carrier gas stream which can influence the measurement, e.g. water and carbon oxides. This is done by channeling the stream through columns filled with reagents such as magnesium perchlorate, sodium hydroxide and Schuetze reagent, which oxidize and absorb unwanted components. If a mass spectrometer is used for detection, no elaborate gas cleaning is required, as the components of the gas stream are distinguished by their masses. Nonetheless, it is common practice to remove humidity when measuring hydrogen, as the H_2O molecule can be broken down in the spectrometer during ionization and falsely result in detection of hydrogen. Since vacuum is necessary for the mass spectrometer's operation, an inlet system is required to inject minimal amounts of the gas stream into the vacuum system without raising the pressure.

As the analysis can start immediately after loading the sample, no effusing hydrogen is lost for detection, and materials with significant hydrogen release at room temperature can be precisely analyzed. Another advantage is the simplicity and lower cost of carrier gas systems, especially when thermal conductivity sensors are used for detection. The disadvantages are a relatively long path between the heated sample compartment and the detector as well as the necessity of a carrier gas flow, which can influence the measurement and lower the quality of analysis, particularly at lower heating rates. [45,214]

2.4.2.3 Hydrogen Desorption Models

2.4.2.3.1 Kissinger Model

A publication by Kissinger from 1956 [231] mathematically describes the decomposition of kaolinite minerals under constant heating as first order reaction. He showed that variations in peak temperatures appearing in differential thermal analysis (DTA) measurements can be used to determine the activation energy for first order reactions. [229,231]

In 1957, Kissinger proposed a simple analytic method [229] for the determination of the activation energy of chemical reactions by measuring the heat release. It was based on the previous publication from 1956 and extended the method to reactions of any given order. The generic model was originally developed for analyzing gas desorption reactions from minerals in DTA and determining the reaction order from the shape of the DTA peak, but was later adopted to evaluate TDA data. [34,42,149,229]

Under the assumption that gas desorption from a solid material is a thermally activated process, most reactions of the type *solid* ⟶ *solid* + *gas* can be described by the equation

$$\frac{dX}{dt} = A(1-X)^n \exp\left(\frac{-E_a}{RT_P}\right) \quad , \qquad (57)$$

where X is the fraction of species of interest released and with t being the time, dX/dt is the desorption rate of this species, A the reaction rate constant or frequency factor, n the empirical order of reaction, E_a the desorption activation energy, R the universal gas constant, and T_p the desorption or peak temperature. [42,110,225,229] The order of reaction n usually equals unity (first-order reaction, valid for hydrogen desorption) or a fraction and is assumed to stay constant throughout the reaction [110,229]. On the right side of Equation (57), the term $(1-X)$ describes the amount of material left unreacted and the term $A \exp(-E_a/RT_p)$ respresents the probability of successful release of an atom or molecule of the desorbing species from the sample material, with A describing the non-thermal fraction of the probability. A high value of the reaction rate constant A results in a high desorption rate. In the case of hydrogen release, an increase in specimen thickness and higher trap densities decrease the reaction rate constant and hydrogen desorption, as more trap-to-trap jumps are necessary for a hydrogen atom to escape the sample. [126,229]

When a specimen is heated at a constant heating rate ϕ, a desorption rate is recorded as a function of temperature. For hydrogen desorption, the hydrogen evolution rate is related to the activation energy of the trap sites present in the sample. At the maximum desorption rate, the first derivative of Equation (57) is zero, resulting in

$$\frac{E_a \phi}{{RT_P}^2} = A\, n\, {(1-X)_m}^{n-1} \exp\left(\frac{-E_a}{RT_P}\right) \quad , \qquad (58)$$

where ϕ is the heating rate and the subscript m stands for maximum desorption rate. [225,229]

When taking the logarithm and differentiating with respect to $1/T_p$, Equation (58) yields [225]

$$\frac{d\left(\ln\frac{\phi}{{T_P}^2}\right)}{d\left(\frac{1}{T_P}\right)} = -\frac{E_a}{R} \quad . \qquad (59)$$

With Equation (59), the desorption energy or activation energy of hydrogen traps can be determined from the slope of the Arrhenius plot of $\ln(\phi/T_p^2)$ vs. $1/T_p$. As the desorption peaks shift to higher temperatures with faster heating rates, the energy value can be calculated from two or (ideally) more TDA measurements at different heating rates.

Equation (59) is fully satisfied for first-order reactions and approximate when n takes other values than one. As described in Section 2.4.2.1, the condition $n = 1$ is customarily true for hydrogen desorption from metals and alloys. [110]

The method by Kissinger is based upon a few assumptions and prerequisites. Detrapping is considered as the rate-limiting step, retrapping is not taken into account, and traps are sparsely distributed so there is no interaction between them [34,67]. It is assumed that hydrogen atoms only escape from traps due to thermal energy input from heating [42]. Furthermore, diffusion is fully neglected in this model, as it is not necessary for the determination of the energy of desorption and significantly simplifies the calculations [34,67,110,126]. To minimize the effect of diffusion in the analysis and to justify its omission in the evaluation, small sample sizes, clean sample surfaces, and slow heating rates are essential requirements [34,110,126]. At high heating rates, diffusion is likely to have an influence in practical measurements, as Wei et al. assume [67]. A low lattice diffusion activation energy, i.e. high diffusivity, is an additional requisite for neglecting diffusion. Large diffusion activation energies relative to trap activation energies result in measuring diffusion-controlled hydrogen evolution. [34,225] Hence, hydrogen trap analysis of bcc materials such as iron is considerably less challenging and moreover permits larger sample dimensions compared to fcc materials such as nickel [110]. [34,67,110,126,225]

2.4.2.3.2 Choo-Lee Model

Kissinger's reaction kinetic approach (see Sect. 2.4.2.3.1) is widely known as the Choo-Lee [44] or Lee-Lee model [103,232] when applied to hydrogen desorption from bulk metals, as W. Y. Choo, J. Y. Lee, J. L. Lee, and S. M. Lee extensively used the method in its first-order form to examine trap activation energies [42,126,149]. W. Y. Choo and J. Y. Lee [44] first applied the model to determine the activation energy of hydrogen trapped at grain boundaries, dislocations, and microvoids in deformed pure iron. Today, it is a very popular method for hydrogen trap analysis in metals using TDA [67].

For first-order reactions with $n = 1$, Kissinger's general equation for gas desorption from solids (Equation (57)) specifically describes the release of hydrogen from metals and becomes

$$\frac{dX}{dt} = A(1 - X) \exp\left(\frac{-E_a}{RT_P}\right) \quad , \qquad (60)$$

where X is the fraction of hydrogen desorbed and with t being the time, dX/dt is the desorption rate of hydrogen, A the reaction rate constant or frequency factor, E_a the hydrogen trap activation energy, R the universal gas constant, and T_p the desorption or peak temperature.

For uniform heating, the maximum hydrogen desorption rate from a trap can be determined when the first derivative of Equation (61) equals zero, yielding

$$\frac{E_a \phi}{RT_P{}^2} = A \exp\left(\frac{-E_a}{RT_P}\right) \quad , \qquad (61)$$

where ϕ is the heating rate [42,44].

Analogous to Kissinger's formulation, taking the logarithm of Equation (61) and differentiating with respect to $1/T_p$ results in [46]

$$\frac{\partial \ln\left(\frac{\phi}{T_P{}^2}\right)}{\partial \left(\frac{1}{T_P}\right)} = -\frac{E_a}{R} \quad . \qquad (62)$$

Equation (62) allows the determination of trap activation energies from the slope of the Arrhenius plot of $\ln(\phi/T_p^2)$ vs. $1/T_p$ after performing a series of measurements at different heating rates and analyzing the temperature peak shift of the Gaussian-shaped curves below the desorption spectra. A TDS spectrum of hydrogen desorption from aluminum with deconvoluted peaks and trap activation energy determination from the corresponding Arrhenius plot are shown in Figure 30.

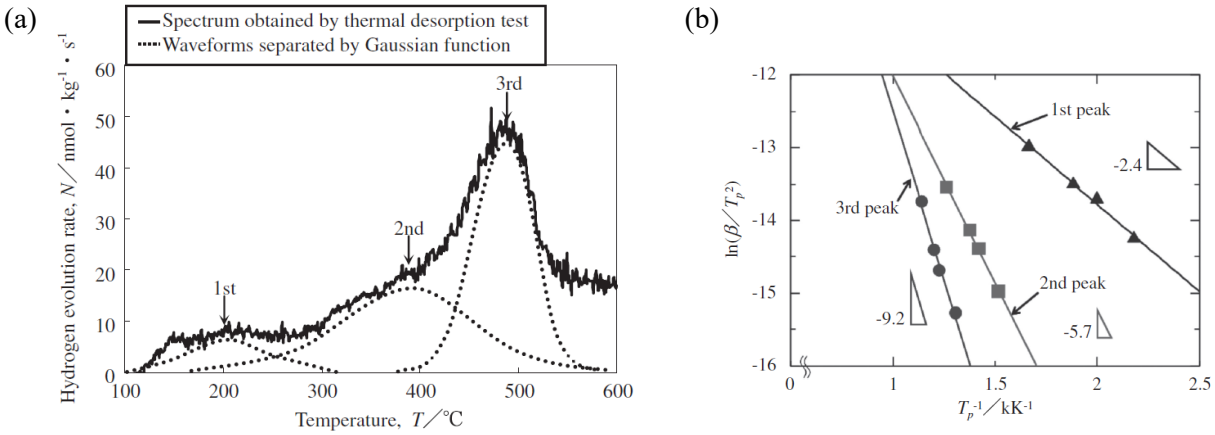

Figure 30: (a) TDS spectrum for hydrogen desorption from aluminum and (b) corresponding Arrhenius plot for the determination of trapping energies [233]

The same conditions and limitations apply to Choo and Lee's model as to Kissinger's. Hydrogen detrapping is considered to be the rate-limiting step and is assumed to happen only due to thermal energy input from heating. Diffusion and retrapping are neglected and a sparse distribution of traps implies there is no interaction between them [45,67]. To obtain valid results, small sample sizes and clean sample surfaces are essential. A small lattice diffusion activation energy in comparison to the trap activation energies is an additional necessity, as is the case in materials with large diffusion coefficients for hydrogen. [34,42,45,67,110,126,225] Wei et al. [67] showed that the Choo-Lee model is applicable for TDA measurements on many steel materials if sample geometry, surface treatment, and heating rates are adequately chosen.

2.4.2.3.3 Turnbull et al. Model

Turnbull et al. [51] proposed a mathematical model for the description of thermal desorption of hydrogen from metals incorporating the rates of all temperature-dependent processes. It was developed in succession of analyzing several hydrogen desorption models and is based on a modified Fick's second diffusion equation and McNabb and Foster's theory (see Sect. 2.3.3.1), extending it to the case of coexisting weak and strong traps. The computerized model accounts for lattice diffusion as well as detrapping and retrapping at one or more types of traps and for varying trap occupancy. [34,51,67,70]

Assuming the sample to be shaped as a slab with length and width much greater than the thickness, a one-dimensional analysis can be adopted. Thermal desorption is described by one formulation for the mass conservation of hydrogen in the material and one additional equation for the trap occupancy for each trap type. Considering two types of traps, the mass conservation of hydrogen atoms in the metal lattice is defined by

$$\frac{\partial \mathrm{c}}{\partial t} = D_0 \exp\left[-\frac{E_D}{R(\phi t + T_i)}\right]\frac{\partial^2 c}{\partial x^2} - N_1\frac{\partial \theta_1}{\partial t} - N_2\frac{\partial \theta_2}{\partial t} \quad , \qquad (63)$$

where t is time, x the distance through the specimen, c the hydrogen concentration at x, D_0 the pre-exponential factor of the lattice diffusion coefficient, E_D the activation energy for lattice diffusion, N the trap density, θ the fractional occupancy of the trap sites, R the universal gas constant, ϕ the heating rate, and T_i the initial temperature. The numeral subscripts identify the different specific trap types.

For two types of trap sites, the time-dependent hydrogen occupancies influenced by capture and release rates are described by

$$\frac{\partial \theta_1}{\partial t} = k_1^0 \exp\left[-\frac{E_1^t}{R(\phi t + T_i)}\right] c(1-\theta_1) - p_1^0 \exp\left[-\frac{E_1^d}{R(\phi t + T_i)}\right]\theta_1 \quad , \qquad (64)$$

and

$$\frac{\partial \theta_2}{\partial t} = k_2^0 \exp\left[-\frac{E_2^t}{R(\phi t + T_i)}\right] c(1-\theta_2) - p_2^0 \exp\left[-\frac{E_2^d}{R(\phi t + T_i)}\right]\theta_2 \quad , \qquad (65)$$

where k_0 and p_0 are the pre-exponential constants for the capture and release rates, E^t and E^d the activation energies for trapping and detrapping. The numeral subscripts identify the different trap types. The traps are considered to be independent of each other, no direct jumps of hydrogen from one trap to the next are allowed, but an intermediate diffusion path must be followed. It is possible to expand the model to more than two types of traps by adding terms with succeeding subscripts to Equation (63) and formulating additional equations analogous to Equations (64) and (65) for each supplemental trap type. [51]

Equations (63) to (65) are non-linear with time-dependent coefficients, therefore a numerical solution is necessary, and suitable initial and boundary conditions must be defined. It is assumed that the sample is uniformly charged at the beginning of the experiment and that during the analysis, the hydrogen concentration at the surface as well as the flux at the central point of the slab are zero, the latter due to symmetry. Further assumptions are that hydrogen recombination and molecular desorption take place very fast in comparison to other processes. The complexity of the calculations of trap densities depends on the discreteness of the peaks. In the simplest case of one singular peak, the trap density can be determined from the total hydrogen content, which in turn can be derived from integrating the flux over time. [51]

2.4.2.3.4 Other Hydrogen Desorption Models

Carter Model and Redhead Model

Carter [209] and Redhead [207] proposed desorption models in the early 1960s. Their formulations are similar to Choo and Lee's model, with the difference that theirs focus on surface sites without considering diffusion in the bulk of the material [51].

Wilson and Baskes Model

Wilson and Baskes [234] described an analysis of thermal hydrogen desorption based on experiments on 316 stainless steel implanted with deuterium. The model considers only one type of trap but accounts for all temperature-dependent processes, i.e. hydrogen diffusion in the metal lattice as well as hydrogen capture and release from trap sites. The equations proposed by Turnbull et al. (see Sect. 2.4.2.3.3) reduce to those published by Wilson and Baskes when applied to one single type of trap. [51,70]

Iino Model

Iino [121] published a formulation for describing hydrogen desorption which incorporates diffusion and takes into account two types of traps. Even though both types of traps are considered to be irreversible, the trap occupancy is assumed to be low. This contradiction was resolved by removing the detrapping term from one of the equations. [51]

Ono and Meshii Model

Ono and Meshii [65] suggested a model based on a simplified diffusion equation and on Oriani's proposition of local equilibrium between trapped and lattice hydrogen. They considered the kinetic reactions of hydrogen trapping or detrapping and calculated an approximate desorption rate using a diffusion equation containing an effective diffusion coefficient. The trap activation energy can be determined by numerically simulating an experimental desorption spectrum with an equation containing diffusion and trapping parameters. [51,67,235]

3 Experimental Section

3.1 Material

3.1.1 Material Overview

Four material classes were analyzed in this work: monocrystalline pure iron, polycrystalline pure iron, carbide containing model alloys (binary, ternary, and quaternary alloys), and industrial steel grades. Materials of different compositions and microstructures were chosen, the aim was to investigate hydrogen behavior and trapping aspects and to provide a complete characterization of the identified hydrogen trap sites. Each material contained specific types and densities of hydrogen traps.

The following list gives an overview of the investigated materials:

I. Single-crystalline Iron

II. Polycrystalline Pure Iron (ARMCO® Iron)

1. Recrystallized state
2. Annealed state (1000 °C/1 h)
3. Annealed + cold deformed
   i. 30%CR: annealed (1000 °C/1 h) + 30 % cold deformed
   ii. 60%CR: annealed (1000 °C/1 h) + 60 % cold deformed
4. Deformed by high pressure torsion (HPT)
   i. HPTu: only deformed by HPT
   ii. HPT320: HPT-deformed + annealed (320 °C/1 h)
   iii. HPT700: HPT-deformed + annealed (700 °C/1 h)

III. Model Alloys

Binary model alloys

1. Fe-0.02C: Fe with 0.02 % C added
2. Fe-0.10C: Fe with 0.10 % C added

Ternary and quaternary alloys

3. Fe-Mo-C
4. Fe-Cr-C
5. Fe-Ti-C
6. Fe-V-Nb-C

IV. Industrial Steel Grades

1. Steel A/P110
2. Steel B/T95-1(m)
3. Steel C/T95-1(g)

3.1.2 Material Characterization

3.1.2.1 Microstructure and Grain Size

The material microstructure was analyzed by optical microscopy or scanning electron microscopy (SEM), depending on the grain size. For most pure iron samples, the average grain size was determined by optical microscopy according to ASTM E112 - 12 [236]. Materials with grain sizes in the low micrometer or nanometer range were analyzed by SEM and grain size was determined by electron backscatter diffraction (EBSD). EBSD imaging was done with a Symmetry EBSD detector from Oxford Instruments at a resolution of 1462 × 714 pixels and a detection area of 370 × 250 µm at a speed of 1880 pps. The grain size is determined by summing up all detected pixels of a grain and calculating the equivalent spherical diameter.

3.1.2.2 Hardness

Material hardness was determined according to the Vickers microhardness test method with a Future Tech FM-300 microhardness tester. The chosen load level was HV1 for all materials except for single-crystalline iron and recrystallized pure iron, which were measured at a load level of HV0.5 due to their low hardness. At least seven hardness indentations were done, and an average value was calculated.

3.1.2.3 Dislocation Density

X-ray diffraction (XRD) measurements were performed to estimate the dislocation density of the materials. The measurements were done using a Bruker D8 Advance Davinci diffractometer, equipped with a Cu-K_α-X-ray tube (operated at 40 kV and 40 mA) and a position sensitive, energy discriminated Lynxeye XE-T 1D detector. The device was configured in Bragg Brentano geometry utilizing a divergence slit with a 0.06° (0.1 mm) opening on the primary side and 2.5° axial Soller slits on the primary and secondary side. All scans were performed within an angular range of 35–125° 2θ applying a counting time of 1 s/step and variable step size of 0.25° in ranges without respective peaks and 0.005° for the ranges including the $\alpha\text{-Fe}_{110}$, $\alpha\text{-Fe}_{200}$, $\alpha\text{-Fe}_{211}$, $\alpha\text{-Fe}_{220}$, $\alpha\text{-Fe}_{310}$ reflections ± 1.5° 2θ. The evaluation of the measurements was done using Topas 6 software provided by Bruker AXS. Prior to the actual evaluation, an LaB_6 line profile standard of type 660c provided by NIST [237] was measured for instrumental parametrization applying the same experimental settings as for the measurements of the respective α-Fe peaks. Subsequently, the dislocation densities were estimated by whole powder pattern modeling using a Topas macro based on the Krivoglaz-Wilkens theory [238–241], which was recently introduced by Scardi et al. [242]. [243]

The determined dislocation densities for pure iron samples in different conditions given in Table 6 show very good correlation with dislocation values reported in literature [82,244–246].

3.1.3 Single-Crystalline Iron

Iron single crystals with a minimum purity of 99.994 % were provided by MaTecK GmbH. The diameter of the cylindrical samples was 25 mm and the height 1 mm, the orientation was (100). The surface was polished to a roughness < 0.01 µm and an accuracy of orientation < 1°. Material hardness was 61 ± 1 HV, determined according to the Vickers microhardness test method applying a load level of HV0.5.

Iron single crystal samples are shown in Figure 31.

(a) (b)

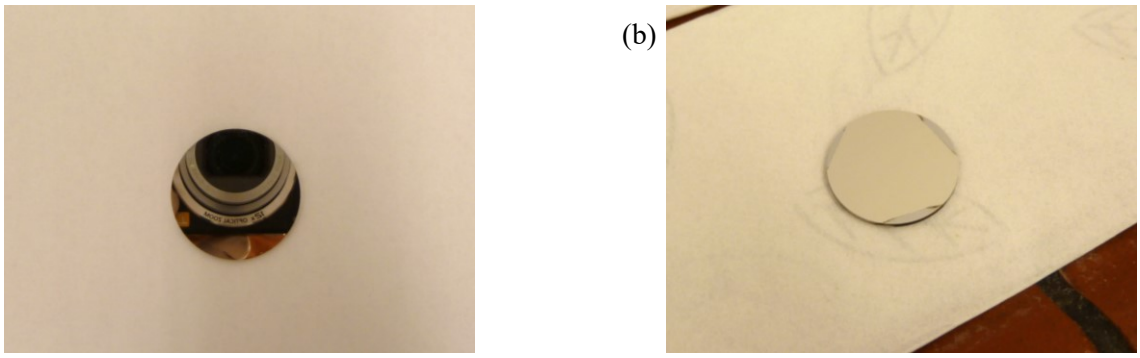

Figure 31: Iron single crystal samples with (a) bare surface,
(b) a 100 nm layer of Pd for electrochemical permeation

3.1.4 Pure Iron Materials

An overview of pure iron material data is given in Table 6, followed by detailed descriptions of the materials and their production processes.

Table 6: Pure iron material data

Material code	Material details	Grain size [µm]	Hardness [HV]	Dislocation density (XRD) [m^{-2}]
Recr	Recrystallized state	2000	61 ± 1	Not determinable
Ann	Annealed state (1000 °C/1 h)	80	79 ± 2	$6.0 \cdot 10^{13}$
30%CR	Annealed (1000 °C/1 h) + 30 % cold rolled	70	215 ± 1	$6.9 \cdot 10^{14}$
60%CR	Annealed (1000 °C/1 h) + 60 % cold rolled	60	230 ± 3	$9.4 \cdot 10^{14}$
HPT700	HPT-deformed + annealed (700 °C/1 h)	17	84 ± 5	$6.0 \cdot 10^{13}$
HPT320	HPT-deformed + annealed (320 °C/1 h)	0.3	400 ± 10	$3.9 \cdot 10^{14}$
HPTu	HPT-deformed, no further treatment (untreated)	0.2	430 ± 10	$6.8 \cdot 10^{15}$

The raw material for the production of pure iron samples in different polycrystalline microstructural conditions as well as iron-based model alloys was ARMCO® pure iron, delivered by AK Steel International B.V. The product was labeled as Grade 4 by the manufacturer and delivered in the form of hot rolled billets, approximately 80 × 80 × 300 mm in size. Various billets were analyzed by optical emission spectrometry (OEM) at voestalpine Stahl Donawitz GmbH to determine the chemical composition. The averaged result of a total of 12 test runs is shown in Table 7.

Table 7: Chemical composition of ARMCO® iron, given in wt%

C	Si	Mn	P	S	Cu	Cr	Ni	Mo	Al	Zn	Co	N_2	Others	Fe
0.003	< 0.001	0.054	0.005	0.003	0.008	0.026	0.017	0.003	0.002	0.002	0.002	0.004	< 0.001	Bal.

The ARMCO® pure iron was subjected to a particle analysis by scanning electron microscopy-energy-dispersive X-ray spectroscopy (SEM-EDX) at voestalpine Stahl Donawitz GmbH to determine purity and analyze inclusions. Analyses were done on two different locations, each of them comprising an area of 110 mm^2. The resulting image of one scan with detected particles

enlarged in size by a factor of 20 is shown in Figure 32. The relative amounts of the detected inclusions are given in Table 8 and a size overview of the three most common phases found in ARMCO® iron is shown in Figure 33.

The quantitative evaluation of the impurities showed that approximately 1 oxide species with a size between 2 and 10 µm is present per mm^2 of ARMCO® iron surface and 0.3 sulfide species with a size ranging from 2 to 6 µm. Over 98 % of detected sulfide species consisted of MnS. The largest fraction of inclusions regarding surface area was found to be Al_2O_3, at approximately 50 %, SiO_2 makes up for roughly 12 % of inclusions. Nonmetallic inclusions such as Al_2O_3, SiO_2, and MnS are known to possess hydrogen trapping capacity and hence the ability to influence hydrogen measurements. However, due to weight percentages of 0.002 % of Al and below 0.001 % of Si in the base material and the resulting low number of inclusions, no significant trapping effect is expected. Consisting of 0.54 % of all inclusions regarding surface area, the trapping effect of MnS is assumed to be negligible.

For the production of deformed and heat treated polycrystalline iron specimens, the raw ARMCO® iron billets were cut along the longitudinal axis in steps of 5 mm and the sections subsequently cut in half to obtain slices with a cross section of 40 × 80 mm and a thickness of around 5 mm. These slices served as the starting point for ensuing material treatment.

The necessary mechanical and thermal treatment steps to generate the desired material states are described below.

Figure 32: Qualitative SEM-EDX image of particles in ARMCO® iron, scan area 110 mm^2, particle enlargement 20 ×

Table 8: Relative amounts of particle inclusions in ARMCO® iron

Inclusion phase	Relative amount (regarding area) [%]
Al_2O_3	50.31
MnO	21.04
SiO_2	11.85
TiO	1.51
MnS	0.56
Others	< 1

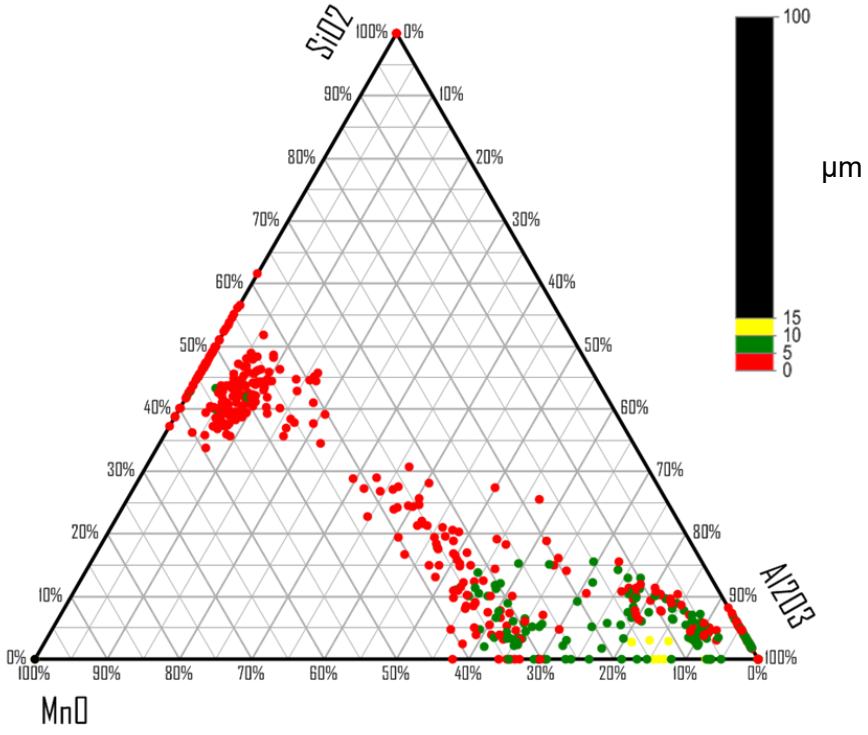

Figure 33: Size overview of the three most common inclusion phases found in ARMCO® iron, given in µm

3.1.4.1 Recrystallized Iron

To achieve primary recrystallization and pronounced grain growth, metal is plastically deformed above a critical strain and subsequently annealed at temperatures higher than the recrystallization temperature. The lower the plastic deformation, i.e. the closer to the critical strain, the larger the grains will grow during the recrystallization progress. However, with lower grades of deformation, higher annealing temperatures are necessary for grain growth (see Figure 34). [247,248] For iron, iron-based materials, and steel, the critical strain region ranges from around 3 to 5 % reduction up to 10 to 15 % reduction. [248–250] The recrystallization temperature T_R for pure metals can be estimated from the melting point T_m by an approximate proportionality ($T_R \approx 0.4\, T_m$), resulting in $T_R \approx 450$ °C for iron [74].

With the exact degree of deformation for severe grain growth being unknown, a trial-and-error approach proved useful. Raw ARMCO® iron slices were deformed to reductions of 3, 4, 5, and 6 % and subsequently annealed in a Leybold-Heraeus PD 1000 furnace at 850 °C under vacuum atmosphere for 150 hours. The best results were achieved with plastic deformation to 5 % reduction, with these samples showing the most pronounced and uniform grain growth.

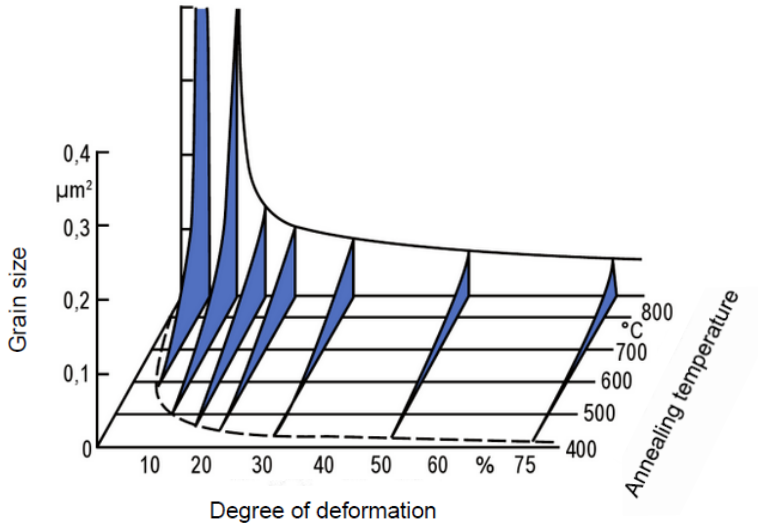

Figure 34: Recrystallization diagram for pure iron, annealing time 1 h [251]

The created recrystallized microstructure is shown in Figure 35. Strong grain growth with very satisfactory uniformity of grain size distribution and an average grain size of 2000 µm or 2 mm was achieved. The large size of grains results in a minimum number of grain boundaries serving as potential hydrogen traps in the material. Due to the long annealing time of 150 hours and the recrystallization progress, dislocations and other lattice imperfections were presumably annihilated to a high extent. The determination of the dislocation density by XRD crystallography was not possible owing to the large grain size, but the low material hardness value of approximately 60 HV indicates a lattice with low dislocation density and few grain boundaries.

Material characteristics and conducted material treatment steps for the production are given in Table 9.

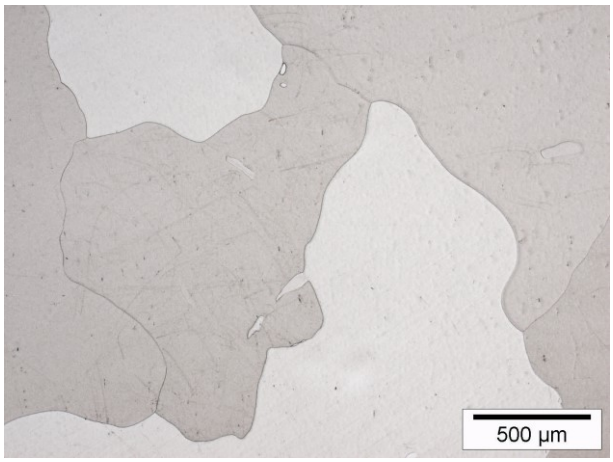

Figure 35: Recrystallized pure iron

Table 9: Material characteristics of recrystallized pure iron

Material code	Material treatment steps	Grain size [µm]	Hardness [HV]	Dislocation density (XRD) [m^{-2}]
Recr	1. Cold rolling to 5 % reduction 2. Vacuum annealing (850 °C/150 h)	2000	61 ± 1	Not determinable

3.1.4.2 Annealed Iron

To produce material in an annealed state, slices of raw ARMCO® iron were annealed in air at 1000 °C for one hour. To reduce contact with oxygen and minimize the resulting surface oxidation, the iron slices were wrapped in Ticronic Type 321 stainless steel heat treating foil.

The microstructure was analyzed by optical microscopy and is shown in Figure 36. The resulting grain size was 80 µm. The annealing process caused lattice relaxation accompanied by a low dislocation density, identified as $6.0 \cdot 10^{13}$ m^{-2} by XRD measurements, and a low hardness value of 79 HV. Table 10 gives a summary of material data.

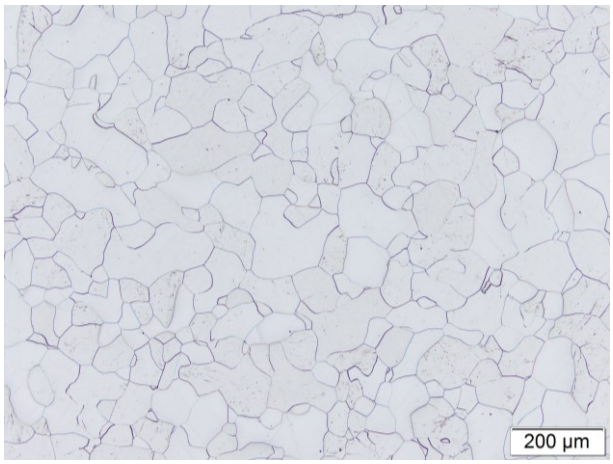

Figure 36: Annealed (1000 °C/1 h) pure iron

Table 10: Material characteristics of annealed pure iron

Material code	Material treatment steps	Grain size [µm]	Hardness [HV]	Dislocation density (XRD) [m^{-2}]
Ann	Annealing in air (1000 °C/1 h)	80	79 ± 2	$6.0 \cdot 10^{13}$

3.1.4.3 Annealed + Cold Deformed Iron

The iron slices in an annealed state (see Sect. 3.1.4.2) served as starting point for the annealed and subsequently cold worked material condition. After annealing at 1000 °C in air for 1 hour, the iron slices were plastically deformed by cold rolling to two different grades of thickness reduction: 30 % and 60 %. The material temperature did not exceed 50 °C during the rolling process.

Cold rolling had a minimum impact on the average grain size, but caused a notable elongation of grains, as optical microscope images in Figure 37 reveal. Cold working strengthens the material by introducing dislocations. XRD crystallography confirmed an increase in the density of dislocations by over one order of magnitude compared to the annealed state. The dislocation density after cold rolling the material to 30 % reduction was approximately $7 \cdot 10^{14}$ m^{-2} and around $9 \cdot 10^{14}$ m^{-2} after rolling to 60 % reduction. Likewise, material hardness was increased by cold deformation, resulting in hardness values of 215 HV and 230 HV for the 30 % and 60 % rolled materials, respectively. An overview of material characteristics is given in Table 11.

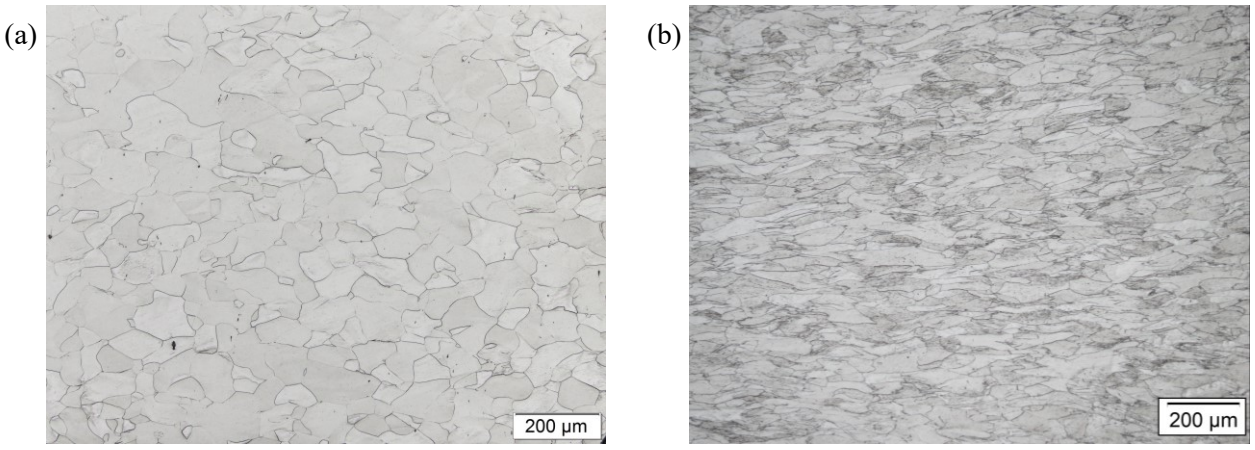

Figure 37: Pure iron annealed and subsequently cold rolled to
(a) 30 % and (b) 60 % reduction

Table 11: Material characteristics of annealed and cold worked pure iron

Material code	Material treatment steps	Grain size [µm]	Hardness [HV]	Dislocation density (XRD) [m^{-2}]
30%CR	1. Annealing in air (1000 °C/1 h) 2. Cold rolling to 30 % reduction	70	215 ± 1	$6.9 \cdot 10^{14}$
60%CR	1. Annealing in air (1000 °C/1 h) 2. Cold rolling to 60 % reduction	60	230 ± 3	$9.4 \cdot 10^{14}$

3.1.4.4 HPT-Deformed Iron

To obtain iron samples in severe plastically deformed state, discs with a diameter of 40 mm and a thickness of 2 mm were produced from the raw ARMCO® iron material by turning. The discs were then deformed by high pressure torsion (HPT). The deformation conditions were a pressure between the anvils of about 3 GPa and a sample rotation of 1080°, the temperature of the material did not exceed 80 °C during deformation. A schematic illustration of the equipment is shown in Figure 38. HPT processing was described in further detail by Pippan et al. [252].

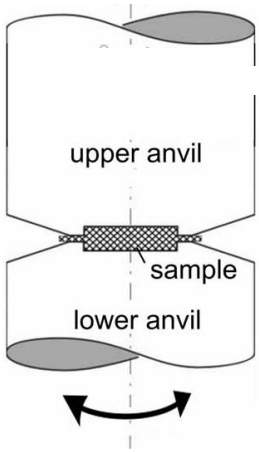

Figure 38: Tool for HPT deformation. Adapted from [253].

A total of three different forms of HPT material states were created: one without heat treatment after HPT deformation (designated as *HPT untreated* or *HPTu*), and two with a heat treatment step following the HPT process, each at a different temperature. The low annealed material denoted as *HPT320* was annealed in air for 1 hour at 320 °C, and the high annealed material denoted as *HPT700* was annealed in air for 1 hour at 700 °C. The samples were wrapped in Ticronic Type 321 stainless steel heat treating foil to minimize surface oxidation during the annealing process.

SEM-EBSD images of the three HPT material conditions are presented in Figure 39. Severe plastic deformation by HPT caused a very pronounced refinement of grains, generating grain sizes in the nanometer region. The grain size after HPT processing was approximately 200 nm or 0.2 µm. To examine the uniformity of the material after the deformation, the grain size was determined at three different locations of the cylindrical samples: near the center, at half the radius, and close to the outer edge. With the exception of a region of negligible size in the center, the rotation of 1080° was sufficient to ensure satisfactory microstructure homogeneity throughout the mate-rial. The dislocation density determined by XRD measurements for ARMCO® iron after HPT deformation was approximately $7 \cdot 10^{15}$ m^{-2}. This value is close to the maximum achievable dislocation density in iron of roughly 10^{16} m^{-2} (see Sect. 2.2.4.2) and is an indicator for the severity of deformation achievable by HPT processing.

Heat treatment after the deformation causes grain coarsening as well as a relaxation of the lattice and the annihilation of dislocations. The annealing temperature of 320 °C was not enough to cause pronounced grain growth after 1 hour of annealing time, and grain size increased only slightly to 300 nm. Dislocations were, however, annihilated to a great extent, the dislocation density dropped by over one order of magnitude to approximately $3.9 \cdot 10^{14}$ m^{-2}. As to be expected, more pronounced effects are observed at a higher annealing temperature. At 700 °C, 1 hour of annealing caused grains to grow to an average size of 17 µm. The impact on the dislocation density was even more profound, reducing it to $6 \cdot 10^{13}$ m^{-2}, which is the same value as for ARMCO® iron annealed at 1000 °C without prior deformation by HPT.

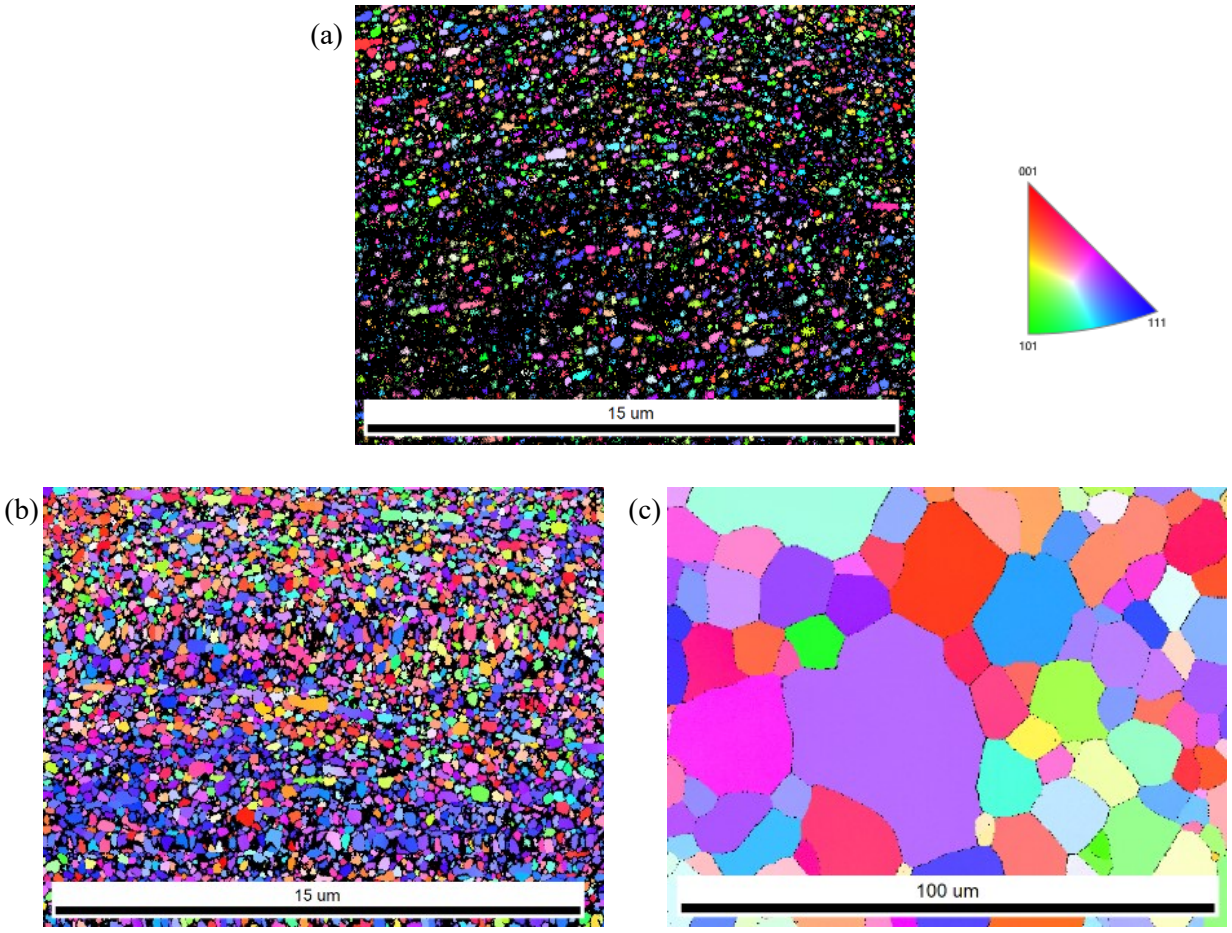

Figure 39: Pure iron deformed by HPT with (a) no further treatment (HPTu), (b) subsequent annealing at 320 °C (HPT320), (c) subsequent annealing at 700 °C (HPT700)

For the HPT700 material, the dislocation density was additionally estimated from transmission electron microscopy (TEM) images. At least three images at different locations of the sample were selected and the dislocation density as total dislocation length per volume (measured area × sample thickness) was calculated. TEM images are shown in Figure 40. The resulting value of $8.96 \pm 4.21 \cdot 10^{13}$ m^{-2} is in good agreement with the value determined by XRD.

In addition to dislocations, severe plastic deformation creates a high concentration of vacancies in metals [254,255]. In iron, vacancies are reported to gain mobility at temperatures between 200 and 300 °C [256,257], and annealing to achieve crystal recovery and annihilation of vacancies in steels is done in the temperature region of 200 to 400 °C [258–260]. Fuchigami et al. [261] reported that point defects in steel are annihilated largely by annealing at 250 °C. Vacancies introduced by HPT are hence assumed to be fully annihilated in the material annealed at 700 °C, and by annealing at 320 °C, a severe reduction or close to full annihilation of vacancies is expected. The density of vacancies created by severe plastic deformation is considered to be markedly higher than by conventional material deformation [262].

Material hardness was determined to be 430 HV after HPT deformation. Again, low annealing resulted in a slight decrease to 400 HV, while annealing at higher temperature caused hardness to drop to a value as low as 84 HV. Table 12 shows a summary of HPT material data.

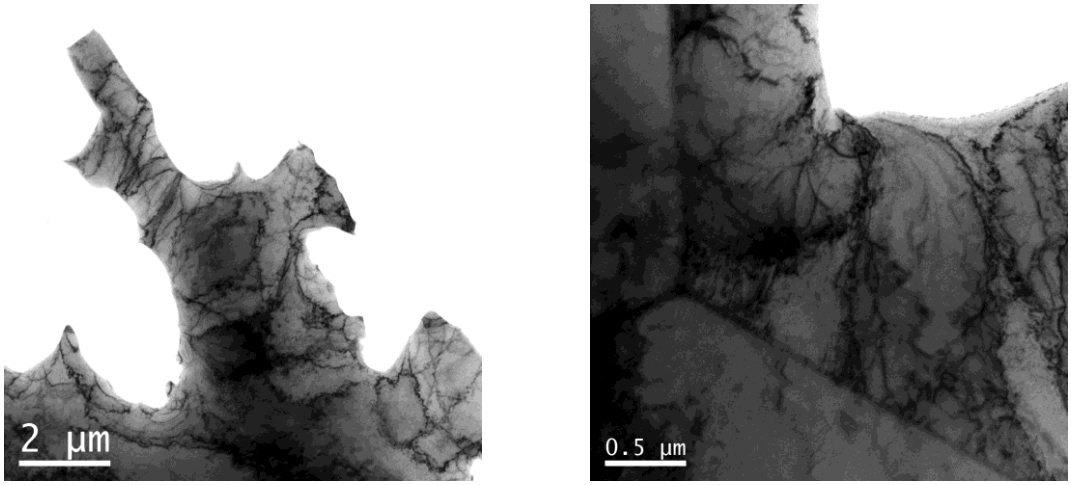

Figure 40: TEM images of HPT700 iron material
for subsequent dislocation density estimation

Table 12: Characteristics of HPT-deformed pure iron materials

Material code	Material treatment steps	Grain size [µm]	Hardness [HV]	Dislocation density (XRD) [m^{-2}]	Dislocation density (TEM) [m^{-2}]
HPTu	HPT deformation	0.2	430 ± 10	$6.8 \cdot 10^{15}$	-
HPT320	1. HPT deformation 2. Annealing in air (320 °C/1 h)	0.3	400 ± 10	$3.9 \cdot 10^{14}$	-
HPT700	1. HPT deformation 2. Annealing in air (700 °C/1 h)	17	84 ± 5	$6.0 \cdot 10^{13}$	$8.96 \pm 4.21 \cdot 10^{13}$

3.1.5 Model Alloys

An overview of model alloy material data is given in Table 13 followed by a detailed description of sample production and material testing.

The base material for the model alloys was the same ARMCO® iron as used for the production of pure iron samples (see Sect. 3.1.4). The alloys were produced at voestalpine Stahl Donawitz GmbH in a vacuum induction melting system for experimental alloy production. Melting, alloying, and casting were done under vacuum conditions. The produced bars had a dimension of 55 × 55 × 500 mm and were subsequently heat treated under appropriate conditions to form the desired industrially relevant carbides.

Table 13: Material data of model alloys

Material	Composition [wt%]	Grain size [µm]	Hardness [HV]
Fe-0.02C	C: 0.022% Fe: Balance	17	74 ± 2
Fe-0.10C	C: 0.100 % Fe: Balance	16	83 ± 2
Fe-Cr-C	Cr: 1.230 % C: 0.810 % Fe: Balance	4	178 ± 7
Fe-Mo-C	Mo: 1.212 % C: 0.073 % Fe: Balance	5	236 ± 7
Fe-Ti-C	Ti: 0.298 % C: 0.102 % Fe: Balance	5	341 ± 3
Fe-V-Nb-C	V: 0.270 % Nb: 0.093 % C: 0.102 % Fe: Balance	5	292 ± 25

3.1.5.1 Binary Model Alloys Fe-0.02C and Fe-0.10C

Two binary Fe-C alloys with different carbon contents (target contents 0.02 % and 0.10% C) were produced with the aim of creating spheroidal cementite. Melting, alloying, and casting of the ingots were done under vacuum conditions. The ingots were annealed in steps under an inert atmosphere at 700 °C, interrupted to conduct metallographic analyses to monitor the spheroidizing process. The total annealing time to achieve the desired microstructure was approximately 37 hours. Target and actual material compositions are given in Table 14.

SEM and EBSD images are shown in Figure 41 for Fe-0.02C and in Figure 42 for Fe-0.10C. The resulting grain size was very similar for both materials, 17 µm for Fe-0.02C and 16 µm for Fe-0.10C. A correlation of the hardness value with the carbon content was apparent, it resulted in 74 HV for the low-carbon material and was slightly higher at 83 HV for the alloy with higher carbon content. Material characteristics for the binary model alloys are summarized in Table 14.

Table 14: Material data of binary Fe-C model alloys

Model alloy	Stoichiometric target composition [wt%]	Actual composition [wt%]	Target carbide stoich.	Material treatment	Grain size [µm]	Hardness [HV]
Fe-0.02C	C: 0.020 % Fe: Balance	C: 0.022 % Fe: Balance	Fe_3C	Annealing (700 °C/37 h)	17	74 ± 2
Fe-0.10C	C: 0.100 % Fe: Balance	C: 0.100 % Fe: Balance	Fe_3C	Annealing (700 °C/37 h)	16	83 ± 2

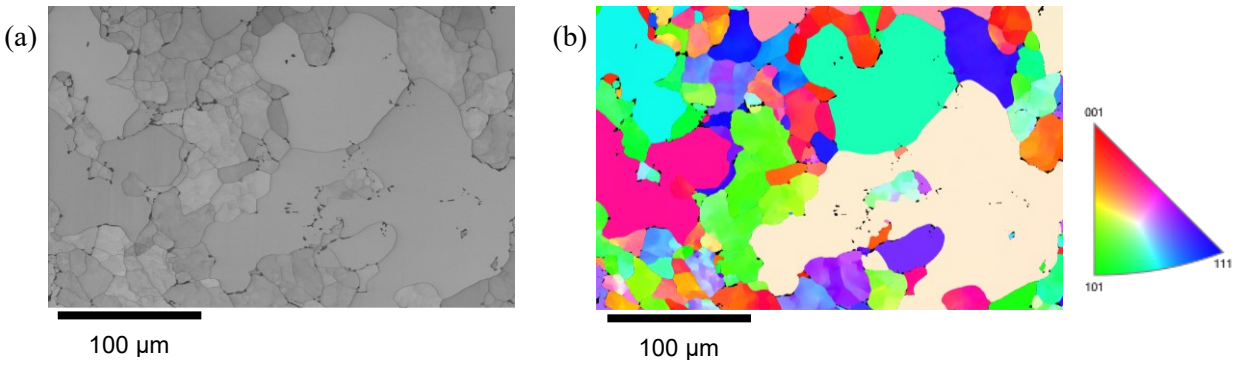

Figure 41: Fe-0.02C model alloy in SEM-EBSD images in (a) gray scale and (b) color scale

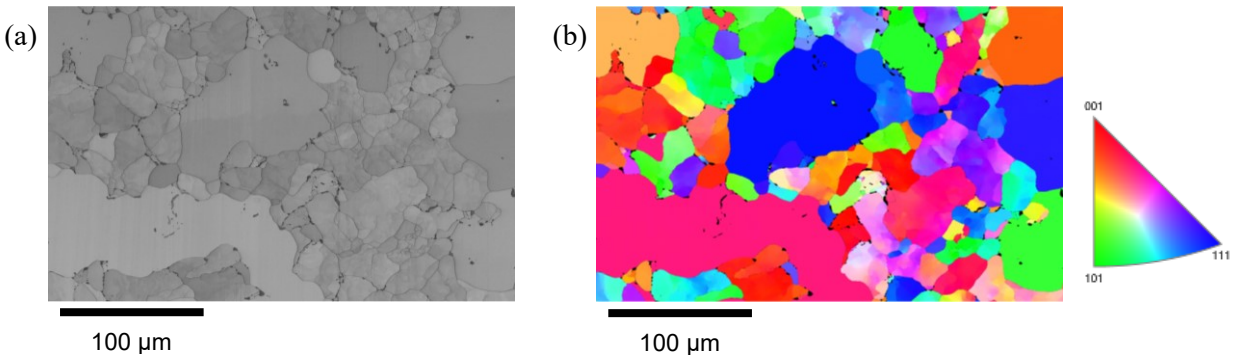

Figure 42: Fe-0.10C model alloy in SEM-EBSD images in (a) gray scale and (b) color scale

SEM-EDX analyses were done to analyze the formed carbides and other precipitates. An exemplary image for model alloy Fe-0.02C can be seen in Figure 43, the elemental compositions determined using EDX for the locations shown in the image are given in Table 15. The analyses revealed that the heat treatment led to the creation of precipitates: apart from larger inclusions detected already in prior analyses of the ARMCO® raw material as e.g. MnS, nanometer-sized iron carbides with small impurities of N, O, and Al, as well as mixed precipitates containing Fe, C, N, and Al and lower amounts of O were found. It is to be noted that the quantification of the elements C, N, and O by EDX spectroscopy proves to be challenging and the results for these elements should be treated with caution.

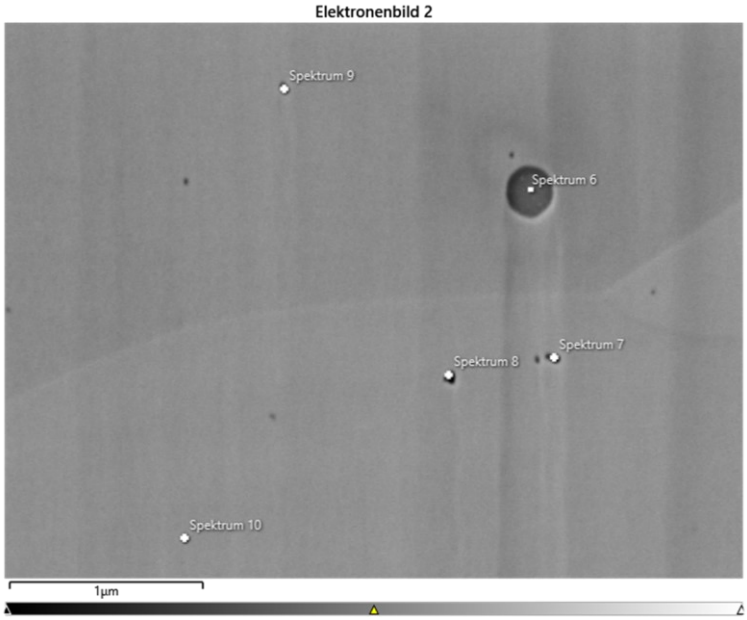

Figure 43: SEM-EDX image of model alloy Fe-0.02C

Table 15: Elemental composition of SEM-EDX spectra in Fe-0.02C, given in at%

Element	Spektrum 6	Spektrum 7	Spektrum 8	Spektrum 9	Spektrum 10
C	8.07	6.66	7.09	10.13	10.00
N	0.27	12.00	14.32	2.42	2.09
O	3.31	3.60	3.31	5.01	6.00
Al		14.31	15.57	2.11	2.15
S	43.17		5.12		
Mn	42.30				
Fe	2.87	63.43	54.60	80.32	79.74
Total	100.00	100.00	100.00	100.00	100.00

For the model alloy with higher carbon content, Fe-0.10C, SEM-EDX analyses showed a similar result. Apart from inclusions already detected in the raw ARMCO® material, the heat treatment evidently resulted in the formation of precipitates with sizes in the nanometer region. No pure iron carbides were found, but carbides with impurities of mostly N, O, and Al were present. These elements were generally found in lower quantities than C. An exemplary SEM-EDX image for Fe-0.10C is shown in Figure 44. The corresponding compositions are given in Table 16.

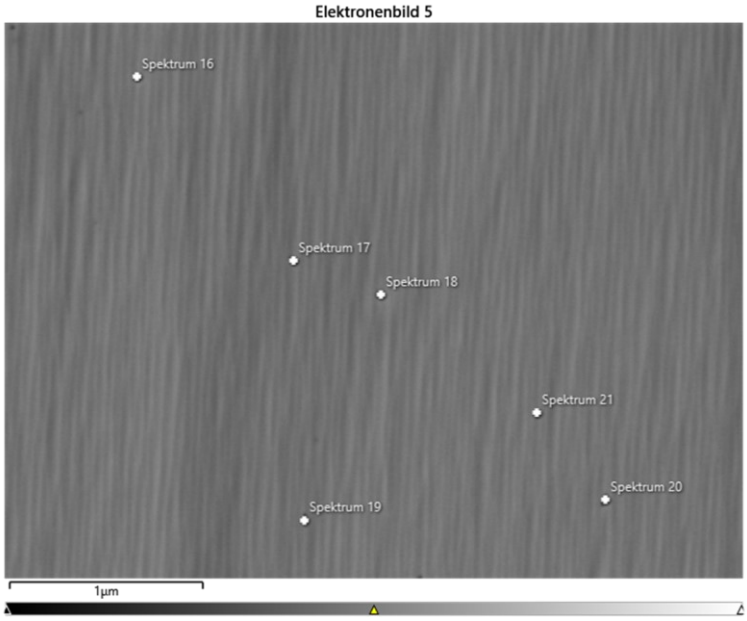

Figure 44: SEM-EDX image of model alloy Fe-0.10C

Table 16: Elemental composition of SEM-EDX spectra in Fe-0.10C, given in at%

Element	Spektrum 16	Spektrum 17	Spektrum 18	Spektrum 19	Spektrum 20	Spektrum 21
C	8.89	10.12	9.27	9.89	10.35	10.19
N	2.96	7.70	9.79	3.33	2.61	2.66
O	3.58	4.47	4.24	4.88	5.28	4.94
Al	4.79	9.15	13.03	3.03	1.69	1.72
S	9.70					
Fe	70.08	68.57	63.66	78.87	80.07	80.50
Total	100.00	100.00	100.00	100.00	100.00	100.00

3.1.5.2 Ternary and Quaternary Model Alloys

Four experimental model alloys, three ternary (Fe-Cr-C, Fe-Mo-C, and Fe-Ti-C) and one quaternary (Fe-V-Nb-C), were produced by adding carbon and carbide-forming elements to ARMCO® iron. Ingots of the desired composition were melted, alloyed, and cast under vacuum conditions and heat treated to form carbides. All four model alloys underwent austenization at 1250 °C for 90 minutes and subsequent quenching in water, followed by annealing at 550 or 600 °C for 2 hours under an inert atmosphere. The goal was the creation of industrially relevant carbides. The contents of carbon and carbide-forming elements were chosen considering stoichiometric composition of common carbides and with the aim of generating comparable carbide contents in the different alloys. The reason for producing one quaternary alloy of combined V- and Nb-carbides is industrial practice: these alloying elements are generally jointly added. The stoichiometric target compositions for carbide creation and the resulting real composition as well as the material treatment steps conducted are shown in Table 17.

SEM-EBSD images were taken to analyze microstructure and grain size and are shown in Figure 45 to Figure 48. All four materials exhibit a tempered martensitic lath structure due to austenizing and quenching, with ferrite at the grain boundaries. Innergranular shade gradients in gray scale EBSD images indicate a stressed microstructure with high dislocation density. For all four model alloys, the grain size was very similar and in the range of 4 to 5 µm.

The hardness was the lowest for Fe-Cr-C at 178 HV and Fe-Mo-C at 236 HV. It reached 292 HV for the quaternary alloy Fe-V-Nb-C and had the highest value for Fe-Ti-C at 341 HV. Material characteristics are summarized in Table 17.

SEM-EDX analyses provided information on the formed carbides. Inclusions and precipitates could be detected down to a minimum size of 3 to 5 nm. Fe-Ti-C and Fe-V-Nb-C showed the presence of carbides: in the Fe-Ti-C alloy, finely dispersed Ti-carbides with sizes ranging from approximately 50 to over 200 nm were detected. Additionally, but to a lower extent, Ti-carbonitrides and Ti-oxynitrides, as well as occasional Ti-sulfides were present. In the quaternary alloy Fe-V-Nb-C, carbides were larger in size, ranging from approximately 500 nm to 2 µm. Most carbides were the desired mixed carbides of V and Nb, with varying ratios of V to Nb. Furthermore, mixed carbides e.g. of the elements Si, V, and Nb were found, as well as scarce Nb-oxides. In addition to carbides, in both the Fe-Ti-C and Fe-V-Nb-C material, Si- and Al-oxides were present. Exemplary SEM-EDX images and the composition of the corresponding analyzed locations are shown in Figure 49 and Table 18 for Fe-Ti-C and in Figure 50 and Table 19 for Fe-V-Nb-C.

For the alloys Fe-Cr-C and Fe-Mo-C, carbides in the detectable size range could not be seen. It is possible that carbides with sizes below 5 nm were formed, which are not visible in the performed analyses. Detected inclusions were mostly in the µm range and consisted almost exclusively of Si-oxides.

Table 17: Material data of ternary and quaternary model alloys

Model alloy	Stoichiometric target composition [wt%]	Actual composition [wt%]	Target carbide stoich.	Material treatment steps	Grain size [µm]	Hardness [HV]
Fe-Cr-C	Cr: 1.240 % C: 0.075 % Fe: Balance	Cr: 1.230 % C: 0.810 % Fe: Balance	$Cr_{23}C_6$	1. Austenization (1250 °C/90 min) 2. Quenching in water 3. Annealing (550 °C/2 h)	4	178 ± 7
Fe-Mo-C	Mo: 1.200 % C: 0.075 % Fe: Balance	Mo: 1.212 % C: 0.073 % Fe: Balance	Mo_2C	1. Austenization (1250 °C/90 min) 2. Quenching in water 3. Annealing (600 °C/2 h)	5	236 ± 7
Fe-Ti-C	Ti: 0.300 % C: 0.075 % Fe: Balance	Ti: 0.298 % C: 0.102 % Fe: Balance	TiC	1. Austenization (1250 °C/90 min) 2. Quenching in water 3. Annealing (600 °C/2 h)	5	341 ± 3
Fe-V-Nb-C	V: 0.270 % Nb: 0.080 % C: 0.075 % Fe: Balance	V: 0.270 % Nb: 0.093 % C: 0.102 % Fe: Balance	VC and NbC in molar ratio 6.08 : 1	1. Austenization (1250 °C/90 min) 2. Quenching in water 3. Annealing (600 °C/2 h)	5	292 ± 25

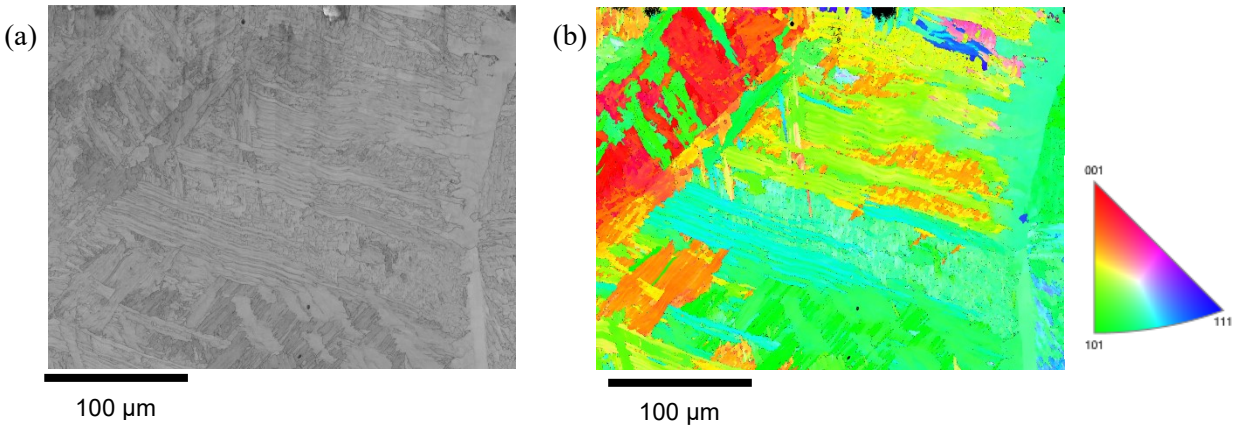

Figure 45: Fe-Cr-C model alloy in SEM-EBSD images in (a) gray scale and (b) color scale

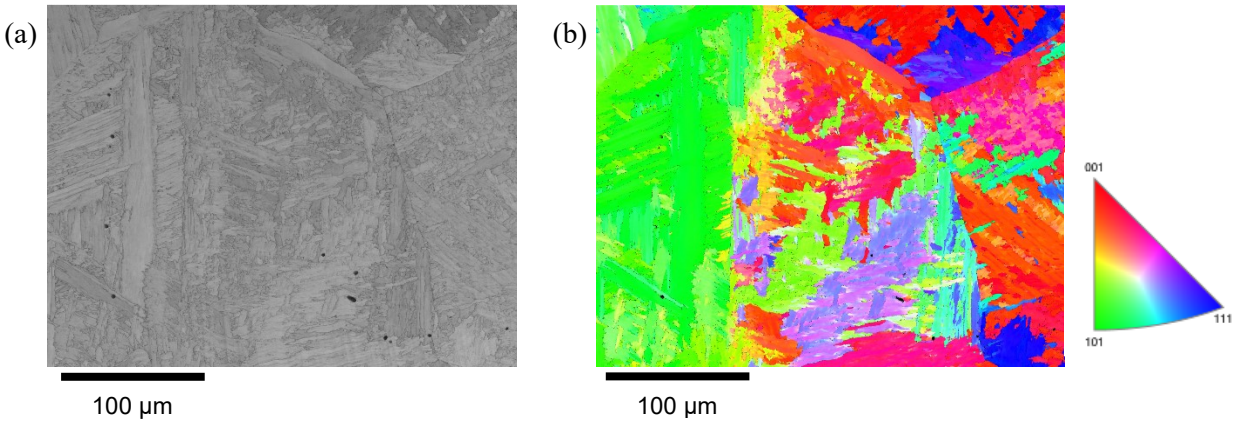

Figure 46: Fe-Mo-C model alloy in SEM-EBSD images in (a) gray scale and (b) color scale

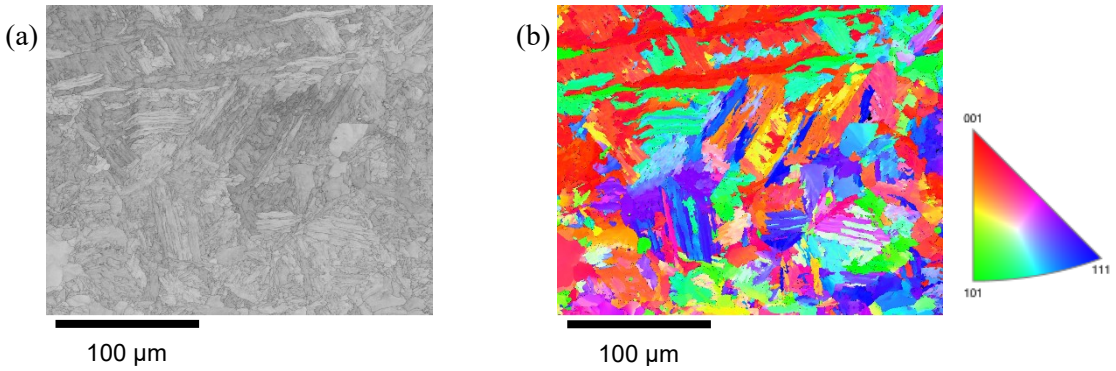

Figure 47: Fe-Ti-C model alloy in SEM-EBSD images in (a) gray scale and (b) color scale

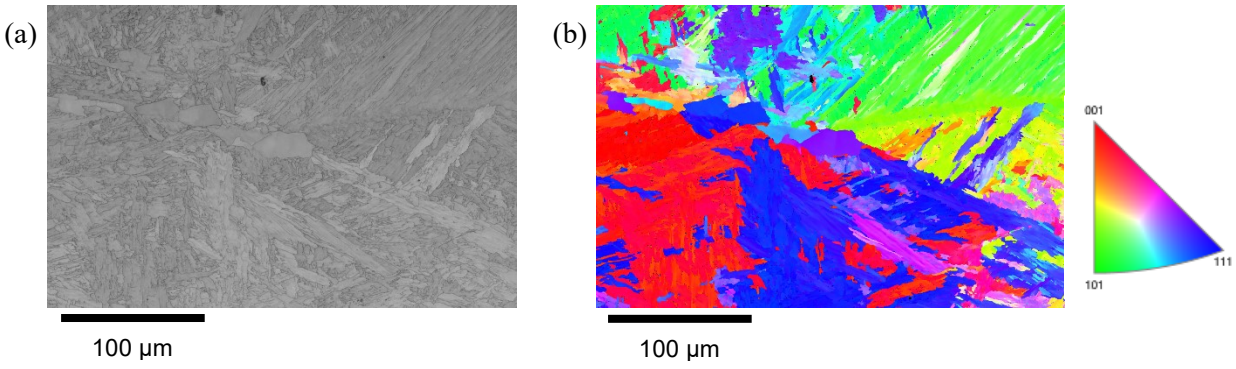

Figure 48: Fe-V-Nb-C model alloy in SEM-EBSD images in (a) gray scale and (b) color scale

Figure 49: SEM-EDX image of model alloy Fe-Ti-C

Table 18: Elemental composition of SEM-EDX spectra in Fe-Ti-C, given in at%

Element	Spektrum 1	Spektrum 2	Spektrum 3	Spektrum 4	Spektrum 5
C	47.16	46.39	46.77	48.34	47.33
Ti	51.49	50.87	48.37	48.59	48.77
Fe	1.35	2.74	4.86	3.07	3.91
Total	100.00	100.00	100.00	100.00	100.00

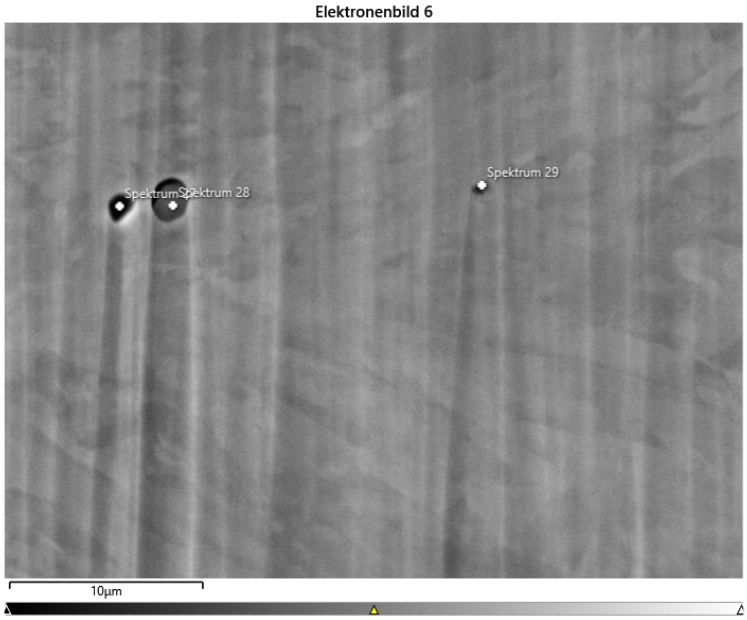

Figure 50: SEM-EDX image of model alloy Fe-V-Nb-C

Table 19: Elemental composition of SEM-EDX spectra in Fe-V-Nb-C, given in at%

Element	Spektrum 27	Spektrum 29	Spektrum 28
C	5.69	15.65	29.72
O	25.79		
Si	10.32		
Ti			1.06
V	0.25	1.74	13.43
Mn		0.46	
Fe	57.96	77.65	25.84
Nb	0.00	4.50	29.96
Total	100.00	100.00	100.00

3.1.6 Industrial Steel Grades

Three commercially available steel grades provided by voestalpine Tubulars GmbH & Co KG were analyzed. They show different resistivity to hydrogen embrittlement, determined by their resistivity to sour gas (H_2S) in sulfide stress cracking (SSC) tests according to NACE [263].To comply with confidentiality policies, the three steel grades are referred to as *Steel A*, *Steel B*, and *Steel C* in this work. Steel A/P110 is defined as not sour gas resistant, failing the NACE Standard TM0177-2016 Method A test. Steel B/T95-1(m) and Steel C/T95-1(g) both pass the NACE Standard TM0177-2016 Method A test, classifying them as resistant to sour gas. Based on the more satisfactory results in NACE Standard TM0177-2016 Method D tests, Steel C/T95-1(g) is attested a good resistance against hydrogen embrittlement caused by sour gas, and Steel B/T95-1(m) is defined as moderately sour gas resistant. To facilitate distinction of the two T95-1 steel grades analyzed in this work, the suffix *(m)* or *(g)* is added to their designations, referring to their moderate or good sour gas resistivity, respectively.

Material properties of the three industrial steels are shown in Table 20, and the five main defining chemical components are listed in Table 21. Optical microscope images are shown in Figure 51 to Figure 53.

Table 20: Material data of analyzed industrial steel grades

Steel grade	Min. yield strength [MPa]	Hardness Rockwell [HRC]	Hardness Vickers [HV]	NACE Method A	NACE Method D K_{ISSC} [MPa m$^{1/2}$]
Steel A/P110	758	29.5 ± 0.3	298 ± 3	failed	20.4
Steel B/T95-1(m)	655	23.7 ± 0.4	258 ± 3	passed	33.9
Steel C/T95-1(g)	655	23.7 ± 0.3	258 ± 2	passed	37.2

Table 21: Main components of analyzed industrial steel grades, given in wt%

Steel grade	Element				
	C	Si	Mn	P	S
Steel A/P110	0.308	0.206	1.319	0.150	0.016
Steel B/T95-1(m)	0.321	0.291	0.494	0.010	0.001
Steel C/T95-1(g)	0.256	0.264	0.338	0.008	0.002

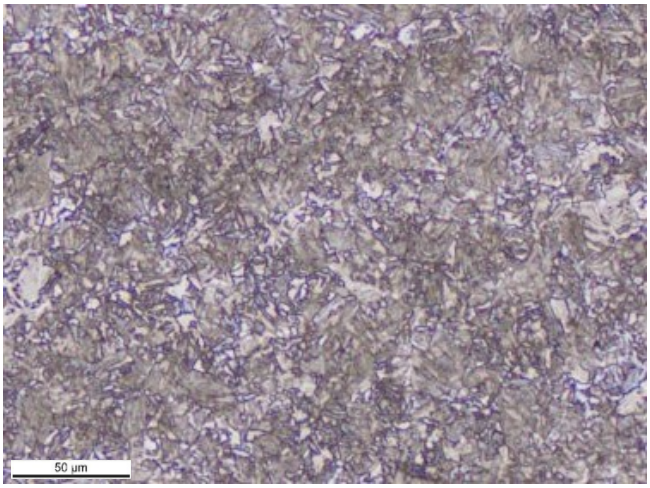

Figure 51: Microstructure of Steel A/P110

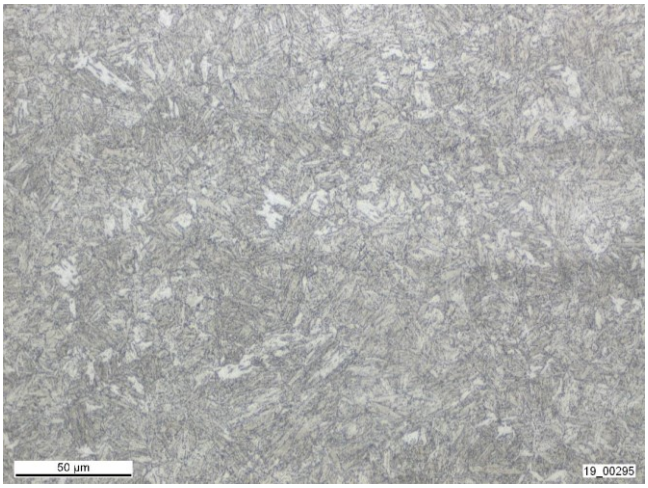

Figure 52: Microstructure of Steel B/T95-1(m)

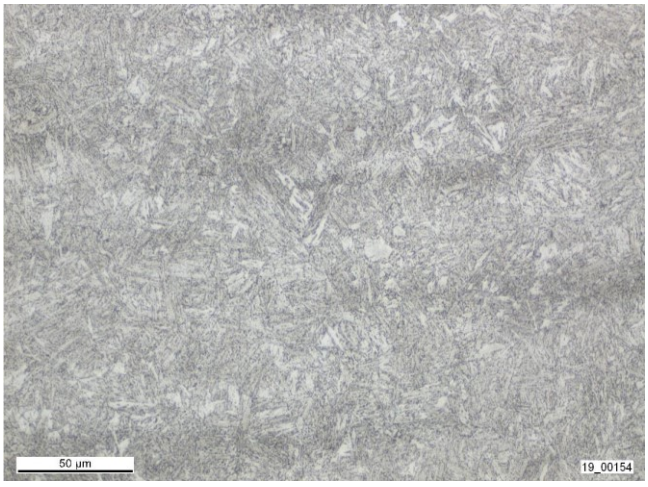

Figure 53: Microstructure of Steel C/T95-1(g)

The industrial steel grades were subjected to a particle analysis by SEM-EDX at voestalpine Stahl Donawitz GmbH to characterize inclusions. An area of 110 mm^2 was scanned and a qualitative image created, which depicts particles enlarged in size by a factor of 20. The results show the precipitated species and their relative amount regarding the total surface area of inclusions detected in the image.

In Steel A/P110, two thirds of the detected inclusions consisted of MnS, in addition Al_2O_3 and CaS were present, which accounted for approximately 10 % of the total amount each. The qualitative image scan is shown in Figure 54 and the relative amounts are given in Table 22.

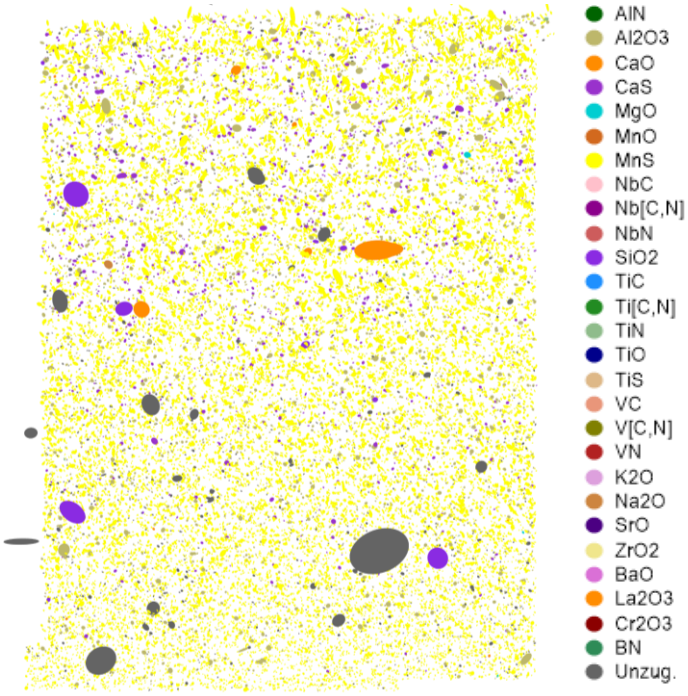

Figure 54: SEM-EDX image of particles in Steel A/P110, scan area 110 mm^2, particle enlargement 20 ×

Table 22: Relative amounts of inclusions in Steel A/P110

Inclusion phase	Relative amount (regarding area) [%]
MnS	65.34
Al_2O_3	9.93
CaS	7.98
CaO	1.99
SiO_2	1.59
Others	< 1

The inclusions in Steel B/T95-1(m) consisted mainly of Al_2O_3 and SiO_2, in addition smaller amounts of CaS, MgO, and CaO were found. The qualitative scan image is shown in Figure 55, and the detected relative amounts are given in Table 23.

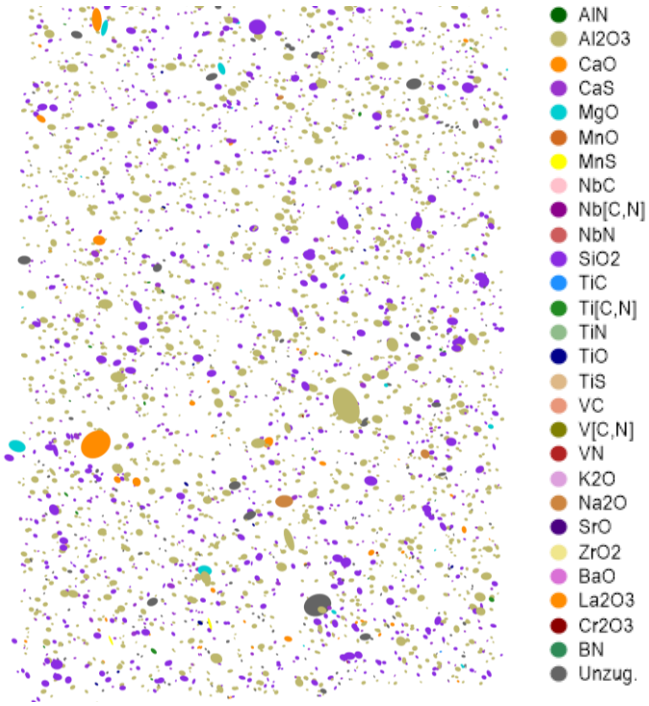

Figure 55: SEM-EDX image of particles in Steel B/T95-1(m), scan area 110 mm^2, particle enlargement 20 ×

Table 23: Relative amounts of inclusions in Steel B/T95-1(m)

Inclusion phase	Relative amount (regarding area) [%]
Al_2O_3	45.59
SiO_2	23.57
CaS	8.14
MgO	5.97
CaO	5.68
Others	< 1

In Steel C/T95-1(g), the largest amount of inclusions consisted of Al_2O_3 at approximately 44 %. Ti-carbonitrides accounted for a relative amount of 12 % of inclusions, they possess beneficial hydrogen trapping capacity. A series of other species was detected with an amount below 10 %, including SiO_2 and Nb-carbonitrides, which are also capable of trapping hydrogen. The image scan is shown in Figure 56 and the relative amounts of precipitates in Table 24.

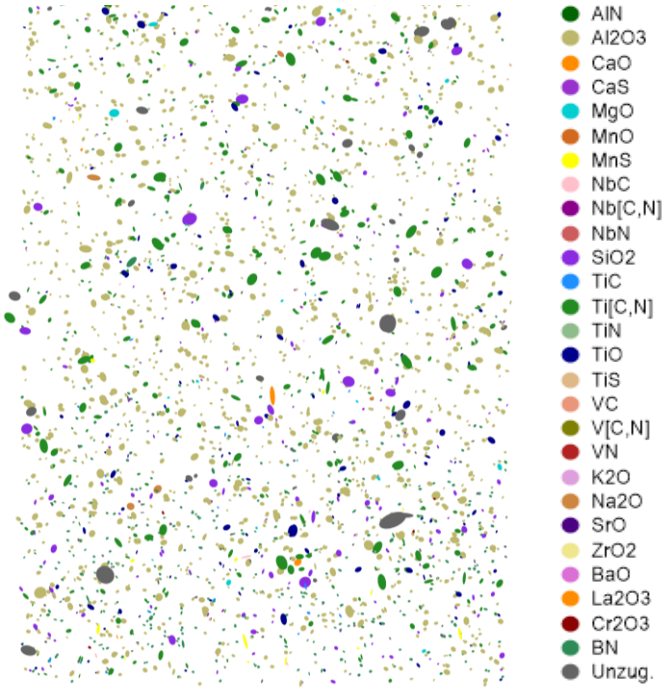

Figure 56: SEM-EDX image of particles in Steel C/T95-1(g), scan area 110 mm^2, particle enlargement 20 ×

Table 24: Relative amounts of inclusions in Steel C/T95-1(g)

Inclusion phase	Relative amount (regarding area) [%]
Al_2O_3	43.75
Ti[C,N]	12.19
SiO_2	6.91
BN	4.06
TiO	4.04
Nb[C,N]	4.00
MgO	3.21
CaS	2.89
CaO	2.89
TiS	1.78
MnS	1.01
Others	< 1

3.2 Electrochemical Permeation

3.2.1 Experimental Conditions

Electrochemical permeation experiments were carried out in a glass double cell according to Devanathan and Stachurski. The method is described in detail in Section 2.4.1. Parameters were chosen in respect of the recommendations given in the standard ISO 17081:2014 [187].

The electrolyte in the charging cell was 3.5 % NaCl solution with 1 g/l CH_4N_2S (thiourea) added as a promoter of hydrogen uptake. In the oxidation cell, the electrolyte used was 0.1 mol/l NaOH solution. Hydrogen charging was done galvanostatically at a constant cathodic current density of 1 mA cm^{-2}, while a constant anodic potential of 546 mV vs. standard hydrogen electrode (SHE), correspondent to 347 mV vs. Ag/AgCl (saturated KCl), was applied in the oxidation cell throughout the experiment. Both current and potential were supplied by a galvanostat/potentiostat Gamry Reference 600. The electrolytes were purged with Ar gas for at least 24 hours prior to the experiment, and purging continued in both cells throughout the experiment. The reason for inert gas purging is to minimize the dissolved oxygen content in the electrolyte solutions in order to reduce the oxidation of the sample material and the buildup of oxide layers, as well as to minimize hydrogen oxidation by oxygen on the exit side. The temperature in the cells was maintained at 25 ± 0.5 °C with a thermostat at all times. On both the charging and oxidation sides, the sample membrane served as the working electrode. Each cell was equipped with a Pt counter electrode and an Ag/AgCl (sat. KCl) reference electrode to measure electric current or potential. The surface area exposed to electrolyte on the charging side was 1.348 cm^2 and the exposed area on the oxidation side 1.094 cm^2. The variation of area was necessary to satisfy the requirements of the standard ISO 17081:2014 regarding the ratio of membrane area in contact with electrolyte to membrane thickness. Experimental conditions are listed in Table 25 and the experimental setup is shown in Figure 57.

Table 25: Experimental conditions

Electrolyte charging cell	3.5 % NaCl + 1 g/l CH_4N_2S
Electrolyte oxidation cell	0.1 mol/l NaOH
Charging current density	1 mA cm^{-2} (constant)
Oxidation potential	546 mV vs. SHE (constant)
Gas purging	0.2 l/min Ar (purity ≥ 99,999 %)
Counter electrode	Pt
Reference electrodes	Ag/AgCl (sat. KCl)
Temperature	25 ± 0.5 °C
Sample thickness	1 mm
Sample coating	100 nm Pd on exit side
Sample area on charging side	1.348 cm^2
Sample area on oxidation side	1.094 cm^2

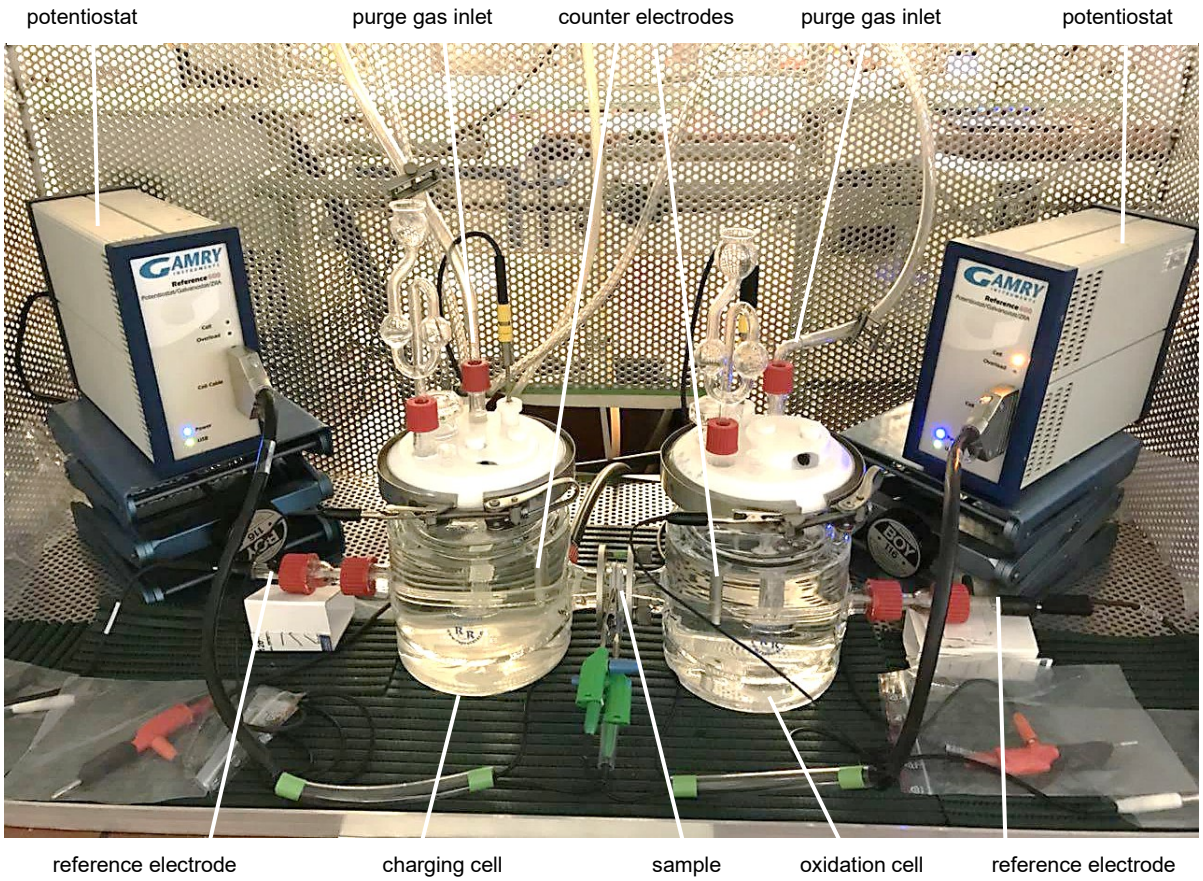

Figure 57: Electrochemical permeation setup

3.2.2 Sample Preparation

The sample thickness was 1 ± 0.01 mm for all materials. Both sides of the membrane (hydrogen entry and exit surface areas during EP experiment) were grinded with P1200 grit (FEPA) abrasive paper under flowing water and one side (the designated hydrogen exit side) subsequently coated with a Pd layer of 100 nm. Pd coating was done by sputtering after etching the surface with Ar ions. Directly before the start of the experiment, the designated charging side of the prepared samples, which was not coated by Pd, was very briefly dry grinded with P1200 grit abrasive paper to remove a potentially formed oxide layer, followed by ultrasonic cleaning of the sample in acetone and isopropyl alcohol for 15 minutes each.

3.2.3 Experimental Procedure

The cleaned sample membrane was clamped between the charging and the oxidation cell and electrically contacted. In a first step, the open circuit potential (OCP) on the oxidation side was measured as an indicator for the quality of the Pd layer. A cracked or damaged Pd coating results in a different OCP value than a uniform and undamaged one. The next step was applying

the potential in the oxidation cell and measuring the background current, which settled at a low constant value after a time span generally dependent on the sample material.

By adding the electrolyte to the charging cell and starting the cathodic current, the hydrogen charging process was started. When the measured anodic current on the oxidation side reached a constant maximum level (steady-state permeation current), charging was interrupted and the oxidation current decayed again to a low value, ideally the value of background current. This completed the first charging cycle. After stopping the cathodic charging, the electrolyte was removed from the charging cell, and the sample surface facing the charging side was cleaned from electrolyte to prevent surface deterioration and therefore negative influences on the measurement.

To start the next charging run, fresh electrolyte was added to the charging cell. The experimental procedure was identical to the first run. At least two charging cycles were carried out.

3.2.4 Evaluation

The effective diffusion coefficient was determined for the first and second permeation transients by means of the time lag method (see Sect. 2.4.1.3). The duration for the transient to reach 0.63 times its steady-state value was measured and the time lag for galvanostatic charging used to calculate the diffusion coefficient according to

$$D_{eff} = \frac{L^2}{2\ {t_{lag}}^g} = \frac{L^2}{2\ t(0.63 i_\infty)} \quad , \qquad (66)$$

resulting from Equation (50).

The apparent hydrogen solubility c_{app} beneath the membrane surface at the hydrogen entry side was estimated according to

$$c_{app} = \frac{j_\infty L}{D_{eff}} \quad , \qquad (67)$$

which results from Equation (43). Consequently, c_{app} was used to determine the permeation coefficient in analogy to Equation (45) according to

$$\Phi = c_{app} \cdot D_{eff} \quad , \qquad (68)$$

as well as to provide an estimation of the density of hydrogen trap sites in the material according to

$$N_T = \frac{c_{app}}{3}\left(\frac{D_L}{D_{eff}} - 1\right) N_A \quad , \qquad (69)$$

which is in analogy to Equation (46).

3.3 Thermal Desorption Spectroscopy

3.3.1 Sample Geometry and Preparation

To generate comparable results, the focus was set on ensuring that all TDS samples exhibited the same geometrical surface-to-volume ratio. Hydrogen traps are located in the bulk, while the sample's surface areas allow hydrogen adsorption and uptake. The constant surface-to-volume ratio guaranteed that for all samples, the given volume of bulk material had equivalent access to adsorbed surface hydrogen. This was necessary as single-crystalline iron and HPT-deformed samples naturally have a cylindrical shape, resulting from the production process, while the samples of the other materials were in cuboid form. The thickness was 1 ± 0.01 mm for all samples, the geometries are given in Table 26. The samples were grinded with P1200 grit (FEPA) abrasive paper under flowing water. Prior to the electrolytic hydrogen charging process, a brief final dry grinding step with P1200 grit paper was done and the samples ultrasonically cleaned in acetone and isopropyl alcohol for 15 minutes each.

Table 26: TDS sample geometry data

Material / Geom. data	I) Fe single crystal	II) Pure iron materials (except HPT), III) model alloys, IV) industrial steels	II.4) HPT-deformed pure iron materials
Sample shape	cylinder segment (¼ of circular base area)	cuboid	cylinder segment (¼ of circular base area)
Dimensions	r = 12.5 mm h = 1 mm	20 × 20 × 1 mm	r = 20 mm h = 1 mm
Total surface area	290 mm^2	880 mm^2	700 mm^2
Volume	123 mm^3	400 mm^3	314 mm^3
Surface-to-volume ratio	2.36 m^{-1}	2.20 m^{-1}	2.23 m^{-1}

3.3.2 Hydrogen Charging

The samples were electrolytically hydrogen charged for 1 hour under galvanostatic charging conditions at 1 mA cm^{-2} cathodic current density in 0.5 mol/l H_2SO_4 solution with 1 g/l CH_4N_2S (thiourea) added to promote hydrogen entry. The temperature was maintained at 25 ± 0.5 °C with a thermostat. A cylindrical Pt mesh electrode was used as the counter electrode. The sample acting as the working electrode was placed in the hollow interior and thus enclosed by the counter electrode, as schematically shown in Figure 58. Table 27 provides an overview of the charging conditions.

When the charging procedure was completed, the sample was quickly taken out of the electrolyte and rinsed with acetone. If rapidly effusing mobile hydrogen was to be analyzed, the sample was immediately placed in liquid nitrogen until the analysis to minimize diffusivity and loss of hydrogen.

Table 27: Charging conditions

Electrolyte	0.5 mol/l H_2SO_4 + 1 g/l CH_4N_2S
Current density	1 mA cm^{-2} (constant)
Charging time	1 h
Temperature	25 ± 0.5 °C
Counter electrode	Pt

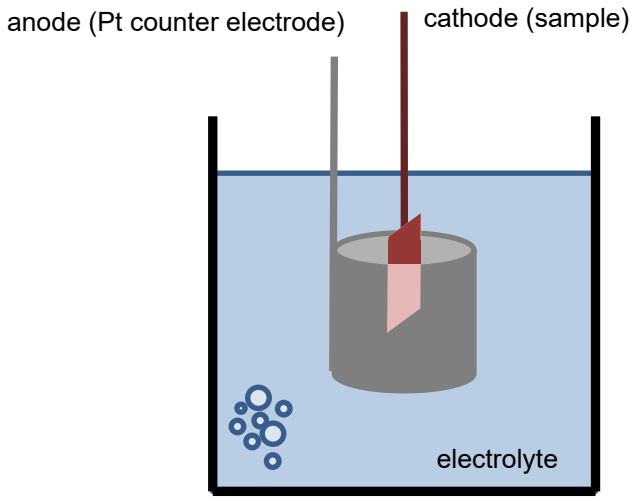

Figure 58: Hydrogen charging setup

3.3.3 Experimental Procedure

TDS measurements were done in a Bruker Galileo G8 system equipped with an external infrared furnace capable of temperature ramping and a quadrupole mass spectrometer for hydrogen detection. The temperature was measured with a thermocouple in direct contact with the sample. The system is shown in Figure 59.

Depending on the sample and the aim of the analysis, whether the focus was on analyzing hydrogen mobile at room temperature or trapped hydrogen, the samples were inserted into the furnace in a frozen state (directly taken out of liquid nitrogen) or at room temperature. To gain deeper insight into hydrogen residence time in the material and in traps, samples were either measured immediately after hydrogen charging or analyzed after allowing hydrogen to effuse for two hours. In this case, hydrogen effusion took place at room temperature in the TDS system, and the effusing hydrogen was detected and quantified. This variation of sample states and analysis modes allowed to gain an overall picture and understanding of hydrogen behavior in different materials and the effects of different types of traps.

For classical TDS experiments with temperature ramping, heating rates applied ranged between 200 K/h (0.06 K/s) and 1200 K/h (0.33 K/s). Additionally, the total hydrogen content was determined by hot extraction at 950 °C without ramping for all materials.

Figure 59: Bruker Galileo G8 system

3.3.4 Evaluation

Thermal desorption spectra were interpreted using the Choo-Lee model (see Sect. 2.4.2.3.2). Of each material, several identical samples were hydrogen charged and their hydrogen release under different heating rates analyzed. The overall desorption spectrum was fitted with the number of Gaussian-shaped curves that resulted in best correlation. Each Gaussian peak represents one single trap type or one group of different types of traps with similar activation energies. If different types of traps exhibit similar peak temperatures and therefore trap activation energies in a close range, no distinction is possible in the spectrum, and they must be treated collectively. An example is grain boundaries and dislocations in pure iron, which possess very similar activation energies. It must be considered that, depending on whether the sample was frozen in liquid nitrogen after charging or whether hydrogen was allowed to effuse, hydrogen diffusible at room temperature may be detected and interfere with hydrogen peaks resulting from traps, especially at lower temperatures. To obtain reliable results from deconvoluting the desorption curve, it is furthermore important to ensure the shape of the Gaussian peaks as well as the relative area below the Gaussian-shaped curves is similar for different heating rates of the same material.

An example of the procedure for the determination of activation energies of traps and their hydrogen contents is presented here for the Fe-Ti-C model alloy: Figure 60 shows the desorption spectra of the model alloy at three different heating rates. Hydrogen could effuse for 2 hours at room temperature prior to the analysis, hence the hydrogen detected is interpreted as trapped. The overall desorption spectrum was best fitted with two Gaussian peaks. With the temperatures corresponding to the peak maximum (desorption or peak temperature) and the heating rate, the trap activation energies can be determined from the slope of the Arrhenius plot of $\ln(\phi/T_p^2)$ vs. $1/T_p$ using Equation (62) described before:

$$\frac{\partial \ln\left(\frac{\phi}{{T_P}^2}\right)}{\partial\left(\frac{1}{T_P}\right)} = -\frac{E_a}{R} \quad . \qquad (62)$$

The resulting Arrhenius plot for the two identified Gaussian peaks and three heating rates is shown in Figure 61, and the determined trap activation energies are given in Table 28.

Table 28: Trap activation energies for Fe-Ti-C model alloy

Trap no.	Trap activation energy [kJ mol^{-1}]
1	37.0
2	60.6

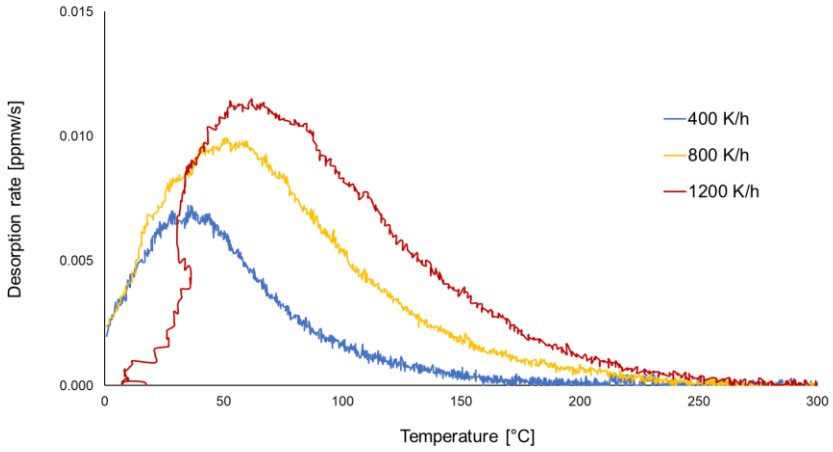

Figure 60: TDS spectra of Fe-Ti-C at heating rates of 1200, 800, and 400 K/h

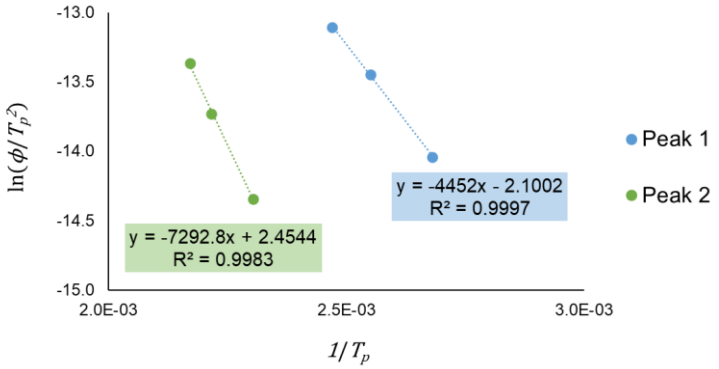

Figure 61: Arrhenius plot of two identified traps in Fe-Ti-C

By detecting the hydrogen content in the material directly after charging and after an effusion time of 2 hours, the amounts of total hydrogen, trapped hydrogen, and hydrogen mobile at room temperature could be determined. The areas below the Gaussian-shaped curves in the TDS spectra correspond to the amount of hydrogen accumulated in that specific trap. The resulting hydrogen content is shown in Table 29.

Table 29: Hydrogen content in Fe-Ti-C model alloy

Hydrogen location	Hydrogen content	
	[ppmw]	[%]
Total	4.40	100.0
Mobile at RT	3.21	73.0
Trap 1	0.86	19.5
Trap 2	0.33	7.5

4 Experimental Results

4.1 Single-Crystalline Iron and Pure Iron Materials

The permeation transients in normalized form resulting from the first charging run of electrochemical permeation experiments are shown in Figure 62. Single-crystalline iron and the three pure iron materials being subjected to annealing as the last treatment step (recrystallized, annealed, HPT700) showed nearly identical diffusivities for hydrogen and very similar transient progressions. The determined diffusion coefficients for these materials of approximately $1 \cdot 10^{-4}$ cm^2 s^{-1} are in the region of the theoretical value for hydrogen diffusion in the ideal α-iron lattice, which is reported to be in the range of $1 \cdot 10^{-4}$ to $7 \cdot 10^{-4}$ cm^2 s^{-1} (see Sect. 2.3.1). This indicates the absence of hydrogen traps in these materials. A more detailed depiction of the four transients is given in Figure 63.

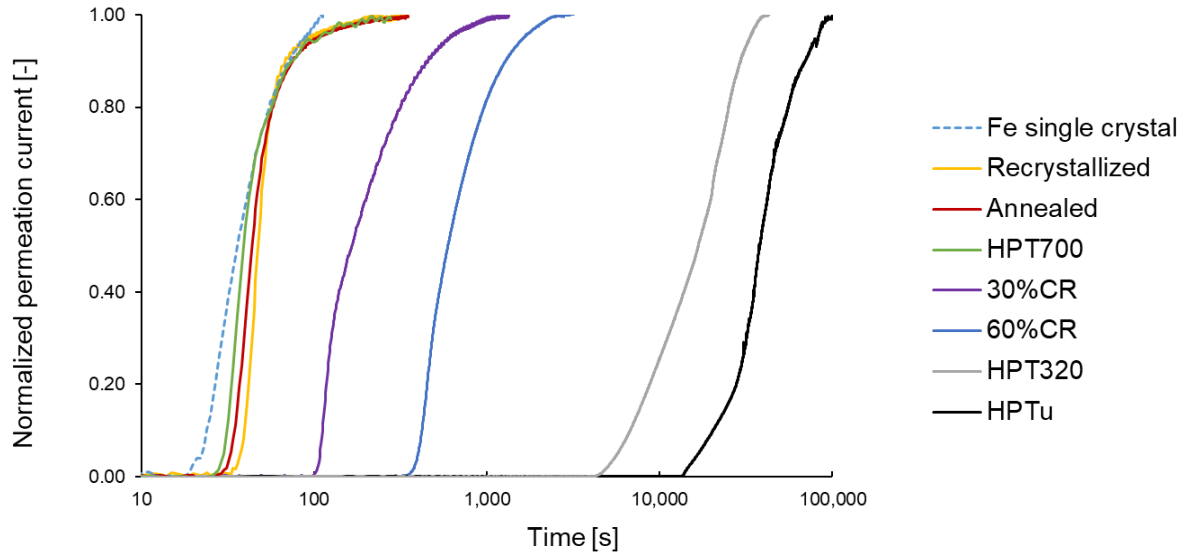

Figure 62: Normalized permeation transients of the first charging cycle of single-crystalline iron and pure iron materials

The introduction of hydrogen traps into the material by mechanical deformation resulted in hindered hydrogen diffusion and hence decreased diffusivity values. The decrease of diffusivity was more pronounced with increasing intensity of deformation. For pure iron, cold rolling to 60 % reduction of thickness caused a more notable decrease of diffusivity than cold rolling to 30 %, as the permeation transients demonstrate. Even stronger material deformation and hindering of diffusion was achieved by HPT deformation, while annealing allowed the highly disturbed lattice of HPT-deformed material to recover. Annealing at low temperature (320 °C) for 1 hour led to a slight increase of diffusivity compared to the HPT material without subsequent heat treatment, whereas by annealing at higher temperature (700 °C) for 1 hour, the diffusivity of the undisturbed lattice could be regained.

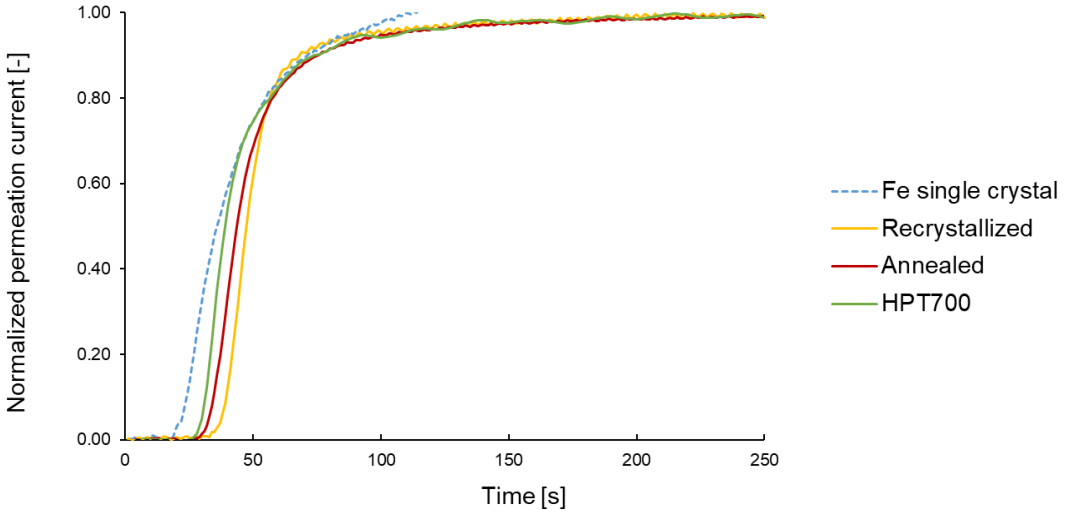

Figure 63: Normalized permeation transients of the first charging cycle of single-crystalline iron and recrystallized, annealed, and HPT700 iron materials

Results of electrochemical permeation experiments are shown in Table 30. Numeral subscripts for the effective diffusivity, the steady-state current and current density, and the steady-state hydrogen flux indicate whether the values were determined from the first or second charging cycle. The general trend shows higher hydrogen diffusivities for the second charging cycle than for the first for all materials except 60%CR. Also, apart from single-crystalline iron and 60%CR, values of steady-state current and hydrogen flux were larger for the first charging cycle than for the second. Due to the lack of additional sample material, no further investigations could be done to explain the discrepancies in the determined permeation results for single-crystalline iron and 60%CR. The apparent hydrogen concentration c_{app} beneath the membrane surface at the hydrogen entry side as well as the estimated trap density N_T increased with an increasing degree of deformation. The values of the effective diffusion coefficients resulting from the first charging cycle are graphically represented in Figure 64.

Table 30: Results of electrochemical permeation experiments for single-crystalline iron and pure iron materials

Material	$D_{eff,1}$ [$cm^2\,s^{-1}$]	$I_{\infty,1}$ [µA]	$i_{\infty,1}$ [$\mu A\,cm^{-2}$]	$j_{\infty,1}$ [$mol\,cm^{-2}\,s^{-1}$]	$D_{eff,2}$ [$cm^2\,s^{-1}$]	$I_{\infty,2}$ [µA]	$i_{\infty,2}$ [$\mu A\,cm^{-2}$]	$j_{\infty,2}$ [$mol\,cm^{-2}\,s^{-1}$]	c_{app} [ppmw]	Φ [$mol\,cm^{-1}\,s^{-1}$]	N_T [cm^{-3}]
Fe single crystal	$1.16 \cdot 10^{-4}$	13.70	12.52	$1.30 \cdot 10^{-10}$	$1.32 \cdot 10^{-4}$	15.19	13.88	$1.44 \cdot 10^{-10}$	0.01	$1.30 \cdot 10^{-11}$	$7.61 \cdot 10^{16}$
Recryst.	$1.03 \cdot 10^{-4}$	6.68	6.10	$6.32 \cdot 10^{-11}$	$1.36 \cdot 10^{-4}$	6.09	5.57	$5.77 \cdot 10^{-11}$	0.01	$6.37 \cdot 10^{-12}$	$4.94 \cdot 10^{16}$
Annealed	$1.17 \cdot 10^{-4}$	6.70	6.12	$6.35 \cdot 10^{-11}$	$1.33 \cdot 10^{-4}$	6.42	5.86	$6.08 \cdot 10^{-11}$	0.01	$6.38 \cdot 10^{-12}$	$3.76 \cdot 10^{16}$
HPT700	$1.11 \cdot 10^{-4}$	6.55	5.98	$6.20 \cdot 10^{-11}$	$1.45 \cdot 10^{-4}$	6.01	5.49	$5.67 \cdot 10^{-11}$	0.01	$6.11 \cdot 10^{-12}$	$4.10 \cdot 10^{16}$
30%CR	$2.34 \cdot 10^{-5}$	6.94	6.34	$6.57 \cdot 10^{-11}$	$3.18 \cdot 10^{-5}$	6.06	5.54	$5.74 \cdot 10^{-11}$	0.04	$6.58 \cdot 10^{-12}$	$1.18 \cdot 10^{18}$
60%CR	$6.90 \cdot 10^{-6}$	6.92	6.33	$6.56 \cdot 10^{-11}$	$6.55 \cdot 10^{-6}$	9.10	8.32	$8.62 \cdot 10^{-11}$	0.12	$6.55 \cdot 10^{-12}$	$1.39 \cdot 10^{19}$
HPT320	$2.20 \cdot 10^{-7}$	25.86	23.64	$2.45 \cdot 10^{-10}$	$2.65 \cdot 10^{-7}$	23.38	21.37	$2.21 \cdot 10^{-10}$	14.35	$2.44 \cdot 10^{-11}$	$5.36 \cdot 10^{22}$
HPTu	$1.08 \cdot 10^{-7}$	29.40	26.87	$2.79 \cdot 10^{-10}$	$1.36 \cdot 10^{-7}$	14.17	12.95	$1.34 \cdot 10^{-10}$	31.90	$2.70 \cdot 10^{-11}$	$2.36 \cdot 10^{23}$

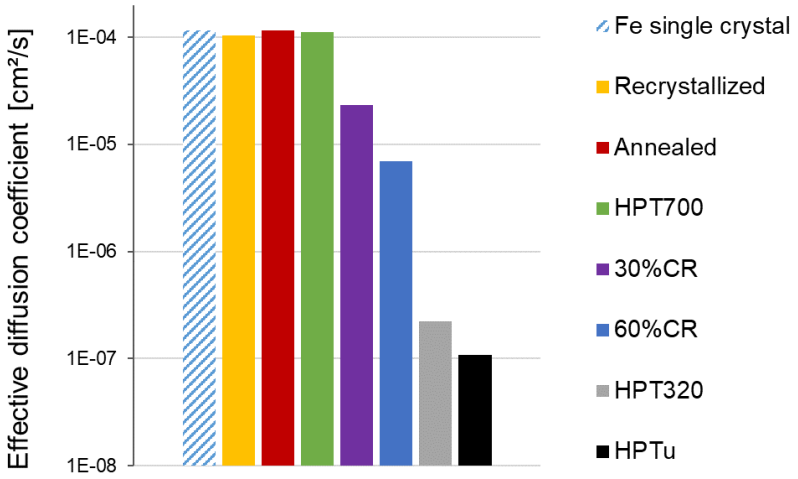

Figure 64: Effective diffusion coefficients of the first charging cycle determined by EP for single-crystalline iron and pure iron materials

Thermal desorption analyses on iron materials drew a similar picture. For single-crystalline iron, recrystallized and annealed iron, as well as HPT-deformed iron subsequently annealed at 700 °C (HPT700), no hydrogen trapping effect was detected. The hydrogen present in the material after electrolytic charging effused in a time span of a few seconds, suggesting its classification as hydrogen mobile at room temperature. Due to the absence of trapped hydrogen, lattice hydrogen mobile at room temperature constituted the total hydrogen present in these materials. By placing the samples in liquid nitrogen immediately after charging, hydrogen was immobilized and made accessible to detection. The total hydrogen content for each of these four materials ranged from 0.1 to 0.2 ppmw.

The effect of hydrogen traps is evident for the pure iron materials, which underwent mechanical deformation without subsequent heat treatment (30%CR, 60%CR, HPTu) or followed by an annealing step at low temperature (HPT320). In these materials, the deformed lattice was not given the chance to recover, or the heat treatment was insufficient to allow full recovery. TDS spectra presented in Figure 65 show increasing hydrogen content and desorption rates with increasing hydrogen trap density, resulting from increasing severity of deformation. The spectra of the 30 % and 60 % cold rolled materials and the HPT320 material were best fitted with one single Gaussian peak with a calculated trap activation energy of approximately 33 kJ mol^{-1}. Two Gaussian peaks could be identified for the spectrum of the untreated HPT material: one peak with a trap activation energy of approximately 37 kJ mol^{-1} and a second peak appearing at higher temperatures, exposing an activation energy of 51 kJ mol^{-1}.

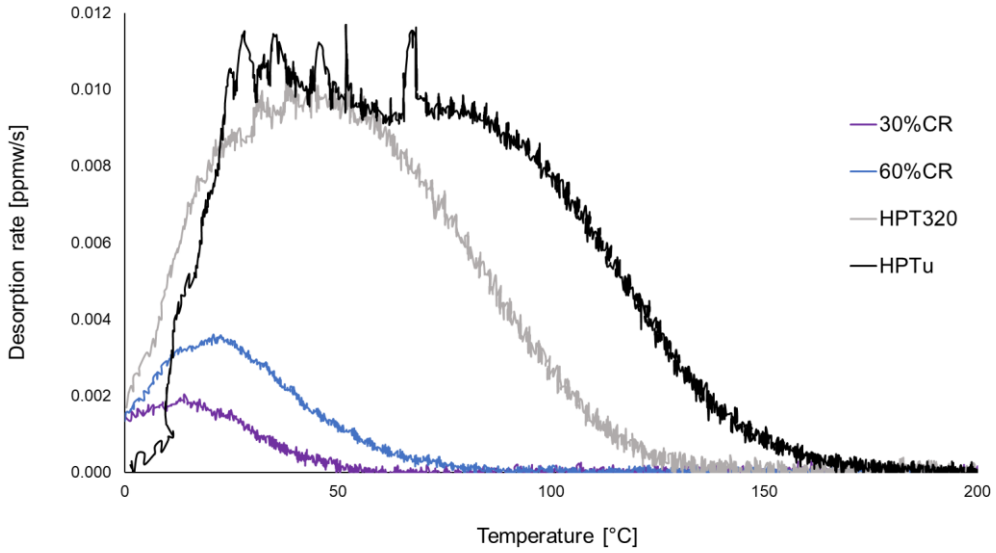

Figure 65: TDS spectra of pure iron materials at heating rate 200 K/h

As mentioned above and shown in Table 31, the total hydrogen content of the materials increased with the intensity of material deformation. It was below 1 ppwm for the 30 % cold rolled material and reached over 17 ppmw for the untreated HPT-deformed material. The amount of hydrogen mobile at room temperature and the amount of trapped hydrogen as well as the fraction of total hydrogen located in traps increased from materials 30%CR through 60%CR up to HPT320. While the HPTu material exhibited over 40 % higher total hydrogen content compared to the HPT320 material, the absolute amount of hydrogen in the lower-energy trap was notably smaller. Likewise, the amount of hydrogen mobile at room temperature decreased from 1.6 ppmw for the HPT320 material to 1.1 ppmw for the untreated HPT material. With close to 10 ppmw, the largest part of hydrogen in the HPTu material was located in its higher-energy trap.

Table 31: TDS results for single-crystalline iron and pure iron materials

Material	Total H [ppmw]	H mobile at RT [ppmw]	E_a trap 1 [kJ mol^{-1}]	H in trap 1 [ppmw]	E_a trap 2 [kJ mol^{-1}]	H in trap 2 [ppmw]
Fe single crystal	0.1	0.1	-	-	-	-
Recrystallized	0.2	0.2	-	-	-	-
Annealed	0.1	0.1	-	-	-	-
HPT700	0.2	0.2	-	-	-	-
30%CR	0.6	0.2	32.2	0.4	-	-
60%CR	1.8	0.4	32.5	1.4	-	-
HPT320	12.4	1.6	33.3	10.8	-	-
HPTu	17.8	1.1	36.6	7.2	50.9	9.5

4.1.1.1 Single-Crystalline Iron

Analysis of electrochemical permeation experiments revealed an effective diffusion coefficient for the first charging cycle of $1.16 \cdot 10^{-4}$ cm^2 s^{-1}. This is in the range of literature values for the diffusivity of hydrogen in the ideal α-iron lattice (see Sect. 2.3.1). While the first transient exhibited a flattening of the curve starting at around 0.4 times the stead-state value, the second charging cycle's slope displayed a more uniform rise and starts flattening out at around 0.7 times the steady-state value, as shown in Figure 66. This led to a slightly higher diffusivity for the second charging process of $1.32 \cdot 10^{-4}$ cm^2 s^{-1}. First and second transients showing a notably different course was not expected for this material due to the lack of hydrogen traps, which was confirmed by TDS measurements. It cannot be excluded that a measurement artifact or the buildup of a layer on the hydrogen entry side was the cause for the discrepancy between first and second permeation transients, and as only one sample of this material type was available for permeation analysis, no comparative measurements could be done. Compared to poly-crystalline iron materials of similar diffusivities, the steady-state permeation current densities i_∞ reached relatively high values of 12.52 µA cm^{-2} for the first and 13.88 µA cm^{-2} for the second charging cycle, resulting in hydrogen permeation fluxes j_∞ of $1.30 \cdot 10^{-10}$ mol cm^{-2} s^{-1} for the first and $1.44 \cdot 10^{-11}$ mol cm^{-2} s^{-1} for the second charging. From the permeation data, the hydrogen concentration c_{app} at the entry side of the sample was determined as 0.01 ppmw and the permeability Φ resulted in $1.30 \cdot 10^{-11}$ mol cm^{-2} s^{-1}. The density of hydrogen traps N_T calculated from electrochemical permeation data was $7.61 \cdot 10^{16}$ cm^{-3}.

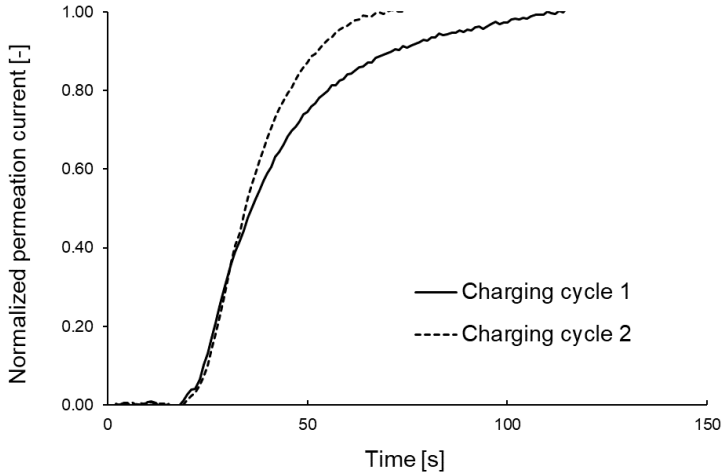

Figure 66: Normalized permeation transients of single-crystalline iron

The total hydrogen content after electrolytic charging of 0.1 ppmw measured by TDS and hot extraction was identified as lattice hydrogen, it effused from the sample within a few seconds. As mentioned before, no trapping effect was observed in single-crystalline iron. The results of electrochemical permeation measurements and TDS analyses are outlined in Table 30 and Table 31 above.

4.1.1.2 Recrystallized Iron, Annealed Iron, HPT-Deformed Iron Annealed at 700 °C (HPT700)

ARMCO® pure iron in a recrystallized state, annealed at 1000 °C for 1 hour, and HPT-deformed and subsequently annealed at 700 °C for 1 hour (HPT700) exhibited very similar characteristics. The effective diffusion coefficients determined from the first charging cycle were in the range of $1.03 \cdot 10^{-4}$ to $1.17 \cdot 10^{-4}$ $cm^2\,s^{-1}$ for the three materials, the small variation can be considered as experimental uncertainty. The same applies to the steady-state current densities i_∞, which ranged from 5.98 to 6.12 $\mu A\,cm^{-2}$, and the steady-state hydrogen permeation flux j_∞, which resulted to be approximately $6 \cdot 10^{-11}$ $mol\,cm^{-2}\,s^{-1}$ for all three material states.

A notable effect occurred during the second permeation charging cycle: as the cathodic charging current was imposed, an immediate overshoot of the anodic oxidation current to around 1.2 to 1.4 times the steady state value was observed, followed by the transient dropping from this peak value and reaching a steady state after approximately 600 to 800 seconds. The emergence of this peak overshoot was associated with the formation and degradation of a layer on the hydrogen charging side of the sample. In addition to the overshoot during charging, the decay transients of the second and subsequent charging cycles did not exhibit a continuous

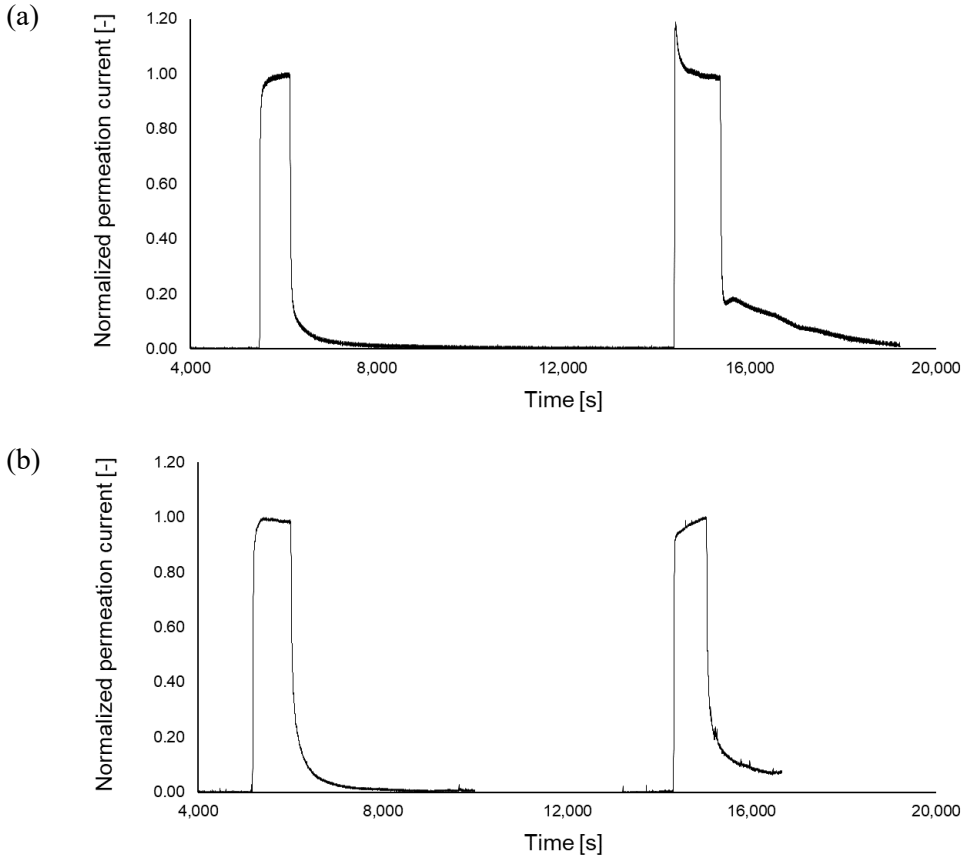

Figure 67: Normalized permeation transients of annealed pure iron showing first and second charging sequences with subsequent decay: (a) with and (b) without peak overshoot of the second charging transient due to layer formation on the hydrogen charging side

decay as theoretically expected but revealed an intermediate short current increase during the hydrogen discharge, visible as a shoulder or slight peak in the oxidation current signal during its drop off from the steady-state value plateau. The presumed reason is a surface layer building up on the charging side when the sample is exposed to the electrolyte and no charging current is applied, i.e. when the sample remains in contact with the electrolyte during the discharge process after the first charging cycle. The issue could be satisfactorily solved by draining the electrolyte from the charging cell after the charging cycle and subsequently cleaning and drying the sample surface, all with the sample remaining in place, without dismantling the experimental setup, and without exposing the sample to air or oxygen. During the decay process between the charging cycles, the drained charging cell was purged with Ar gas to provide an inert atmosphere, and fresh electrolyte was poured in when starting the following charging cycle. Figure 67 shows the resulting transients for permeation experiments on two identical annealed pure iron samples: in Figure 67(a), the electrolyte was not removed after the first charging process, consequently resulting in a peak overshoot and non-ideal decay of the oxidation current for the second charging cycle. In Figure 67(b), the electrolyte was drained from the charging cell, the sample surface cleaned, and fresh electrolyte provided for the second charging run, resulting in an unaffected second transient showing nearly ideal behavior.

The effect of overshooting permeation current was only observed in the three materials with high diffusivities and hence fast permeation transients, which are discussed in this present section: recrystallized pure iron, annealed pure iron, and pure iron subjected to HPT deformation and subsequent annealing at 700 °C (HPT700). Nonetheless, the approach of electrolyte draining and sample cleaning was adopted for the permeation measurements on all tested materials, with two exceptions: due to the lack of additional identical sample material, electrochemical permeation experiments on recrystallized pure iron and HPT700 could not be repeated, and hence the shown transients exhibit overshooting oxidation currents for the second charging cycle. Permeation transients for the three materials are presented in Figure 68.

Effective diffusion coefficients for the second charging resulted in $1.36 \cdot 10^{-4}$ cm^2 s^{-1} for the recrystallized sample and $1.45 \cdot 10^{-4}$ cm^2 s^{-1} for HPT700. These results were possibly affected by the current overshoot, as the permeation transient slope is assumed to be slightly larger when the overshooting effect takes place. For annealed iron, this could be confirmed as the comparison of transients with and without current overshoot shows in Figure 68(b). The deviation of the effective diffusivity, however, is minor and within the range of measurement uncertainty. The adopted value for the effective diffusion coefficient of the second charging cycle of annealed iron is an arithmetic mean of four experiments, two with and two without overshooting effect, and resulted in $1.33 \cdot 10^{-4}$ cm^2 s^{-1}.

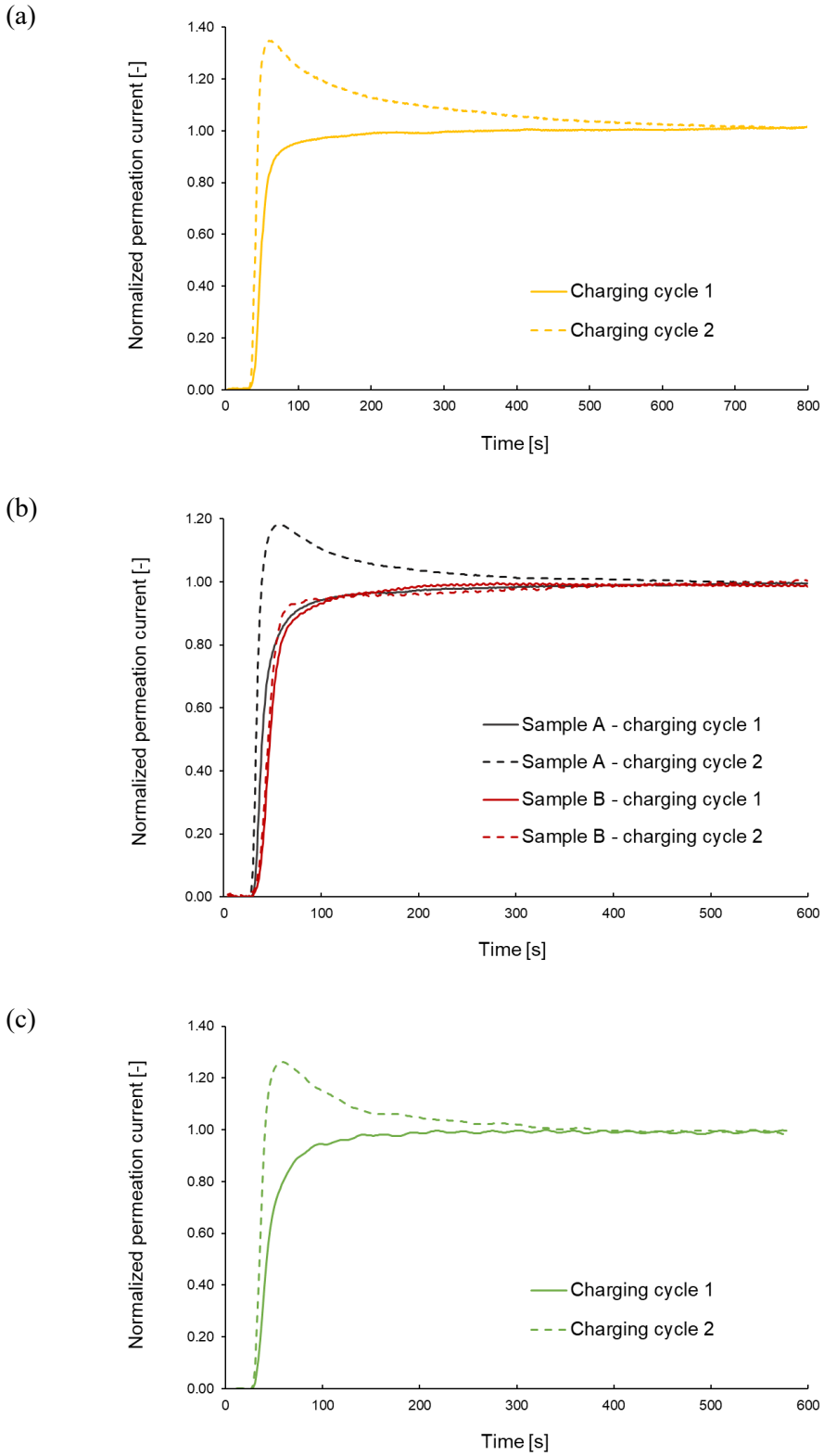

Figure 68: Normalized permeation transients of (a) recrystallized iron, (b) annealed iron with and without second transient overshoot, and (c) HPT-deformed iron subsequently annealed at 700 °C (HPT 700)

Additional permeation characteristics determined from the experimental data were not affected by the current overshoot, as they do not consider the effective diffusivity resulting from the second transient. Again, the three materials showed similar results: hydrogen concentration c_{app} at the entry side was 0.01 ppmw, permeability Φ in the range of $6.11 \cdot 10^{-12}$ mol cm^{-1} s^{-1} to $6.38 \cdot 10^{-12}$ mol cm^{-1} s^{-1}, and the trap density N_T estimated from permeation data ranged from $3.78 \cdot 10^{16}$ to $4.94 \cdot 10^{16}$ cm^{-3}.

An overview of the results of electrochemical permeation is given in Table 30 above.

In TDS measurements, no trapping effect was observed in pure iron in recrystallized and annealed states or HPT700. A small amount of lattice hydrogen mobile at room temperature ranging between 0.1 and 0.2 ppmw was detected in the materials after the electrolytic charging procedure, it effused readily due to the high diffusivity and the lack of hydrogen traps. The hydrogen contents of the three materials are shown in Table 31.

4.1.1.3 Annealed + Cold Deformed Iron

The effect of material deformation on the diffusivity of iron is evident for annealed iron cold rolled to 30 and 60 % reduction. The impact was more pronounced with increasing severity of deformation. The first charging cycle of electrochemical permeation tests revealed an effective diffusion coefficient of $2.34 \cdot 10^{-5}$ cm^2 s^{-1} for 30%CR and $6.90 \cdot 10^{-6}$ cm^2 s^{-1} for 60%CR. The steady-state current density i_∞ and the steady-state permeation flux j_∞, however, can be considered equal for both materials considering measurement uncertainty: for 30%CR, the steady-state current density reached 6.34 µA cm^{-2} and the hydrogen flux $6.57 \cdot 10^{-11}$ mol cm^{-2} s^{-1}; for 60%CR, the current density was 6.33 µA cm^{-2} and the flux $6.56 \cdot 10^{-11}$ mol cm^{2} s^{-1}.

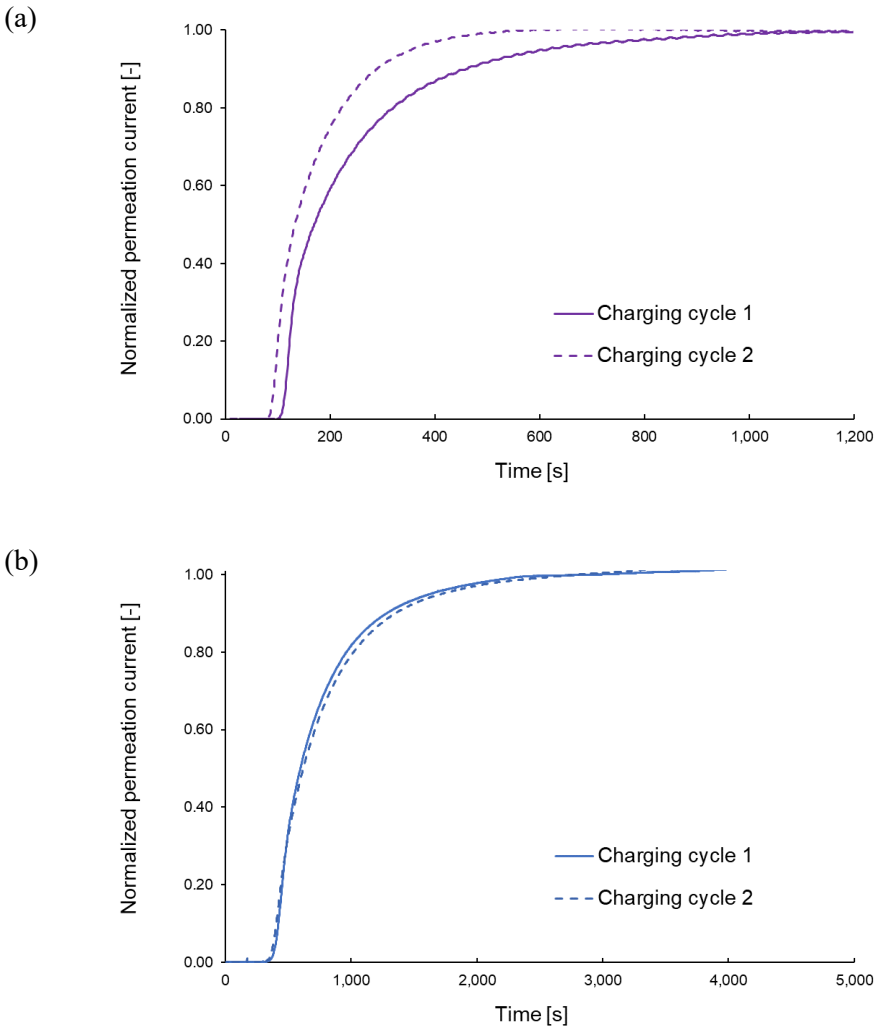

Figure 69: Normalized permeation transients of (a) 30 % cold rolled pure iron, and (b) 60 % cold rolled pure iron

The permeation curves are shown in Figure 69. For 60%CR material, the transients extended over a longer time span compared to 30%CR, indicating lower diffusivity values. It is notable that for 60%CR, the first and second transients were almost identical, while for 30%CR the second charging transient exhibited a shorter breakthrough time and progressed minimally faster than the first. The provenance of this discrepancy in behavior between the materials is unclear, an error in the experimental procedure or incorrect recording of time cannot be excluded, and no additional measurements could be made to address this issue. The result was a slightly higher effective diffusion coefficient for the second charging compared to the first for 30%CR, yet, at $3.18 \cdot 10^{-5}$ cm^2 s^{-1}, it ranged in the same order of magnitude. For 60%CR, the diffusivity for the second transient was marginally lower than for the first, resulting in $6.55 \cdot 10^{-6}$ cm^2 s^{-1}. Deviation between the materials was also observed for the steady-state permeation current densities and steady-state hydrogen fluxes of the second transients, which for 30%CR resulted in 5.54 µA cm^{-2} and $5.74 \cdot 10^{-11}$ mol cm^{-2} s^{-1}, respectively, and for 60%CR yielded 8.32 µA cm^{-2} and $8.62 \cdot 10^{-11}$ mol cm^{-2} s^{-1}, respectively.

The calculated hydrogen permeability Φ was very similar for both materials, resulting in approximately $6.6 \cdot 10^{-12}$ mol cm^{-1} s^{-1}. The influence of the deformation intensity was apparent for the estimated values of hydrogen concentration c_{app} at the hydrogen entry side and trap density N_T, which were determined to be 0.04 ppmw and $1.18 \cdot 10^{18}$ cm^{-3} for 30%CR and 0.12 ppmw and $1.39 \cdot 10^{19}$ cm^{-3} for 60%CR.

An overview of electrochemical permeation results can be found in Table 30.

In TDS analyses of 30%CR and 60%CR, the different degrees of deformation were also perceptible. Total hydrogen content after charging was 0.6 ppmw for 30%CR and 1.8 ppmw for 60%CR. Thereof, 0.2 ppmw was identified as hydrogen mobile at room temperature for 30%CR and 0.4 ppmw for 60%CR. Desorption spectra of both materials were best fitted with one Gaussian peak, representing one hydrogen trap or a combined contribution of different trap types of similar activation energies. The trap activation energy associated with the peak was determined as 32.2 kJ mol^{-1} for 30%CR and 32.5 kJ mol^{-1} for 60%CR. The good agreement of these values implies that the peak corresponds to the same type of trap or group of traps present in both materials. Desorption spectra are shown in Figure 70 and the associated Arrhenius plots in Figure 71. TDS results are summarized in Table 31 above.

(a)

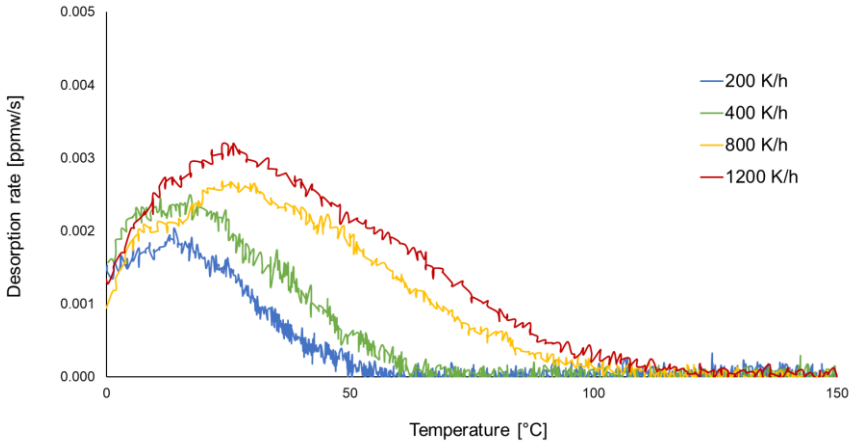

(b)

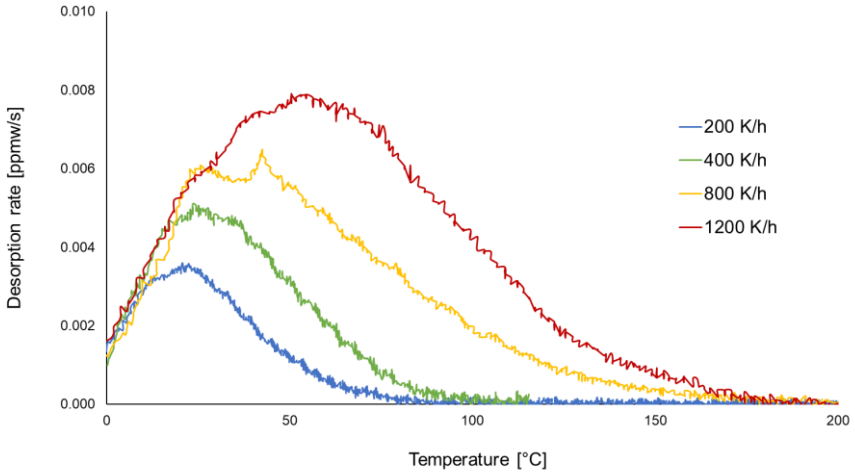

Figure 70: TDS spectra at different heating rates of (a) 30 % cold rolled iron and (b) 60 % cold rolled iron

(a)

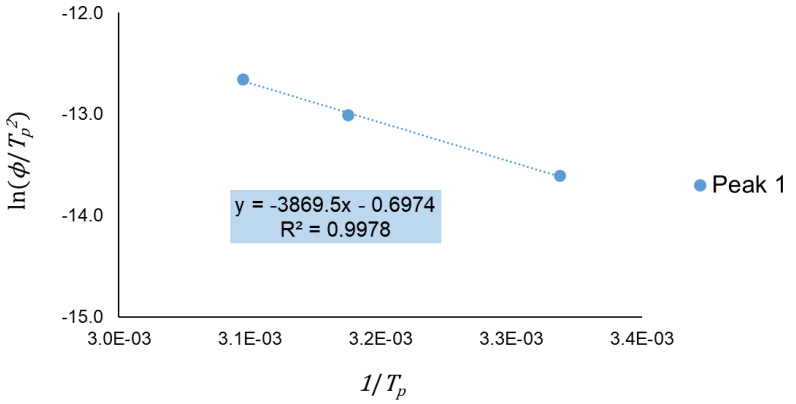

(b)

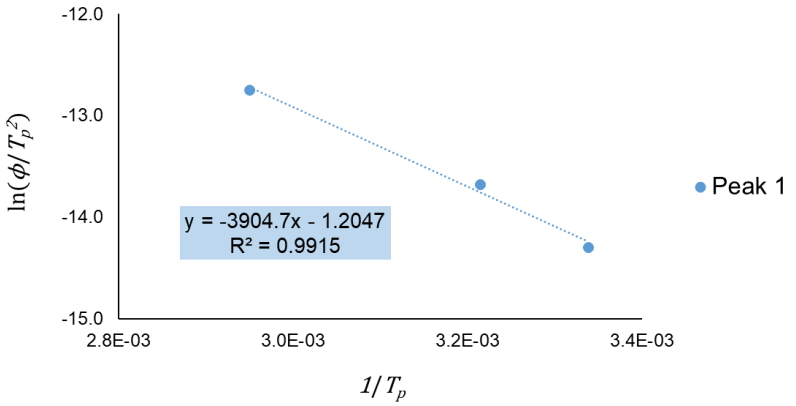

Figure 71: Arrhenius plot of one identified trap in (a) 30 % cold rolled iron and (b) 60 % cold rolled iron

4.1.1.4 HPT-Deformed Iron Annealed at 320 °C (HPT320)

The annealing process at 320 °C did not allow the HPT-deformed iron lattice to fully recover, an influence of the deformation on hydrogen diffusion and trapping behavior was clearly visible. Electrochemical permeation transients showed similar progressions for the first and second charging cycle, as seen in Figure 72. The time necessary for the permeation current to reach a steady state was approximately 30 hours. This made the permeation experiments quite challenging, as signal jumps and delayed diffusion due to layer formation are experienced more often with increasing duration of charging and demanded the repetition of the experiment in several cases. The effective diffusivity for the first charging ($D_{eff,1} = 2.20 \cdot 10^{-7}$ cm^2 s^{-1}) was slightly lower than for the second charging ($D_{eff,2} = 2.65 \cdot 10^{-7}$ cm^2 s^{-1}), while the steady-state permeation current density i_∞ and the hydrogen flux j_∞ were minimally larger for the first charging at 23.64 µA cm^{-2} and $2.45 \cdot 10^{-10}$ mol cm^{-2} s^{-1} compared to the values for the second charging, which resulted in 21.37 µA cm^{-2} and $2.21 \cdot 10^{-10}$ mol cm^{-2} s^{-1}.

In comparison to cold deformed ARMCO® iron, HPT320 material showed a pronounced increase in hydrogen concentration c_{app} at the membrane entry side, hydrogen permeability Φ, and trap density N_T calculated from experimental permeation data. The hydrogen concentration was 14.35 ppmw, the hydrogen permeability $2.44 \cdot 10^{-11}$ mol cm^{-1} s^{-1}, and the trap density was estimated to be $5.36 \cdot 10^{22}$ cm^{-3}.

The results from electrochemical permeation experiments are shown in Table 30 above.

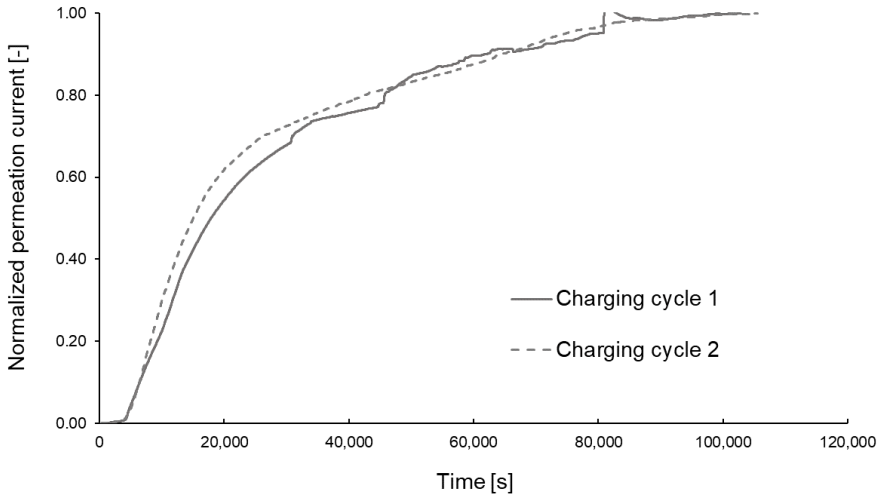

Figure 72: Normalized permeation transients of HPT320 material

The total hydrogen content in HPT320 iron material detected by TDS and hot extraction was 12.4 ppmw. Of this, 1.6 ppmw was classified as hydrogen mobile at room temperature and 10.8 ppmw was bound in hydrogen traps. Desorption spectra for different heating rates are shown in Figure 73 and the corresponding Arrhenius plot in Figure 74. The best fitting of the spectra was achieved with one Gaussian peak, its trap activation energy was determined to be 33.3 kJ mol^{-1}. This is close to the value observed for traps in the cold deformed iron materials, and it is hence assumed that it corresponds to the same trap type. An overview of TDS results for HPT320 material is shown in Table 31 at the beginning of this section.

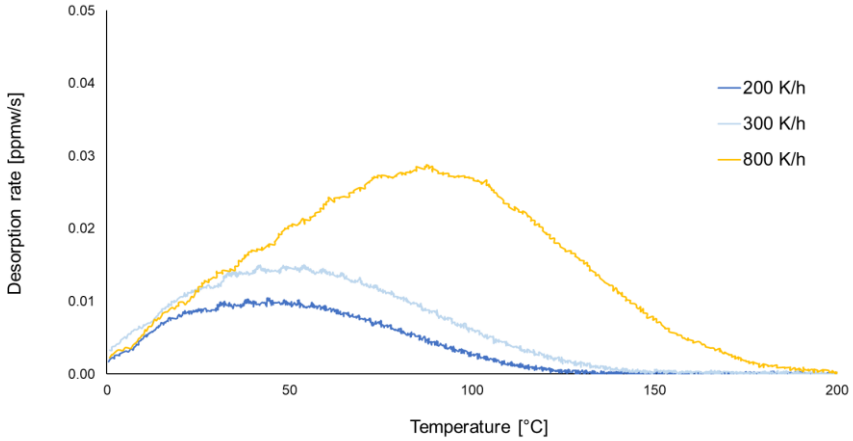

Figure 73: TDS spectra of HPT320 material at different heating rates

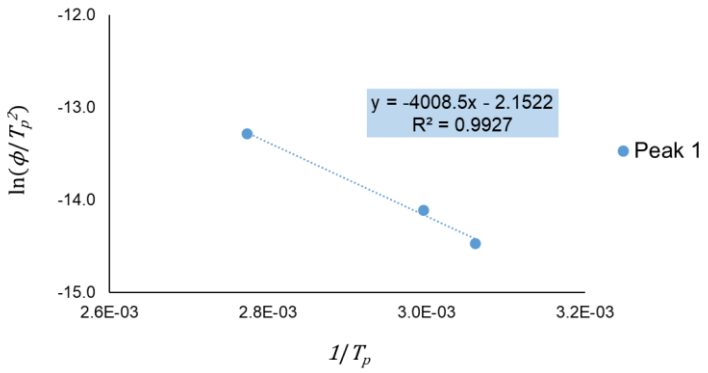

Figure 74: Arrhenius plot of one identified trap in HPT320

4.1.1.5 Untreated HPT-Deformed Iron (HPTu)

Of all material treatment procedures performed on pure iron in this work, deformation by high pressure torsion without subsequent heat treatment had the strongest effect on hydrogen diffusion and trapping behavior, resulting in the lowest diffusivity value and highest amount of trapped hydrogen. Electrochemical permeation experiments revealed effective diffusion coefficients of $1.08 \cdot 10^{-7}$ cm^2 s^{-1} for the first charging cycle and $1.36 \cdot 10^{-7}$ cm^2 s^{-1} for the second. The transient curves are shown in Figure 75. The transient slope was similar for both charging cycles, while the breakthrough times showed considerable variation: hydrogen was first detected in the oxidation cell after approximately 220 minutes during the first charging cycle and after 110 minutes during the second. Both transients reached a steady state after roughly 35 hours.

Permeation current density i_∞ and hydrogen flux j_∞ in steady state were approximately twice as large for the first cycle, at 26.87 µA cm^{-2} and $2.79 \cdot 10^{-10}$ mol cm^{-2} s^{-1}, compared to the second cycle, at 12.95 µA cm^{-2} and $1.34 \cdot 10^{-10}$ mol cm^{-2} s^{-1}.

The impact of severe plastic deformation is also apparent when contemplating the results of apparent hydrogen concentration at the entry surface c_{app}, permeability Φ, and trap density estimated from permeation measurements N_T. The values were the highest of all the analyzed pure iron materials: hydrogen concentration was 31.90 ppmw, hydrogen permeability $2.70 \cdot 10^{-11}$ mol cm^{-1} s^{-1}, and the trap density was estimated to be $2.36 \cdot 10^{23}$ cm^{-3}.

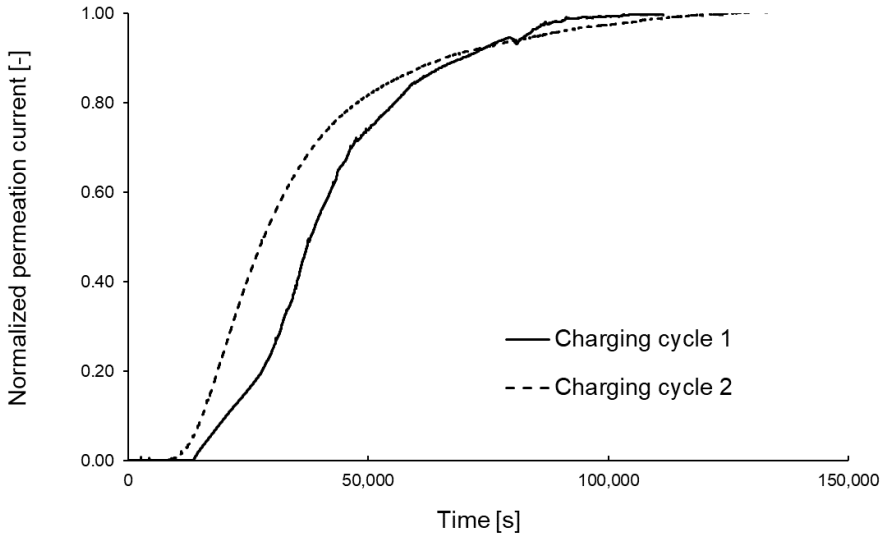

Figure 75: Normalized permeation transients of untreated HPT-deformed iron

A total hydrogen content of 17.8 ppmw was detected by TDS and hot extraction. 1.1 ppmw was identified as hydrogen mobile at room temperature, the rest was found to be trapped. Desorption spectra for different heating rates are shown in Figure 76, the resulting Arrhenius plots for the determination of trapping energies in Figure 77. The best fitting results were achieved with two Gaussian peaks, the trap activation energies were determined as 36.8 kJ mol^{-1} and 50.3 kJ mol^{-1}. The hydrogen content in the lower-energy trap was 7.2 ppmw and in the higher-energy trap 9.5 ppmw. An overview of TDS results for HPTu material is shown in Table 31 at the beginning of this section.

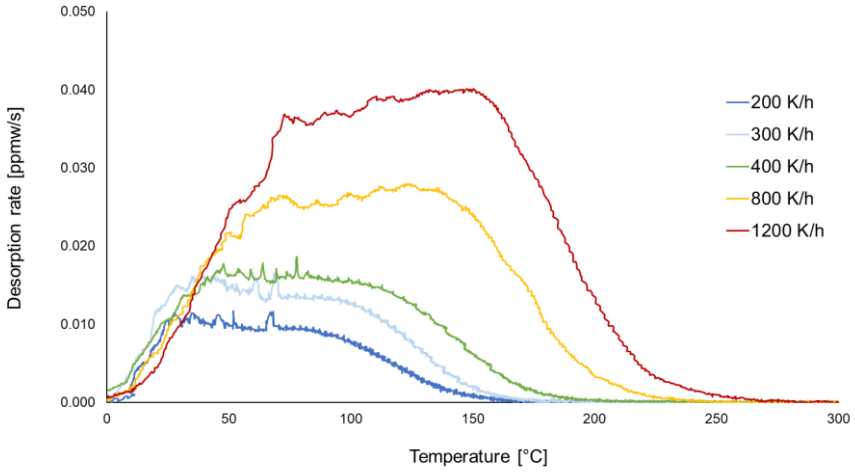

Figure 76: TDS spectra of untreated HPT-deformed iron at different heating rates

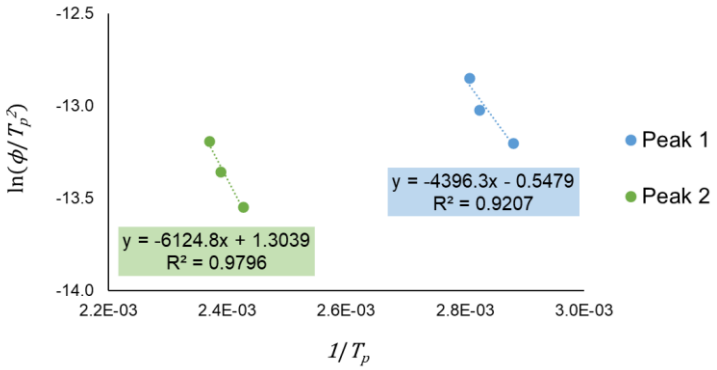

Figure 77: Arrhenius plot of two identified traps in untreated HPT-deformed iron

4.2 Model Alloys

Binary Fe-C model alloys showed very different results compared to ternary and quaternary alloys. The diffusivity of the Fe-C materials was in the range of 30 % cold rolled pure iron, at a magnitude of 10^{-5} $cm^2\,s^{-1}$. Increasing carbon and consequently cementite content resulted in increasing breakthrough times, while the permeation transient slope remained unaffected and similarly steep as in pure iron materials with recovered lattices. Permeation transients of the binary alloys are shown in Section 4.2.1.1. TDS experiments showed rather low hydrogen uptake by Fe-C alloys of approximately 0.4 ppmw. No trap sites were detected, hydrogen quickly effused from the samples at room temperature.

In the ternary and quaternary model alloys, the stressed tempered martensitic lattice and the partially present carbide precipitates led to a notably reduced hydrogen diffusivity and a hydrogen uptake of up to several ppmw. The diffusivity was in the region of 10^{-7} $cm^2\,s^{-1}$. For these four alloys, the breakthrough times of the permeation transients showed a large variation and could be associated with the precipitate contents. TDS experiments revealed one trap with an activation energy of 27 to 37 $kJ\,mol^{-1}$ present in all four materials and an additional trap for each Fe-Ti-C and Fe-V-Nb-C, with an activation energy of 61 and 43 $kJ\,mol^{-1}$, respectively. The total hydrogen content was similar for Fe-Cr-C and Fe-Mo-C at approximately 1 to 1.5 ppmw, around 2 ppmw for Fe-V-Nb-C, and highest for Fe-Ti-C, at over 4 ppmw.

Results of electrochemical permeation experiments are summarized in Table 32 for all six model alloys, and TDS results are shown in Table 33. Figure 78 illustrates the effective diffusion coefficients resulting from electrochemical permeation experiments. A comparison of TDS spectra of ternary and quaternary model alloys can be seen in Figure 81, electrochemical permeation transients of the first charging cycle in Figure 79, and the breakthrough times of the transients in Figure 80.

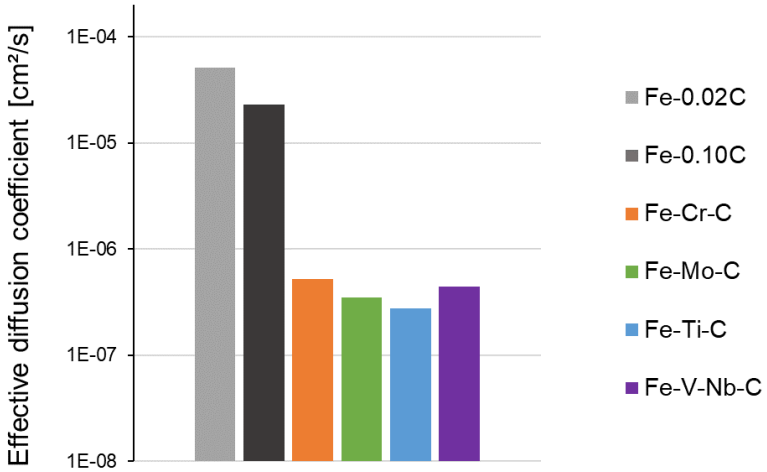

Figure 78: Effective diffusion coefficients of model alloys determined from the first EP charging cycle

Table 32: Electrochemical permeation results for model alloys

Material	$D_{eff,1}$ [$cm^{-2}\,s^{-1}$]	$I_{\infty,1}$ [µA]	$i_{\infty,1}$ [$\mu A\,cm^{-2}$]	$j_{\infty,1}$ [$mol\,cm^{-2}\,s^{-1}$]	$D_{eff,2}$ [$cm^{-2}\,s^{-1}$]	$I_{\infty,2}$ [µA]	$i_{\infty,2}$ [$\mu A\,cm^{-2}$]	$j_{\infty,2}$ [$mol\,cm^{-2}\,s^{-1}$]	c_{app} [ppmw]	Φ [$mol\,cm^{-1}\,s^{-1}$]	N_T [cm^{-3}]
Fe-0.02C	$5.15 \cdot 10^{-5}$	5.96	5.45	$5.65 \cdot 10^{-11}$	$6.07 \cdot 10^{-5}$	5.95	5.44	$5.64 \cdot 10^{-11}$	0.01	$5.70 \cdot 10^{-12}$	$1.98 \cdot 10^{17}$
Fe-0.10C	$2.29 \cdot 10^{-5}$	6.58	6.01	$6.23 \cdot 10^{-11}$	$2.57 \cdot 10^{-5}$	6.12	5.59	$5.80 \cdot 10^{-11}$	0.04	$6.29 \cdot 10^{-12}$	$1.17 \cdot 10^{18}$
Fe-Cr-C	$5.19 \cdot 10^{-7}$	15.93	14.56	$1.51 \cdot 10^{-10}$	$8.31 \cdot 10^{-6}$	10.61	9.70	$1.01 \cdot 10^{-10}$	3.75	$1.52 \cdot 10^{-11}$	$5.78 \cdot 10^{21}$
Fe-Mo-C	$3.50 \cdot 10^{-7}$	11.58	10.59	$1.10 \cdot 10^{-10}$	$3.59 \cdot 10^{-6}$	7.10	6.49	$6.73 \cdot 10^{-11}$	4.03	$1.10 \cdot 10^{-11}$	$9.21 \cdot 10^{21}$
Fe-Ti-C	$2.74 \cdot 10^{-7}$	23.98	21.92	$2.27 \cdot 10^{-10}$	$5.18 \cdot 10^{-7}$	10.76	9.84	$1.02 \cdot 10^{-10}$	10.86	$2.32 \cdot 10^{-11}$	$3.17 \cdot 10^{22}$
Fe-V-Nb-C	$4.45 \cdot 10^{-7}$	34.28	31.33	$3.25 \cdot 10^{-10}$	$7.64 \cdot 10^{-7}$	15.23	13.92	$1.44 \cdot 10^{-10}$	10.31	$3.58 \cdot 10^{-11}$	$1.85 \cdot 10^{22}$

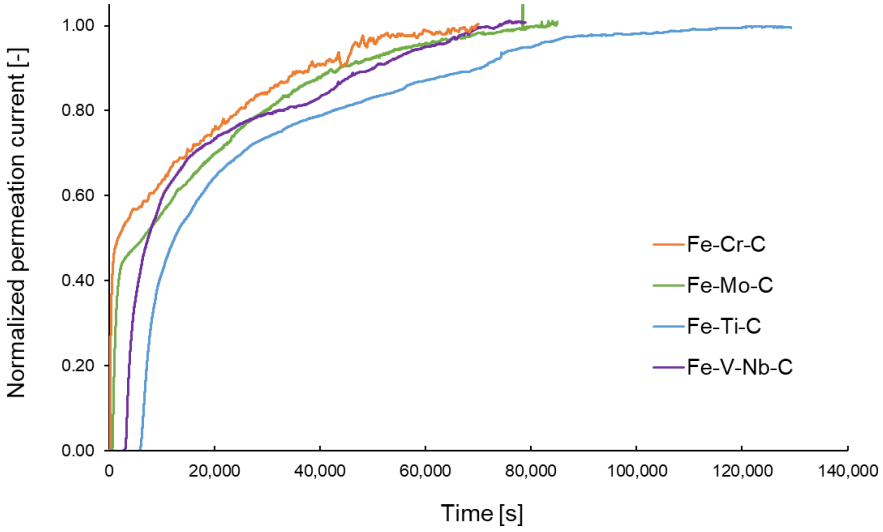

Figure 79: Normalized permeation transients of ternary and quaternary model alloys

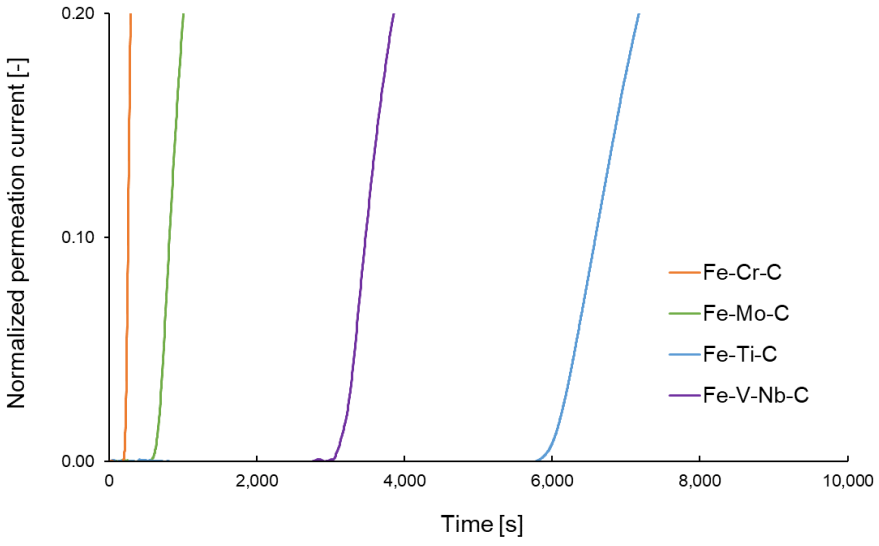

Figure 80: Breakthrough times of the first charging transient of ternary and quaternary model alloys

Table 33: TDS results for model alloys

Material	Total H [ppmw]	H mobile at RT [ppmw]	E_a trap 1 [kJ mol^{-1}]	H in trap 1 [ppmw]	E_a trap 2 [kJ mol^{-1}]	H in trap 2 [ppmw]
Fe-0.02C	0.4	0.4	-	-	-	-
Fe-0.10C	0.4	0.4	-	-	-	-
Fe-Cr-C	1.1	1.3	37.4	0.2	-	-
Fe-Mo-C	1.4	1.2	37.0	0.2	-	-
Fe-Ti-C	4.4	3.2	37.0	0.9	60.6	0.3
Fe-V-Nb-C	2.1	1.4	27.3	0.5	42.9	0.2

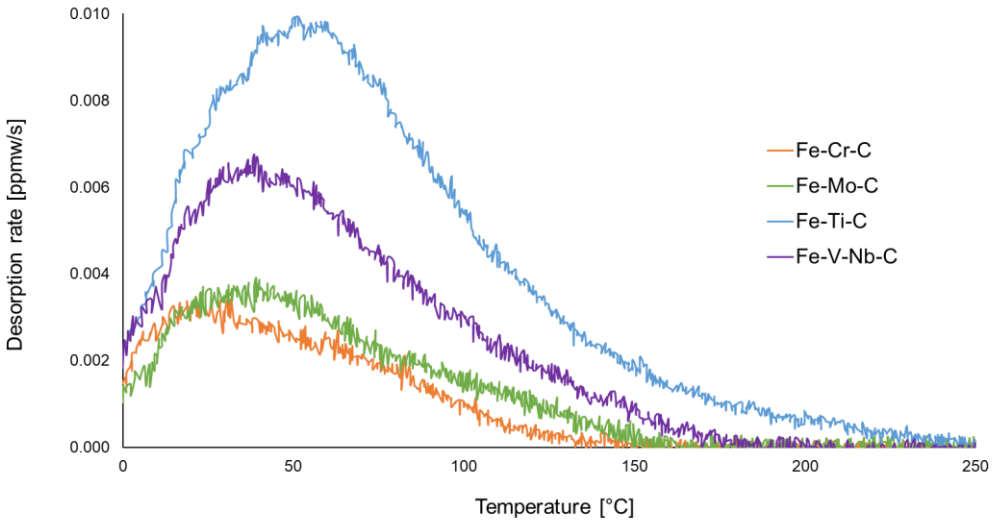

Figure 81: TDS spectra of ternary and quaternary model alloys at heating rate 800 K/h

In the following sections, the experimental results are described in detail for the binary Fe-C alloys (Sect. 4.2.1.1), for Fe-Cr-C and Fe-Mo-C (Sect. 4.2.1.2), for Fe-Ti-C (Sect. 4.2.1.3), and for Fe-V-Nb-C (Sect. 4.2.1.4).

4.2.1.1 Binary Model Alloys Fe-0.02C and Fe-0.10C

The addition of different quantities of carbon (0.02 % and 0.10 %) to raw ARMCO® iron and subsequent heat treatment for carbide formation (see Sect. 3.1.5.1) resulted in delayed hydrogen diffusion and increased hydrogen uptake of the materials. Electrochemical permeation transients are shown in Figure 82 for model alloy Fe-0.02C and in Figure 83 for Fe-0.10C. While the transient slopes were nearly identical for the two materials, the breakthrough times varied. A common feature for both materials was the second charging run exhibiting a slightly shorter breakthrough time. For the material with higher carbon content (Fe-0.10C), breakthrough times were 182 seconds for the first and 158 seconds for the second charging cycle, compared to 56 seconds for the first and 50 seconds for the second cycle for Fe-0.02C. Consequently, the effective hydrogen diffusivities in Fe-0.02C ($D_{eff,1} = 5.15 \cdot 10^{-5}$ cm^2 s^{-1} and $D_{eff,2} = 6.07 \cdot 10^{-5}$ cm^2 s^{-1}) were minimally higher than in Fe-0.10C ($D_{eff,1} = 2.29 \cdot 10^{-5}$ cm^2 s^{-1} and $D_{eff,2} = 2.57 \cdot 10^{-5}$ cm^2 s^{-1}). For each of the two materials, the values of steady-state permeation currents, current densities, and hydrogen fluxes determined from first and second charging cycles showed little variation. Fe-0.10C generally exhibited slightly higher values. The results are shown in Table 32 above.

Hydrogen concentration at the entry side c_{app}, permeability Φ, and estimated trap densities N_T indicate higher hydrogen uptake with increasing carbon content. Total hydrogen concentrations were 0.01 ppmw and 0.04 ppmw for Fe-0.02C and Fe-0.10C, respectively, and permeabilities resulted in $5.70 \cdot 10^{-12}$ mol cm^{-1} s^{-1} for Fe-0.02C and $6.29 \cdot 10^{-12}$ mol cm^{-1} s^{-1} for Fe-0.10C. At $1.17 \cdot 10^{18}$ cm^{-3}, the estimated trap density was approximately one order of magnitude greater for Fe-0.10C than it was for Fe-0.02C, at $1.98 \cdot 10^{17}$ cm^{-3}.

An overview of all electrochemical permeation data collected is given in Table 32 at the beginning of this section.

In Figure 84, the permeation transients of the first charging cycle of the two binary model alloys are compared with those of annealed pure iron and pure iron cold rolled to 30 % reduction. The effects of the addition of carbon and subsequent precipitate formation (binary model alloys) as well as the effect of material deformation (30%CR) are visible when comparing the materials to merely annealed pure iron. The transient slope is similar for the model alloys and the annealed iron, but the initial current signal showed a delay due to longer breakthrough times and hence the steady-state value was reached later. Cold rolling pure iron to a reduction of 30 % caused the breakthrough time to adopt a value in between those determined for the two binary model alloys. Additionally, the transient slope is only comparable to the model alloy's until reaching approximately 0.3 times the steady-state current, and then it flattened notably, while it remained constant for the model alloys until approximately 0.9 times the steady-state current. As a result, 30%CR reached a steady state considerably later than the annealed iron and the model alloys.

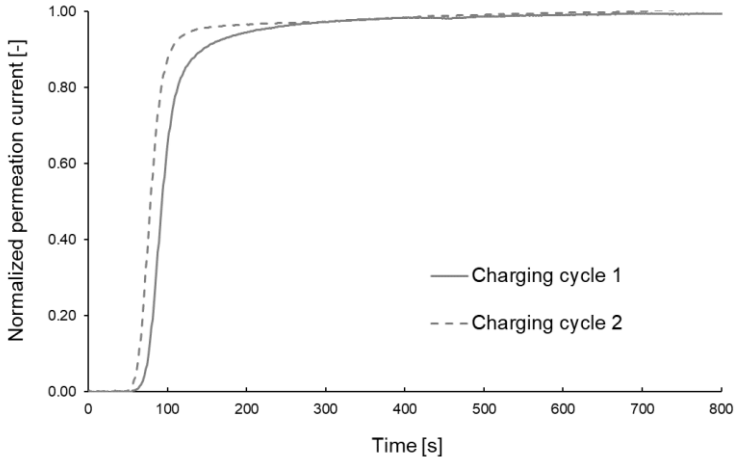

Figure 82: Normalized permeation transients of Fe-0.02C

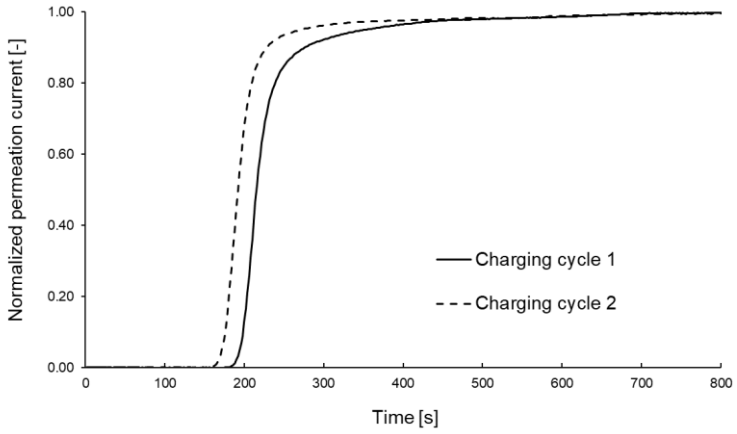

Figure 83: Normalized permeation transients of Fe-0.10C

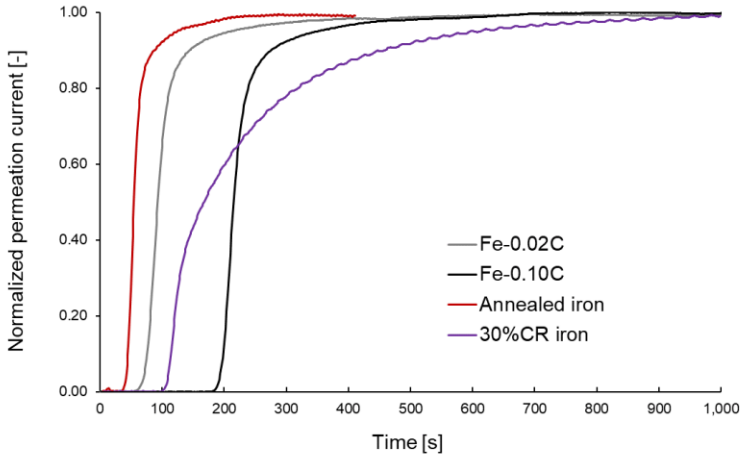

Figure 84: First charging permeation transients of Fe-0.02C and Fe-0.10C compared with pure iron in annealed and 30% cold rolled state

All hydrogen detected in the binary model alloys in TDS measurements was mobile at room temperature. Both alloys showed a similar hydrogen uptake of 0.40 ppmw after charging. Hydrogen trapping could not be confirmed for these materials: although small spikes at higher temperatures were observed in the TDS spectra (see Figure 85), signal intensities were not sufficiently pronounced to identify trapping with certainty.

TDS results are shown in Table 33 at the beginning of this section.

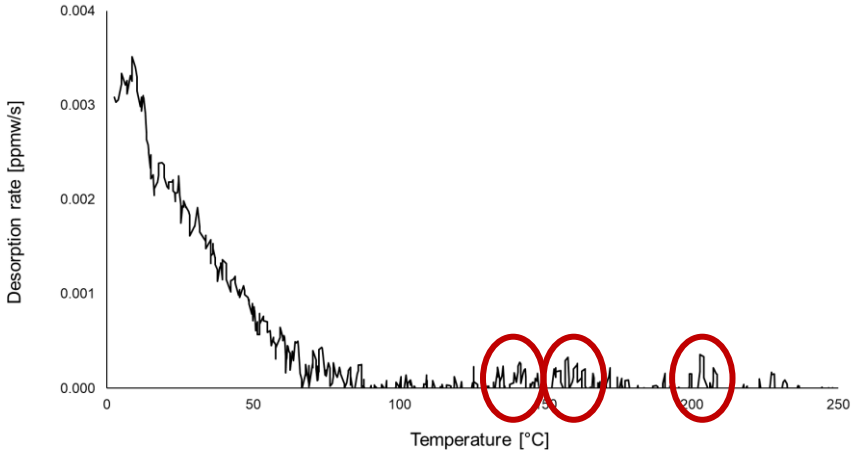

Figure 85: Hydrogen desorption spectrum of Fe-0.10C at a heating rate of 800 K/h with possible but not confirmed peaks indicated in red

4.2.1.2 Model Alloys Fe-Cr-C and Fe-Mo-C

The ternary model alloys Fe-Cr-C and Fe-Mo-C exhibited very similar characteristics regarding diffusivity and uptake of hydrogen. Their microstructures and grain sizes are comparable. In SEM-EDX analyses, no carbides with sizes above the detection limit of 5 µm were found (see Sect. 3.1.5.2).

Electrochemical permeation curves are shown in Figure 86 for Fe-Cr-C and in Figure 87 for Fe-Mo-C. For both materials, the transient of the first charging cycle showed a very steep increase until approximately 0.5 times the steady-state current value and then flattened notably, reaching the steady state after around 20 to 22 hours. The transient of the second charging cycle was also similar for both materials: it started rising minimally steeper than the first charging transient and maintained this slope until approximately 0.9 times the steady-state value, then flattened out and reached a steady state after roughly 3 hours. The breakthrough time was 3 times higher for Fe-Mo-C at around 580 seconds, compared to roughly 200 seconds for Fe-Cr-C, as shown in Figure 88. No notable difference in breakthrough times of first and second charging transient could be seen for either of the materials.

The effective diffusion coefficients were in the same order of magnitude yet slightly higher for alloy Fe-Cr-C ($D_{eff,1} = 5.19 \cdot 10^{-7}$ cm^2 s^{-1} and $D_{eff,2} = 8.31 \cdot 10^{-6}$ cm^2 s^{-1}) than for alloy Fe-Mo-C ($D_{eff,1} = 3.50 \cdot 10^{-7}$ cm^2 s^{-1} and $D_{eff,2} = 3.59 \cdot 10^{-6}$ cm^2 s^{-1}). For both materials, hydrogen diffusivity increased by approximately a factor of 10 for the second charging cycle, while steady-state permeation currents, current densities, and hydrogen fluxes decreased for the second charging process. In general, higher values could be observed for Fe-Cr-C than for Fe-Mo-C, as shown in Table 32 above.

Coefficients calculated from permeation data are of comparable magnitudes. Hydrogen concentration c_{app} at the entry side of the permeation membrane was 3.75 ppmw for Fe-Cr-C and 4.03 ppmw for Fe-Mo-C. The permeation coefficient Φ was $1.52 \cdot 10^{-11}$ mol cm^{-1} s^{-1} for Fe-Cr-C and $1.10 \cdot 10^{-11}$ mol cm^{-1} s^{-1} for Fe-Mo-C. Due to the faster hydrogen diffusion and hence higher diffusion coefficient, the estimated trap density was lower for Fe-Cr-C ($N_T = 5.78 \cdot 10^{21}$ cm^{-3}) than for Fe-Mo-C ($N_T = 9.21 \cdot 10^{21}$ cm^{-3}).

An overview of electrochemical permeation results is shown in Table 32 at the beginning of this section.

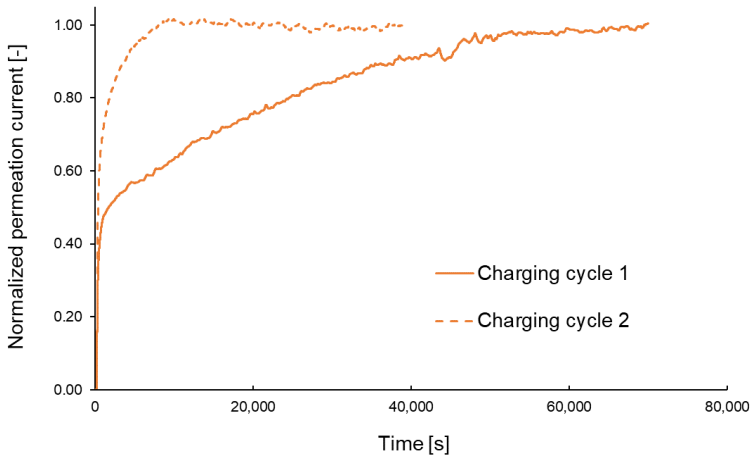

Figure 86: Normalized permeation transients of model alloy Fe-Cr-C

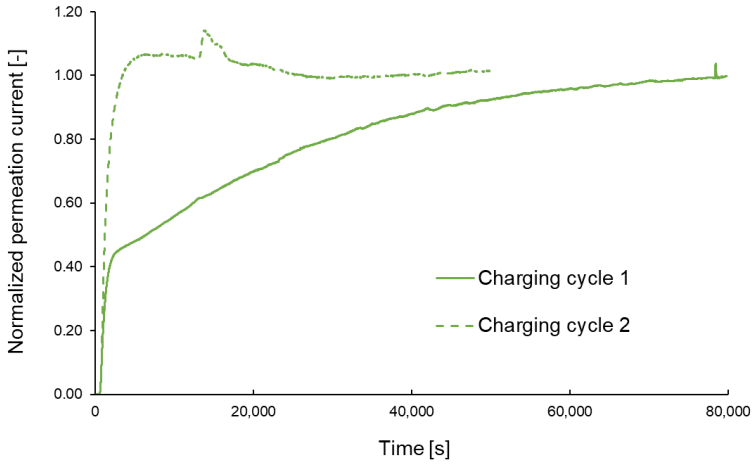

Figure 87: Normalized permeation transients of model alloy Fe-Mo-C

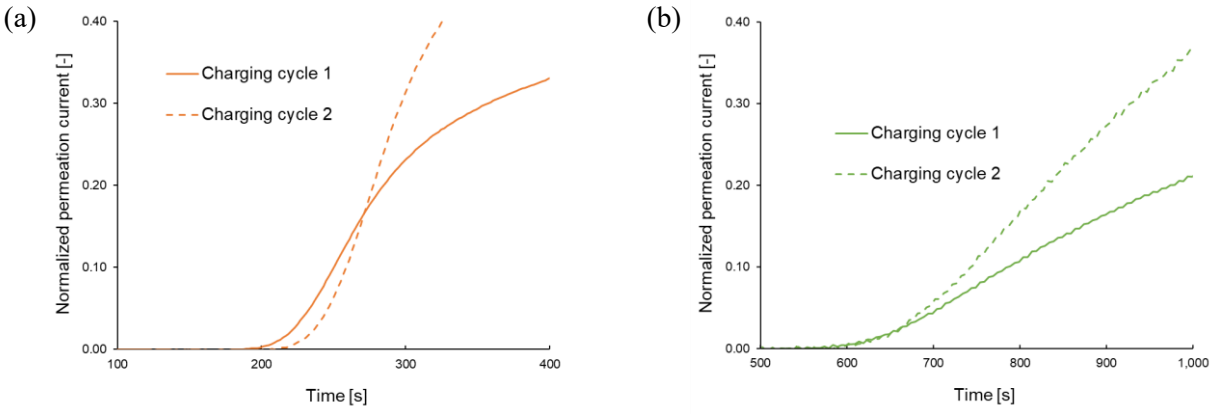

Figure 88: Breakthrough times of permeation transients of ternary model alloys (a) Fe-Cr-C and (b) Fe-Mo-C

For both alloys, TDS spectra were best described with one Gaussian peak. The spectra for different heating rates are shown in Figure 89 for Fe-Cr-C and in Figure 90 for Fe-Mo-C. The Arrhenius plots resulting from the desorption spectra are illustrated in Figure 91 for Fe-Cr-C and in Figure 92 for Fe-Mo-C. Similar trap activation energies resulted for the detected peak, 37.4 kJ mol^{-1} for Fe-Cr-C and 37.0 kJ mol^{-1} for Fe-Mo-C. It can be assumed that it corresponds to the same type of trap in both materials. The same amount of hydrogen of 0.2 ppmw was trapped in this trap in both materials. The amount of hydrogen mobile at room temperature and the total hydrogen content after charging were slightly higher for Fe-Mo-C, at 1.2 ppmw and 1.4 ppmw, respectively. For Fe-Cr-C, 0.9 ppmw of hydrogen was identified as mobile at room temperature, and the total hydrogen content was 1.1 ppmw.

TDS results are shown in Table 33 at the beginning of this section.

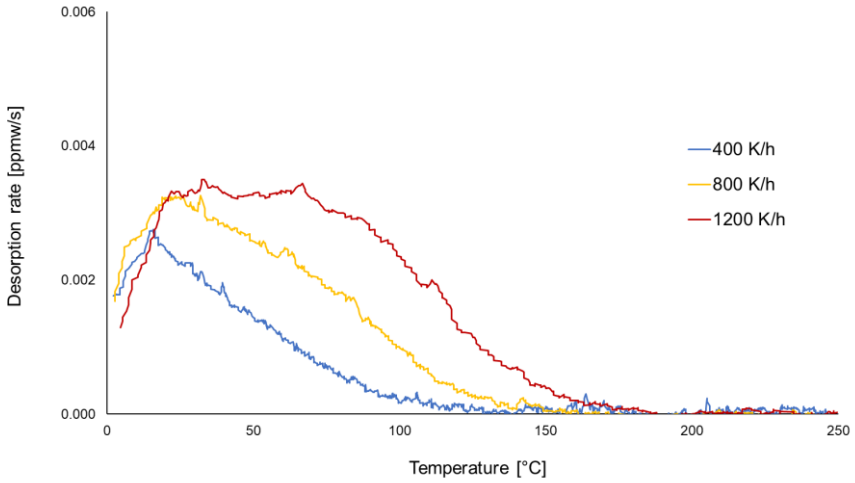

Figure 89: Thermal desorption spectra of model alloy Fe-Cr-C

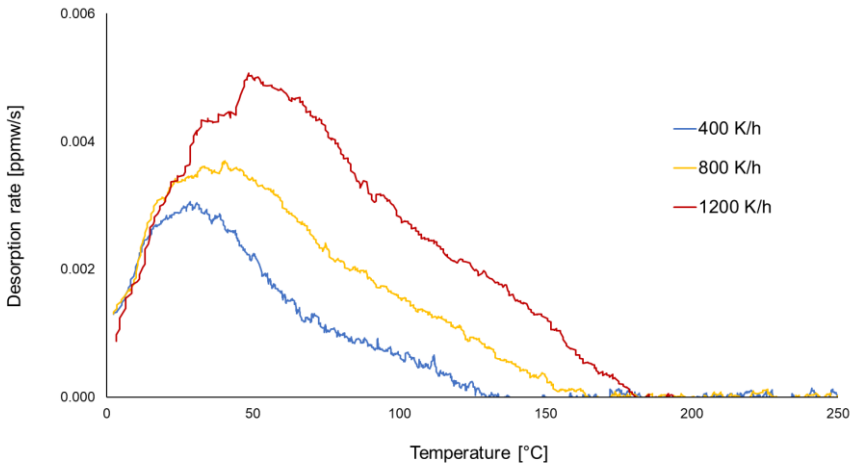

Figure 90: Desorption spectra of model alloy Fe-Mo-C

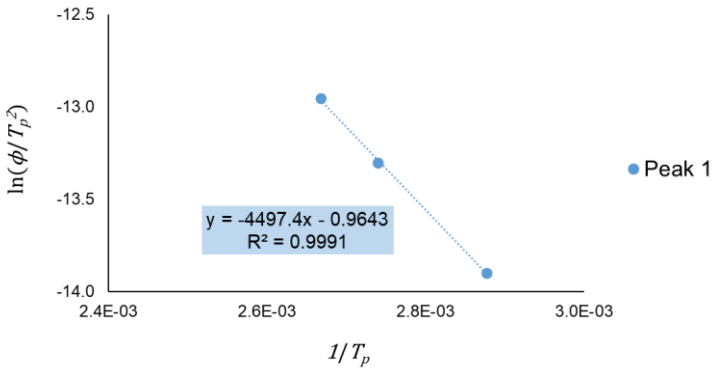

Figure 91: Arrhenius plot of one identified trap in Fe-Cr-C

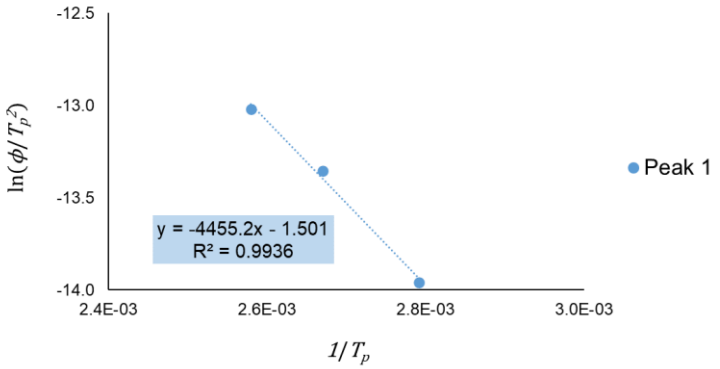

Figure 92: Arrhenius plot of one identified trap in Fe-Mo-C

4.2.1.3 Model Alloy Fe-Ti-C

Of the six analyzed model alloys, Fe-Ti-C showed the lowest effective hydrogen diffusivity and highest hydrogen content. In electrochemical permeation experiments, the comparably slow hydrogen permeation through the material caused the steady-state current to be reached approximately 36 hours after the start of the first charging process. The transient of the second charging was notably faster, reaching a steady state after roughly 10 hours. The permeation transients are shown in Figure 93. As can be seen in Figure 94, the breakthrough time of the first charging cycle was notably higher than of the second, taking on values of roughly 5800 and 5300 seconds, respectively. The effective diffusion coefficients resulted in $2.74 \cdot 10^{-7}$ cm^2 s^{-1} for the first and $5.18 \cdot 10^{-7}$ cm^2 s^{-1} for the second charging run. Steady-state permeation current density i_∞ and hydrogen flux j_∞ were 21.92 µA cm^{-2} and $2.27 \cdot 10^{-10}$ mol cm^{-2} s^{-1} for the first charging cycle and decreased to 9.84 µA cm^{-2} and $1.02 \cdot 10^{-10}$ mol cm^{-2} s^{-1} for the second.

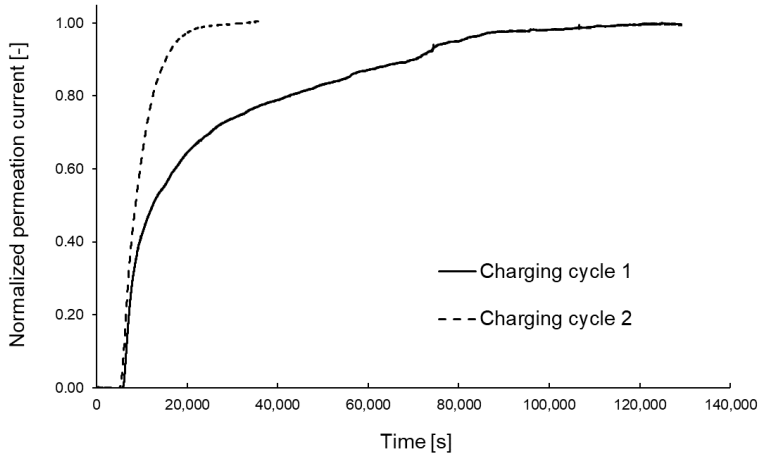

Figure 93: Normalized permeation transients of model alloy Fe-Ti-C

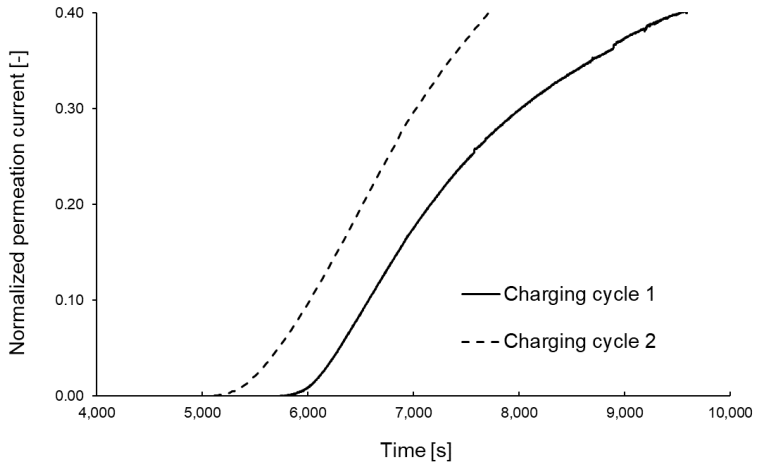

Figure 94: Breakthrough times of permeation transients of model alloy Fe-Ti-C

Estimated from electrochemical permeation data, the hydrogen concentration at the hydrogen entry side of the permeation membrane c_{app} and the estimated trap density N_T were 10.56 ppmw and $3.17 \cdot 10^{22}$ cm^{-3}, the largest values of all six model alloys. The permeation coefficient Φ was determined to be $2.32 \cdot 10^{-11}$ mol cm^{-1} s^{-1}.

Electrochemical permeation results are shown in Table 32 at the beginning of this section.

Fe-Ti-C showed the highest hydrogen uptake of all analyzed model alloys. After electrolytic charging, a total concentration of 4.4 ppmw of hydrogen was found in the material, of which the largest part of 3.2 ppmw was hydrogen mobile at room temperature. Two Gaussian peaks could be identified in the desorption spectra: one at lower temperature, which exhibited a trap activation energy of 37.0 kJ mol^{-1} and trapped 0.9 ppmw of hydrogen, and one peak at higher temperature, which revealed an energy of 60.6 kJ mol^{-1} and trapped 0.3 ppmw of hydrogen. Desorption spectra are shown in Figure 95 and the corresponding Arrhenius plot in Figure 96. The lower-energy peak coincided very well with the trap found in the alloys Fe-Cr-C and Fe-Mo-C, while the higher-energy peak was exclusive to this material.

TDS results are shown in Table 33 at the beginning of this section.

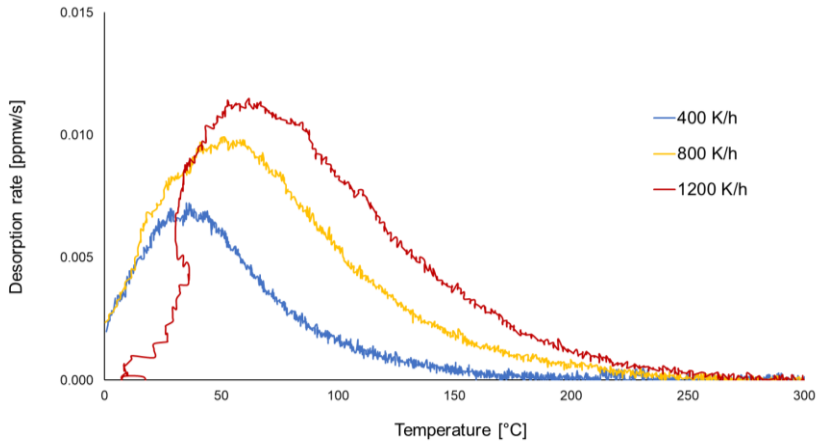

Figure 95: Thermal desorption spectra of model alloy Fe-Ti-C

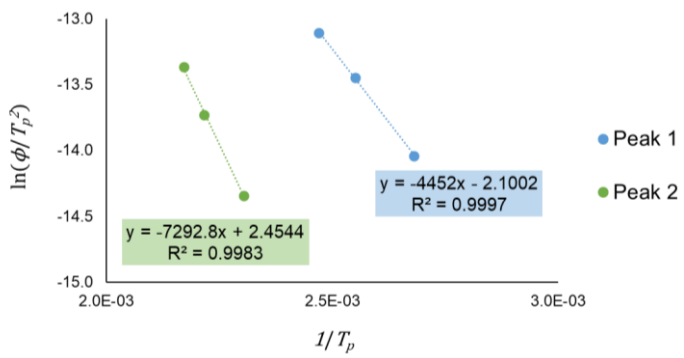

Figure 96: Arrhenius plot of two identified traps in Fe-Ti-C

4.2.1.4 Model Alloy Fe-V-Nb-C

The transient resulting from electrochemical permeation experiments for the quaternary alloy Fe-V-Nb-C is shown in Figure 97. A detailed view of the curves to illustrate the breakthrough times is given in Figure 98: no relevant difference could be seen between first and second charging, the breakthrough time resulted to be approximately 3000 seconds for both cycles. The determined effective diffusivities were $4.45 \cdot 10^{-7}$ cm^2 s^{-1} for the first and $7.64 \cdot 10^{-7}$ cm^2 s^{-1} for the second charging run. The steady-state current densities and hydrogen fluxes observed in the first ($i_{\infty,1} = 31.33$ µA cm^{-2} and $j_{\infty,1} = 3.25 \cdot 10^{-10}$ mol cm^{-2} s^{-1}) and in the second charging cycle ($i_{\infty,2} = 13.92$ µA cm^{-2} and $j_{\infty,2} = 1.44 \cdot 10^{-10}$ mol cm^{-2} s^{-1}) were the highest of the six analyzed model alloys.

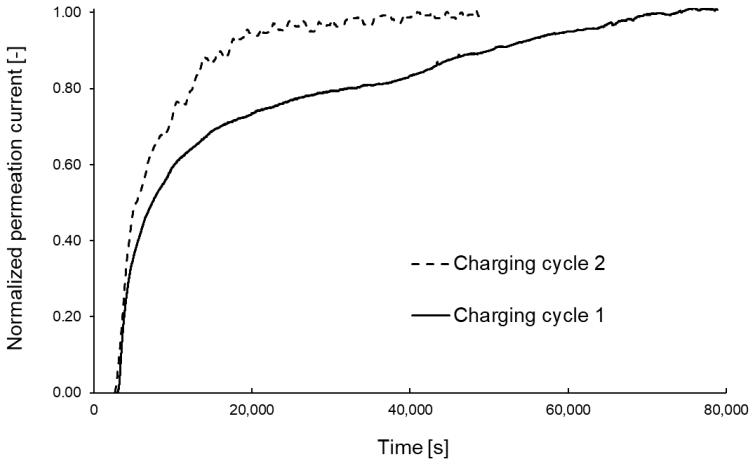

Figure 97: Normalized permeation transients of model alloy Fe-V-Nb-C

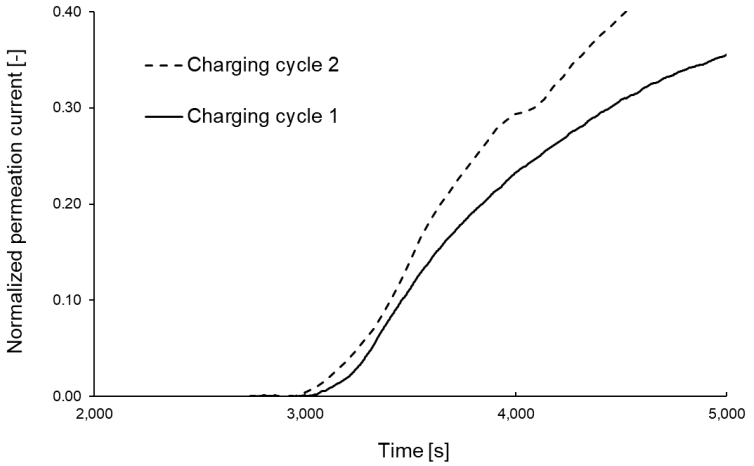

Figure 98: Breakthrough times of permeation transients of model alloy Fe-V-Nb-C

From the high steady-state current and hydrogen flux resulted a large permeation coefficient Φ, which was calculated to be $3.58 \cdot 10^{-11}$ mol cm^{-1} s^{-1}. The estimated hydrogen concentration at the entry side (c_{app} = 10.31 ppmw) as well as the estimated trap density ($N_T = 1.85 \cdot 10^{22}$ cm^{-3}) in the material were slightly lower than the maximum values calculated for Fe-Ti-C.

Electrochemical permeation results are shown in Table 32 at the beginning of this section.

TDS experiments and hot extraction revealed a total hydrogen concentration in the material of 2.1 ppmw after 1 hour of electrolytic charging. 1.4 ppmw of the detected hydrogen was mobile at room temperature, and 0.7 ppmw was trapped hydrogen. The best fit of the desorption spectra was achieved with two Gaussian peaks. The lower-temperature peak contained 0.5 ppwm of hydrogen and its activation energy resulted in 27.3 kJ mol^{-1}. In the higher-temperature peak, 0.2 ppmw of hydrogen was found and its activation energy was 42.9 kJ mol^{-1}. Interestingly, these traps do not correlate with those found in the other model alloys. The desorption spectra for Fe-V-Nb-C are shown in Figure 99 and the corresponding Arrhenius plot in Figure 100.

TDS results are summarized in Table 33 at the beginning of this section.

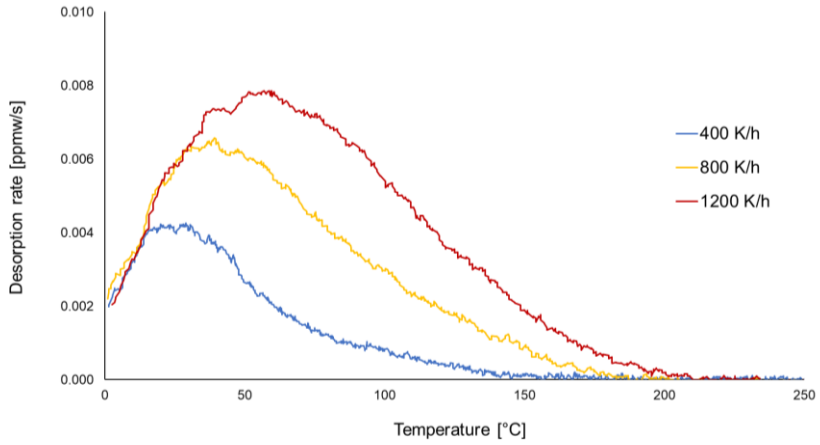

Figure 99: Thermal desorption spectra of model alloy Fe-V-Nb-C

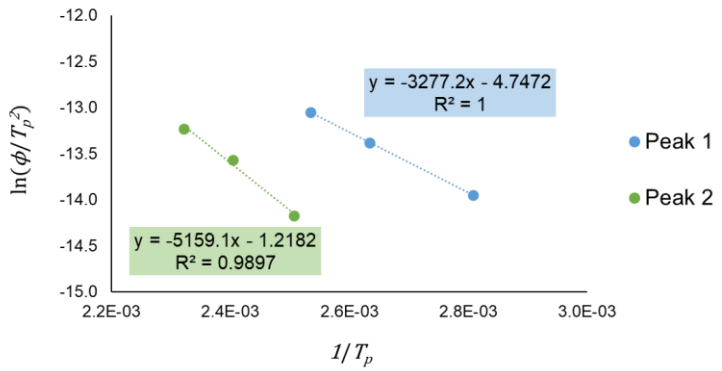

Figure 100: Arrhenius plot of two identified traps in Fe-V-Nb-C

4.3 Industrial Steel Grades

Electrochemical permeation tests for the three analyzed industrial steel grades A/P110, B/T95-1(m), and C/T95-1(g) turned out to be quite challenging under the chosen experimental conditions due to very extensive charging cycle durations of 100,000 to 200,000 seconds (28 to 56 hours). While acceptable results were achievable for the first charging process, which are presented in Table 34, no replicable data could be generated from subsequent cycles. Nevertheless, for the sake of completeness, results determined from the second charging cycle are shown in Table 35. Permeation transients of the first cycle are shown in Figure 101. An increase in diffusivity was seen from Steel A/P110 over Steel B/T95-1(m) to Steel C/T95-1(g). For the three materials, the steady-state permeation current densities i_∞ took on comparable values of slightly below 20 µA cm^{-2}, and consequently, the steady-state hydrogen fluxes j_∞ were also similar, reaching approximately $2 \cdot 10^{-10}$ mol cm^{-2} s^{-1}.

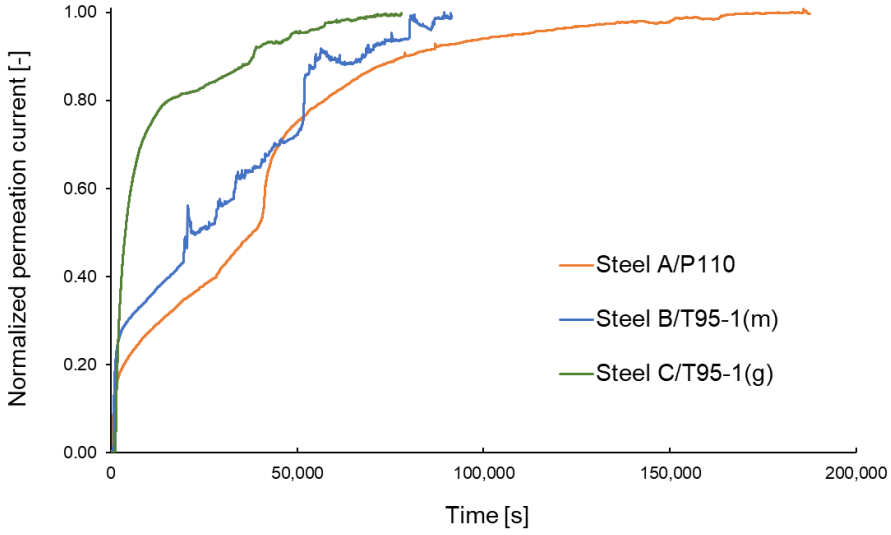

Figure 101: Normalized permeation transients of the first charging cycle of industrial steel grades

The breakthrough times of the first permeation transients are visualized in Figure 102. A notable increase is seen from approximately 400 seconds for Steel A/P110 over 550 seconds for Steel B/T95-1(m) to 1100 seconds for Steel C/T95-1(g). For none of the three steels, a noteworthy difference in the breakthrough times of first and second charging transients was observed.

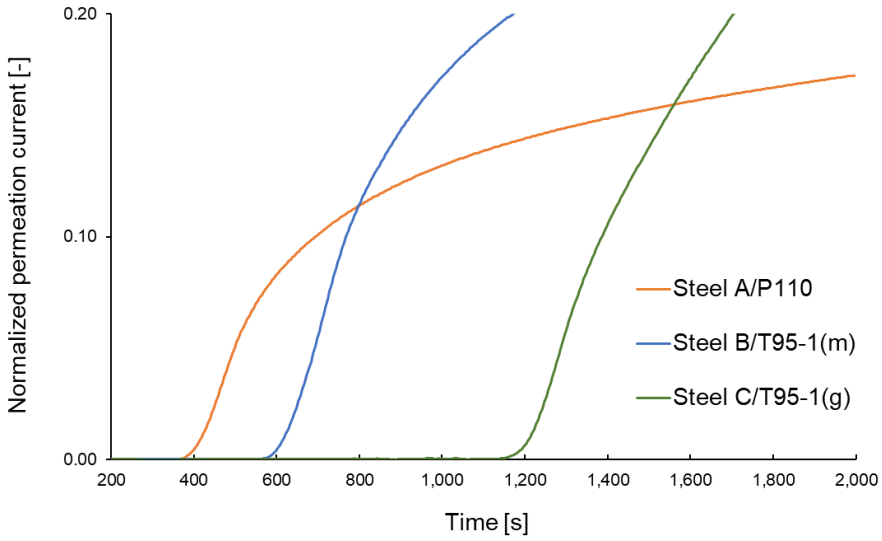

Figure 102: Breakthrough times of the first charging transient of industrial steel grades

As apparent in Table 34, the permeation coefficients Φ are very uniform for all steel grades, while the hydrogen concentration at the entry side of the membrane c_{app} as well as the estimated trap densities N_T exhibit significantly different values. The highest concentration and trap density were determined for Steel A/P110, intermediate values for Steel B/T95-1(m), and a comparably low hydrogen concentration and trap density for Steel C/T95-1(g).

Table 34: Electrochemical permeation results for industrial steel grades

Material	$D_{eff,1}$ [cm² s⁻¹]	$I_{\infty,1}$ [µA]	$i_{\infty,1}$ [µA cm⁻²]	$j_{\infty,1}$ [mol cm⁻² s⁻¹]	c_{app} [ppmw]	Φ [mol cm⁻¹ s⁻¹]	N_T [cm⁻³]
Steel A/P110	$1.19 \cdot 10^{-7}$	21.64	19.78	$2.05 \cdot 10^{-10}$	22.05	$2.04 \cdot 10^{-11}$	$1.49 \cdot 10^{23}$
Steel B/T95-1(m)	$1.49 \cdot 10^{-7}$	19.37	17.71	$1.84 \cdot 10^{-10}$	15.79	$1.84 \cdot 10^{-11}$	$8.50 \cdot 10^{22}$
Steel C/T95-1(g)	$8.21 \cdot 10^{-7}$	19.41	17.74	$1.84 \cdot 10^{-10}$	2.87	$1.84 \cdot 10^{-11}$	$2.80 \cdot 10^{21}$

Table 35: Non-reproducible electrochemical permeation results for the second charging cycle for industrial steel grades.

Material	$D_{eff,2}$ [cm² s⁻¹]	$I_{\infty,2}$ [µA]	$i_{\infty,2}$ [µA cm⁻²]	$j_{\infty,2}$ [mol cm⁻² s⁻¹]
Steel A/P110	~~$4.14 \cdot 10^{-7}$~~	~~16.96~~	~~15.50~~	~~$1.61 \cdot 10^{-10}$~~
Steel B/T95-1(m)	~~$1.32 \cdot 10^{-6}$~~	~~17.56~~	~~16.05~~	~~$1.66 \cdot 10^{-10}$~~
Steel C/T95-1(g)	~~$3.85 \cdot 10^{-7}$~~	~~14.99~~	~~13.70~~	~~$1.42 \cdot 10^{-10}$~~

Permeation transients of the first and second charging cycles are shown individually for each of the three steel grades in Figure 103 to Figure 105. It is to be noted again that the curves of the second charging cycles could not be reproduced and should be considered with caution.

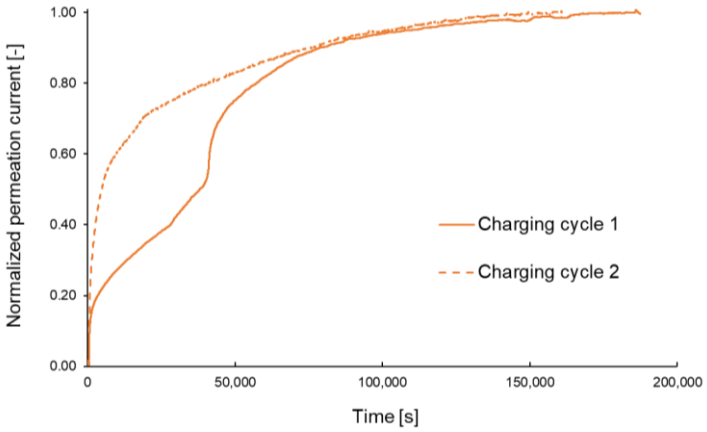

Figure 103: Normalized permeation transients of Steel A/P110

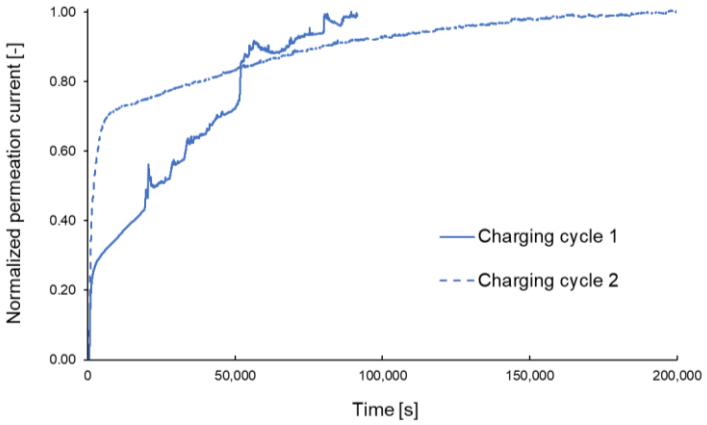

Figure 104: Normalized permeation transients of Steel B/T95-1(m)

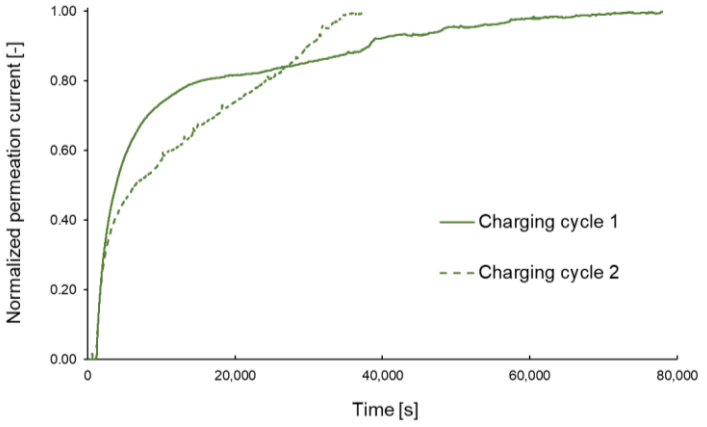

Figure 105: Normalized permeation transients of Steel C/T95-1(g)

Spectra of TDS measurements of the three steel grades after 1 hour of electrolytic charging are shown in Figure 106 and Figure 107, the experimental results are given in Table 36. The spectra of all three materials were best fit with one Gaussian peak, corresponding to one trap or one group of traps with similar trapping energies. The largest amount of hydrogen was found in Steel A/P110: a total hydrogen content of 3.3 ppmw was detected, of which 1.1 ppmw was diffusible hydrogen mobile at room temperature and 2.2 ppmw was trapped. The trap activation energy resulted in 23.7 kJ mol^{-1}, slightly lower than for the other two analyzed steel grades. In Steel B/T95-1(m), the total hydrogen content was 1.6 ppmw, thereof 0.3 ppmw mobile at room temperature and 1.3 ppmw trapped hydrogen. In Steel C/T95-1(g), of the total amount of 2.2 ppmw, 0.8 ppmw was mobile at room temperature and 1.4 ppmw was found trapped. The trap activation energy was similar for the latter two materials, it was determined to be 28.6 kJ mol^{-1} for Steel B/T95-1(m) and 27.3 kJ mol^{-1} for Steel C/T95-1(g).

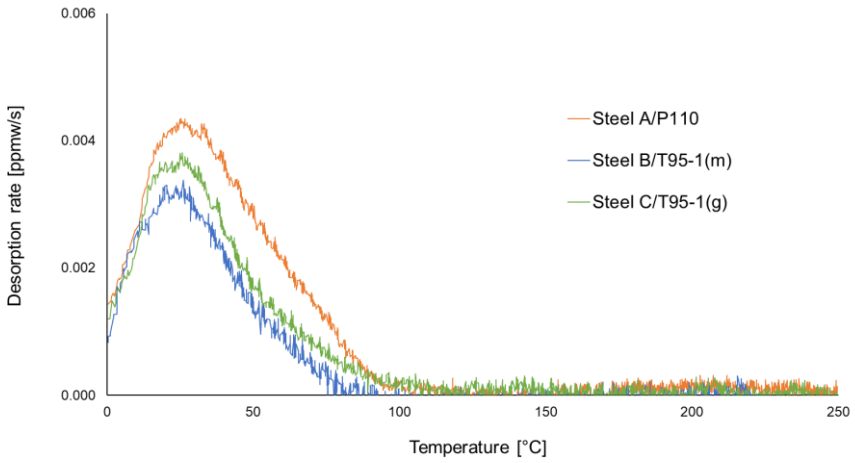

Figure 106: TDS spectra of industrial steel grades at heating rate 200 K/h

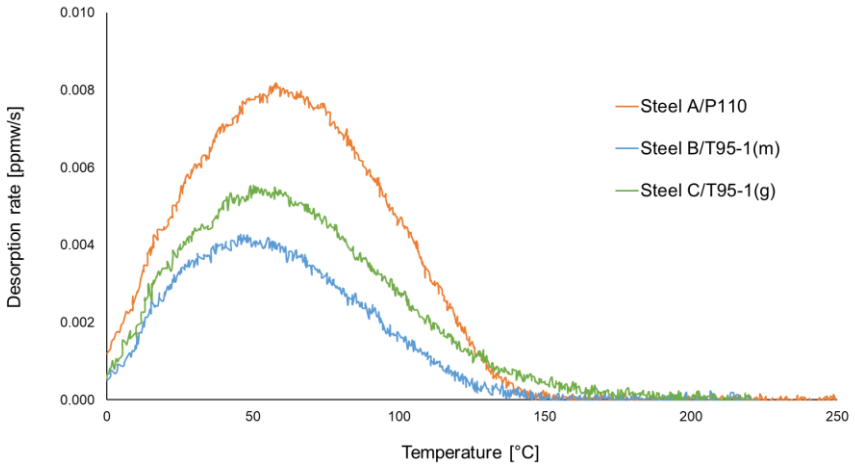

Figure 107: TDS spectra of industrial steel grades at heating rate 800 K/h

Table 36: TDS results for industrial steel grades

Material	Total H [ppmw]	H mobile at RT [ppmw]	E_a trap 1 [kJ mol^{-1}]	H in trap 1 [ppmw]
Steel A/P110	3.3	1.1	23.7	2.2
Steel B/T95-1(m)	1.6	0.3	28.6	1.3
Steel C/T95-1(g)	2.2	0.8	27.3	1.4

Desorption spectra at different heating rates are shown in Figure 108 to Figure 110 and the corresponding Arrhenius plots for the determination of trapping energies in Figure 111 to Figure 113.

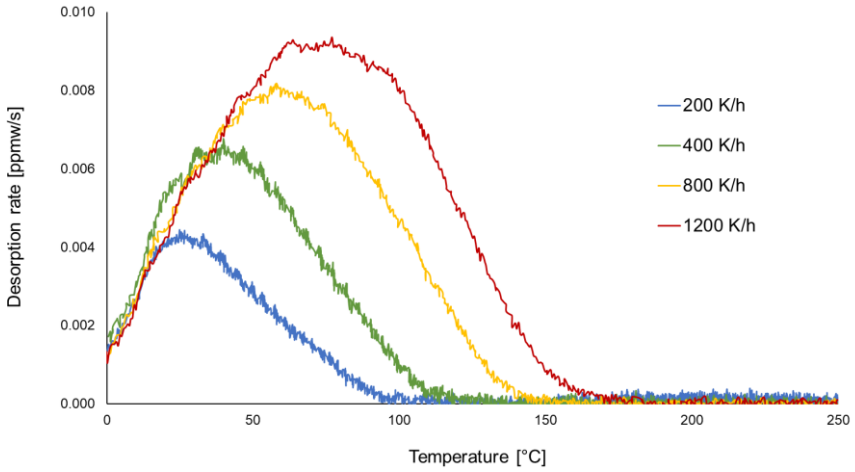

Figure 108: TDS spectra at different heating rates of Steel A/P110

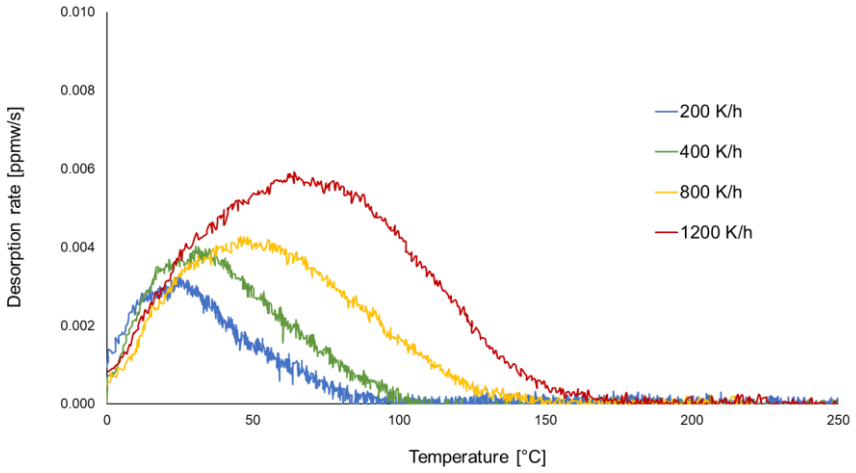

Figure 109: TDS spectra at different heating rates of Steel B/T95-1(m)

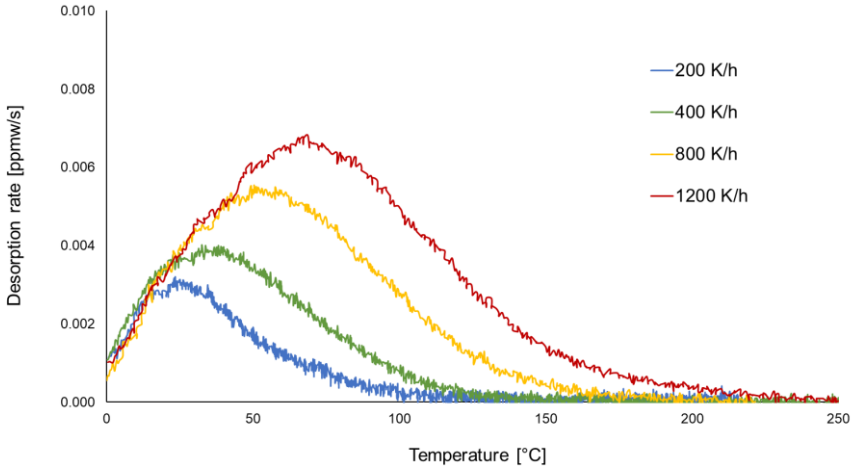

Figure 110: TDS spectra at different heating rates of Steel C/T95-1(g)

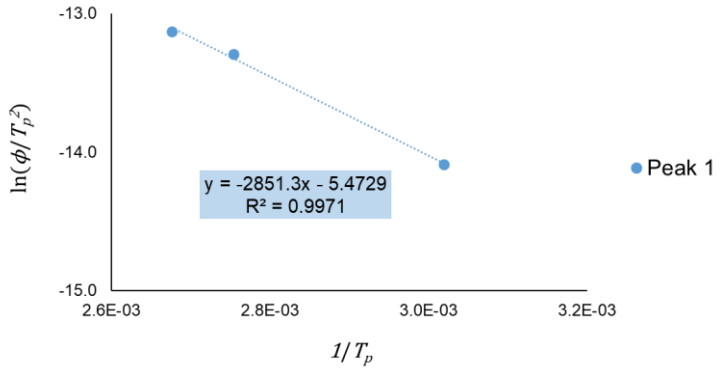

Figure 111: Arrhenius plot of one identified trap in Steel A/P110

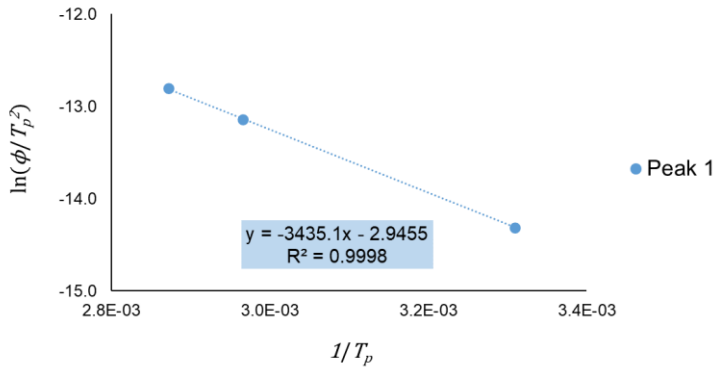

Figure 112: Arrhenius plot of one identified trap in Steel B/T95-1(m)

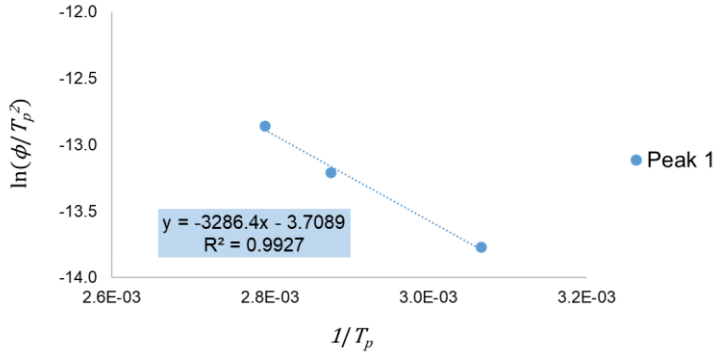

Figure 113: Arrhenius plot of one identified trap in Steel C/T95-1(g)

5 Discussion

5.1 Single-Crystalline Iron and Pure Iron Materials

Single-crystalline iron, recrystallized iron, annealed iron, and HPT-deformed iron subsequently annealed at 700 °C (HPT700) exhibited diffusion coefficients of approximately $1 \cdot 10^{-4}$ $cm^2\,s^{-1}$, which is in the range of values given in literature for hydrogen diffusion in the ideal lattice of α-iron. Lacking grain boundaries and with a minimum density of dislocations, single-crystalline material is practically free of hydrogen traps and comes close to resembling an ideal metal lattice. Similarly, thermal material treatment resulted in a minimum number of lattice defects in the three pure iron materials, as a completely recovered iron microstructure is achieved by annealing at temperatures over 500 °C [264] and the three materials were all subjected to thermal treatment at higher temperatures. Consequently, diffusivity values close to ideal lattice diffusion were obtained for these materials, as the density of lattice imperfections capable of trapping hydrogen was negligible. Hydrogen was therefore located only in the lattice and readily effused from the material at room temperature due to the high diffusivity. Due to the absence of trap sites, electrolytic charging resulted in small hydrogen concentrations in these materials, ranging from 0.1 to 0.2 ppmw.

For the three pure iron materials mentioned above, the steady-state permeation currents and hydrogen fluxes as well as the permeation coefficients were nearly identical, while these values notably differed for the single crystal. Steady-state permeation fluxes were in the range of $6 \cdot 10^{-11}$ $mol\,cm^{-2}\,s^{-1}$ for the three polycrystalline iron materials and $1.30 \cdot 10^{-10}$ $mol\,cm^{-2}\,s^{-1}$ for the single crystal. Also, the permeation transient had a slightly different shape for single-crystalline iron: compared to the very uniformly shaped transients of the three pure iron materials, it exhibited a shorter breakthrough time and a minimally flatter slope. Despite this, as mentioned before, the diffusion coefficients can be considered equal for all four materials. A possible explanation for the steady-state current and flux as well as transient shape differing for the single crystal is the sample's surface condition: while the pure iron samples were grinded with P1200 grit (FEPA) abrasive paper, the single crystal was tested as delivered, with a polished surface (see Sect. 3.1.3). Louthan et al. [188,265] described steady-state permeation fluxes of stainless steels to be influenced by the surface quality and Charca et al. [266] observed increasing steady-state currents and permeation fluxes with increasing surface smoothness on AF1410 steel.

The grain sizes of pure iron in recrystallized and in annealed state and HPT700 range from millimeter-sized grains for recrystallized iron down to 17 µm for HPT700. For the three materials, no difference in diffusion and trapping characteristics was observed, which indicates that the total grain boundary area in the material is not extensive enough to have a noticeable effect on hydrogen diffusion and trapping. This observation is only valid for the grain size region of the three mentioned materials. It is in agreement with the findings of Kim and Bush [63], who reported that for micrometer-sized or larger grains, the relative volume fraction of

grain boundaries, triple junctions, and quadratic nodes, which represent disturbed regions capable of trapping hydrogen, is negligibly small in comparison to the volume fraction of the crystallite (see Sect. 2.2.4.1).

As the results for HPT700 show, even very intense alterations of the microstructure through severe material deformation by high pressure torsion and the resulting high impact on hydrogen behavior can be reversed by appropriate heat treatment. One hour of annealing at 700 °C allows HPT-deformed iron to regain the diffusivity of the undisturbed lattice.

In materials lacking trap sites, identical diffusivities are expected for the first and the second charging transients. Nonetheless, a minimally larger diffusion coefficient was observed for the second charging cycle of single-crystalline iron, annealed and recrystallized iron, and HPT700. The ARMCO® iron used as a base material for the production of polycrystalline iron samples contained inclusions of Al_2O_3, MnO, and SiO_2, which can act as hydrogen traps (see Sect. 3.1.4). Even though the contents were low, they could account for the slightly increased diffusion coefficient determined from the second charging cycle of annealed and recrystallized iron and HPT700 by irreversibly trapping hydrogen during the first charging run. For the single-crystalline material, inclusions are not a valid explanation for the increase in diffusivity due to the material's high purity. As no more sample material was available, no additional permeation experiments could be done with single-crystalline iron to verify the higher diffusivity observed for the second charging process.

While the four described materials (iron single crystal, annealed and recrystallized iron, HPT700) exhibited diffusion coefficients close to the ideal lattice diffusivity due to fully recovered microstructures and an absence of hydrogen traps, the influence of material deformation and hence the generation of diffusion-hindering trap sites could clearly be seen in the cold deformed iron materials (30%CR and 60%CR) and in HPT-deformed iron without subsequent heat treatment (HPTu) or with subsequent heat treatment at a temperature too low to allow full material recovery (HPT320). The degrees of cold rolling of 30 % and 60 % investigated in this work reduced hydrogen diffusivity in iron by one to two orders of magnitude in comparison to the ideal lattice diffusivity in α-iron, and HPT deformation caused a reduction of up to three orders of magnitude. The trap densities estimated from electrochemical permeation data increased from a magnitude of 10^{16} cm^{-3} for single-crystalline iron, annealed and recrystallized iron, and HPT700 to 10^{18} cm^{-3} and 10^{19} cm^{-3} for 30%CR and 60%CR, respectively, up to 10^{22} cm^{-3} for HPT320, and 10^{23} cm^{-3} for HPTu. Even though this method of determining the trap density can only be considered an estimation, a trend of increasing trap density with increasing grade of deformation is clearly visible.

Subjecting annealed pure iron to cold deformation resulted in the dislocation density increasing from $6 \cdot 10^{13}$ m^{-2} in the annealed material to approximately $7 \cdot 10^{14}$ m^{-2} in the material rolled to 30 % reduction and to $9 \cdot 10^{14}$ m^{-2} in the material rolled to 60 %. The grain size was only affected to a small extent: it decreased from 80 µm in the annealed material to 70 µm and 60 µm in

the materials rolled to 30 % and 60 %, respectively. As the experimental results for annealed and recrystallized iron and HPT700 material indicate no noticeable effect of grain boundaries on hydrogen diffusion and trapping for grain sizes in the micrometer region, reduced hydrogen diffusivity as well as larger hydrogen uptake in cold deformed iron in comparison to the annealed state is consequently associated with the increase in dislocation density.

The HPT deformation performed on pure iron in this work resulted in a dislocation density of around $7 \cdot 10^{15}$ m^{-2} and a grain size of approximately 200 nm. Annealing HPT-deformed iron at 320 °C resulted in minimal grain growth to a size of around 300 nm, while the dislocation density decreased by over one order of magnitude, to approximately $4 \cdot 10^{14}$ m^{-2}.

As discussed in Section 2.4.1.1, the breakthrough time is proposed to be an indicator for the overall trap density of a material. The comparison of the first charging transient of single-crystalline iron and pure iron materials (see Figure 62) clearly shows increasing breakthrough times with stronger material deformation. The similar breakthrough times of approximately 30 seconds for single-crystalline iron and materials with recovered lattices (recrystallized and annealed iron, HPT700) imply a minimum amount of trap sites. The most severely deformed material, untreated HPT-deformed iron, exhibited the longest breakthrough time of roughly 220 minutes, indicating the highest trap density. Furthermore, the breakthrough time showed excellent correlation with the detected hydrogen content in the material after electrolytic charging, with longer breakthrough times aligning with higher hydrogen concentrations, which in turn result from higher trap densities. In conclusion, it is assumed that the breakthrough time of the permeation transient is a valid indicator for the hydrogen trap density.

A different progression of first and second permeation transients and a higher diffusivity determined for the second charging run can indicate the presence of irreversible traps, which are not depleted of hydrogen during the discharge process between the charging cycles. Different progressions and breakthrough times of the first and second cycle's transient of the untreated HPT-deformed iron suggest the existence of irreversible hydrogen traps in the material. For HPT320, first and second charging transients were very similar; the slight deviation could stem from a small number of irreversible traps or from measurement uncertainty. From these results is it assumed that irreversible traps present in HPT-deformed iron were fully or to a large extent eliminated by the annealing step at 320 °C. The cold rolled materials 30%CR and 60%CR only differed in the degree of deformation, therefore no fundamental difference in diffusion behavior was expected beforehand. It cannot be explained at this point why 60%CR showed identical breakthrough times for both transients, while they varied for 30%CR. Furthermore, it must be stated that transients of the second and of subsequent charging cycles tend to be affected by the buildup of surface layers and other distorting events, which are more common with increasing experiment duration and can complicate the evaluation and interpretation of electrochemical permeation experiments.

In TDS experiments, the presence of one hydrogen trap or a group of traps with very similar activation energies was observed for 30%CR, 60%CR, and HPT320 material. Its activation energy was found to be 32.2 kJ mol^{-1} for 30%CR, 32.5 kJ mol^{-1} for 60%CR, and 33.3 kJ mol^{-1} for HPT320. Due to the good correlation of these energy values, it is assumed that they correspond to the same type of trap or group of traps in the three materials. As illustrated in Table 37, the hydrogen detected in this trap increased from 0.4 ppmw for 30%CR to 1.4 ppmw for 60%CR. Considering the similar grain size of these two cold deformed materials, which is located in the micrometer range and was shown not to provide a relevant number of grain boundaries for a noticeable trapping effect, this rise could be associated with the increase in dislocation density. For HPT320, the amount of hydrogen trapped in the identified site was significantly higher, reaching 10.8 ppmw, even though the dislocation density is lower than for the 30 % and 60 % cold rolled materials. However, the grain size of HPT320 is substantially smaller, located in the nanometer region. As described in Section 2.2.4.1, the volume fraction of grain boundaries increases exponentially for grains in the nanometer range, whereas the fraction of crystallites decreases, resulting in significantly larger numbers of trap sites than in materials of larger grain sizes. It is therefore concluded that the detected trap sites in 30%CR, 60%CR, and HPT320 with a determined trap activation energy of 32 to 34 kJ mol^{-1} correspond to the joint contribution of dislocations and grain boundaries. This implies that the trapping energies of dislocations and grain boundaries in iron are very similar, making their distinction challenging.

Table 37: Material and hydrogen trap data for ARMCO® iron materials

Material	Grain size	Dislocation density (XRD)	Total H	H mobile at RT	E_a trap 1	H in trap 1	E_a trap 2	H in trap 2
	[µm]	[m^{-2}]	[ppmw]	[ppmw]	[kJ mol^{-1}]	[ppmw]	[kJ mol^{-1}]	[ppmw]
30%CR	70	$6.9 \cdot 10^{14}$	0.6	0.2	32.2	0.4	-	-
60%CR	60	$9.4 \cdot 10^{14}$	1.8	0.4	32.5	1.4	-	-
HPT320	0.3	$3.9 \cdot 10^{14}$	12.4	1.6	33.3	10.8	-	-
HPTu	0.2	$6.8 \cdot 10^{15}$	17.8	1.1	36.6	7.2	50.9	9.5

The trapped hydrogen content in HPT-deformed iron without an annealing step (HPTu) was 16.7 ppmw, distributed between two traps of different activation energies, as can be seen in Table 37. The determined trap activation energy for the trap activated at a lower temperature is 36.6 kJ mol^{-1}, and it contained 7.2 ppmw of hydrogen. Even though the energy level is slightly higher than the value determined for dislocations and grain boundaries in 30%CR, 60%CR, and HPT320, it is assumed that it corresponds to the same group of traps, as large amounts of dislocations and grain boundaries are present and accessible for hydrogen in HPTu. The second trap exhibits a higher activation energy of 50.9 kJ mol^{-1}, and it was not found in other pure iron materials but is exclusive to HPTu. This trap is thought to correspond to vacancies: as described

in Section 3.1.4.4, HPT deformation creates a large number of vacancy defects in the material. Significantly more vacancies are introduced by HPT than by conventional deformation, and vacancies are annihilated to a great extent by annealing at 320 °C. This explains why the trapping effect was only visible in HPTu but not in HPT320 or cold deformed materials. Even though the grain size of HPTu was smaller and the dislocation density considerably higher in comparison to HPT320, the amount of hydrogen trapped at grain boundaries and dislocations was determined to be over 3 ppmw lower than in HPT320. The presumed reason for this is that one hour of electrolytic charging was not sufficient to saturate the hydrogen traps in the HPTu material. In this case, deeper traps are saturated first, and only afterwards hydrogen becomes available for traps of lower activation energies. Hence, it can be assumed that vacancies were saturated with the 9.5 ppmw of hydrogen that they contained, while the determined hydrogen content of 7.2 ppmw in grain boundaries and dislocations did not represent full saturation. The amount of hydrogen mobile at room temperature was higher for HPT320 than for HPTu, at 1.6 and 1.1 ppmw, respectively. The reason is assumed to be the presence of stronger trap sites in HPTu material: while hydrogen can escape from reversible traps at room temperature and a presumed equilibrium exists between trapped and lattice hydrogen, hydrogen desorption from traps becomes more difficult with increasing trap activation energy. As described in Section 2.4.2.1, in TDS experiments, Wei and Tsuzaki [110] observed a peak shift towards lower temperatures with increasing hydrogen content and consequently increasing trap saturation. This is particularly the case when a material contains traps of different activation energies or a specific lattice defect offers different trapping positions for hydrogen with varying activation energies, as e.g. trap sites of lower or higher energies at grain boundaries or trap sites around dislocations exhibiting increasing trapping energies with increasing proximity to the dislocation core. This phenomenon provides a plausible explanation why the determined trap activation energy of grain boundaries and dislocations were slightly higher for HPTu than for 30%CR, 60%CR, and HPT320: as full hydrogen saturation was not realized for HPTu, only the positions along grain boundaries and dislocations with stronger binding energies for hydrogen were occupied, consequently resulting in overall higher averaged energy values for these traps when compared to the materials which experienced full hydrogen saturation after charging.

The proposed trapping energies for different types of traps found in pure iron in the course of this work are shown in Table 38.

Table 38: Activation energies determined in this work for hydrogen traps in pure iron

Trap type	E_a [kJ mol^{-1}]
Grain boundaries	32.2–36.6
Dislocations	32.2–36.6
Vacancies	50.9

The hydrogen concentration at the membrane entry side was also estimated from electrochemical permeation results and is summarized in Table 30 in the previous section. When compared to the hydrogen content determined by TDS shown in Table 31, the values are of similar dimensions. A strong deviation is, however, seen for HPTu: the hydrogen concentration calculated from EP results was 31.9 ppmw, while the hydrogen content after charging determined by TDS and hot extraction was 17.8 ppmw. This is an additional indication that the material was not fully saturated with hydrogen after one hour of electrolytic charging, as already assumed from the hydrogen distribution among weak and strong traps.

5.2 Model Alloys

In electrochemical permeation and TDS experiments, different characteristics were observed for binary Fe-C model alloys and ternary and quaternary model alloys. The binary alloys showed diffusivities and hydrogen contents after electrolytic charging in a magnitude between annealed and cold deformed pure iron, while the diffusivities were significantly lower and the hydrogen contents higher for ternary and quaternary alloys.

The shape of the permeation transients of the binary model alloys Fe-0.02C and Fe-0.10C is shown in Section 4.2.1.1. For each of the two alloys, the slope and shape of both first and second charging transients showed great resemblance to the transient of annealed pure iron with a recovered lattice. Differences could be seen regarding the breakthrough times: an increasing carbon content of the model alloy resulted in a longer breakthrough time. As the binary model alloys underwent extended annealing of 37 hours at 700 °C in the production phase, they are assumed to possess a recovered lattice with low dislocation densities. The grain size ranged from 16 to 17 µm, a region where no perceivable trapping effect by grain boundaries is expected (see Sect. 5.1). Therefore, the increasing breakthrough time is believed to be associated with the increasing cementite content of the materials.

No clear answer can be given regarding the trapping strength of cementite, as inconsistencies arise in the interpretation: for both binary alloys, a decrease in breakthrough time could be observed for the second charging transient. This could indicate the presence of irreversible traps, which do not get depleted of hydrogen during the discharge between the first and second charging process. However, no trapping effect was seen in TDS measurements. In some desorption spectra, a small peak could be identified at higher temperatures, nonetheless, its intensity was not pronounced enough to be unmistakably interpreted as a trap site. It is possible that cementite or cementite phase boundaries around cementite act as strong trap sites, yet their explicit detection, identification, and characterization was not possible due to e.g. suboptimal TDS device setup or unsuitable electrolytic charging conditions. On the other hand, the hydrogen content after electrolytic charging was higher for the Fe-C alloys (0.4 ppmw) than it was for trap-free pure iron materials (0.1 to 0.2 ppmw), and it was identified as mobile lattice hydrogen effusing at room temperature. This allows the conclusion of cementite acting as a very weak hydrogen trap, with an activation energy close to the energy of normal lattice diffusion. This would cause hydrogen trapped at cementite to be released quickly at room temperature and make it difficult to distinguish from lattice hydrogen. The steep permeation transient slope speaks against the assumption of traps being present, as they would cause a flattening of the curve. In the scientific community, different opinions exist on the trapping ability of cementite: it is attested a negligible trapping effect by e.g. Wei and Tsuzaki [1,88], or believed to trap hydrogen with trap activation energies ranging from 18 to as high as 47 kJ mol^{-1}, as shown in Section 2.2.4.4. Additional work will be necessary to clarify this issue.

The three ternary (Fe-Cr-C, Fe-Mo-C, Fe-Ti-C) and the quaternary (Fe-V-Nb-C) model alloys exhibited diffusivities in the order of 10^{-7} cm^2 s^{-1}, significantly lower than the diffusivities of the binary alloys, which were in the order of 10^{-5} cm^2 s^{-1}. The tempered martensitic microstructure, high dislocation density, precipitated phases, and the resulting trapping effects substantially hinder hydrogen diffusion in the ternary and quaternary alloys.

Trapping effects were explicitly determined for the three ternary (Fe-Cr-C, Fe-Mo-C, Fe-Ti-C) and the quaternary (Fe-V-Nb-C) model alloys. In TDS experiments, a hydrogen trap with an activation energy of 27 to 37 kJ mol^{-1} was found in all four ternary and quaternary alloys and for both Fe-Ti-C and Fe-V-Nb-C, one additional trap with higher trapping energy was identified. The activation energy of this second trap was 61 kJ mol^{-1} for Fe-Ti-C and 43 kJ mol^{-1} for Fe-V-Nb-C. In electrochemical permeation experiments, Fe-Cr-C and Fe-Mo-C showed short breakthrough times of less than 600 seconds compared to approximately 3000 seconds for Fe-V-Nb-C and 6000 seconds for Fe-Ti-C. Generally, a longer breakthrough time is associated with a larger overall trap density (see Sect. 2.4.1.1). For ternary and quaternary model alloys, the breakthrough time of the first permeation cycle correlated well with the trap density estimated from permeation data as well as with the total hydrogen concentration determined by TDS and hot extraction. As higher hydrogen concentrations in the material result from higher trap densities, it is very probable that the breakthrough time is a valid indicator for the trap density. The relationship between breakthrough time, hydrogen content, and estimated trap density is shown in Table 39.

Table 39: Hydrogen content after electrolytic charging, permeation breakthrough time, and trap density estimated from EP data for model alloys

Material	Total H	breakthrough time $t_{b,1}$	N_T
	[ppmw]	[s]	[cm^{-3}]
Fe-Cr-C	1.1	200	$5.78 \cdot 10^{21}$
Fe-Mo-C	1.4	580	$9.21 \cdot 10^{21}$
Fe-V-Nb-C	2.1	3050	$1.85 \cdot 10^{22}$
Fe-Ti-C	4.4	5800	$3.17 \cdot 10^{22}$

To characterize the trap sites, the link between the results of hydrogen analyses and the material microstructure was investigated. Except for the presence of precipitates, all four ternary and quaternary alloys exhibited comparable microstructures due to similar material production and treatment steps, hence a common trapping feature was expected. The alloys consisted primarily of a tempered martensite lath matrix resulting from quenching and tempering. SEM-EBSD images suggested a stressed lattice with considerable dislocation density. It is assumed that the lower-energy trap found in all four materials is associated with the common microstructural

features, i.e. dislocations and tempered martensite lath boundaries. The trap activation energy was approximately 37 kJ mol^{-1} in Fe-Cr-C, Fe-Mo-C, and Fe-Ti-C, the good correlation allows the conclusion that it corresponded to the same trapping feature in all three materials. At 27 kJ mol^{-1}, the trap activation energy of the lower-temperature trap was perceptibly lower in Fe-V-Nb-C. It must be noted that at this point it cannot be clarified whether this discrepancy was due to measurement uncertainty or whether the physically correct values are actually found in a range between 27 and 37 kJ mol^{-1}. No strong contribution to trapping is expected from grain boundaries for grain sizes in the region of 5 µm (see Sect. 5.1).

Only in Fe-Ti-C and Fe-V-Nb-C, carbide precipitates with sizes above 5 nm were found using SEM-EDX analyses and only for these two materials an additional higher-temperature peak was identified in the desorption spectra. It is therefore assumed that the higher-energy traps correspond to precipitates formed in these materials, which are mostly Ti-carbides in Fe-Ti-C and mixed V-Nb-carbides in Fe-V-Nb-C. Experimental data found in literature generally defines higher trapping energies for carbides than for dislocations and tempered martensite lath boundaries (see Sect. 2.2.4.4), hence it is plausible that the higher-energy trap corresponds to precipitates and the lower-energy trap to the tempered martensite lattice, and not vice versa.

The trapping energies of hydrogen traps found in ternary and quaternary model alloys are given in Table 40. They show reasonable correlation with literature values. For dislocations, trap activation energies of 26.1 kJ mol^{-1} in a Fe-Ti-C alloy were published by Pressouyre and Bernstein [59] and 33.9 kJ mol^{-1} in a Fe-0.2C martensite by Wei and Tsuzaki [88]. In a series of publications, Depover et al. [108,112–114] described activation energies of martensitic lath boundaries ranging from 23 to 33 kJ mol^{-1} for Fe-Cr-C, Fe-Mo-C, and Fe-V-C alloys; and from 26 to 48 kJ mol^{-1} for a Fe-Ti-C alloy. For semi-coherent Ti-carbides and vacancies in the carbide/matrix interface, trap activation energies published by Wei and Tsuzaki [110] and Drexler et al. [43] range from 56 to 76 kJ mol^{-1}. Values for trapping energies of V-carbides were given as 32 to 35 kJ mol^{-1} by Asahi et al. [123] and Drexler et al. [43], and of Nb-carbides as 39 to 68 kJ mol^{-1} by Wallaert et al. [68].

Table 40: Activation energies determined in this work for hydrogen traps in ternary and quaternary model alloys

Trap type	E_a [kJ mol^{-1}]
Tempered martensite lath boundaries	27.3–37.4
Dislocations	27.3–37.4
V-Nb-carbides	42.9
Ti-carbides	60.6

5.3 Industrial Steel Grades

In industrial practice, the three analyzed steel grades have proven to be affected to different extents by hydrogen embrittlement caused by H_2S. By evaluating the results of hydrogen analyses performed on the three steel grades, it is sought to identify material features enhancing or reducing hydrogen resistivity.

Steel A/P110 is considered not to be resistant to embrittlement, showing detrimental impairment when employed in H_2S environments and failing the NACE Standard TM0177-2016 Method A test. Steel B/T95-1(m) and Steel C/T95-1(g) both pass the NACE Standard TM0177-2016 Method A test, classifying them as resistant to hydrogen embrittlement. Based on the better results in NACE Standard TM0177-2016 Method D tests, Steel C/T95-1(g) is attested a good resistance against hydrogen embrittlement, and Steel B/T95-1(m) is classified as moderately resistant. Higher yield strength and hardness levels usually come along with higher susceptibility to hydrogen embrittlement, and the required concentration of hydrogen to cause failure decreases with increasing strength [1,2]. Steel A/P110 has a minimum yield strength of 758 MPa compared to 655 MPa for both Steel B/T95-1(m) and Steel C/T95-1(g), which represents one factor for its increased susceptibility to hydrogen embrittlement.

The shape of electrochemical permeation transients can provide information on hydrogen trapping behavior, as described in Section 2.4.1. The increasing breakthrough time from Steel A/P110 over Steel B/T95-1(m) to Steel C/T95-1(g) can indicate an increasing density of strong hydrogen traps in the material, an attribute considered beneficial regarding resistance against embrittlement, as hydrogen is trapped with minimal chance of escaping and diffusing towards stressed lattice regions. SEM-EDX analyses revealed that only in Steel C/T95-1(g), Ti- and Nb-carbonitrides were present. These can act as beneficial traps and may be the reason for the longer breakthrough time for Steel C/T95-1(g) in comparison to the other materials.

The time to reach the steady-state permeation current was inverse to the breakthrough time: it took the longest for Steel A/P110 and the shortest for Steel C/T95-1(g) to reach a steady state. As a result, Steel C/T95-1(g) exhibited the highest diffusion coefficient as well as the steepest average transient slope and Steel A/P110 the lowest diffusivity and flattest slope. The slope is associated with the overall trap density and in some cases more specifically with the density of reversible traps. A large amount of weak hydrogen traps can have unfavorable effects, as hydrogen can escape at moderate temperatures or due to mechanical stress, resulting in large concentrations of hydrogen in the lattice.

In TDS experiments, only one trap was detected for all materials. The trapping energy was similar for Steel B/T95-1(m) and Steel C/T95-1(g), at approximately 28 kJ mol^{-1}, and slightly lower for Steel A/P110, at around 24 kJ mol^{-1}. Considering the results of the permeation experiments, the presence of irreversible traps is imaginable, but could not be confirmed by TDS. It is possible that traps with higher activation energies existed in the material but could not be detected individually, resulting in the determination of one joint trap with an average activation

energy instead of various traps with graduated energies. In either case, the lower trapping energy identified for Steel A/P110 could be a reason for its increased susceptibility to hydrogen embrittlement.

After one hour of electrolytic charging, the largest hydrogen concentrations were detected in Steel A/P110. Apart from taking up the most hydrogen in total, the amount of trapped hydrogen and hydrogen mobile at room temperature were also higher than for the steel grades more resistant to embrittlement. As discussed before, especially hydrogen freely diffusible in the lattice and weakly trapped hydrogen are considered as problematic, as the former readily diffuses to stressed areas in the material and the latter can easily be released into the lattice, consequently having the same effect. Nonetheless, a general correlation of the susceptibility to hydrogen embrittlement with hydrogen content was not observed: while nearly equal amounts of trapped hydrogen were found in Steel B/T95-1(m) and Steel C/T95-1(g), the amounts of total hydrogen and hydrogen mobile at room temperature were higher for Steel C/T95-1(g), the material more resistant to embrittlement.

Material characteristics determined from electrochemical permeation experiments can be used to assess the susceptibility to hydrogen embrittlement. Huang et al. [267] analyzed the values of effective diffusivity, permeability, and apparent hydrogen solubility at the hydrogen entry side to compare X120 pipeline steels and concluded that a low diffusivity and permeability as well as a high apparent solubility result in higher hydrogen concentrations and thus more pronounced susceptibility to embrittlement. Figures for the industrial steel grades analyzed in this work are shown in Table 41. The permeability was very similar for all three materials and can therefore not be used to assess differences in the material quality. For effective diffusivity and apparent hydrogen concentration, a correlation in accordance with Huang et al. is visible. As discussed above, the diffusivity increases with increasing resistivity against hydrogen embrittlement. The apparent hydrogen concentration c_{app} is the highest for Steel A/P110 at approximately 22 ppmw and diminishes notably for the materials with stronger resistivity, falling to around 3 ppmw for Steel C/T95-1(g). Although the apparent solubility is an estimated

Table 41: Material data and experimental results for industrial steel grades

Material	Min. yield strength	Hardness	EP results			TDS results			
			$D_{eff,1}$	Φ	c_{app}	Total H	H mobile at RT	E_a trap	H in trap
	[MPa]	[HV]	[cm² s⁻¹]	[mol cm⁻¹ s⁻¹]	[ppmw]	[ppmw]	[ppmw]	[kJ mol⁻¹]	[ppmw]
Steel A/ P110	758	298 ± 3	$1.19 \cdot 10^{-7}$	$2.04 \cdot 10^{-11}$	22.05	3.3	1.1	23.7	2.2
Steel B/ T95-1(m)	655	258 ± 3	$1.49 \cdot 10^{-7}$	$1.84 \cdot 10^{-11}$	15.79	1.6	0.3	28.6	1.3
Steel C/ T95-1(g)	655	258 ± 2	$8.21 \cdot 10^{-7}$	$1.84 \cdot 10^{-11}$	2.87	2.2	0.8	27.3	1.4

value calculated from permeation data, the results suggest it may be useful to assess the tendency of taking up hydrogen and to evaluate the hydrogen embrittlement resistivity.

In summary, it must be stated that a deeper analysis and additional experimental work is necessary to reveal reliable links between results of hydrogen analyses and a material's susceptibility to hydrogen embrittlement. It is assumed that strong, irreversible traps have a positive effect, while reversible traps as well as high concentrations of lattice hydrogen have a negative impact. The effective diffusion coefficient and the apparent hydrogen concentration determined from electrochemical permeation experiments are potentially useful to assess the resistivity against hydrogen embrittlement.

6 Summary

The aim of this work was to study the behavior of hydrogen in iron and iron-based alloys and how this behavior is influenced by material microstructure. Lattice defects such as vacancies and dislocations as well as grain and phase boundaries and precipitates can act as hydrogen traps, accumulating hydrogen and releasing it at lower or higher temperatures, depending on the trap's activation energy.

To systematically analyze the effect of different microstructural constituents on hydrogen trapping and hydrogen diffusion, a variety of pure iron and iron-based materials in different conditions was created. Single-crystalline iron comes close to an ideal iron lattice and is almost free of traps. Pure iron was subjected to a series of mechanical and thermal material treatment steps to create distinct microstructures and to introduce lattice defects to different extents. By adding carbon and other alloying elements to pure iron, precipitate phases known to have strong hydrogen trapping abilities were created. Industrial steel grades with varying resistivity to hydrogen embrittlement were the most complex materials analyzed.

Electrochemical permeation (EP) and thermal desorption spectroscopy (TDS) were the chosen experimental methods. Permeation experiments allow the determination of hydrogen diffusivity and give an idea of the material's trapping behavior. Two galvanostatic charging cycles with intermediate hydrogen discharge were done. By recording thermal desorption spectra at various heating rates of hydrogen-charged samples, the number of different types of traps in the material and the corresponding trapping energies can be determined as well as the hydrogen content and its distribution among the traps. All samples were electrolytically hydrogen charged under identical conditions prior to TDS analyses.

The experimental results reveal how hydrogen traps influence the interaction between hydrogen and the material. Lattice defects created by deformation as well as precipitates and phase boundaries can accumulate hydrogen and hinder its diffusion. Increasing severity of mechanical deformation increases the number of created traps, resulting in larger hydrogen concentrations and lower diffusion coefficients. This effect can be reversed by subjecting the material to heat treatment at temperatures high enough to allow the lattice to recover. Precipitates and phase boundaries are traps that can be created without mechanically deforming the material and have a pronounced impact on hydrogen behavior.

Activation energies of traps found in the analyzed iron and iron-based materials were determined. In pure iron, dislocations and grain boundaries exhibit very similar energy values in the range of 32 to 37 kJ mol^{-1}. The trapping effect of grain boundaries was only seen in materials with grain sizes in the nanometer range, implying that in materials of larger grain sizes, the number of grain boundaries is not sufficient to trap notable amounts of hydrogen. The trap activation energy of vacancies in iron was determined to be 51 kJ mol^{-1}.

The trapping effects of carbide precipitates and phase boundaries were studied in model alloys specifically produced for this purpose. A trap with an activation energy ranging from 27 to 37 kJ mol^{-1} was associated with tempered martensite lath boundaries and dislocations. Mixed V-Nb-carbides revealed a trap activation of approximately 43 kJ mol^{-1}, the activation energy for Ti-carbides was 61 kJ mol^{-1}.

Industrial steel grades were analyzed with the aim of identifying material features impeding or promoting hydrogen embrittlement. No definite answer was found to this question, yet the experimental results suggest that strong, irreversible traps have a positive effect by lowering the concentration of detrimental lattice hydrogen, while reversible traps are detrimental, as they tend to readily release hydrogen into the lattice. Furthermore, it is assumed that a high hydrogen diffusivity may increase the resistance against hydrogen embrittlement.

7 References

[1] F.G. Wei, K. Tsuzaki, Hydrogen trapping phenomena in martensitic steels, in: B.P. Somerday, R.P. Gangloff (Eds.), Gaseous hydrogen embrittlement of materials in energy technologies: Volume 1: The problem, its characterisation and effects on particular alloy classes, Woodhead Publishing Ltd., Cambridge, 2012, pp. 493–525.

[2] E. Riecke, Wasserstoff in Eisen und Stahl, Archiv für das Eisenhüttenwesen 49 (1978) 509–520. https://doi.org/10.1002/srin.197804672.

[3] J.-Y. Lee, J.-L. Lee, A trapping theory of hydrogen in pure iron, Philosophical Magazine A 56 (1987) 293–309. https://doi.org/10.1080/01418618708214387.

[4] W.H. Johnson, On Some Remarkable Changes Produced in Iron and Steel by the Action of Hydrogen and Acids, Proceedings of the Royal Society of London 23 (1874) 168–179. https://doi.org/10.1098/rspl.1874.0024.

[5] L. Darken, R. Smith, Behavior of Hydrogen in Steel During and After Immersion in Acid, Corrosion (1949) 1–16. https://doi.org/10.5006/0010-9312-5.1.1.

[6] M.A.V. Devanathan, Z. Stachurski, The Adsorption and Diffusion of Electrolytic Hydrogen in Palladium, Proceedings of the Royal Society A 270 (1962) 90–102. https://doi.org/10.1098/rspa.1962.0205.

[7] A. Turnbull, Hydrogen diffusion and trapping in metals, in: R.P. Gangloff, B.P. Somerday (Eds.), Mechanisms, modelling and future developments, Woodhead Publishing Ltd., Oxford, 2012, pp. 89–128.

[8] R. Kirchheim, Solid Solutions of Hydrogen in Complex Materials, in: H. Ehrenreich, F. Seitz, D. Turnbull, F. Spaepen, R.E. Camley, R.L. Stamps (Eds.), Solid state physics: Advances in research and applications, Elsevier, 1994-2009, pp. 203–291.

[9] H.J. Grabke, E. Riecke, Absorption and diffusion of hydrogen in steels, Materiali in tehnologije 6 (2000) 331-342.

[10] F. Martin, X. Feaugas, A. Oudriss, D. Tanguy, L. Briottet, J. Kittel, State of Hydrogen in Matter: Fundamental Ad/Absorption, Trapping and Transport Mechanisms, in: Mechanics - Microstructure - Corrosion Coupling: Concepts, Experiments, Modeling and Cases, first ed., ISTE Press Ltd. - Elsevier, 2019, pp. 169–222.

[11] A. San-Martin, F.D. Manchester, The Fe-H (Iron-Hydrogen) system, Bulletin of Alloy Phase Diagrams 11 (1990) 173–184. https://doi.org/10.1007/BF02841704.

[12] Q. Liu, A.D. Atrens, Z. Shi, K. Verbeken, A. Atrens, Determination of the hydrogen fugacity during electrolytic charging of steel, Corrosion Science 87 (2014) 239–258. https://doi.org/10.1016/j.corsci.2014.06.033.

[13] B. Pound, Hydrogen Ingress during Corrosion, in: A.J. Bard, G.S. Frankel, M. Stratmann (Eds.), Corrosion and Oxide Films, Wiley-VCH, Berlin, 2003, pp. 108–155.

[14] J. Friedel, Electronic structure of primary solid solutions in metals, Advances in Physics 3 (1954) 446–507. https://doi.org/10.1080/00018735400101233.

[15] J. Friedel, On the electronic structure of hydrogen in metals, Berichte der Bunsengesellschaft für physikalische Chemie 76 (1972) 828–831. https://doi.org/10.1002/bbpc.19720760852.

[16] E.E. Fletcher, A.R. Elsea, Hydrogen movement in steel - entry, diffusion, and elimination, Battelle Columbus Labs., Columbus, Ohio, USA, 1965.

[17] H. Wipf, Solubility and Diffusion of Hydrogen in Pure Metals and Alloys, Physica Scripta T94 (2001) 43. https://doi.org/10.1238/Physica.Topical.094a00043.

[18] K. Kiuchi, R.B. McLellan, The solubility and diffusivity of hydrogen in well-annealed and deformed iron, Acta Metallurgica 31 (1983) 961–984. https://doi.org/10.1016/B978-0-08-034813-1.50009-7.

[19] J. Da Silva, S.W. Stafford, R.B. McLellan, The thermodynamics of the hydrogen-iron system, Journal of the Less Common Metals 49 (1976) 407–420. https://doi.org/10.1016/0022-5088(76)90052-7.

[20] J.P. Hirth, Effects of hydrogen on the properties of iron and steel, Metallurgical Transactions 11 (1980) 861–890. https://doi.org/10.1007/BF02654700.

[21] M. Nagumo, Fundamentals of Hydrogen Embrittlement, Springer, Singapore, 2016.

[22] R.L.S. Thomas, D. Li, R.P. Gangloff, J.R. Scully, Trap-governed hydrogen diffusivity and uptake capacity in ultrahigh-strength AERMET 100 steel, Metallurgical and Materials Transactions A 33 (2002) 1991–2004. https://doi.org/10.1007/s11661-002-0032-6.

[23] R.A. Oriani, J.P. Hirth, M. Smialowski (Eds.), Hydrogen degradation of ferrous alloys, Noyes Publications, Park Ridge, NJ, USA, 1985.

[24] R. Griessen, A. Driessen, Heat of formation and band structure of binary and ternary metal hydrides, Physical Review B 30 (1984) 4372–4381. https://doi.org/10.1103/physrevb.30.4372.

[25] R.A. Oriani, Hydrogen Embrittlement of Steels, Annual Review of Materials Science 8 (1978) 327–357. https://doi.org/10.1146/annurev.ms.08.080178.001551.

[26] A.D. McQuillan, An experimental and thermodynamic investigation of the hydrogen-titanium system, Proceedings of the Royal Society A 204 (1950) 309–323. https://doi.org/10.1098/rspa.1950.0176.

[27] H. Brodowsky, Das System Palladium/Wasserstoff, Zeitschrift für Physikalische Chemie 44 (1965) 129–142. https://doi.org/10.1524/zpch.1965.44.3_4.129.

[28] R. McLellan, W. Oates, The solubility of hydrogen in rhodium, ruthenium, iridium and nickel, Acta Metallurgica 21 (1973) 181–185. https://doi.org/10.1016/0001-6160(73)90001-1.

[29] W.J. Arnoult, R.B. McLellan, Thermodynamics of transition metal-hydrogen solid solutions, Acta Metallurgica 21 (1973) 1397–1403. https://doi.org/10.1016/0001-6160(73)90089-8.

[30] R.B. McLellan, Solid solutions of hydrogen in gold, silver and copper, Journal of Physics and Chemistry of Solids 34 (1973) 1137–1141. https://doi.org/10.1016/S0022-3697(73)80022-8.

[31] R. Oriani, The diffusion and trapping of hydrogen in steel, Acta Metallurgica 18 (1970) 147–157. https://doi.org/10.1016/0001-6160(70)90078-7.

[32] A.H.M. Krom, A. Bakker, Hydrogen trapping models in steel, Metallurgical and Materials Transactions B 31 (2000) 1475–1482. https://doi.org/10.1007/s11663-000-0032-0.

[33] A.J. Kumnick, H.H. Johnson, Hydrogen Transport Through Annealed and Deformed Armco Iron, Metallurgical Transactions 5 (1974) 1199–1206. https://doi.org/10.1007/BF02644334.

[34] A. Raina, V.S. Deshpande, N.A. Fleck, Analysis of thermal desorption of hydrogen in metallic alloys, Acta Materialia 144 (2018) 777–785. https://doi.org/10.1016/j.actamat.2017.11.011.

[35] J. Venezuela, Q. Zhou, Q. Liu, M. Zhang, A. Atrens, Hydrogen Trapping in Some Automotive Martensitic Advanced High-Strength Steels, Advanced Engineering Materials 20 (2018) 1700468. https://doi.org/10.1002/adem.201700468.

[36] F.D. Fischer, G. Mori, J. Svoboda, Modelling the influence of trapping on hydrogen permeation in metals, Corrosion Science 76 (2013) 382–389. https://doi.org/10.1016/j.corsci.2013.07.010.

[37] A. Turnbull, Stress Corrosion Cracking: Mechanisms, in: K.H.J. Buschow (Ed.), Encyclopedia of materials: Science and technology, Elsevier, Amsterdam, 2001, pp. 8886–8891.

[38] S.P. Lynch, Hydrogen embrittlement (HE) phenomena and mechanisms, in: V.S. Raja, T. Shoji (Eds.), Stress Corrosion Cracking, first ed., Elsevier, 2011, pp. 90–130.

[39] A. Pundt, R. Kirchheim, Hyrogen in Metals: Microstructural Aspects, Annual Review of Materials Research 36 (2006) 555–608. https://doi.org/10.1146/annurev.matsci.36.090804.094451.

[40] J.V. Badding, R.J. Hemley, H.K. Mao, High-pressure chemistry of hydrogen in metals: in situ study of iron hydride, Science 253 (1991) 421–424. https://doi.org/10.1126/science.253.5018.421.

[41] V.E. Antonov, M. Baier, B. Dorner, V.K. Fedotov, G. Grosse, A.I. Kolesnikov, E.G. Ponyatovsky, G. Schneider, F.E. Wagner, High-pressure hydrides of iron and its alloys, Journal of Physics: Condensed Matter 14 (2002) 6427–6445. https://doi.org/10.1088/0953-8984/14/25/311.

[42] R. Silverstein, D. Eliezer, E. Tal-Gutelmacher, Hydrogen trapping in alloys studied by thermal desorption spectrometry, Journal of Alloys and Compounds 747 (2018) 511–522. https://doi.org/10.1016/j.jallcom.2018.03.066.

[43] A. Drexler, T. Depover, S. Leitner, K. Verbeken, W. Ecker, Microstructural based hydrogen diffusion and trapping models applied to Fe–C-X alloys, Journal of Alloys and Compounds (2020) 154057. https://doi.org/10.1016/j.jallcom.2020.154057.

[44] W.Y. Choo, J.Y. Lee, Thermal analysis of trapped hydrogen in pure iron, Metallurgical Transactions 13 (1982) 135–140. https://doi.org/10.1007/BF02642424.

[45] K. Bergers, E. Camisão de Souza, I. Thomas, N. Mabho, J. Flock, Determination of Hydrogen in Steel by Thermal Desorption Mass Spectrometry, Steel Research International 81 (2010) 499–507.

[46] W.Y. Choo, J.Y. Lee, Hydrogen trapping phenomena in carbon steel, Journal of Materials Science 17 (1982) 1930–1938. https://doi.org/10.1007/BF00540409.

[47] G.M. Pressouyre, Trap theory of Hydrogen embrittlement, Acta Metallurgica 28 (1980) 895–911. https://doi.org/10.1016/0001-6160(80)90106-6.

[48] F.-G. Wei, T. Hara, T. Tsuchida, K. Tsuzaki, Hydrogen Trapping in Quenched and Tempered 0.42C-0.30Ti Steel Containing Bimodally Dispersed TiC Particles, ISIJ International 43 (2003) 539–547. https://doi.org/10.2355/isijinternational.43.539.

[49] R. Gibala (Ed.), Hydrogen embrittlement and stress corrosion cracking: A Troiano Festschrift, ASM International, Metals Park, OH, USA, 1984.

[50] G.M. Pressouyre, I.M. Bernstein, A kinetic trapping model for hydrogen-induced cracking, Acta Metallurgica 27 (1979) 89–100. https://doi.org/10.1016/0001-6160(79)90059-2.

[51] A. Turnbull, R. Hutchings, D. Ferriss, Modelling of thermal desorption of hydrogen from metals, Materials Science and Engineering: A 238 (1997) 317–328. https://doi.org/10.1016/S0921-5093(97)00426-7.

[52] M. Dadfarnia, P. Sofronis, T. Neeraj, Hydrogen interaction with multiple traps: Can it be used to mitigate embrittlement?, International Journal of Hydrogen Energy 36 (2011) 10141–10148. https://doi.org/10.1016/j.ijhydene.2011.05.027.

[53] G. Alefeld, J. Völkl, G. Schaumann, Elastic Diffusion Relaxation, Physica Status Solidi (B) 37 (1970) 337–351. https://doi.org/10.1002/pssb.19700370139.

[54] G.M. Pressouyre, A classification of hydrogen traps in steel, Metallurgical Transactions 10 (1979) 1571–1573. https://doi.org/10.1007/BF02812023.

[55] R.L.S. Thomas, J.R. Scully, R.P. Gangloff, Internal hydrogen embrittlement of ultrahigh-strength AERMET 100 steel, Metallurgical and Materials Transactions A 34 (2003) 327–344. https://doi.org/10.1007/s11661-003-0334-3.

[56] T. Depover, O. Monbaliu, E. Wallaert, K. Verbeken, Effect of Ti, Mo and Cr based precipitates on the hydrogen trapping and embrittlement of Fe–C–X Q&T alloys, International Journal of Hydrogen Energy 40 (2015) 16977–16984. https://doi.org/10.1016/j.ijhydene.2015.06.157.

[57] A. Turnbull, Perspectives on hydrogen uptake, diffusion and trapping, International Journal of Hydrogen Energy 40 (2015) 16961–16970. https://doi.org/10.1016/j.ijhydene.2015.06.147.

[58] R.P. Gangloff, Hydrogen-assisted Cracking, in: I. Milne, R.O. Ritchie, B.L. Karihaloo (Eds.), Comprehensive Structural Integrity: Vol. 6: Environmentally Assisted Fatigue, Elsevier Science, New York, NY, USA, 2003, pp. 31–101.

[59] G.M. Pressouyre, I.M. Bernstein, A quantitative analysis of hydrogen trapping, Metallurgical Transactions 9 (1978) 1571–1580. https://doi.org/10.1007/BF02661939.

[60] S.M. Myers, M.I. Baskes, H.K. Birnbaum, J.W. Corbett, G.G. DeLeo, S.K. Estreicher, E.E. Haller, P. Jena, N.M. Johnson, R. Kirchheim, S.J. Pearton, M.J. Stavola, Hydrogen interactions with defects in crystalline solids, Reviews of Modern Physics 64 (1992) 559–617. https://doi.org/10.1103/RevModPhys.64.559.

[61] Y.A. Du, L. Ismer, J. Rogal, T. Hickel, J. Neugebauer, R. Drautz, First-principles study on the interaction of H interstitials with grain boundaries in α- and γ-Fe, Physical Review B 84 (2011) 456. https://doi.org/10.1103/PhysRevB.84.144121.

[62] R. Matsumoto, M. Riku, S. Taketomi, N. Miyazaki, Hydrogen-Grain Boundary Interaction in Fe, Fe-C, and Fe-N Systems, Progress in Nuclear Science and Technology 2 (2011) 9–15. https://doi.org/10.15669/pnst.2.9.

[63] H.S. Kim, M.B. Bush, The effects of grain size and porosity on the elastic modulus of nanocrystalline materials, Nanostructured Materials 11 (1999) 361–367. https://doi.org/10.1016/S0965-9773(99)00052-5.

[64] N. Yazdipour, A.J. Haq, K. Muzaka, E.V. Pereloma, 2D modelling of the effect of grain size on hydrogen diffusion in X70 steel, Computational Materials Science 56 (2012) 49–57. https://doi.org/10.1016/j.commatsci.2012.01.003.

[65] K. Ono, M. Meshii, Hydrogen detrapping from grain boundaries and dislocations in high purity iron, Acta Metallurgica et Materialia 40 (1992) 1357–1364. https://doi.org/10.1016/0956-7151(92)90436-I.

[66] I.M. Bernstein, The effect of hydrogen on the deformation of iron, Scripta Metallurgica 8 (1974) 343–349. https://doi.org/10.1016/0036-9748(74)90136-7.

[67] F.G. Wei, T. Hara, K. Tsuzaki, Precise determination of the activation energy for desorption of hydrogen in two Ti-added steels by a single thermal-desorption spectrum, Metallurgical and Materials Transactions B 35 (2004) 587–597. https://doi.org/10.1007/s11663-004-0057-x.

[68] E. Wallaert, T. Depover, M. Arafin, K. Verbeken, Thermal Desorption Spectroscopy Evaluation of the Hydrogen-Trapping Capacity of NbC and NbN Precipitates, Metallurgical and Materials Transactions A 45 (2014) 2412–2420. https://doi.org/10.1007/s11661-013-2181-1.

[69] E.I. Galindo-Nava, B. Basha, P. Rivera-Díaz-del-Castillo, Hydrogen transport in metals: Integration of permeation, thermal desorption and degassing, Journal of Materials Science & Technology 33 (2017) 1433–1447. https://doi.org/10.1016/j.jmst.2017.09.011.

[70] E. Dabah, V. Lisitsyn, D. Eliezer, Performance of hydrogen trapping and phase transformation in hydrogenated duplex stainless steels, Materials Science and Engineering: A 527 (2010) 4851–4857. https://doi.org/10.1016/j.msea.2010.04.016.

[71] A. Turnbull, M. Carroll, D. Ferriss, Analysis of hydrogen diffusion and trapping in a 13% chromium martensitic stainless steel, Acta Metallurgica 37 (1989) 2039–2046. https://doi.org/10.1016/0001-6160(89)90089-8.

[72] P. Sofronis, M. Dadfarnia, P. Novak, R. Yuan, B. Somerday, Im Robertson, R.O. Ritchie, T. Kanezaki, Y. Murakami, A combined applied mechanics/materials science approach toward quantifying the role of hydrogen on material degradation, in: 12th International Conference on Fracture 2009, Curran Associates, Red Hook, NY, USA, 2009.

[73] D. Hull, D.J. Bacon, Introduction to Dislocations, fifth ed., Butterworth-Heinemann, Amsterdam, 2011.

[74] G. Gottstein, Materialwissenschaft und Werkstofftechnik, Springer, Berlin, Heidelberg, 2014.

[75] R. Kirchheim, Hydrogen solubility and diffusivity in defective and amorphous metals, Progress in Materials Science 32 (1988) 261–325. https://doi.org/10.1016/0079-6425(88)90010-2.

[76] S. Taketomi, R. Matsumoto, N. Miyazaki, Atomistic study of hydrogen distribution and diffusion around a {112}<111> edge dislocation in alpha iron, Acta Materialia 56 (2008) 3761–3769. https://doi.org/10.1016/j.actamat.2008.04.011.

[77] R. Kirchheim, Interaction of hydrogen with dislocations in palladium - I. Activity and diffusivity and their phenomenological interpretation, Acta Metallurgica 29 (1981) 835–843. https://doi.org/10.1016/0001-6160(81)90126-7.

[78] A.J. Kumnick, H.H. Johnson, Deep trapping states for hydrogen in deformed iron, Acta Metallurgica 28 (1980) 33–39. https://doi.org/10.1016/0001-6160(80)90038-3.

[79] D.K. Ross, K.L. Stefanopoulos, K.S. Forcey, I. Iordanova, Small Angle Neutron Scattering Studies of H(D) Trapping on Dislocations in Metals, Zeitschrift für Physikalische Chemie 183 (1994) 29–37. https://doi.org/10.1524/zpch.1994.183.Part_1_2.029.

[80] M. Maxelon, A. Pundt, W. Pyckhout-Hintzen, J. Barker, R. Kirchheim, Interaction of hydrogen and deuterium with dislocations in palladium as observed by small angle neutron scattering, Acta Materialia 49 (2001) 2625–2634. https://doi.org/10.1016/S1359-6454(01)00185-9.

[81] H. Kimizuka, S. Ogata, Slow diffusion of hydrogen at a screw dislocation core in α -iron, Physical Review B 84 (2011) 368. https://doi.org/10.1103/PhysRevB.84.024116.

[82] K. Nakashima, M. Suzuki, Y. Futamura, T. Tsuchiyama, S. Takaki, Limit of Dislocation Density and Dislocation Strengthening in Iron, Materials Science Forum 503-504 (2006) 627–632. https://doi.org/10.4028/www.scientific.net/MSF.503-504.627.

[83] K. Takita, K. Sakamoto, Low temperature internal friction peak and hydrogen cold-work peak in deformed α-iron, Scripta Metallurgica 10 (1976) 399–403. https://doi.org/10.1016/0036-9748(76)90160-5.

[84] R. Gibala, Internal friction in hydrogen-charged iron, Transactions of the Metallurgical Society of AIME 239 (1967) 1574–1585.

[85] W.Y. Choo, J.Y. Lee, Effect of cold working on the hydrogen trapping phenomena in pure iron, Metallurgical Transactions A 14 (1983) 1299–1305. https://doi.org/10.1007/BF02664812.

[86] H. Hagi, Y. Hayashi, Effects of Interstitial Impurities on Dislocation Trapping of Hydrogen in Iron, Transactions of the Japan Institute of Metals 28 (1987) 375–382. https://doi.org/10.2320/matertrans1960.28.375.

[87] W.G. Wolfer, M.I. Baskes, Interstitial solute trapping by edge dislocations, Acta Metallurgica 33 (1985) 2005–2011. https://doi.org/10.1016/0001-6160(85)90123-3.

[88] F.-G. Wei, K. Tsuzaki, Response of hydrogen trapping capability to microstructural change in tempered Fe–0.2C martensite, Scripta Materialia 52 (2005) 467–472. https://doi.org/10.1016/j.scriptamat.2004.11.008.

[89] V.P. Ramunni, T.D.P. Coelho, P. de Miranda, Interaction of hydrogen with the microstructure of low-carbon steel, Materials Science and Engineering: A 435-436 (2006) 504–514. https://doi.org/10.1016/j.msea.2006.07.089.

[90] S. Asano, K. Hara, Y. Nakai, N. Ohtani, The Trapping Effect of Dislocations on Hydrogen Diffusion in Mild Steel, Journal of the Japan Institute of Metals 38 (1974) 626–632. https://doi.org/10.2320/jinstmet1952.38.7_626.

[91] R.J.M. Konings, T.R. Allen (Eds.), Comprehensive Nuclear Materials, Elsevier, Amsterdam, 2012.

[92] R. Idczak, R. Konieczny, J. Chojcan, A study of defects in iron-based binary alloys by the Mössbauer and positron annihilation spectroscopies, Journal of Applied Physics 115 (2014) 103513. https://doi.org/10.1063/1.4868471.

[93] J.K. Nørskov, F. Besenbacher, Theory of hydrogen interaction with metals, Journal of the Less Common Metals 130 (1987) 475–490. https://doi.org/10.1016/0022-5088(87)90145-7.

[94] Y. Tateyama, T. Ohno, Stability and clusterization of hydrogen-vacancy complexes in α−Fe: An ab initio study, Physical Review B 67 (2003) L1256. https://doi.org/10.1103/PhysRevB.67.174105.

[95] R. Matsumoto, N. Nishigushi, S. Taketomi, N. Miyazaki, First-Principles Calculation of Hydrogen Effects on the Formation and Diffusion of Vacancies in Alpha Iron: Discussion of the Hydrogen-Enhanced Strain-Induced Vacancy Mechanism, Journal of the Society of Materials Science, Japan 63 (2014) 182–187. https://doi.org/10.2472/jsms.63.182.

[96] M. Iwamoto, Y. Fukai, Superabundant Vacancy Formation in Iron under High Hydrogen Pressures: Thermal Desorption Spectroscopy, Materials Transactions, JIM 40 (1999) 606–611. https://doi.org/10.2320/matertrans1989.40.606.

[97] F. Besenbacher, S.M. Myers, P. Nordlander, J.K. Nørskov, Multiple hydrogen occupancy of vacancies in Fe, Journal of Applied Physics 61 (1987) 1788–1794. https://doi.org/10.1063/1.338020.

[98] P. Nordlander, J.K. Nørskov, F. Besenbacher, S.M. Myers, Multiple deuterium occupancy of vacancies in Pd and related metals, Physical Review B 40 (1989) 1990–1992. https://doi.org/10.1103/physrevb.40.1990.

[99] S.M. Myers, S.T. Picraux, R.E. Stoltz, Defect trapping of ion-implanted deuterium in Fe, Journal of Applied Physics 50 (1979) 5710–5719. https://doi.org/10.1063/1.326761.

[100] S.T. Picraux, Defect trapping of gas atoms in metals, Nuclear Instruments and Methods 182-183 (1981) 413–437. https://doi.org/10.1016/0029-554X(81)90715-1.

[101] F. Besenbacher, S.M. Myers, J.K. Nørskov, Interaction of hydrogen with defects in metals, Nuclear Instruments and Methods in Physics Research Section B: Beam Interactions with Materials and Atoms 7-8 (1985) 55–66. https://doi.org/10.1016/0168-583X(85)90529-4.

[102] S.M. Myers, D.M. Follstaedt, F. Besenbacher, J. Bøttiger, Trapping and surface permeation of deuterium in He-implanted Fe, Journal of Applied Physics 53 (1982) 8734–8744. https://doi.org/10.1063/1.330473.

[103] J.L. Lee, J.Y. Lee, Hydrogen trapping in AISI 4340 steel, Metal Science 17 (1983) 426–432. https://doi.org/10.1179/030634583790420619.

[104] S.M. Lee, J.Y. Lee, The effect of the interface character of TiC particles on hydrogen trapping in steel, Acta Metallurgica 35 (1987) 2695–2700. https://doi.org/10.1016/0001-6160(87)90268-9.

[105] S. Yamasaki, T. Takahashi, Evaluation Method of Delayed Fracture Property of High Strength Steels, Tetsu-to-Hagane 83 (1997) 454–459. https://doi.org/10.2355/tetsutohagane1955.83.7_454.

[106] J. Takahashi, K. Kawakami, Y. Kobayashi, T. Tarui, The first direct observation of hydrogen trapping sites in TiC precipitation-hardening steel through atom probe tomography, Scripta Materialia 63 (2010) 261–264. https://doi.org/10.1016/j.scriptamat.2010.03.012.

[107] M.F. Stevens, I.M. Bernstein, Microstructural trapping effects on hydrogen induced cracking of a microalloyed steel, Metallurgical Transactions 20 (1989) 909–919. https://doi.org/10.1007/BF02651657.

[108] T. Depover, K. Verbeken, The effect of TiC on the hydrogen induced ductility loss and trapping behavior of Fe-C-Ti alloys, Corrosion Science 112 (2016) 308–326. https://doi.org/10.1016/j.corsci.2016.07.013.

[109] T. Asaoka, G. Lapasset, M. Aucouturier, P. Lacombe, Observation of Hydrogen Trapping in Fe-0.15 Wt% Ti Alloy by High Resolution Autoradiography, Corrosion 34 (1978) 39–47. https://doi.org/10.5006/0010-9312-34.2.39.

[110] F.G. Wei, K. Tsuzaki, Quantitative analysis on hydrogen trapping of TiC particles in steel, Metallurgical and Materials Transactions A 37 (2006) 331–353. https://doi.org/10.1007/s11661-006-0004-3.

[111] F.-G. Wei, T. Hara, K. Tsuzaki, Nano-Preciptates Design with Hydrogen Trapping Character in High Strength Steel, in: Y. Weng, H. Dong, Y. Gan (Eds.), Advanced Steels, Springer, Berlin, Heidelberg, 2011, pp. 87–92.

[112] T. Depover, K. Verbeken, Evaluation of the effect of V4C3 precipitates on the hydrogen induced mechanical degradation in Fe-C-V alloys, Materials Science and Engineering: A 675 (2016) 299–313. https://doi.org/10.1016/j.msea.2016.08.053.

[113] T. Depover, K. Verbeken, Evaluation of the role of Mo2C in hydrogen induced ductility loss in Q&T Fe-C-Mo alloys, International Journal of Hydrogen Energy 41 (2016) 14310–14329. https://doi.org/10.1016/j.ijhydene.2016.05.176.

[114] T. Depover, K. Verbeken, Hydrogen trapping and hydrogen induced mechanical degradation in lab cast Fe-C-Cr alloys, Materials Science and Engineering: A 669 (2016) 134–149. https://doi.org/10.1016/j.msea.2016.05.018.

[115] X.Y. Huang, W. Mader, J.A. Eastman, R. Kirchheim, Modulating the composition of a metal/oxide interface and using hydrogen as a probe, Scripta Metallurgica 22 (1988) 1109–1114. https://doi.org/10.1016/S0036-9748(88)80113-3.

[116] X.Y. Huang, W. Mader, R. Kirchheim, Hydrogen and oxygen at metal/oxide interfaces, Acta Metallurgica et Materialia 39 (1991) 893–907. https://doi.org/10.1016/0956-7151(91)90289-D.

[117] G.-W. Hong, J.-Y. Lee, The interaction of hydrogen and the cementite-ferrite interface in carbon steel, Journal of Materials Science 18 (1983) 271–277. https://doi.org/10.1007/BF00543835.

[118] H. Hagi, Effect of Interface between Cementite and Ferrite on Diffusion of Hydrogen in Carbon Steels, Materials Transactions, JIM 35 (1994) 168–173. https://doi.org/10.2320/matertrans1989.35.168.

[119] K. Kawakami, T. Matsumiya, Ab-initio Investigation of Hydrogen Trap State by Cementite in bcc-Fe, ISIJ International 53 (2013) 709–713. https://doi.org/10.2355/isijinternational.53.709.

[120] K.Y. Lee, J.-Y. Lee, D.R. Kim, A study of hydrogen-trapping phenomena in AISI 5160 spring steel, Materials Science and Engineering 67 (1984) 213–220. https://doi.org/10.1016/0025-5416(84)90053-3.

[121] M. Iino, Evaluation of hydrogen-trap binding enthalpy l, Metallurgical Transactions 18 (1987) 1559–1564. https://doi.org/10.1007/BF02646139.

[122] M. Mizuno, H. Anzai, T. Aoyama, T. Suzuki, Determination of Hydrogen Concentration in Austenitic Stainless Steels by Thermal Desorption Spectroscopy, Materials Transactions, JIM 35 (1994) 703–707. https://doi.org/10.2320/matertrans1989.35.703.

[123] H. Asahi, D. Hirakami, S. Yamasaki, Hydrogen Trapping Behavior in Vanadium-added Steel, ISIJ International 43 (2003) 527–533. https://doi.org/10.2355/isijinternational.43.527.

[124] A. Drexler, T. Depover, K. Verbeken, W. Ecker, Model-based interpretation of thermal desorption spectra of Fe-C-Ti alloys, Journal of Alloys and Compounds 789 (2019) 647–657. https://doi.org/10.1016/j.jallcom.2019.03.102.

[125] M.A. Stopher, P. Lang, E. Kozeschnik, P.E. Rivera-Diaz-del-Castillo, Modelling hydrogen migration and trapping in steels, Materials & Design 106 (2016) 205–215. https://doi.org/10.1016/j.matdes.2016.05.051.

[126] F.G. Wei, K. Tsuzaki, T. Hara, A New Method to Determine the Activation Energy for Hydrogen Desorption from Steels, Materials Science Forum 475-479 (2005) 229–232. https://doi.org/10.4028/www.scientific.net/MSF.475-479.229.

[127] F.G. Wei, K. Tsuzaki, Hydrogen absorption of incoherent TiC particles in iron from environment at high temperatures, Metallurgical and Materials Transactions A 35 (2004) 3155–3163. https://doi.org/10.1007/s11661-004-0060-5.

[128] H.G. Lee, J.-Y. Lee, Hydrogen trapping by TiC particles in iron, Acta Metallurgica 32 (1984) 131–136. https://doi.org/10.1016/0001-6160(84)90210-4.

[129] D. Pérez Escobar, E. Wallaert, L. Duprez, A. Atrens, K. Verbeken, Thermal desorption spectroscopy study of the interaction of hydrogen with TiC precipitates, Metals and Materials International 19 (2013) 741–748. https://doi.org/10.1007/s12540-013-4013-7.

[130] H. Hagi, Diffusion Coefficient of Hydrogen in Iron without Trapping by Dislocations and Impurities, Materials Transactions, JIM 35 (1994) 112–117. https://doi.org/10.2320/matertrans1989.35.112.

[131] A.T. Paxton, From quantum mechanics to physical metallurgy of steels, Materials Science and Technology 30 (2014) 1063–1070. https://doi.org/10.1179/1743284714Y.0000000521.

[132] A. Fick, Ueber Diffusion, Annalen der Physik und Chemie 170 (1855) 59–86. https://doi.org/10.1002/andp.18551700105.

[133] P. Kedzierzawski, Diffusivity of hydrogen and its isotopes in iron alloys, in: R.A. Oriani, J.P. Hirth, M. Smialowski (Eds.), Hydrogen degradation of ferrous alloys, Noyes Publications, Park Ridge, NJ, USA, 1985, 251-270.

[134] S. Frappart, X. Feaugas, J. Creus, F. Thebault, L. Delattre, H. Marchebois, Study of the hydrogen diffusion and segregation into Fe–C–Mo martensitic HSLA steel using electrochemical permeation test, Journal of Physics and Chemistry of Solids 71 (2010) 1467–1479. https://doi.org/10.1016/j.jpcs.2010.07.017.

[135] E. Riecke, B. Johnen, H.J. Grabke, Einflüsse von Legierungselementen auf die Korrosion und Wasserstoffaufnahme von Eisen in Schwefelsäure - Teil I: Permeation, Diffusion und Löslichkeit von Wasserstoff in binären Eisenlegierungen, Materials and Corrosion 36 (1985) 435–441. https://doi.org/10.1002/maco.19850361002.

[136] W. Beck, J. Bockris, J. McBreen, L. Nanis, Hydrogen permeation in metals as a function of stress, temperature and dissolved hydrogen concentration, Proceedings of the Royal Society A 290 (1966) 220–235. https://doi.org/10.1098/rspa.1966.0046.

[137] N. Quick, H. Johnson, Hydrogen and deuterium in iron, 49–506°C, Acta Metallurgica 26 (1978) 903–907. https://doi.org/10.1016/0001-6160(78)90041-X.

[138] W. Raczyński, Permeability, diffusivity, and solubility of hydrogen and deuterium in pure iron at 10 to 60 °C, Physica Status Solidi (A) 48 (1978) K27-K30. https://doi.org/10.1002/pssa.2210480143.

[139] J. Völkl, G. Alefeld, Diffusion of hydrogen in metals, in: G. Alefeld, J. Völkl (Eds.), Hydrogen in metals, Springer, Berlin, New York, 1978, pp. 321–348.

[140] R. Kirchheim, Activity and diffusivity of hydrogen in deformed palladium, Scripta Metallurgica 14 (1980) 905–910. https://doi.org/10.1016/0036-9748(80)90318-X.

[141] P. Castaño-Rivera, N.S. de Vincentis, R.E. Bolmaro, P. Bruzzoni, Relationship between Dislocation Densityand Hydrogen Trappingin a Cold Worked API 5L X60 Steel, Procedia Materials Science 8 (2015) 1031–1038. https://doi.org/10.1016/j.mspro.2015.04.165.

[142] E. van den Eeckhout, A. Laureys, Y. van Ingelgem, K. Verbeken, Hydrogen permeation through deformed and heat-treated Armco pure iron, Materials Science and Technology 33 (2017) 1515–1523. https://doi.org/10.1080/02670836.2017.1342015.

[143] S.M. Teus, V.G. Gavriljuk, Grain-Boundary Diffusion of Hydrogen Atoms in the alpha-Iron, Metallofizika i Noveishie Tekhnologii 36 (2014) 1399–1410. https://doi.org/10.15407/mfint.36.10.1399.

[144] D.F. Araújo, E.O. Vilar, J. Palma Carrasco, A critical review of mathematical models used to determine the density of hydrogen trapping sites in steels and alloys, International Journal of Hydrogen Energy 39 (2014) 12194–12200. https://doi.org/10.1016/j.ijhydene.2014.06.036.

[145] A. McNabb, P.K. Foster, A new analysis of the diffusion of hydrogen in iron and ferritic steels, Transactions of the Metallurgical Society of AIME (1963) 618–627.

[146] J. Svoboda, G. Mori, A. Prethaler, F.D. Fischer, Determination of trapping parameters and the chemical diffusion coefficient from hydrogen permeation experiments, Corrosion Science 82 (2014) 93–100. https://doi.org/10.1016/j.corsci.2014.01.002.

[147] G.R. Caskey, W.L. Pillinger, Effect of trapping on hydrogen permeation, Metallurgical Transactions 6 (1975) 467–476. https://doi.org/10.1007/BF02658404.

[148] M. Iino, A more generalized analysis of hydrogen trapping, Acta Metallurgica 30 (1982) 367–375. https://doi.org/10.1016/0001-6160(82)90216-4.

[149] E.J. Song, D.-W. Suh, H. Bhadeshia, Theory for hydrogen desorption in ferritic steel, Computational Materials Science 79 (2013) 36–44. https://doi.org/10.1016/j.commatsci.2013.06.008.

[150] M. Koiwa, Trapping effect in diffusion of interstitial impuritl atoms in B.C.C. lattices, Acta Metallurgica 22 (1974) 1259–1268. https://doi.org/10.1016/0001-6160(74)90139-4.

[151] S. Wach, A.P. Miodownik, J. Mackowiak, The diffusion of hydrogen through pure iron membranes, Corrosion Science 6 (1966) 271–285. https://doi.org/10.1016/S0010-938X(66)80087-2.

[152] F. Vucko, C. Bosch, A. Aoufi, D. Delafosse, Palladium coating on quenched-tempered martensitic steel for hydrogen electrochemical permeation tests, 2014. https://hal-emse.ccsd.cnrs.fr/emse-00951142/document.

[153] S.X. Xie, J.P. Hirth, Permeation of Hydrogen, Trapping, and Damage in Spheroidized AISI 1090 Steel, Corrosion 38 (1982) 486–493. https://doi.org/10.5006/1.3577364.

[154] P. Castaño Rivera, V.P. Ramunni, P. Bruzzoni, Hydrogen trapping in an API 5L X60 steel, Corrosion Science 54 (2012) 106–118. https://doi.org/10.1016/j.corsci.2011.09.008.

[155] M.J. Danielson, Use of the Devanathan-Stachurski cell to measure hydrogen permeation in aluminum alloys, Corrosion Science 44 (2002) 829–840. https://doi.org/10.1016/S0010-938X(01)00103-2.

[156] C. Zheng, B. Yan, K. Zhang, G. Yi, Electrochemical investigation on the hydrogen permeation behavior of 7075-T6 Al alloy and its influence on stress corrosion cracking, International Journal of Minerals, Metallurgy, and Materials 22 (2015) 729–737. https://doi.org/10.1007/s12613-015-1128-5.

[157] J. WU, Electrochemical method for studying hydrogen in iron, nickel and palladium, International Journal of Hydrogen Energy 17 (1992) 917–921. https://doi.org/10.1016/0360-3199(92)90051-W.

[158] A. Oudriss, J. Creus, J. Bouhattate, E. Conforto, C. Berziou, C. Savall, X. Feaugas, Grain size and grain-boundary effects on diffusion and trapping of hydrogen in pure nickel, Acta Materialia 60 (2012) 6814–6828. https://doi.org/10.1016/j.actamat.2012.09.004.

[159] E. Legrand, A. Oudriss, C. Savall, J. Bouhattate, X. Feaugas, Towards a better understanding of hydrogen measurements obtained by thermal desorption spectroscopy using FEM modeling, International Journal of Hydrogen Energy 40 (2015) 2871–2881. https://doi.org/10.1016/j.ijhydene.2014.12.069.

[160] P. Manolatos, M. Jerome, C. Duret-Thual, J. Le Coze, The electrochemical permeation of hydrogen in steels without palladium coating. Part I: Interpretation difficulties, Corrosion Science 37 (1995) 1773–1783. https://doi.org/10.1016/0010-938X(95)00079-Y.

[161] C. Gabrielli, G. Maurin, L. Mirkova, H. Perrot, B. Tribollet, Transfer function analysis of hydrogen permeation through a metallic membrane in a Devanathan cell. I. Theory, Journal of Electroanalytical Chemistry 590 (2006) 1–14. https://doi.org/10.1016/j.jelechem.2006.01.029.

[162] L. Vecchi, H. Simillion, R. Montoya, D. van Laethem, E. van den Eeckhout, K. Verbeken, H. Terryn, J. Deconinck, Y. van Ingelgem, Modelling of hydrogen permeation experiments in iron alloys: Characterization of the accessible parameters – Part I – The entry side, Electrochimica Acta 262 (2018) 57–65. https://doi.org/10.1016/j.electacta.2017.12.172.

[163] N. Boes, H. Züchner, Electrochemical methods for studying diffusion, permeation and solubility of hydrogen in metals, Journal of the Less Common Metals 49 (1976) 223–240. https://doi.org/10.1016/0022-5088(76)90037-0.

[164] H.J. Grabke, F. Gehrmann, E. Riecke, Hydrogen in microalloyed steels, Steel Research 72 (2001) 225–235. https://doi.org/10.1002/srin.200100110.

[165] W. Siegl, G. Mori, W. Ecker, J. Klarner, G. Kloesch, A. Drexler, G. Winter, H. Schnideritsch, Hydrogen Trapping in Heat Treated and Deformed Armco Iron, NACE International, Houston, TX, USA (2019).

[166] T. Zakroczymski, Electrochemical determination of hydrogen in metals, Journal of Electroanalytical Chemistry 475 (1999) 82–88. https://doi.org/10.1016/S0022-0728(99)00355-1.

[167] E. Riecke, Untersuchungen zum Einfluß des Stahlgefüges auf die stationäre Wasserstoffpermeation, Materials and Corrosion 32 (1981) 66–72. https://doi.org/10.1002/maco.19810320203.

[168] T. Zakroczymski, Adaptation of the electrochemical permeation technique for studying entry, transport and trapping of hydrogen in metals, Electrochimica Acta 51 (2006) 2261–2266. https://doi.org/10.1016/j.electacta.2005.02.151.

[169] U. Hadam, T. Zakroczymski, Absorption of hydrogen in tensile strained iron and high-carbon steel studied by electrochemical permeation and desorption techniques, International Journal of Hydrogen Energy 34 (2009) 2449–2459. https://doi.org/10.1016/j.ijhydene.2008.12.088.

[170] P. Marcus, Corrosion mechanisms in theory and practice, third ed., CRC Press, Boca Raton, FL, USA, 2012.

[171] B.N. Popov, Hydrogen Permeation and Hydrogen-Induced Cracking, in: Corrosion Engineering, Elsevier, 2015, pp. 327–364.

[172] G.S. Frankel, D. Landolt, Fundamentals of Corrosion, in: A.J. Bard, G.S. Frankel, M. Stratmann (Eds.), Corrosion and Oxide Films, Wiley-VCH, Berlin, 2003.

[173] R.N. Iyer, H.W. Pickering, M. Zamanzadeh, A mechanistic analysis of hydrogen entry into metals during cathodic hydrogen charging, Scripta Metallurgica 22 (1988) 911–916. https://doi.org/10.1016/S0036-9748(88)80074-7.

[174] M. de Chialvo, A.C. Chialvo, Hydrogen evolution reaction: Analysis of the Volmer-Heyrovsky-Tafel mechanism with a generalized adsorption model, Journal of Electroanalytical Chemistry 372 (1994) 209–223. https://doi.org/10.1016/0022-0728(93)03043-O.

[175] N. Amokrane, C. Gabrielli, G. Maurin, L. Mirkova, Effect of organic additives on hydrogen permeation into an iron membrane studied by frequency analysis techniques, Electrochimica Acta 53 (2007) 1962–1971. https://doi.org/10.1016/j.electacta.2007.08.053.

[176] J. Kafle, D. Qu, Enhancement of Hydrogen Insertion into Carbon Interlayers by Surface Catalytic Poisoning, The Journal of Physical Chemistry C 114 (2010) 19108–19115. https://doi.org/10.1021/jp1064006.

[177] S.Y. Qian, B.E. Conway, G. Jerkiewicz, Kinetic rationalization of catalyst poison effects on cathodic H sorption into metals: relation of enhancement and inhibition to H coverage, Journal of the Chemical Society, Faraday Transactions 94 (1998) 2945–2954. https://doi.org/10.1039/a804113j.

[178] L. Vecchi, H. Simillion, R. Montoya, D. van Laethem, E. van den Eeckhout, K. Verbeken, H. Terryn, J. Deconinck, Y. van Ingelgem, Modelling of hydrogen permeation experiments in iron alloys: Characterization of the accessible parameters – Part II – The exit side, Electrochimica Acta 262 (2018) 153–161. https://doi.org/10.1016/j.electacta.2017.12.173.

[179] P. Manolatos, C. Duret-Thual, J. Le Coze, M. Jerome, E. Bollinger, The electrochemical permeation of hydrogen in steels without palladium coating. Part II: Study of the influence of microstructure on hydrogen diffusion, Corrosion Science 37 (1995) 1785–1796. https://doi.org/10.1016/0010-938X(95)00080-4.

[180] P. Manolatos, M. Jerome, J. Galland, Necessity of a palladium coating to ensure hydrogen oxidation during electrochemical permeation measurements on iron, Electrochimica Acta 40 (1995) 867–871. https://doi.org/10.1016/0013-4686(94)00343-Y.

[181] P. Bruzzoni, R. Garavaglia, Anodic iron oxide films and their effect on the hydrogen permeation through steel, Corrosion Science 33 (1992) 1797–1807. https://doi.org/10.1016/0010-938X(92)90010-Z.

[182] P. Bruzzoni, R.M. Carranza, J.R. Collet Lacoste, E.A. Crespo, Hydrogen diffusion in α-iron studied using an electrochemical permeation transfer function, Electrochimica Acta 44 (1999) 2693–2704. https://doi.org/10.1016/S0013-4686(98)00406-X.

[183] C. Azevedo, P. Bezerra, F. Esteves, C. Joia, O.R. Mattos, Hydrogen permeation studied by electrochemical techniques, Electrochimica Acta 44 (1999) 4431–4442. https://doi.org/10.1016/S0013-4686(99)00158-9.

[184] P. Manolatos, M. Jerome, A thin palladium coating on iron for hydrogen permeation studies, Electrochimica Acta 41 (1996) 359–365. https://doi.org/10.1016/0013-4686(95)00379-7.

[185] S.J. Kim, D.W. Yun, H.G. Jung, K.Y. Kim, Determination of Hydrogen Diffusion Parameters of Ferritic Steel from Electrochemical Permeation Measurement under Tensile Loads, Journal of The Electrochemical Society 161 (2014) E173-E181. https://doi.org/10.1149/2.1021412jes.

[186] J.O. Bockris, R.E. White, B.E. Conway, Modern Aspects of Electrochemistry, Kluwer Academic Publishers, Boston, MA, USA, 2002.

[187] International Organization for Standardization, ISO 17081:2014, Method of measurement of hydrogen permeation and determination of hydrogen uptake and transport in metals by an electrochemical technique, Geneva, Switzerland, 2014.

[188] M.R. Louthan, R.G. Derrick, Hydrogen transport in austenitic stainless steel, Corrosion Science 15 (1975) 565–577. https://doi.org/10.1016/0010-938X(75)90022-0.

[189] E. van den Eeckhout, T. Depover, K. Verbeken, The Effect of Microstructural Characteristics on the Hydrogen Permeation Transient in Quenched and Tempered Martensitic Alloys, Metals 8 (2018) 779. https://doi.org/10.3390/met8100779.

[190] L. Lan, X. Kong, Z. Hu, C. Qiu, D. Zhao, L. Du, Hydrogen permeation behavior in relation to microstructural evolution of low carbon bainitic steel weldments, Corrosion Science 112 (2016) 180–193. https://doi.org/10.1016/j.corsci.2016.07.025.

[191] J. Yang, F. Huang, Z. Guo, Y. Rong, N. Chen, Effect of retained austenite on the hydrogen embrittlement of a medium carbon quenching and partitioning steel with refined microstructure, Materials Science and Engineering: A 665 (2016) 76–85. https://doi.org/10.1016/j.msea.2016.04.025.

[192] A.J. Haq, K. Muzaka, D.P. Dunne, A. Calka, E.V. Pereloma, Effect of microstructure and composition on hydrogen permeation in X70 pipeline steels, International Journal of Hydrogen Energy 38 (2013) 2544–2556. https://doi.org/10.1016/j.ijhydene.2012.11.127.

[193] I. Maroef, D.L. Olson, M. Eberhart, G.R. Edwards, Hydrogen trapping in ferritic steel weld metal, International Materials Reviews 47 (2002) 191–223. https://doi.org/10.1179/095066002225006548.

[194] A.M. Brass, J.R. Collet-Lacoste, On the mechanism of hydrogen permeation in iron in alkaline medium, Acta Materialia 46 (1998) 869–879. https://doi.org/10.1016/S1359-6454(97)00311-X.

[195] T.-Y. Zhang, Y.-P. Zheng, Q.-W. Wu, On the Boundary Conditions of Electrochemical Hydrogen Permeation Through Iron, Journal of The Electrochemical Society 146 (1999) 1741. https://doi.org/10.1149/1.1391836.

[196] E. Schmidt, H. Siegenthaler, Zur Kinetik des Diffusionsvorgangs bei Adsorptionsuntersuchungen nach dem Zweielektrodenverfahren, Helvetica Chimica Acta 53 (1970) 321–330. https://doi.org/10.1002/hlca.19700530211.

[197] M.A. Fullenwider, Electrochemical Current Balance with the Hydrogen-Palladium System, Journal of The Electrochemical Society 122 (1975) 648. https://doi.org/10.1149/1.2134283.

[198] J.G. Early, Hydrogen diffusion in palladium by galvanostatic charging, Acta Metallurgica 26 (1978) 1215–1223. https://doi.org/10.1016/0001-6160(78)90005-6.

[199] P.H. Pumphrey, On the boundary conditions for hydrogen permeation through cathodically charged iron and mild steel, Scripta Metallurgica 14 (1980) 695–701. https://doi.org/10.1016/0036-9748(80)90272-0.

[200] J. McBreen, L. Nanis, W. Beck, A Method for Determination of the Permeation Rate of Hydrogen Through Metal Membranes, Journal of The Electrochemical Society 113 (1966) 1218. https://doi.org/10.1149/1.3087209.

[201] B.S. Chaudhari, T.P. Radhakrishnan, On hydrogen diffusivity in metals from electropermeation transients, Surface Technology 22 (1984) 353–366. https://doi.org/10.1016/0376-4583(84)90099-2.

[202] T.-Y. Zhang, Y.-P. Zheng, Effects of absorption and desorption on hydrogen permeation - I. Theoretical modeling and room temperature verification, Acta Materialia 46 (1998) 5023–5033. https://doi.org/10.1016/S1359-6454(98)00176-1.

[203] H. Addach, P. Berçot, M. Rezrazi, M. Wery, Hydrogen permeation in iron at different temperatures, Materials Letters 59 (2005) 1347–1351. https://doi.org/10.1016/j.matlet.2004.12.037.

[204] H.A. Daynes, The process of diffusion through a rubber membrane, Proceedings of the Royal Society A 97 (1920) 286–307. https://doi.org/10.1098/rspa.1920.0034.

[205] ASTM International, ASTM G148-97(2018), Standard Practice for Evaluation of Hydrogen Uptake, Permeation, and Transport in Metals by an Electrochemical Technique, ASTM International, West Conshohocken, PA, USA, Reapproval 2018.

[206] J. Svoboda, F.D. Fischer, Modelling for hydrogen diffusion in metals with traps revisited, Acta Materialia 60 (2012) 1211–1220. https://doi.org/10.1016/j.actamat.2011.11.025.

[207] P.A. Redhead, Thermal desorption of gases, Vacuum 12 (1962) 203–211. https://doi.org/10.1016/0042-207X(62)90978-8.

[208] G. Ehrlich, The Interaction of Nitrogen with a Tungsten Surface, The Journal of Physical Chemistry 60 (1956) 1388–1400. https://doi.org/10.1021/j150544a014.

[209] G. Carter, Thermal resolution of desorption energy spectra, Vacuum 12 (1962) 245–254. https://doi.org/10.1016/0042-207X(62)90526-2.

[210] S.W. Smith, J.R. Scully, The identification of hydrogen trapping states in an Al-Li-Cu-Zr alloy using thermal desorption spectroscopy, Metallurgical and Materials Transactions A 31 (2000) 179–193. https://doi.org/10.1007/s11661-000-0064-8.

[211] A.A. van Gorkum, E.V. Kornelsen, Quantitative thermal desorption spectrometry of ionically implanted inert gases - I. Fundamental aspects, Vacuum 31 (1981) 89–98. https://doi.org/10.1016/S0042-207X(81)80165-0.

[212] E.V. Kornelsen, A.A. van Gorkum, Quantitative thermal desorption spectrometry of ionically implanted inert gases - II. Technical requirements, Vacuum 31 (1981) 99–111. https://doi.org/10.1016/S0042-207X(81)80166-2.

[213] M.H. Mendelsohn, D.M. Gruen, Temperature-programmed desorption (TPD) studies of ZrV1.6Fe0.4Hy and ZrV1.2Cr0.8Hy, Materials Research Bulletin 16 (1981) 1027–1034. https://doi.org/10.1016/0025-5408(81)90146-X.

[214] D. Pérez Escobar, K. Verbeken, L. Duprez, M. Verhaege, On the Methodology of Thermal Desorption Spectroscopy to Evaluate Hydrogen Embrittlement, Materials Science Forum 706-709 (2012) 2354–2359. https://doi.org/10.4028/www.scientific.net/MSF.706-709.2354.

[215] F. von Zeppelin, M. Haluška, M. Hirscher, Thermal desorption spectroscopy as a quantitative tool to determine the hydrogen content in solids, Thermochimica Acta 404 (2003) 251–258. https://doi.org/10.1016/S0040-6031(03)00183-7.

[216] Y.D. Park, I.S. Maroef, A. Landall, D.L. Olson, Retained austenite as a hydrogen trap in steel welds, Welding Journal 81 (2002) 27s-35s.

[217] M. Nagumo, K. Takai, N. Okuda, Nature of hydrogen trapping sites in steels induced by plastic deformation, Journal of Alloys and Compounds 293-295 (1999) 310–316. https://doi.org/10.1016/S0925-8388(99)00322-9.

[218] D. Pérez Escobar, T. Depover, L. Duprez, K. Verbeken, M. Verhaege, Combined thermal desorption spectroscopy, differential scanning calorimetry, scanning electron microscopy and X-ray diffraction study of hydrogen trapping in cold deformed TRIP steel, Acta Materialia 60 (2012) 2593–2605. https://doi.org/10.1016/j.actamat.2012.01.026.

[219] K. Takai, J. Seki, Y. Homma, Hydrogen Occlusion Behavior during Delayed Fracture in Cold Drawn Steel Wire and Heat Treated Steel Bar for Prestressed Concrete, Tetsu-to-Hagane 81 (1995) 1025–1030. https://doi.org/10.2355/tetsutohagane1955.81.10_1025.

[220] J.S. Kim, Y.H. Lee, D.L. Lee, K.-T. Park, C.S. Lee, Microstructural influences on hydrogen delayed fracture of high strength steels, Materials Science and Engineering: A 505 (2009) 105–110. https://doi.org/10.1016/j.msea.2008.11.040.

[221] T. Doshida, K. Takai, Dependence of hydrogen-induced lattice defects and hydrogen embrittlement of cold-drawn pearlitic steels on hydrogen trap state, temperature, strain rate and hydrogen content, Acta Materialia 79 (2014) 93–107. https://doi.org/10.1016/j.actamat.2014.07.008.

[222] F.D. Fischer, J. Svoboda, E. Kozeschnik, Interstitial diffusion in systems with multiple sorts of traps, Modelling and Simulation in Materials Science and Engineering 21 (2013) 25008. https://doi.org/10.1088/0965-0393/21/2/025008.

[223] K. Randerson, H.C. Carey, K. Schomberg, A model for calculating solubility of hydrogen in steel, Ironmaking & Steelmaking 30 (2003) 369–378. https://doi.org/10.1179/030192303225004060.

[224] D. Pérez Escobar, K. Verbeken, L. Duprez, M. Verhaege, Evaluation of hydrogen trapping in high strength steels by thermal desorption spectroscopy, Materials Science and Engineering: A 551 (2012) 50–58. https://doi.org/10.1016/j.msea.2012.04.078.

[225] U. Bernabai, G. Biggiero, R. Torella, Thermal analysis on hydrogen charged annealed and hardened AISI 420 stainless steel, Metallurgical Science and Tecnology 11 (1993) 70–77.

[226] R.B. McLellan, Thermodynamics and diffusion behavior of interstitial solute atoms in non-perfect solvent crystals, Acta Metallurgica 27 (1979) 1655–1663. https://doi.org/10.1016/0001-6160(79)90047-6.

[227] R. Kirchheim, Solubility, diffusivity and trapping of hydrogen in dilute alloys. Deformed and amorphous metals—II, Acta Metallurgica 30 (1982) 1069–1078. https://doi.org/10.1016/0001-6160(82)90003-7.

[228] S. Frappart, A. Oudriss, X. Feaugas, J. Creus, J. Bouhattate, F. Thébault, L. Delattre, H. Marchebois, Hydrogen trapping in martensitic steel investigated using electrochemical permeation and thermal desorption spectroscopy, Scripta Materialia 65 (2011) 859–862. https://doi.org/10.1016/j.scriptamat.2011.07.042.

[229] H.E. Kissinger, Reaction Kinetics in Differential Thermal Analysis, Analytical Chemistry 29 (1957) 1702–1706. https://doi.org/10.1021/ac60131a045.

[230] A.W. Coats, J.P. Redfern, Kinetic Parameters from Thermogravimetric Data, Nature 201 (1964) 68–69. https://doi.org/10.1038/201068a0.

[231] H.E. Kissinger, Variation of Peak Temperature With Heating Rate In Differential Thermal Analysis, Journal of Research of the National Bureau of Standards 57 (1956) 217. https://doi.org/10.6028/jres.057.026.

[232] J.-Y. Lee, S.M. Lee, Hydrogen trapping phenomena in metals with B.C.C. and F.C.C. crystals structures by the desorption thermal analysis technique, Surface and Coatings Technology 28 (1986) 301–314. https://doi.org/10.1016/0257-8972(86)90087-3.

[233] T. Izumi, G. Itoh, Thermal Desorption Spectroscopy Study on the Hydrogen Trapping States in a Pure Aluminum, Materials Transactions 52 (2011) 130–134. https://doi.org/10.2320/matertrans.L-M2010825.

[234] K.L. Wilson, M.I. Baskes, Deuterium trapping in irradiated 316 stainless steel, Journal of Nuclear Materials 76-77 (1978) 291–297. https://doi.org/10.1016/0022-3115(78)90160-5.

[235] M. Nagumo, M. Nakamura, K. Takai, Hydrogen thermal desorption relevant to delayed-fracture susceptibility of high-strength steels, Metallurgical and Materials Transactions A 32 (2001) 339–347. https://doi.org/10.1007/s11661-001-0265-9.

[236] ASTM International, ASTM E112-12, Standard Test Methods for Determining Average Grain Size, ASTM International, West Conshohocken, PA, USA.

[237] D.R. Black, M.H. Mendenhall, C.M. Brown, A. Henins, J. Filliben, J.P. Cline, Certification of Standard Reference Material 660c for powder diffraction, Powder Diffraction 35 (2020) 17–22. https://doi.org/10.1017/S0885715620000068.

[238] M.A. Kriglovaz, K.P. Ryaboshapka, Theory of X-ray scattering by crystals containing dislocations, screw and edge dislocations randomly distributed throughout the crystal, Fizika Metallov i Metallovedenie 15 (1963) 18–31.

[239] M.A. Kriglovaz, Influence of correlation in position of dislocations on X-ray diffraction by deformed crystals, Physics of Metals and Metallography 55 (1984) 1–12.

[240] M. Wilkens, Fundamental aspects of dislocation theory, in: J.A. Simmons, R. de Wit, R. Bullough (Eds.), Fundamental aspects of dislocation theory: conference proceedings, National Bureau of Standards, April 21-25, 1969, US National Bureau of Standards, Washington DC, USA, 1970, pp. 1191–1193.

[241] M. Wilkens, The determination of density and distribution of dislocations in deformed single crystals from broadened X-ray diffraction profiles, Physica Status Solidi (A) 2 (1970) 359–370. https://doi.org/10.1002/pssa.19700020224.

[242] P. Scardi, C.L. Azanza Ricardo, C. Perez-Demydenko, A.A. Coelho, Whole powder pattern modelling macros for TOPAS, Journal of Applied Crystallography 51 (2018) 1752–1765. https://doi.org/10.1107/S160057671801289X.

[243] A. Drexler, W. Siegl, W. Ecker, M. Tkadletz, G. Klösch, H. Schnideritsch, G. Mori, J. Svoboda, F.D. Fischer, Cycled hydrogen permeation through Armco iron – a joint experimental and modeling approach, Corrosion Science (2020) 109017. https://doi.org/10.1016/j.corsci.2020.109017.

[244] J. Syarif, K. Nakashima, T. Tsuchiyama, S. Takaki, Effect of Solute Copper on Yield Strength in Dislocation-strengthened Steels, ISIJ International 47 (2007) 340–345. https://doi.org/10.2355/isijinternational.47.340.

[245] K. Kawasaki, H. Hidaka, T. Tsuchiyama, S. Takaki, Effect of Grain Size on Microstructure Development during Deformation in Polycrystalline Iron, in: M.J. Zehetbauer, R.Z. Valiev (Eds.), Nanomaterials by Severe Plastic Deformation: Proceedings of the Conference "Nanomaterials by Severe Plastic Deformation - NANOSPD 2", December 9-13, 2002, Vienna, Austria, first ed., Wiley-VCH, Weinheim, Germany, 2004, pp. 345–350.

[246] A.I. Yurkova, Y. v. Milman, A. v. Byakova, Structure and mechanical properties of iron subjected to surface severe plastic deformation by attrition: II. Mechanical properties of nano- and submicrocrystalline iron, Russian Metallurgy (Metally) 2010 (2010) 258–263. https://doi.org/10.1134/S0036029510040026.

[247] S. Kalpakjian, S.R. Schmid, E.A. Werner, Werkstofftechnik, fifth ed., Pearson Studium/Pearson Education, Munich, 2011.

[248] W.W. Seidel, F. Hahn, Werkstofftechnik: Werkstoffe - Eigenschaften - Prüfung - Anwendung, eleventh ed., Hanser, Munich, 2018.

[249] H. Gräfen, Lexikon Werkstofftechnik: Berichtigter Nachdruck, Springer, Berlin, Heidelberg, 1993.

[250] J. Cox, Critical stresses for slip, twinning, and cleavage in single crystals of iron, Ship Structure Committee, 1954.

[251] G. Spur, H.-W. Zoch, Handbuch Wärmebehandlung und Oberflächentechnik, second ed., Hanser, Munich, 2015.

[252] R. Pippan, S. Scheriau, A. Hohenwarter, M. Hafok, Advantages and Limitations of HPT: A Review, Materials Science Forum 584-586 (2008) 16–21. https://doi.org/10.4028/www.scientific.net/MSF.584-586.16.

[253] F. Wetscher, R. Pippan, Cyclic high-pressure torsion of nickel and Armco iron, Philosophical Magazine 86 (2006) 5867–5883. https://doi.org/10.1080/14786430600838288.

[254] J. Čížek, O. Melikhova, Z. Barnovská, I. Procházka, R.K. Islamgaliev, Vacancy clusters in ultra fine grained metals prepared by severe plastic deformation, Journal of Physics: Conference Series 443 (2013) 12008. https://doi.org/10.1088/1742-6596/443/1/012008.

[255] J. Čížek, M. Janeček, T. Vlasák, B. Smola, O. Melikhova, R.K. Islamgaliev, S.V. Dobatkin, The Development of Vacancies during Severe Plastic Deformation, Materials Transactions 60 (2019) 1533–1542. https://doi.org/10.2320/matertrans.MF201937.

[256] P. Hautojärvi, T. Judin, A. Vehanen, J. Yli-Kauppila, J. Johansson, J. Verdone, P. Moser, Annealing of vacancies in electron-irradiated α-iron, Solid State Communications 29 (1979) 855–858. https://doi.org/10.1016/0038-1098(79)90507-6.

[257] M. Kiritani, H. Takata, K. Moriyama, F.E. Fujita, Mobility of lattice vacancies in iron, Philosophical Magazine A 40 (1979) 779–802. https://doi.org/10.1080/01418617908234874.

[258] H.-J. Bargel, G. Schulze (Eds.), Werkstoffkunde, 12th ed., Springer Vieweg, Berlin, 2018.

[259] E. Roos, K. Maile, Werkstoffkunde für Ingenieure: Grundlagen, Anwendung, Prüfung, fifth ed., Springer Vieweg, Berlin, 2015.

[260] W. Bleck, E. Moeller (Eds.), Handbuch Stahl: Auswahl, Verarbeitung, Anwendung, Hanser, Munich, 2017.

[261] H. Fuchigami, H. Minami, M. Nagumo, Effect of grain size on the susceptibility of martensitic steel to hydrogen-related failure, Philosophical Magazine Letters 86 (2006) 21–29. https://doi.org/10.1080/09500830500482316.

[262] M. Zehetbauer, G. Steiner, E. Schafler, A.V. Korznikov, E. Korznikova, Deformation Induced Vacancies with Severe Plastic Deformation: Measurements and Modelling, Materials Science Forum 503-504 (2006) 57–64. https://doi.org/10.4028/www.scientific.net/MSF.503-504.57.

[263] NACE International, Standard test method: Laboratory testing of metals for resistance to sulfide stress cracking and stress corrosion cracking in H_2S environments, NACE International, Houston, TX, USA, 2005.

[264] A.D. Rollett, G.S. Rohrer, J. Humphreys, Recrystallization and related annealing phenomena, third ed., Elsevier, Amsterdam, 2017.

[265] M.R. Louthan, J.A. Donovan, G.R. Caskey, Tritium Absorption in Type 304L Stainless Steel, Nuclear Technology 26 (1975) 192–200. https://doi.org/10.13182/NT75-A24418.

[266] S.M. Charca, O.N. Uwakweh, V.S. Agarwala, Hydrogen Transport Conditions and Effects in Cathodically Polarized AF1410 Steel, Metallurgical and Materials Transactions A 38 (2007) 2389–2399. https://doi.org/10.1007/s11661-007-9241-3.

[267] F. Huang, J. Liu, Z.J. Deng, J.H. Cheng, Z.H. Lu, X.G. Li, Effect of microstructure and inclusions on hydrogen induced cracking susceptibility and hydrogen trapping efficiency of X120 pipeline steel, Materials Science and Engineering: A 527 (2010) 6997–7001. https://doi.org/10.1016/j.msea.2010.07.022.

8 List of Abbreviations

A	area or reaction rate constant
at%	atomic percent
Bal.	balance
bcc	body-centered cubic
c	concentration
c_0	equilibrium hydrogen concentration
c_∞	steady-state hydrogen concentration at entry side
c_{app}	apparent hydrogen concentration at entry side
c_H	hydrogen concentration
c_L	lattice hydrogen concentration
c_T	trapped hydrogen concentration
c_{total}	total hydrogen concentration
$c_{x=0}$	hydrogen concentration at entry side
$c_{x=L}$	hydrogen concentration at exit side
d	diameter
D	diffusion coefficient
D_0	frequency factor
D_{app}	apparent diffusion coefficient
D_{eff}	effective diffusion coefficient
$D_{eff,1}$	effective diff. coeff. determined from first charging cycle of EP
$D_{eff,2}$	effective diff. coeff. determined from second charging cycle of EP
D_L	lattice diffusion coefficient
DFT	density functional theory
DTA	differential thermal analysis
E_a	trap activation energy/detrapping energy
E_b	trap binding energy
E_D	activation energy for diffusion/migration energy
E_s	saddle point energy
E	energy
E^d	activation energy for detrapping
E^t	activation energy for trapping
EBSD	electron backscatter diffraction
EDX	energy-dispersive X-ray spectroscopy
EP	electrochemical permeation
f	fugacity
F	Faraday constant
fcc	face-centered cubic

H_{abs}	absorbed hydrogen
H_{ads}	adsorbed hydrogen
HER	hydrogen evolution reaction
HPT	high pressure torsion
i_∞	steady-state oxidation current density
$i_{\infty,1}$	steady-state oxidation current density of first charging cycle of EP
$i_{\infty,2}$	steady-state oxidation current density of second charging cycle of EP
I_∞	steady-state oxidation current
$I_{\infty,1}$	steady-state oxidation current of first charging cycle of EP
$I_{\infty,2}$	steady-state oxidation current of second charging cycle of EP
j	hydrogen permeation flux per area
j_∞	steady-state hydrogen flux per area
$j_{\infty,1}$	steady-state hydrogen flux per area of first charging cycle of EP
$j_{\infty,2}$	steady-state hydrogen flux per area of second charging cycle of EP
j_D	diffusing particle flux
k	trapping rate parameter
k_0	pre-exponential factor for capture rate
K	equilibrium constant
K_S	Sieverts' constant
L	thickness
M	time lag factor
(M)	empty site at metal surface
[M]	empty interstitial lattice site beneath surface
n	reaction order
N_A	Avogadro constant
N_L	density of trap sites per unit volume
N_T	density of lattice sites per unit volume
OCP	open circuit potential
OEM	optical emission spectrometry
p	pressure or detrapping rate parameter
p_0	pre-exponential factor for release rate
p_{H2}	partial pressure of hydrogen
pps	patterns per second
R	universal gas constant
R^2	coefficient of determination
Ref.	reference
S	solubility
SEM	scanning electron microscopy
SHE	standard hydrogen electrode
SPD	severe plastic deformation
t	time

$t_{1/2}$	half-rise time
t_b	breakthrough time
$t_{b,1}$	breakthrough time of first charging cycle of EP
$t_{b,2}$	breakthrough time of second charging cycle of EP
t_b^g	breakthrough time for galvanostatic charging (time characteristic)
t_b^p	breakthrough time for potentiostatic charging (time characteristic)
t_i	inflection-point time
t_i^g	inflection-point time for galvanostatic charging
t_i^p	inflection-point time for potentiostatic charging
t_{lag}	time lag
t_{lag}^g	time lag for galvanostatic charging
t_{lag}^p	time lag for potentiostatic charging
T	temperature
T_i	initial temperature
T_m	melting point
T_p	desorption temperature/peak temperature
T_R	recrystallization temperature
TDA	thermal desorption analysis
TDS	thermal desorption spectroscopy
TEM	transmission electron microscopy
wt%	weight percent
x	location
X	fraction of released species
XRD	X-ray diffraction
Δ	Laplace operator
ΔH^0_{sol}	enthalpy of solution
θ	fractional occupancy
θ_L	fractional occupancy of lattice sites
θ_T	fractional occupancy of trap sites
ϕ	heating rate
Φ	permeation coefficient/permeability
∇	nabla operator